論文 / 著書情報
Article / Book Information

題目(和文)	HETE-2衛星が観測したX線フラッシュとX線過剰ガンマ線バーストの放射スペクトルの研究
Title(English)	Spectral characteristics of X-ray flashes and X-ray rich gamma-ray bursts observed by HETE-2
著者(和文)	坂本貴紀
Author(English)	
出典(和文)	学位:博士(理学), 学位授与機関:東京工業大学, 報告番号:甲第5611号, 授与年月日:2004年3月26日, 学位の種別:課程博士, 審査員:
Citation(English)	Degree:Doctor (Science), Conferring organization: Tokyo Institute of Technology, Report number:甲第5611号, Conferred date:2004/3/26, Degree Type:Course doctor, Examiner:
学位種別(和文)	博士論文
Type(English)	Doctoral Thesis

Spectral characteristics of X-ray flashes and X-ray rich Gamma-Ray Bursts observed by HETE-2

Takanori Sakamoto

Department of Physics. Graduated School of Science,
Tokyo Institute of Technology, Tokyo, Japan

Submitted to the Department of Physics,
Tokyo Institute of Technology on March 1, 2004,
in partial fulfillment of the requirements for
the degree of Doctor of Philosophy

March 1, 2004

Abstract

We present the detailed and systematic study of the spectral characteristics of the X-ray flashes (XRF) and the X-ray rich gamma-ray bursts (GRBs) observed by *HETE*. Eighteen XRFs and X-ray rich GRBs are studied in detail. Total of 45 GRBs observed from January 2001 to September 2003 are used in the systematic study of the prompt emission. We performed joint analyses for both spectral data of the X-ray instrument called Wide-field X-ray Monitor (WXM) and the γ-ray instrument called FREnch GAmma TElescope (FREGATE) on board *HETE*.

The spectral characteristics of the XRFs and the X-ray rich GRBs are very similar to those of hard GRBs except that the peak energy in $\nu \mathrm{F}_\nu$ spectrum (E_{peak}) is lower. The spectrum of both XRFs and X-ray rich GRBs can be expressed with the empirical GRB models (Band function or power-law times exponential cutoff model). The XRFs and the X-ray rich GRBs show similar durations as the long GRBs, the complex time-structures, the spectral softening during the bursts, and lower E_{peak} energies compared to hard GRBs which have typical E_{peak} energies of $\sim$ 250 keV. Six XRFs show E_{peak} energies of a few keV.

From the systematic study of 45 GRBs, we found: 1) X-ray to γ-ray energy fluence ratio forms a single distribution from XRFs to hard GRBs; 2) the number of XRFs is comparable to that of hard GRBs; 3) the lower-energy photon index α is distributed with a centroid around -1.0 for all GRBs; and 4) E_{peak} energy has a good positive correlation with the time-averaged flux, and also with the one-second peak photon flux in the γ-ray range. This may imply that XRFs are intrinsically weaker than hard GRBs.

With 10 redshift-determined *HETE* localized GRBs, the relation between the redshift-corrected E_{peak} and the isotropic-equivalent energy are investigated. Our sample includes one XRF, GRB020903, with the redshift of 0.25. We confirmed the relation, $E_{\mathrm{peak}} \propto E_{\mathrm{iso}}^{0.5}$, for hard GRBs. Furthermore, the properties of GRB020903 are consistent with an extension of this relation by a factor of $\sim$ 300.

The integrated peak-flux distribution ("log N-log P" relation) of XRFs is close to that expected for the Euclidean geometry. This may imply that XRFs have a closer distance scale than that of weak hard GRBs.

We discuss the implication of this observational study on several theoretical XRF models based on the observational results of this study.

Contents

List of Figures

List of Tables

Chapter 1

Introduction

It has been thirty years since the discovery of Gamma-Ray Bursts (GRBs) was first reported in 1973 by Klebesadel et al. [43]. Since that time, two main breakthroughs in GRB research have occurred.

The first was provided by the Burst And Transient Source Experiment (BATSE) instrument on-board the *Compton Gamma-Ray Observatory*. BATSE consisted of eight scintillators, each 51 cm in diameter, situated at the eight corners of the spacecraft. It was capable of determining the arrival direction of GRBs with an accuracy of a few degrees. BATSE observed 2704 GRBs in its 9 year mission, and found that while the distribution of GRBs is isotropic, the paucity of very faint GRBs compared with the number expected from a Euclidean space distribution suggests that the GRB source population is inconsistent with a Galactic distribution [58]. These properties indicated that the distance scale to GRB sources is cosmological. However, confirmation of this inference had to wait for the direct measurement of the distance (see a lively debate of the cosmological and Galactic hypotheses by Paczyński [59] and Lamb [45]).

The second breakthrough was the discovery that GRBs have afterglows. This revolutionary discovery was made by the *Beppo*SAX satellite. *Beppo*SAX had two X-ray instruments; Wide Field Camera (WFC) and Narrow Field Instruments (NFI). WFC had a $40^\circ \times 40^\circ$ field-of-view, and could find the transient sources and localize them with an accuracy of ~ 5 arcminutes. NFI was composed of the X-ray detectors (proportional counters) and the X-ray mirrors, and could obtain localizations accurate to better than an arcminute. On February 28, 1997, the WFC observed Gamma-ray burst GRB970228. NFI was pointed to the burst position 8 hours after the trigger, and detected an uncatalogued X-ray source with a 2–10 keV flux of several 10^{-12} erg cm^{-2} s^{-1} at the edge of the WFC error box. Four days later, the flux of this source had decreased by a factor of ~ 20 [12].

This was only the beginning, however. An optical counterpart of GRB970228 was also detected. Groot et al. [31] discovered a decaying 21st magnitude object with the William Herschel and Isaac Newton Telescope. The deeper images made with the ESO New Technology Telescope [32] and the Keck Telescope [53] showed a $\sim 1''$ extended object at the location of the optical transient. This object later turned out to be a galaxy at redshift $z = 0.695$, and is almost certainly the host galaxy of the GRB. GRB970228 was the first of many detected GRBs with afterglows, whose distances were measured directly by the observation of redshifted spectral lines — either emission lines from the host galaxy, or absorption lines in the spectrum of the afterglow itself. We now know that the distances to most of the long GRBs are cosmological ($z \sim 1$).

Prompt X-ray emission was known to be common in GRBs from the early days of their discovery. The earliest reports of prompt X-ray emission in GRBs concerned the bursts of 1972 April 27 ([52], [104]) and 1972 May 14 [111]. The April 27 event was observed by the X-ray (2.0–7.9 keV) and γ-ray (0.067–5.1 MeV) spectrometers on board *Apollo 16* and also by the *Vela 6A* satellite. The authors performed detailed spectral and temporal studies combining X-ray and γ-ray data. They found similar time variability in both energy ranges, and successfully measured the spectrum ranging over four orders of magnitude. The May 14 event was simultaneously observed by six different X-ray and γ-ray instruments — the γ-ray detectors ($\sim$ 0.1–1.5 MeV) on three *Vela* satellites, the solar-flare γ-ray detector ($\sim$ 0.1–1.5 MeV) on the *IMP-6* satellite, and two X-ray telescopes (7–500 keV) on board *OSO-7*. The authors reported hard-to-soft spectral evolution during the burst using the X-ray data. These early observations confirmed that GRBs produce significant amounts of X-ray emission.

In the early 1980s, unidentified X-ray transient sources called "fast X-ray transients" were reported by several authors. The Sky Survey Instrument (SSI) on *Ariel V* (15 October 1974 - 14 March 1980) scanned the sky for 5.5 yr in the energy band 2–18 keV with a time resolution of $\sim$ 100 minutes. Pye and McHardy [67] performed a systematic search of the SSI database and found 27 candidates, including one coincident with a GRB (GB 751102). Although most of these events might be nearby RS CVn-like systems, some may possibly have been related to transient sources associated with GRBs.

The *HEAO-1* (12 August 1977 - 9 January 1979) A-1 experiment (Large Area Sky Survey experiment; 0.25–25 keV) had complete coverage of the entire sky. Ambruster and Wood [3] searched the first 7 months of the A-1 data and found 10 fast transients. Although the error boxes of three sources included M dwarf flare stars and one source was identified with a RS CVn system, six sources remained unidentified. One source, H0547–14, could have been a weak

GRB with a photon spectral index $\alpha = 1.65 \pm 0.14$, and a high hydrogen column density $N_H = (9.2 \pm 1.7) \times 10^{22}$ cm^{-2} [2].

Gotthelf et al. [33] searched for the X-ray counterparts of GRBs in the data from the *Einstein* (12 November 1978 - April 1981) Imaging Proportional Counter (IPC; 0.2–3.5 keV). They found 42 candidates including 18 hard and 24 soft sources (their definition of hard (soft) is ratio of 0.2–1.3 keV counts to 1.3–3.5 keV counts smaller (larger) than unity). The authors suggested that the hard 18 sources might be the X-ray counterparts of GRBs.

The *ROSAT* (1 June 1990 - 12 February 1999) all-sky survey data were searched by Greiner et al. [34] for X-ray afterglows. Although they found 23 X-ray afterglow candidates, the expected number in RASS was ~ 4 events. The search for the optical counterparts of six randomly selected X-ray sources was also conducted. Five out of six X-ray error circles contained M stars.

Because of the considerable interest in X-ray observations of GRBs, the *Ginga* (February 5, 1987 - November 1, 1991) gamma-ray burst detector (GBD) was specifically designed to investigate burst spectra in the X-ray range. The success of the *Ginga* GBD observation of GRBs paved the way for the next generation GRB satellite, the High Energy Transient Experiment (*HETE*) mission. The details about the GBD observations are summarized in chapter 2.

In this thesis, we focus on the characteristics of the prompt emission of the sub-classes of GRBs called X-ray flashes (XRFs) and X-ray rich GRBs. These GRBs have a high fluence in the X-ray range (e.g. 2–30 keV) unlike the GRBs typically observed by BATSE. XRFs and X-ray rich GRBs were first studied in detail by the *Ginga* satellite [97] and their spectral characteristics were investigated by *Beppo*SAX ([36], [42]). The recent results of Kippen et al. [42], indicate that XRFs and X-ray rich GRBs are probably aspects of the same phenomenon that is responsible for ordinary GRBs.

This thesis comprises analyses of 45 XRFs/X-ray rich GRBs/GRBs observed by *HETE* from February 2001 to September 2003. Of these, 18 XRFs and X-ray rich GRBs are subjected to detailed study. The contents of the thesis are as follows: The review of GRB observations of both prompt emission and afterglows are given in chapter 2. Theoretical XRF/GRB emission models are summarized in chapter 3. Chapter 4 contains the detailed description of the *HETE* satellite. The data reduction and analysis methods are described in chapter 5. The individual prompt emission characteristics of 18 XRFs and X-ray rich GRBs are described in chapter 6. The systematic study of XRFs and X-ray rich GRBs is described in chapter 7. I discuss the sky distribution and event rate of XRFs, logN-logP of XRFs, the magnetic field strength at the shocked region, and theoretical models of XRFs based on our observational results in chapter

8. Chapter 9 contains the conclusions. The development and calibration of the WXM detector response matrix, *HETE* GRB summary tables, figures of the all spectra and light curves, and the description of the *constrained* Band function are presented in the appendices.

Chapter 2

Observational properties of GRBs

2.1 Prompt emission

2.1.1 Spectral parameters of the BATSE GRB sample

The spectral characteristics of the prompt emission of GRBs were studied in detail with the Burst and Transient Source Experiment (BATSE) on the *Compton Gamma Ray Observatory*. Preece et al. [63] selected 156 BATSE bursts with fluence in the 30–1000 keV band larger than 4×10^{-5} ergs cm^{-2} or with a 1s peak flux in the 50–300 keV band exceeding 10 photons cm^{-2} s^{-1}. Each burst is divided into several time intervals, and there are 5500 spectra in total. The BATSE GRB spectra are well fitted with the Band function [6]. The Band function is an empirical spectral model described as following:

$$f_{\rm GRB}(E) = A(E/100)^{\alpha}\exp(-E(2+\alpha)/E_{\rm peak})$$

$$\text{if} \qquad E < (\alpha-\beta)E_{\rm peak}/(2+\alpha) \equiv E_{\rm break},$$

$$\text{and} \qquad f(E) = A(\alpha-\beta)E_{\rm peak}/[100(2+\alpha)]^{\alpha-\beta}\exp(\beta-\alpha)(E/100)^{\beta}$$

$$\text{if} \qquad E \geq (\alpha-\beta)E_{\rm peak}/(2+\alpha), \tag{2.1}$$

where the four model paramters are

1. the amplitude A in photons s^{-1} cm^{-2} keV^{-1}
2. a low-energy spectral index α
3. a high-energy spectral index β, and

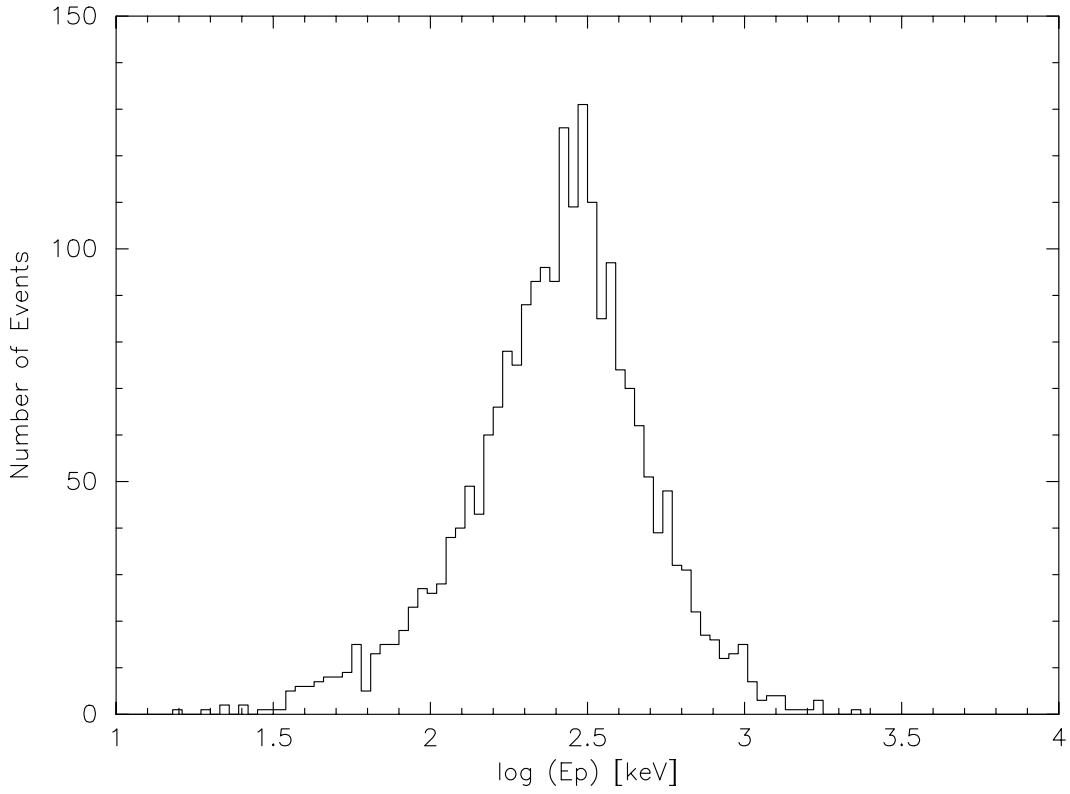

Figure 2.1: BATSE $E_{\rm peak}$ distribution from Band function fit [63].

4. a νF_ν "peak" energy $E_{\rm peak}$.

The distributions of the BATSE spectral parameters ($E_{\rm peak}$, α, and β) in the Band function are shown in figures 2.1, 2.2, and 2.3 respectively. As seen in figure 2.1, $E_{\rm peak}$ is tightly concentrated around 250 keV. The power-law indices α and β are clustered around -1 and -3 respectively. This result suggests that the spectra of the prompt emission has a "universal" shape for most of the bursts.

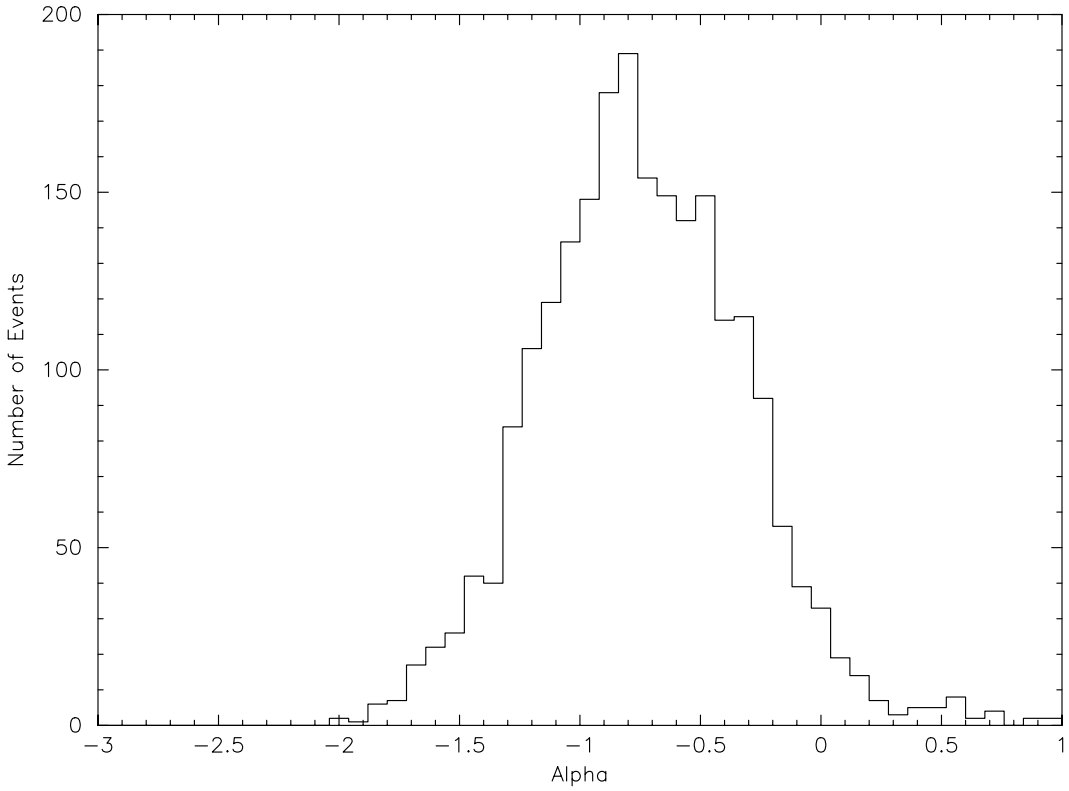

Figure 2.2: BATSE α distribution from Band function fit [63].

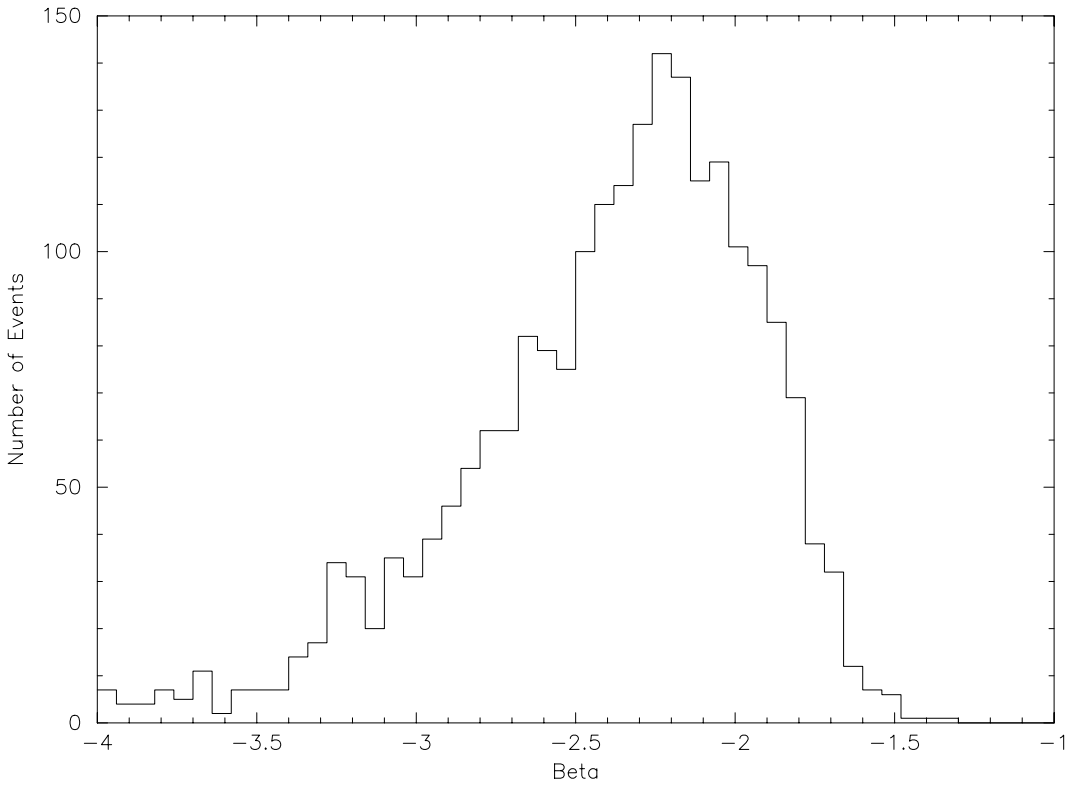

Figure 2.3: BATSE β distribution from Band function fit [63].

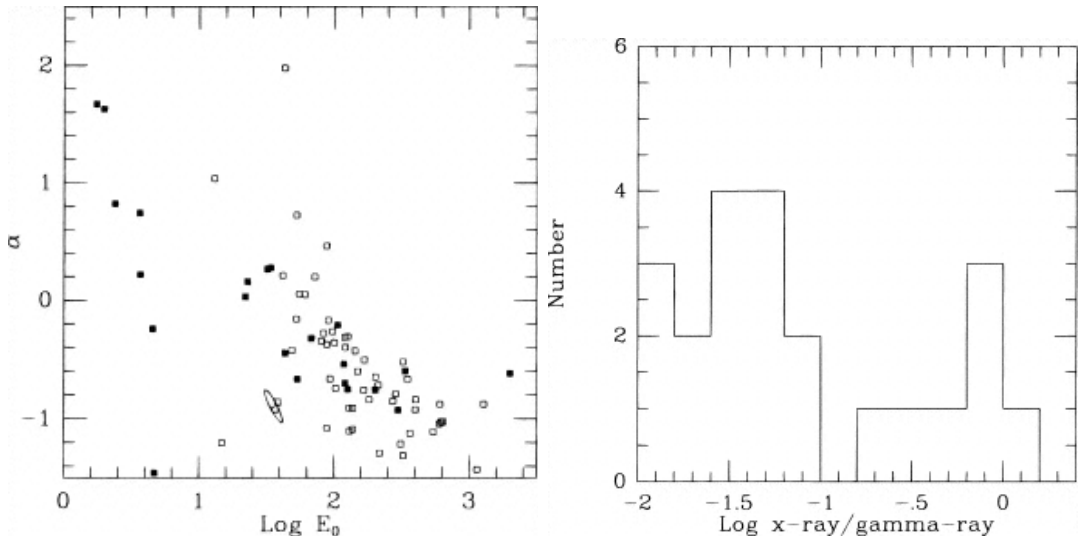

Figure 2.4: Left: The low-energy photon index α vs. the break energy E_0 ($E_0 = E_{\rm peak}$ / (2 + α)). Open squares are 54 BATSE events and the solid squares are the 22 *Ginga* events. Right: Distribution of the fluence ratio between X-rays (2–10 keV) and γ-rays (50–300 keV) [97].

2.1.2 Characteristics of X-ray flashes

There is unique group of the GRBs which exhibit large fluences in the X-ray range (2–30 keV). These GRBs are called X-ray flashes (XRFs). BATSE did not have a good sensitivity for detecting XRFs due to the lower threshold energy of 30 keV. To investigate XRFs, we definitely need an X-ray instrument. Detailed studies of XRFs were performed by the *GINGA* [97] and *Beppo*SAX satellites [36], both of which possessed an X-ray detector.

GINGA XRF sample

Since the *Ginga* gamma-ray burst detector (GBD) consisted of a proportional counter (PC; 2–25 keV) and a scintillation counter (SC; 15–400 keV), GBD had a good capability for observing XRFs. According to Strohmayer et al. [97], GBD observed bursts which show a high X-ray to γ-ray fluence ratio (figure 2.4 right). About 36% of the bright bursts observed by GBD have $E_{\rm peak}$ energy around a few keV (figure 2.4 right). This *Ginga* result is not consistent with the BATSE $E_{\rm peak}$ distribution which is concentrated around 250 keV. The *Ginga* sample indicates that GRB have a much broader range of characteristics, especially considering the lower energy band.

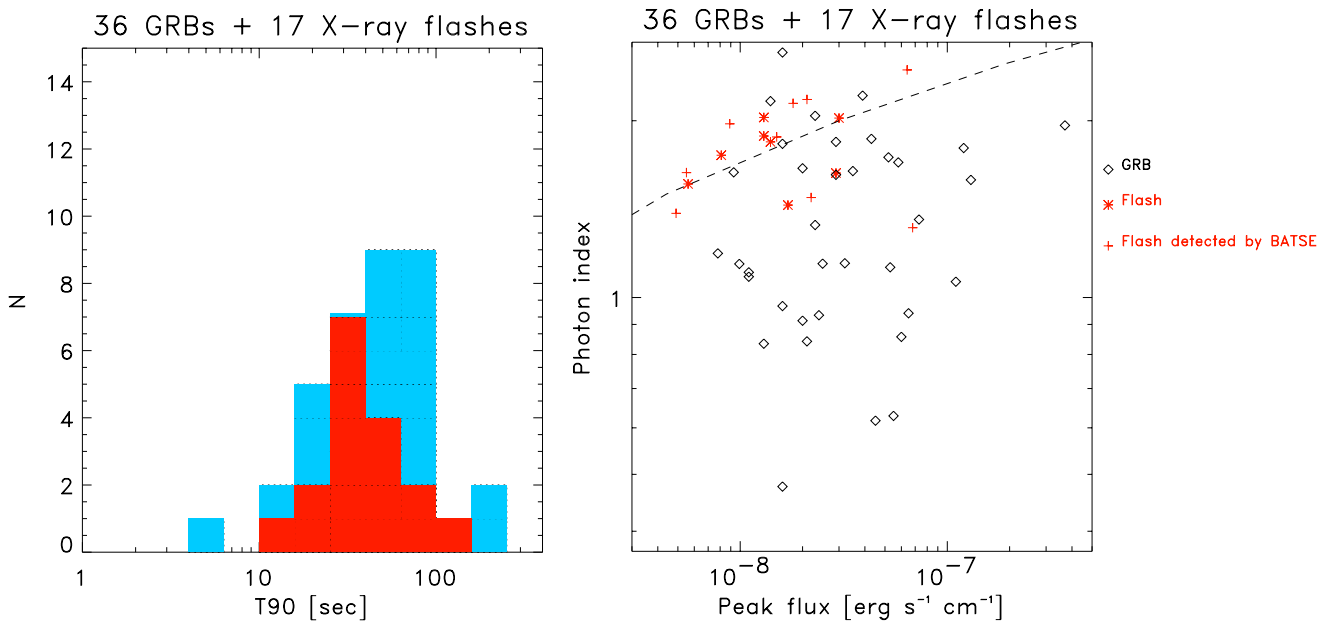

Figure 2.5: Left: Histogram of T90 for hard GRBs (blue) and XRFs (red). Right: The peak flux in 2–25 keV and the photon index in the power-law spectrum [36].

*Beppo*SAX XRF sample

The *Beppo*SAX satellite had a large field of view X-ray instrument called the Wide Field Camera (WFC) which covers an energy range from 2 to 25 keV and a field of view of $40° \times 40°$. The definition of an XRF for the *Beppo*SAX team was a burst which is seen in WFC but not in the γ-ray instrument, called the Gamma Ray Burst Monitor (GRBM; 40–7000 keV). WFC observed 17 XRFs in 5 years [36]. The durations of XRFs are from 10 s to 200 s, which is similar to the long duration GRBs (figure 2.5 left). The peak fluxes in 2–25 keV were in the range of 10^{-8} and 10^{-7} erg s^{-1} cm^{-2}. The spectra in WFC energy range were described by simple power-law model with the photon indices of -3 to -1.2 (figure 2.5 right).

WFC+BATSE XRF sample

Kippen et al. [42] searched for the GRBs and XRFs which were observed in both WXC and BATSE. 36 hard GRBs and 17 XRFs were found in 3.8 years when WXM and BATSE were operated simultaneously. The WFC and BATSE joint spectral analysis of XRF shows that their $E_{\rm peak}$ energies are significantly lower than those of the BATSE sample (figure 2.6). The low and the high energy photon indices are the same as the hard GRB ($\alpha \sim -1$ and $\beta \sim -2.5$). $E_{\rm peak}$ has a good correlation with the 1s peak flux in 50–300 keV, but not with the T_{50} duration

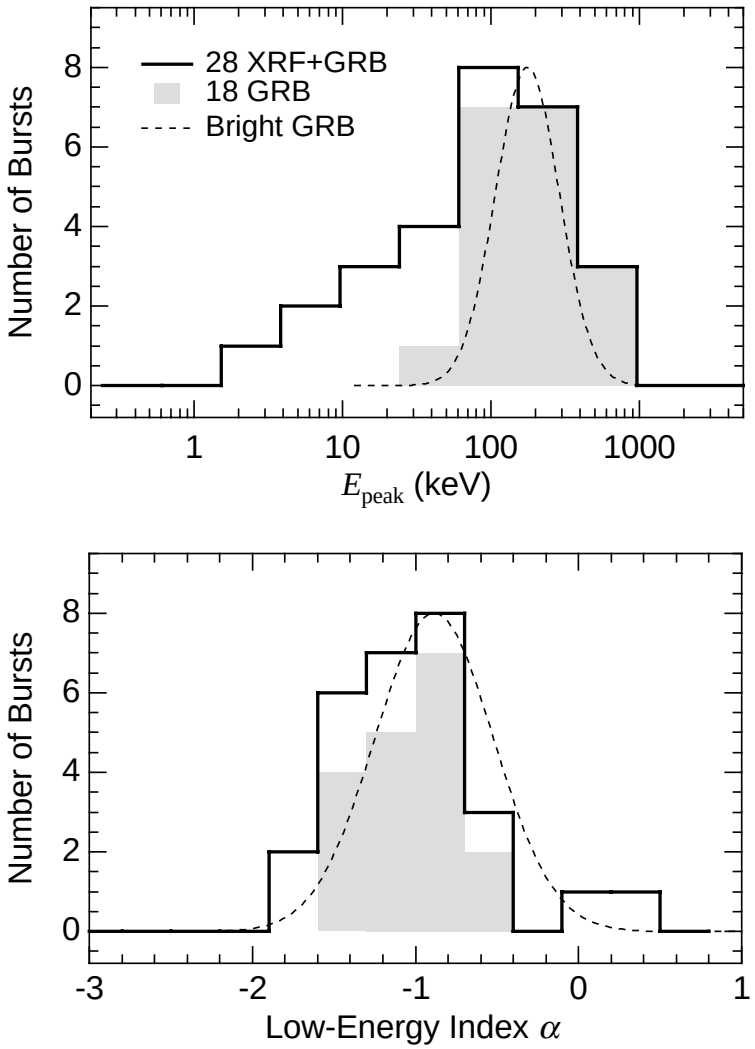

Figure 2.6: The distribution of $E_{\rm peak}$ and α for XRFs compared with the BATSE sample [42].

or the low-energy photon index α (figure 2.7).

2.1.3 $E^{\rm src}_{\rm peak} - E_{\rm iso}$ relation (Amati's relation)

Amati et al. [1] studied the spectral properties of the *Beppo*SAX GRBs with known redshifts (12 GRBs). They investigated the spectral parameters of time-averaged spectra in the GRB source frame (i.e. the redshift corrected spectrum) and found a good correlation between $E_{\rm peak}$ at the source frame and the isotropic equivalent energies in 1–10000 keV; $E^{\rm src}_{\rm peak} \sim E^{0.52\pm0.06}_{\rm iso}$ (figure 2.8). Atteia [5] combined this relation with the duration of the bursts and proposed an empirical redshift indicator.

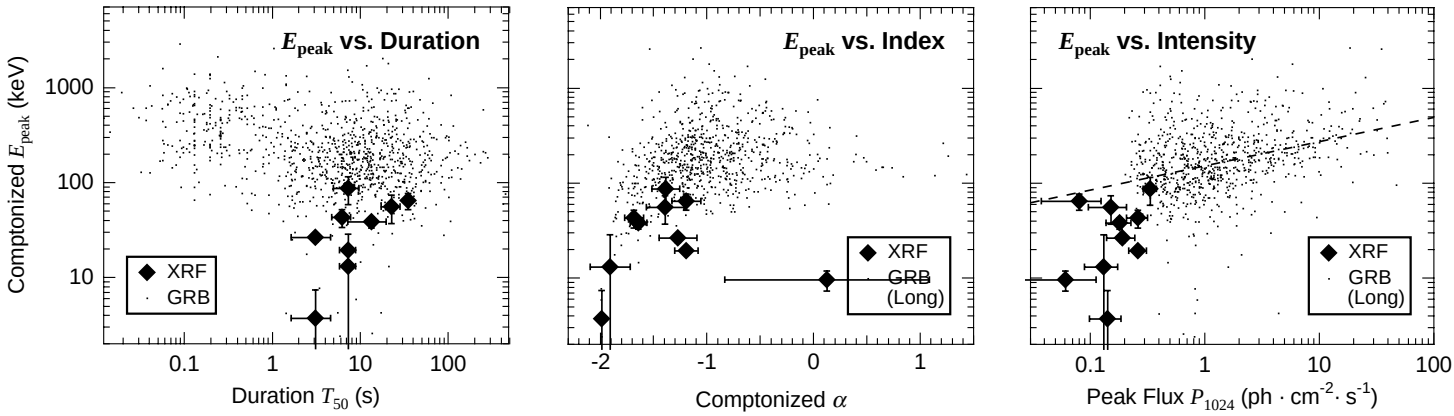

Figure 2.7: The joint fit spectral parameters for XRFs compared with the BATSE sample. The comparison between $E_{\rm peak}$ versus T_{50} duration, α, and 1s peak flux [42].

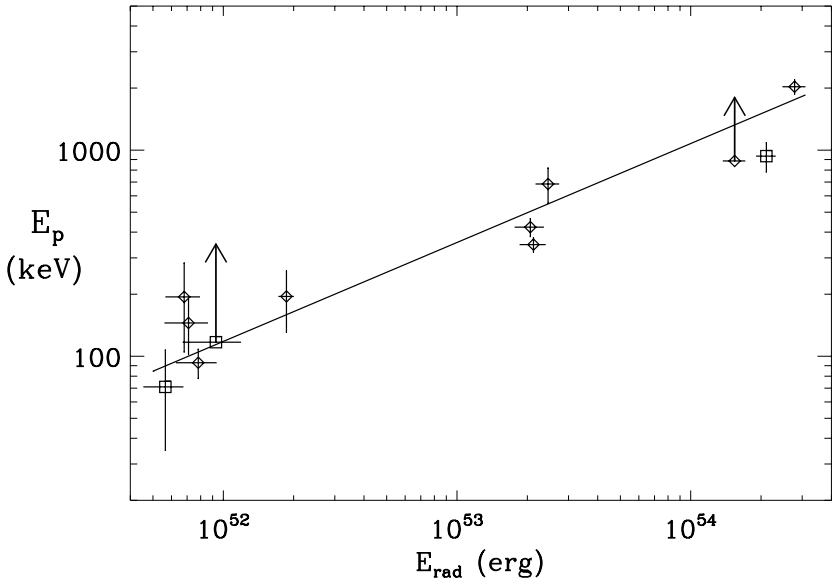

Figure 2.8: The correlation between the isotropic total energy and $E_{\rm peak}$ energy at the GRB source frame [1].

2.1.4 Lag/Variability relation

Norris et al. [56] investigated the spectral lags between two energy bands (25–50 keV and 100-300 keV or > 300 keV) for two samples: the 174 brightest BATSE bursts with durations longer than 2 s and six GRBs with known redshifts. An anti-correlation is found between the γ-ray hardness ratio or peak flux and the spectral lag for the bright BATSE GRB sample (figure 2.9). For the GRBs with known redshift, the relationship between peak luminosity (L) and spectral lag (τ) is well fitted with a power law.

$$\frac{L}{10^{53}\mathrm{erg}} \sim 1.3 \times (\frac{\tau}{0.01\mathrm{s}})^{-1.15}. \tag{2.2}$$

Fenimore and Ramirez-Ruiz [20] (see also [68]) investigated the correlation between the time variability (V) and the luminosity of GRBs (for 7 GRB with redshifts). They found that high (low) variable GRBs are intrinsically more (less) luminous (figure 2.10).

$$\frac{L}{d\Omega} = 3.1 \times 10^{56} V^{3.35}\,\mathrm{erg\,s^{-1}}. \tag{2.3}$$

Schaefer et al. [87] performed a severe test for the lag/variability relation. If both the spectral lag and the variability have correlations with the luminosity, we should see a correlation between the spectral lag and the variability. Since the lag and variability are possible to measure using the large number of BATSE GRBs without any redshift information, the validity of both relations can be examined to high precision. Figure 2.11 shows the plots of lag and variability for 112 BATSE bursts. The correlation coefficient is r = −0.45 (7.6×10^{-7} for chance occurrence), and the lag/variability has a good correlation. Thus both Lag-Luminosity and Variability-Luminosity relation are valid to a high significance.

2.1.5 $\mathbf{V/V_{max}}$

The V/V_{max} test [90] provides a quantitative evaluation of the uniformity of the radial distribution of the objects.

Assuming the Euclidean space, the observed peak count (background subtracted peak counts) of a source will depend on its distance as r^{-2}, so that

$$r_{\max} = r(\frac{C_p}{C_{\lim}})^{\frac{1}{2}}. \tag{2.4}$$

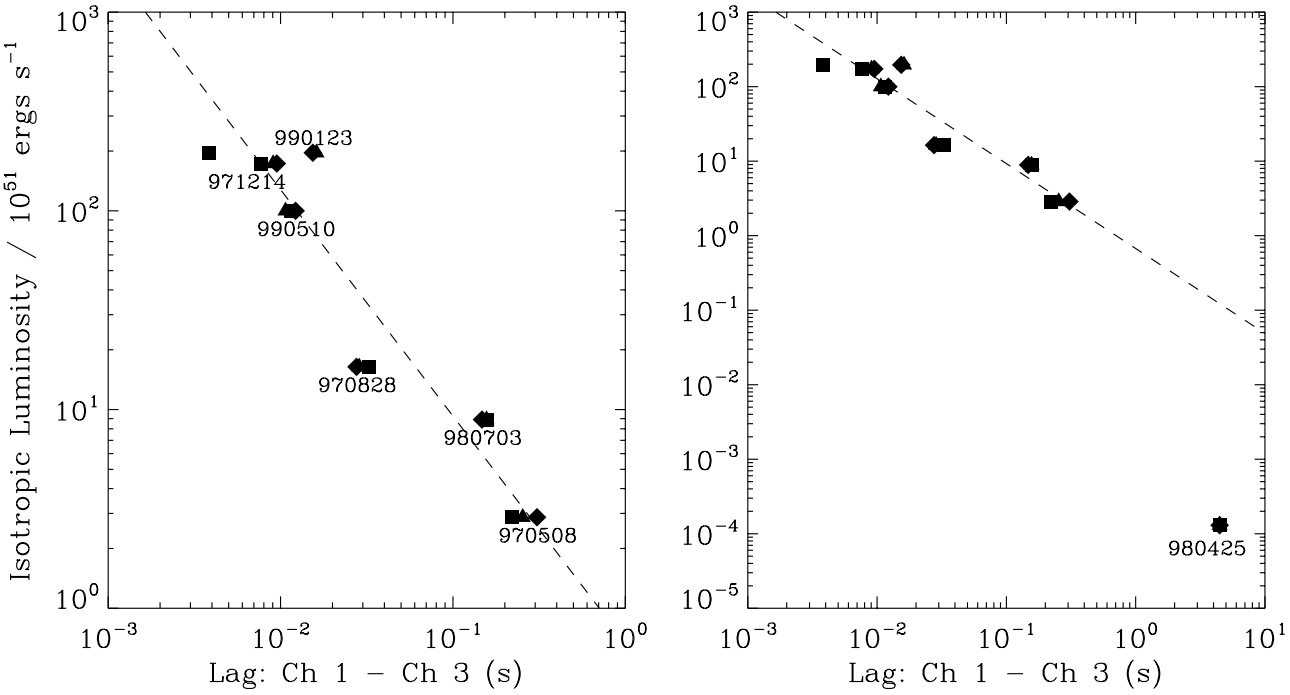

Figure 2.9: Left: the correlation of the spectral lag between 25–50 keV (Ch 1) and 100–300 keV (Ch 3) vs. peak luminosity. The dashed line is the relation of equation (2.2). Right: the luminosity range is expanded to include GRB980425 [56].

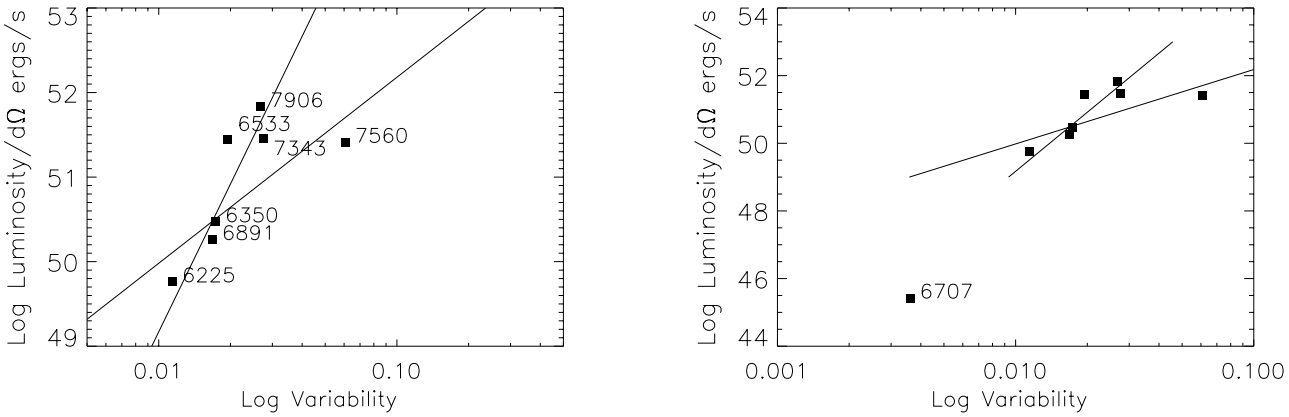

Figure 2.10: Left: Luminosity and variability for BATSE bursts with known redshifts. Right: Luminosity and variability for BATSE bursts including GRB980425 [20].

We characterize the radial location of the source by the ratio of the volume V contained within the radius r to the volume $V_{\max}$ contained within the radius $r_{\max}$. The ratio is $(r/r_{\max})^3$, so

$$V/V_{\max} = (\frac{C_p}{C_{\lim}})^{-\frac{3}{2}}. \tag{2.5}$$

If the sources are have a uniform distribution in space, the distribution of $V/V_{\max}$ should be uniform over the range 0–1. In this case, $< V/V_{\max} >$ is 0.5. Since for sources with a uniform space distribution, $V/V_{\max}$ has a uniform distribution between 0 and 1, the r.m.s. error of $< V/V_{\max} >$ will be $(12n)^{-1/2}$, where n is the number of objects. If the minimum signal-to-noise ratio is set at k, then the limiting count $C_{\lim}$ is

$$C_{\lim} = kB^{0.5}, \tag{2.6}$$

assuming Poisson statistics for the background count B.

Pendleton et al. [60] applied the $V/V_{\max}$ test to the BATSE burst and found that $< V/V_{\max} >$ is 0.329 ± 0.011, which is 15.5 σ away from a homogeneous distribution.

2.1.6 Line of Death Problem in low-energy index α

Preece et al. [62] investigated the low energy spectral index of the BATSE GRBs. The synchrotron shock model (SSM) predicts that the low energy photon index should not exceed $-2/3$ (e.g. [100]). Sari et al. [84] and Sari et al. [85] claimed that the time scale for synchrotron cooling of the particles may be shorter than the duration of the pulses. In this "fast cooling" case, the low energy photon index will be $-3/2$. Figure 2.12 shows the results from the BATSE

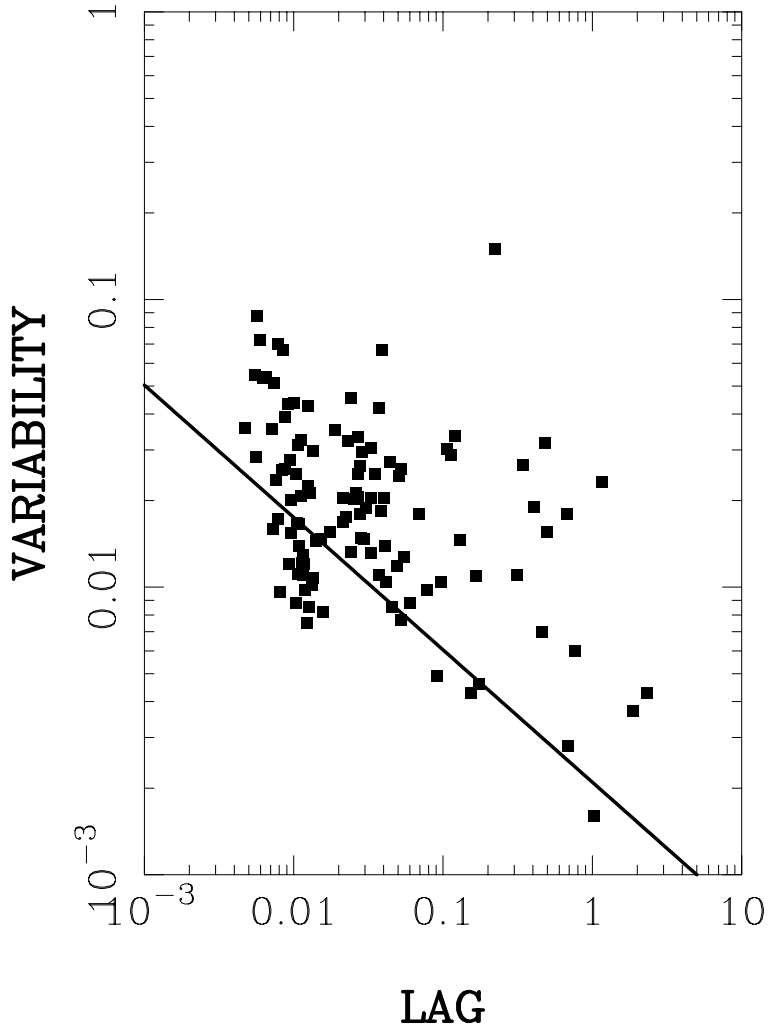

Figure 2.11: Lag/Variability correlation for 112 BATSE bursts. The solid line is the predicted Lag/Variability relation; V = $0.0021\tau_{lag}^{-0.46}$ [87].

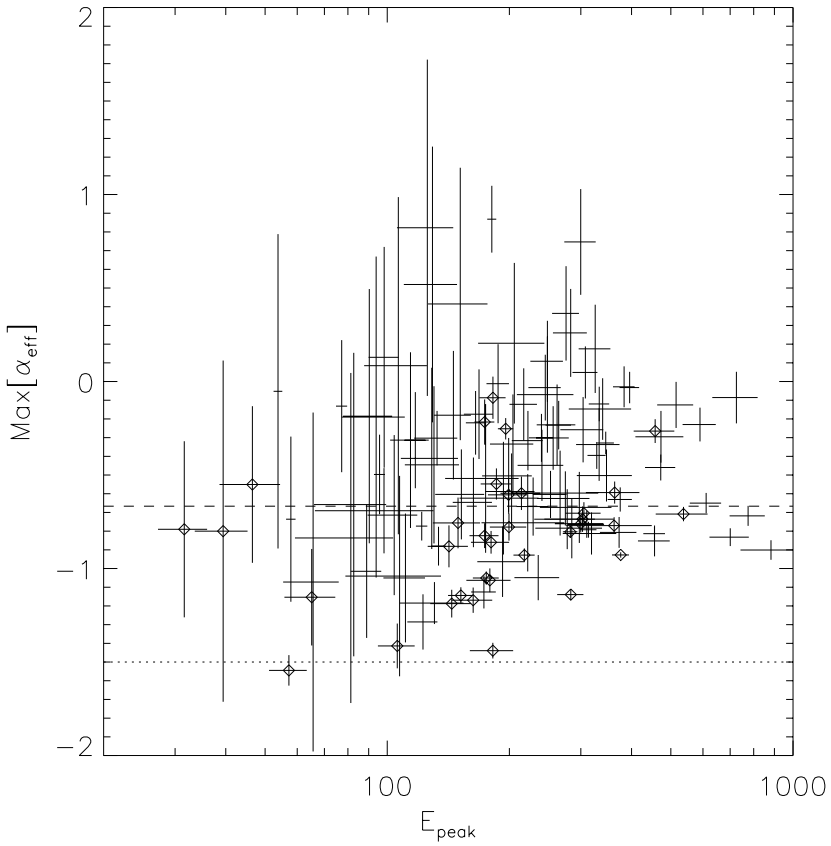

Figure 2.12: Plot of the low energy index vs. $E_{\rm peak}$. The SSM line of death ($\alpha = -2/3$) is drawn as a dashed line and the accepted region in the cooling spectrum ($\alpha = -3/2$) is shown as a dotted line [62].

catalog of time-resolved spectroscopy of bright bursts overlaying the $\alpha = -2/3$ ("death line", dashed line) and the lower boundary of the cooling spectrum ($\alpha = -3/2$, dotted line). It is clear that the observed α is inconsistent with SSM.

Preece et al. [64] applied the additional test of SSM using the observed low and high photon index (α and β) from the BATSE data. Even in this study, Preece et al. [64] claimed that it is not possible to explain the prompt emission of GRB with only SSM.

2.1.7 Extra high-energy spectral component in GRB941017

González et al. [28] analyzed the EGRET's calorimeter TASC (Total Absorption Shower Counter) data for GRB941017 and found an extra high energy component exhibiting a photon index of -1 up to ~ 200 MeV. Its fluence is greater than the lower-energy component observed by BATSE. This high-energy power-law does not show any cutoff, meaning more energy is

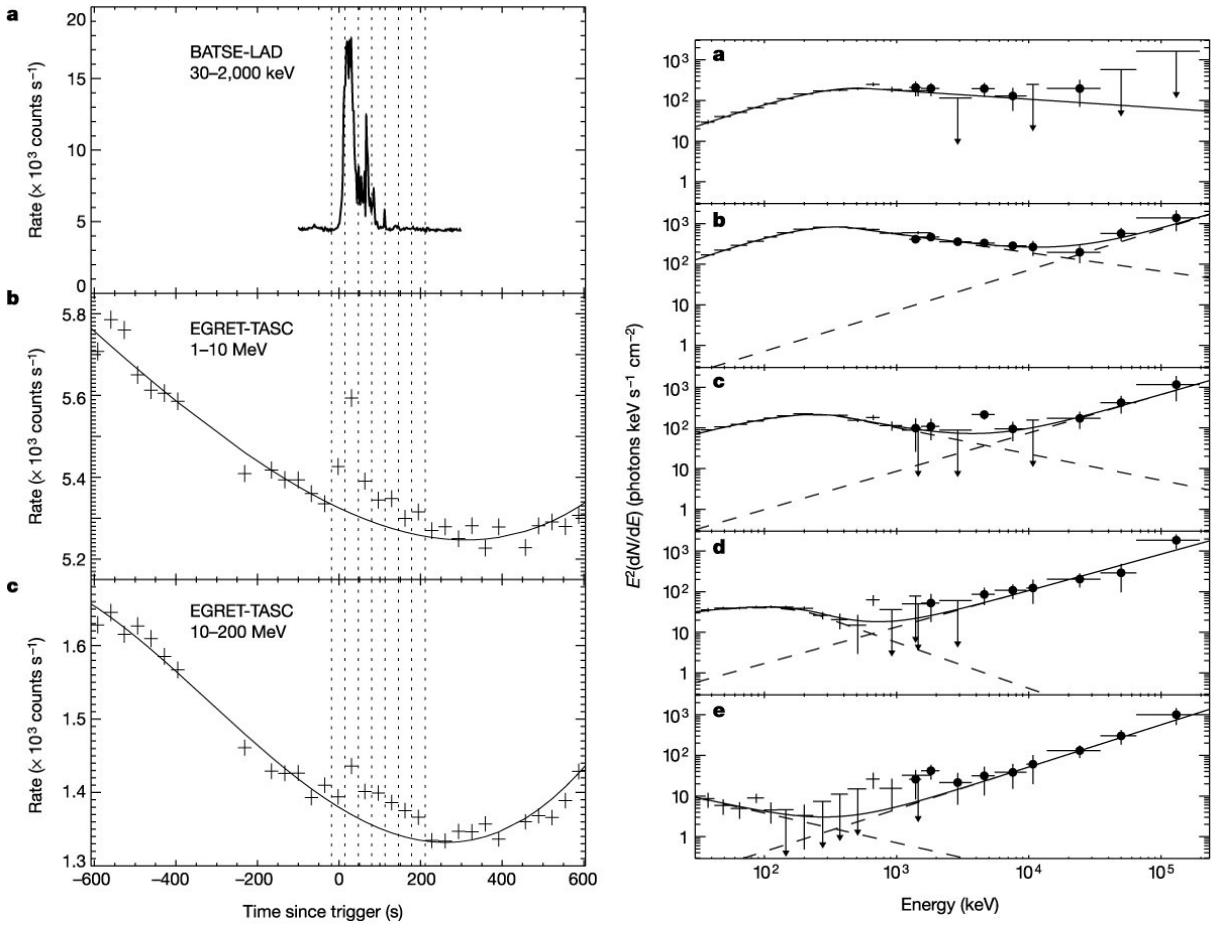

Figure 2.13: Left: light curves of GRB941017 a) BATSE-LAD, b) EGRET-TASC 1–10 MeV, and c) EGRET-TASC 10–200 MeV. Right: time-resolved νF_ν spectrum of GRB941017. The data are jointly analyzed with LAD and TASC [28].

radiated above 200 MeV (figure 2.13). González et al. [28] presented the possibility of ultra-relativistic hadrons producing the MeV γ-rays by inducing electromagnetic cascades through photomeson and photo-pair production.

2.1.8 GRB tail emission

Connaughton [11] developed a sophisticated method of subtracting the background in BATSE data and studied the weak GRB emission on a longer time scale. Connaughton [11] summed and averaged 400 BATSE long GRBs and found the statistically significant tail emission in γ-rays lasting for 1000–2000 seconds after the trigger. The author also found that this tail emission is independent of the duration of the prompt emission and also of the burst intensity. Although it is not clear whether the emission is coming from the prompt emission or from the

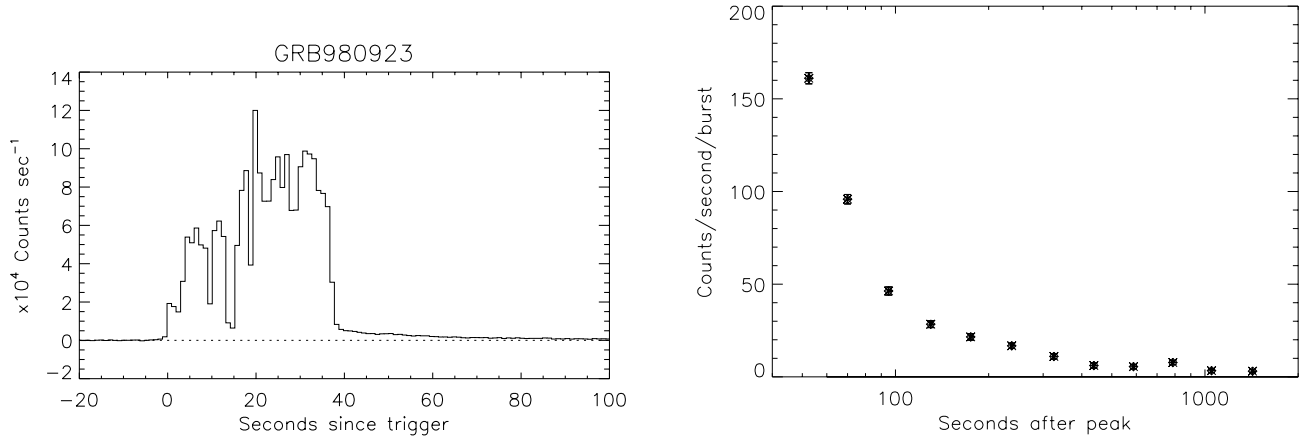

Figure 2.14: Left: background subtracted light curve of GRB980923 [27]. Right: Light curve for 400 long GRBs [11].

afterglow, some signature of the external shock might be seen in the γ-ray region.

2.2 Afterglow

2.2.1 The supernova-GRB connection

Supernova Bump

GRB970228 is the first GRB for which an optical/X-ray counterpart was found. However, the story did not end with this excitement. The optical afterglow of GRB970228 showed a significant deviation from the pure power-law decay about 1–2 weeks after the burst [25]. This might be the evidence for the presence of a supernova component in the light curve. The first suggestion of the supernova bump in the GRB afterglow was made by Bloom et al. [8] for GRB980326. This was a very important observational indication of the association between a supernova and a GRB.

SN1998bw/GRB980425

The most suggestive evidence for the supernova and GRB connection before the *HETE-2* era was SN1998bw/GRB980425. The *BeppoSAX* detected the GRB980425 and the WFC error box contained the supernova SN1998bw located in a spiral arm of the nearby galaxy ESO184-G82 with a distance of 40 Mpc (z=0.0085) [24] (figure 2.16). The chance probability of detecting any supernova with peak optical flux a factor of 10 below that of SN1998bw in the error box is

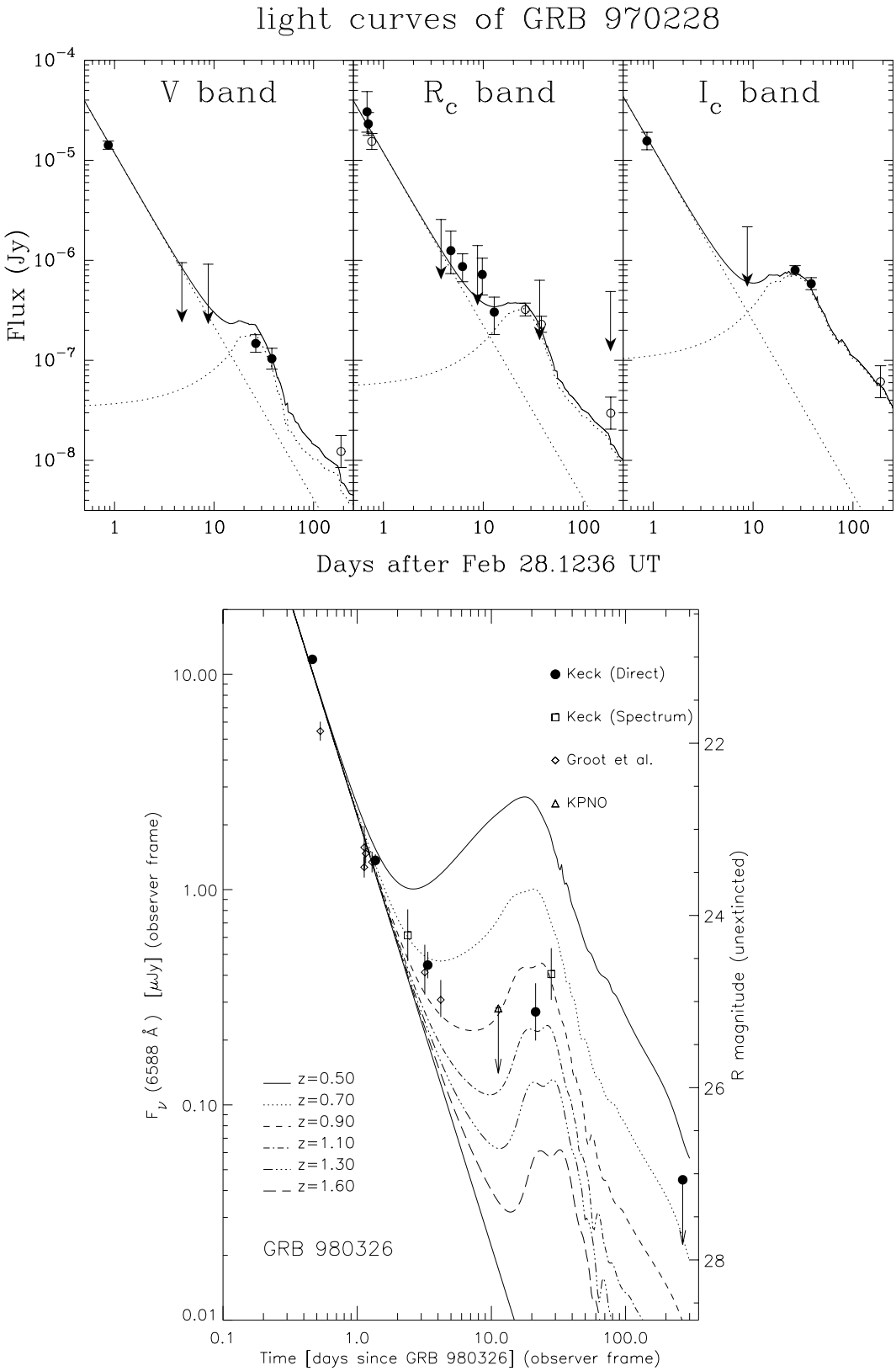

Figure 2.15: Top: V, R_c, I_c band lingt curves of GRB970228. The dotted curves indicate power-law decays with -1.51 and redshifted SN 1998bw light curves [25]. Bottom: the R band light curve of GRB980326. Overlaid curves are the power-law afterglow decline summed with the bright supernova light curve at different redshifts [8].

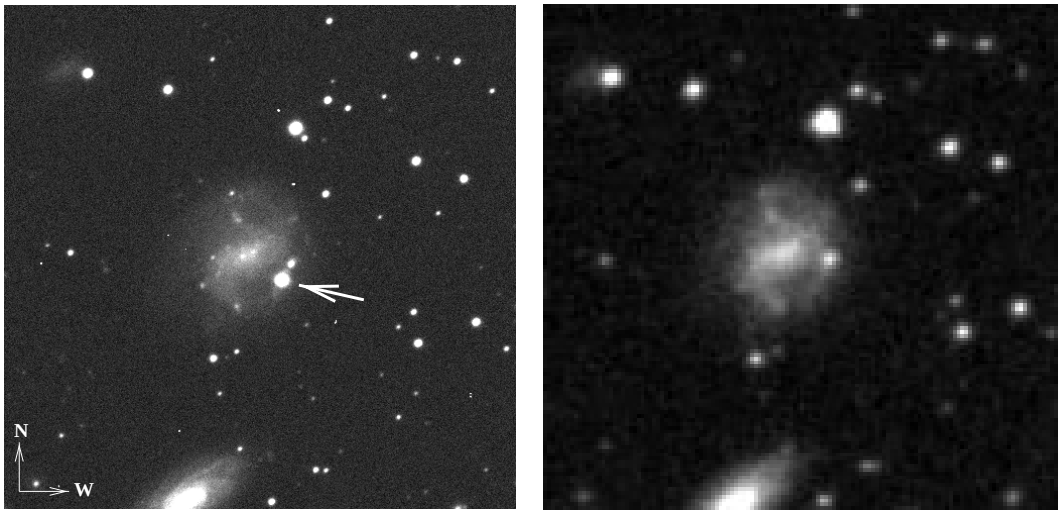

Figure 2.16: Image of the galaxy ESO 184-G82 with (left) and without (right) SN1998bw [24].

10^{-4}. The optical spectrum indicated that SN1998bw is a type Ic supernova.

Iwamoto et al. [39] performed the model fitting to the light curve and the spectrum of SN1998bw. They found that SN1998bw can be well reproduced by an extremely energetic explosion of a massive star composed on mainly of carbon and oxygen (figure 2.17). And the kinetic energy of the ejecta is calculated to be (2–5) $\times$ 10^{52} erg. They argued that this extremely large energy could produce the relativistic shock which is required for a GRB.

Supernova association with GRB030329

HETE-2 observed GRB030329, the one of the brightest GRB ever reported [107]. Its optical afterglow was 12.4^{th} magnitude at 67 minutes after the burst [86]. The redshift of z=0.167 [30] makes it the closest GRB excepting only GRB980425/SN1998bw.

About ten days after the burst, the spectral signature of type Ic supernva emerged in the afterglow ([96] and [37]; figure 2.18). This supernova was designated as SN2003dh. As seen in the figure 2.18, the spectrum of SN2003dh is very similar to the type Ic supernova SN1998bw. The expansion velocity is estimated to be 36,000 $\pm$ 3,000 km s^{-1} (0.12 $\pm$ 0.01c). GRB030329 provided the direct observational evidence that, indeed core-collapse events can produce a GRB.

2.2.2 Optically Dark GRB

Only 50% of the GRB well-localized by *Beppo*SAX had optical transients (afterglow), whereas an X-ray afterglow is present in 90% of cases. Optically dark GRBs are GRBs without an optical transient detection. De Pasquale et al. [17] compared the X-ray afterglows and optically

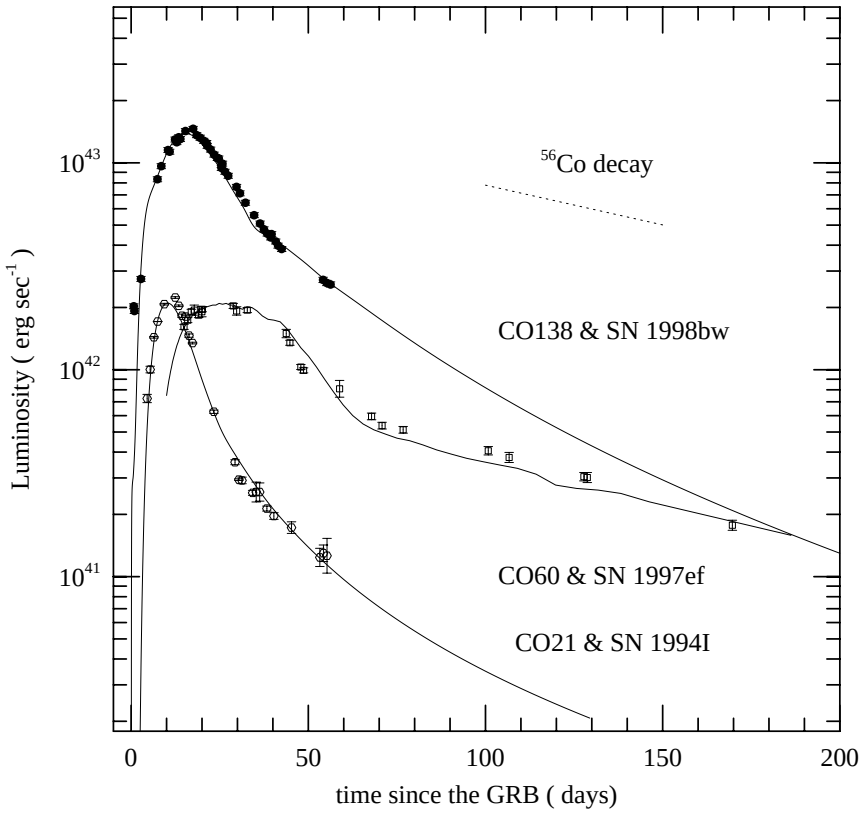

Figure 2.17: Light curves of three type Ic supernova, SN1998bw, 1997ef, and 1994I. The solid curves are the models. The light curve of SN1998bw is well fitted with the following parameters: the stellar mass $M_{CO} = 13.8\ M_{Solar}$, the explosion energy $E_{exp} = 3 \times 10^{52}$ erg, and the mass of the synthesized ^{56}Ni $M_{56} = 0.7\ M_{Solar}$ [39].

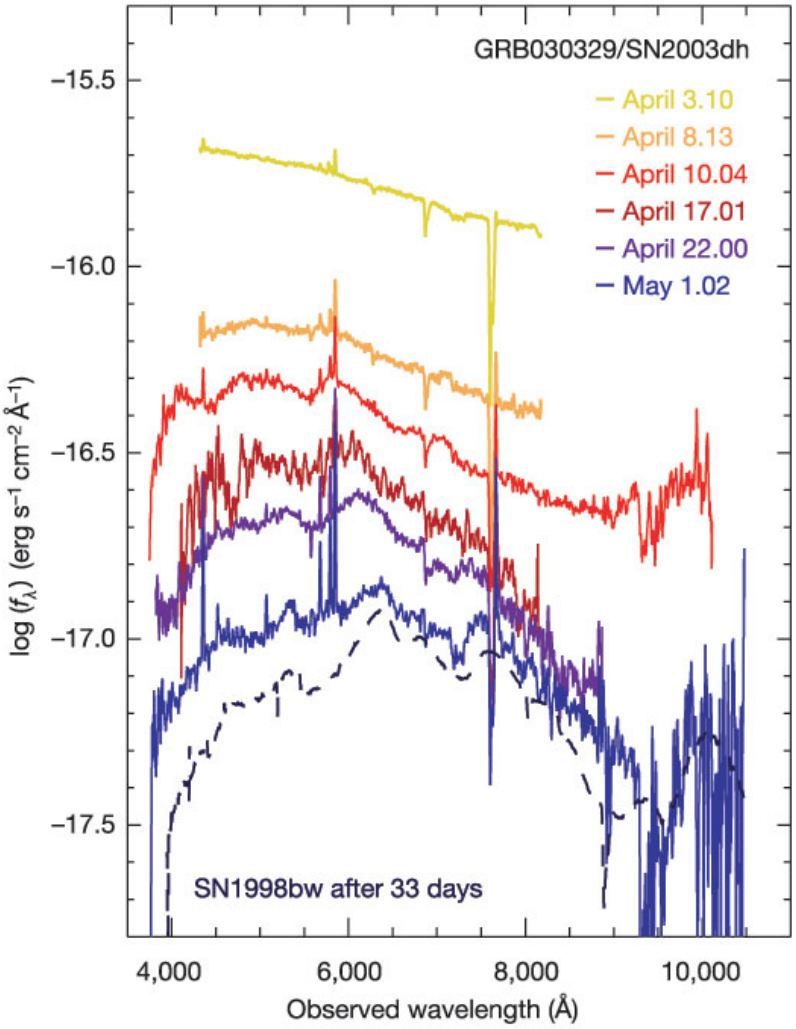

Figure 2.18: Spectral evolution of the afterglow of GRB030329 [37].

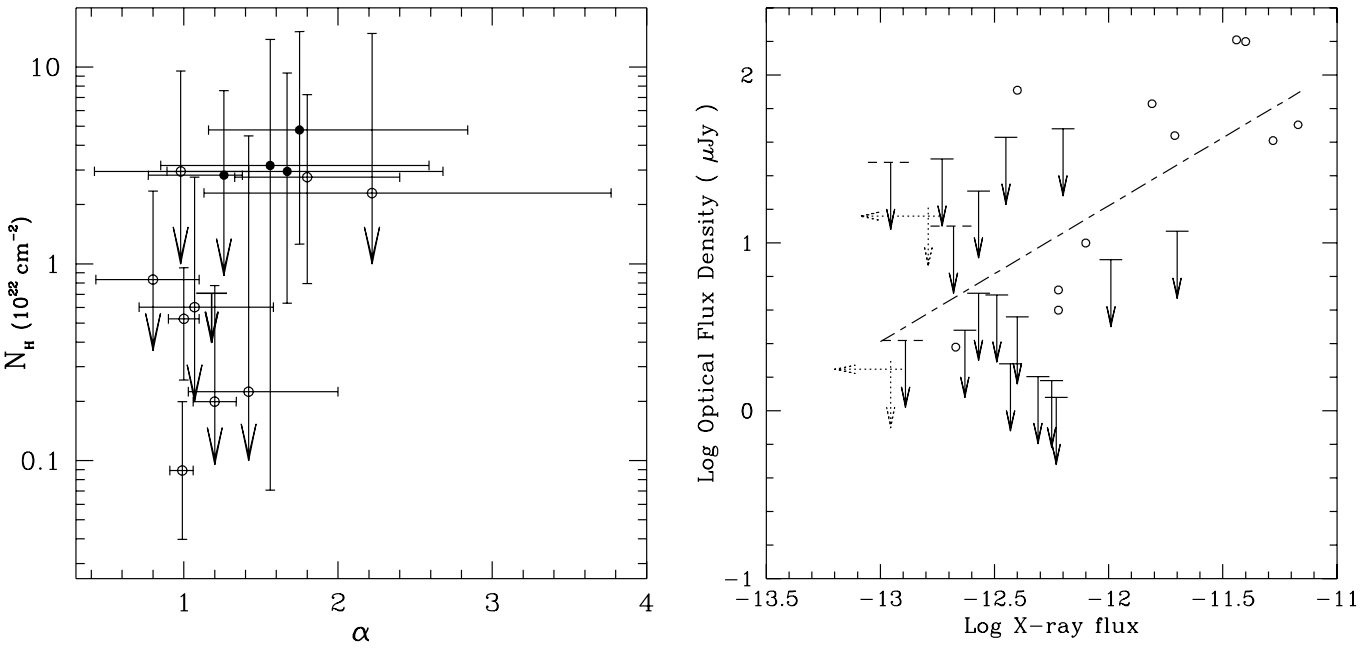

Figure 2.19: Left: N_H vs. spectral index of X-ray afterglows observed by *Beppo*SAX NFI. The filled dots are dark GRBs and empty dots are the optically bright GRBs. There is no significant difference among them. Right: X-ray vs. optical flux. The empty dots are the optically bright GRBs. The solid arrows are optically dark GRBs. [17]

bright/dark GRBs observed by *Beppo*SAX (figure 2.19). They found that the X-ray afterglows of the optically dark GRBs have about 5 times lower flux. Under the assumption that the optical to X-ray spectrum is the same, the optical flux could be ~ 2 magnitudes lower than the optically bright GRBs. They argued that the highly absorbed environment of the optical light might be causing the optically dark GRBs.

Faint optical afterglow: GRB 021211

The nearly real-time localization of GRB021211 [15] provided by *HETE-2* makes it possible to solve the problem of "optically dark" GRBs. The early optical observations had started 90, 108, and 143 seconds after the burst. The optical afterglow of GRB 021211 is intrinsically much fainter than other GRB afterglows (figure 2.20). This burst would have been classified as an "optically dark" GRB without the rapid follow-up observation.

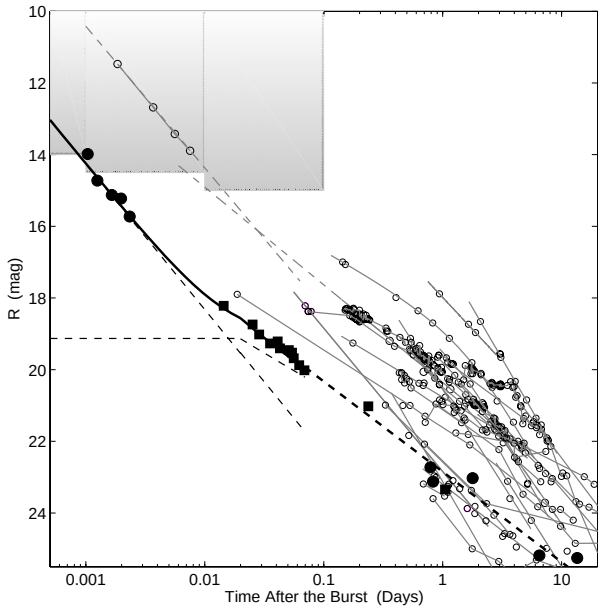

Figure 2.20: Light curve of GRB 021211 and other GRBs. The light curve of GRB021211 can be fitted with a two component power-law; an initial steeply declining "flash", f $\propto$ t$^{-\alpha}$ with α $\approx$ 1.6 and typical afterglow behavior with $\alpha \approx 1$ [21].

Extinction by dust; GRB 030115

Rapid follow-up observations of GRB 030115 which was localized by *HETE-2* show the convincing signature that the optical afterglow is extinguished by dust. Figure 2.21 shows the near infrared and optical afterglow spectrum and the best fit model, assuming dust extinction [48]. The afterglow property of GRB 030115 provides a good case of an "optically dark" GRB caused by dust absorption.

High redshift GRBs

Fynbo et al. [23] suggest one interpretation of optically dark GRBs is that a large fraction of GRBs occur at redshifts z $\geq$ 7 and are hence invisible in the optical due to Ly-α blanketing and absorption by intervening Lyman-limit systems. Authors suggest that it is essential to conduct deep ($R_{\rm lim} \geq 24$ at less than 1 day after the trigger) follow-up imaging at optical and infrared wavelengths to answer the question as to why some bursts are darker than others.

2.2.3 Standard energy reservoir in GRBs

Interpreting the break in the afterglow light curve as the conical jet structure of GRBs, we can correct the geometry and calculate the "true" released energy in γ-rays. In this conical

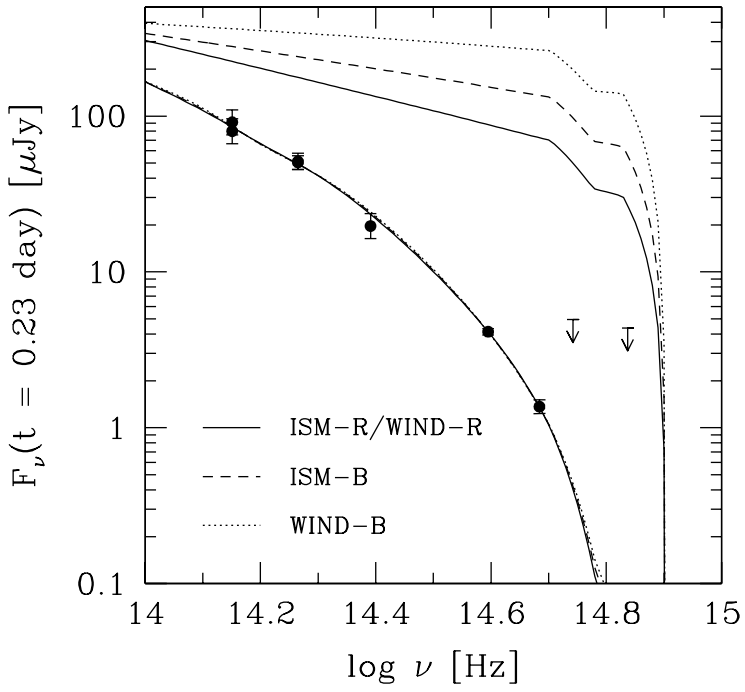

Figure 2.21: Near infrared and optical afterglow spectrum (K, H, J, i*, and r* band) of GRB030115. The solid curve is the best fit model for the data assuming extinction by dust [48].

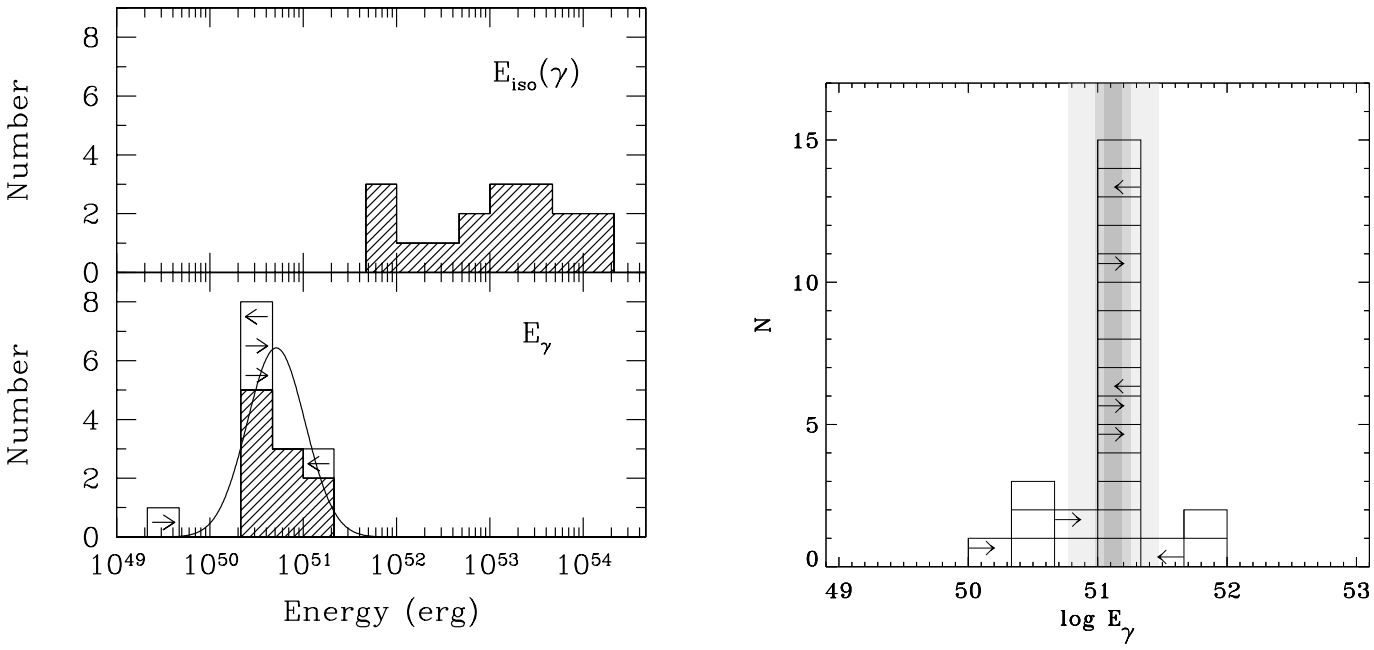

Figure 2.22: Left: Distribution of the isotropic γ-ray energy (top) vs. the jet opening angle corrected γ-ray energy (bottom) [22]. Right: Distribution of the jet opening angle corrected γ-ray energy [9].

jet picture, the break in the afterglow light curve can happen for two reasons. First, when the relativistic shell has slowed down and the bulk Lorentz factor Γ has reached $\Gamma \approx \theta_j$ (where θ_j is the opening angle of the jet), the flux drops suddenly. Second, the side-ways expansion of the jet makes the deceleration of the ejecta much faster.

Frail et al. [22] calculated the jet opening angle for 17 GRBs with known redshifts using the jet break times t_j. The formula is:

$$\theta_j = 0.057 \left(\frac{t_j}{1\mathrm{day}}\right)^{3/8} \left(\frac{1+z}{2}\right)^{-3/8} \left[\frac{E_{\mathrm{iso}}(\gamma)}{10^{53}\mathrm{ergs}}\right]^{-1/8} \left(\frac{\eta_\gamma}{0.2}\right)^{1/8} \left(\frac{n}{0.1\mathrm{cm}^{-3}}\right)^{1/8}, \qquad (2.7)$$

where η_γ is the efficiency of the fireball in converting the energy in the ejecta into γ-rays and n is the mean circumburst density and assuming the constant values for these paramters.

The result is surprising. As seen in figure 2.22, the jet opening angle corrected total γ-ray energy E_γ is tightly concentrated around 5×10^{50} ergs. Bloom et al. [9] calculated the E_γ for a larger GRB sample and a more reliable value of the ambient density. Bloom et al. [9] confirmed the tight E_γ value of $E_\gamma = (1.33 \pm 0.07) \times 10^{51}$ ergs. This energy is comparable to ordinary supernovae.

Chapter 3

GRB theory

3.1 GRB emission models

The dynamics of GRBs are well described in the framework of the "fireball" model (the details of the fireball model are in the review by Piran [61]; here, we refer to the review by Van Paradijs et al. [106]). In this model, a large amont of energy is released into a small volume, resulting in an explosion. The key to the model is that a large fraction of the energy is transferred into a small fraction of the mass. Let us consider the release of an energy $E = 10^{52}$ E_{52} ergs into a sphere with radius r_{in}. A rest mass M_0 of baryons is contained in the volume, and the energy-to-mass ratio in the initial fireball is thus $\eta = E/M_0c^2$. The evolution of the fireball from these initial condition depends on one other paramter, the optical depth. If the photon energies are primarily in the MeV range, the optical depth is very high due to photon-photon scattering and pair production. Thus, the internal energy can only be converted into kinetic energy by adiabatic expansion. Adiabatic expansion can be described from thermodynamics, $T'V^{\gamma_a - 1} = const.$, where T' is the rest-frame temperature, V is the source volume, and γ_a is the adiabatic index of the gas; $\gamma_a = 4/3$ for an ultrarelativistic gas. If we convert V into the radius of the volume R and substitute $\gamma_a = 4/3$, $T' \propto R^{-1}$. The total internal plus kinetic energy in the frame of an external observer is $E = \Gamma M_0(kT'/m_{\mathrm{p}} + c^2)$, where Γ is bulk Lorentz factor of the fireball and m_{p} is the proton mass. For relativistic temperatures, the first term dominates, so $E \propto \Gamma T' = const.$ Combined with the previous thermodynamic relation, we have $\Gamma \propto R$. The bulk Lorentz factor of the gas thus increases linearly with radius, until it saturates at a value $\Gamma_0 \sim \eta$, at a radius $r_{\mathrm{c}} \sim \eta r_{\mathrm{in}}$. Because all the matter has moved with $v \simeq c$ beyond r_{c}, it is all piles up in a thin shell with thickness R/Γ^2. This is the picture how Γ evolves in the fireball model.

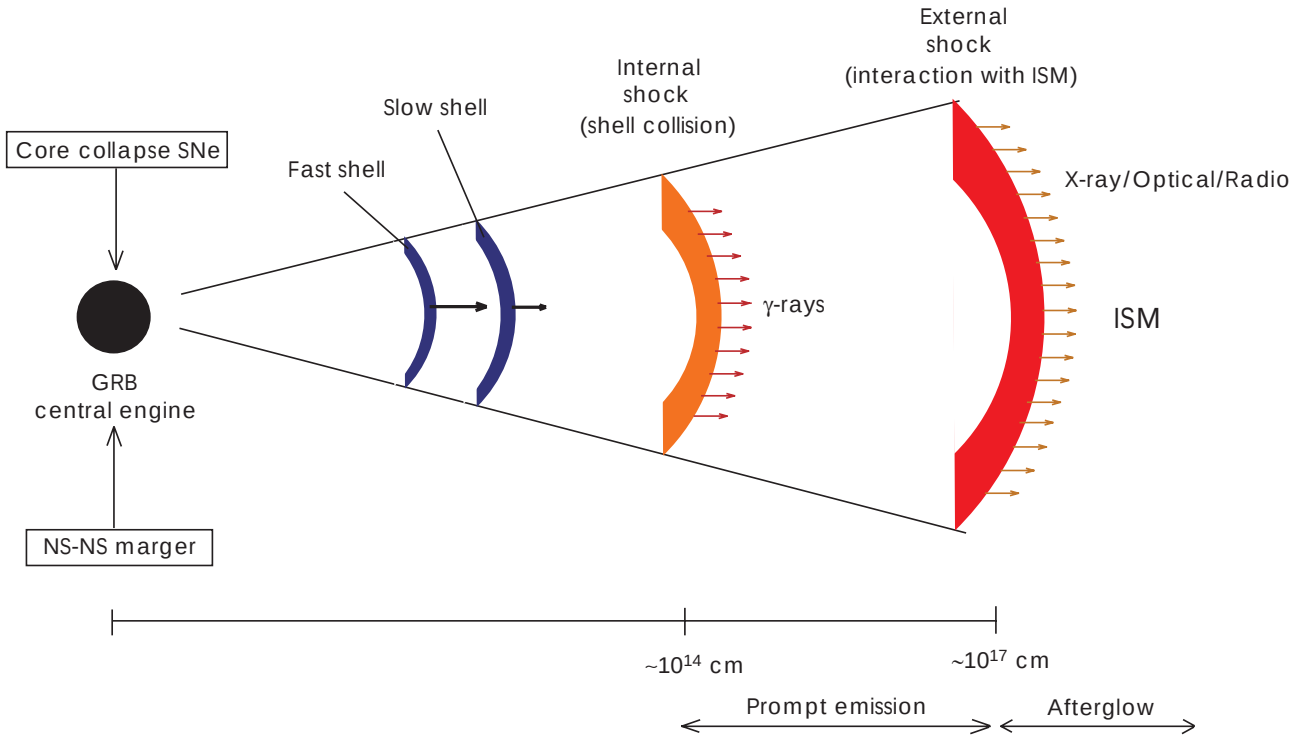

Figure 3.1: Schematic figure of the GRB prompt and afterglow emission model. The collapse of massive star (collapsar) and/or neutron star (NS) merger which finally form a black hole are the most supported models of the central engines of GRBs. In the internal shock model, the prompt emission is produced by particles accelerated via internal shocks, which are due to the collision of relativistic moving shells. The particles radiating to cause the afterglow are accelerated by the external shock, which is the interaction between the merged shell and interstellar material.

When the relativistic fireball expands and becomes optically thin, its kinetic energy translates to thermal energy via a shock; the thermal energy is then radiated as synchrotron radiation. There are two types of shock (see figure 3.1). The *internal shock* is due to the internal collisions of shells of various speeds; The *external shock* originates from the collision between the expanding shell and the surrounding interstellar material. The prompt emission of GRB is considered to be the result of internal shocks, whereas the afterglow is caused by the external shock.

Here, we review the two GRB prompt emission models proposed by Tavani [100] and Sari et al. [84]. These models give us the explanation for how to produce the synchrotron radiation through the shock and how to reproduce the observed GRB spectrum.

3.1.1 Synchrotron shock model (SSM)

Tavani [100] shows that the synchrotron shock model (SSM) predicts a specific shape of GRB spectrum which agrees with broadband GRB spectra (e.g. Band function).

The GRB site is assumed to be surrounded by an optically thin nebular medium (a low-density ISM, a SNR, or a mass outflow from a companion star in a binary system). An MHD relativistic wind is a mixture of electromagnetic fields, $e^{\pm}$ -pairs, and baryons. A relativistic wind is assumed to be produced by a compact star. If the relativistic wind interacts with a nebula not in pressure equilibrium with MHD outflow, the relativistic motion of the resulting shock front is characterized by a bulk Lorentz factor Γ.

Before the relativistic MHD plasma interacts with a shock front, the particle distribution function is assumed to be completely thermalized and characterized by a single (relativistic) particle energy or temperature. Three-dimensional distribution of the radiating particle number per energy interval dγ and solid angle dΩ is described by a relativistic Maxwellian distribution of particles:

$$n_{th}^{3D}(\gamma,\alpha)\,d\gamma\,d\Omega = \frac{N_{\pm}^{M}}{8\pi}\frac{\gamma^2}{\gamma_*^3}e^{-\gamma/\gamma_*}\,d\gamma\,d\Omega, \tag{3.1}$$

where $\gamma = E_{\pm}/m_{\pm}c^2$, $\gamma_* = k_B T^*/m_{\pm}c^2$, where T^* is the preshock distribution temperature of radiating particles of energy $E_{\pm}$, k_B is the Boltzmann constant, c is the speed of light, $d\Omega = d\cos\alpha d\phi$ is the solid angle where α is the pitch angle of the particle trajectory with respect to the local magnetic field direction, ϕ is the azimuthal angle, and $N_{\pm}^{M}$ is a normalization constant.

The postacceleration particle energy distribution function can be drastically altered by the formation of a suprathermal component when the acceleration process takes place at the shock front. The altered postshock distribution function with a suprathermal power-law tail of index p:

$$n_{ps}^{3D}(\gamma,\alpha) = \frac{f_\alpha N_{\pm}}{4\pi}\left[\left(\frac{\gamma^2}{\gamma_*^3}e^{-\gamma/\gamma_*}\right) + K\left(\frac{\gamma}{\gamma_*}\right)^{-p}\right], \tag{3.2}$$

where $N_{\pm}$ and K are normalization constants, and f_α takes into account the possible spatial nonuniformity of the pitch angle distribution with respect to the pitch angle. The energy range of the power-law distribution is $\gamma_* \le \gamma \le \gamma_m$, where γ_m, which is to be determined by balancing acceleration and cooling loss in the shock frame, is a maximum energy of shock-accelerated particles.

The most efficient acceleration process will be at a condition where K = 1 / ($e\gamma_*$). This

condition is achieved at $\gamma = \gamma_*$ when the particles at the initial average energy γ_* and thermal low-energy tail is modified at the top of the distribution resulting from fast acceleration. The condition $\tau'_a \leq \tau'_r$, where τ'_a and τ'_r are the acceleration and radiating timescale at the rest frame, is the crucial requirement for a suprathermal component in GRB spectra.

The synchrotron spectral energy emissivity per unit volume and solid angle $J^s_\nu(\alpha)$ is

$$\begin{aligned} J^s_\nu(\alpha) &= \int_1^\infty p^s_\nu(\gamma,\alpha)\, n^{3D}_{ps}(\gamma,\alpha)\, d\gamma \\ &= \left(\frac{3^{1/2}}{16\pi^2}\right)\left(\frac{N_\pm}{c_2}\right)\left(\frac{q'^3}{m_\pm c^2}\right) f_\alpha B_{ps}\sin\alpha \left[\mathcal{F}\left(\frac{\nu}{\nu^*_\rfloor \sin\alpha}\right)\right] \end{aligned} \tag{3.3}$$

where ν^*_c is the critical frequency corresponding to the preshock temperature γ_* of particles of charge e′, $p^s_\nu(\gamma,\alpha)$ is the single-particle synchrotron power, $N_\pm$ is the local $q^\pm$-pair number density, c_2 is a normalization constant, $c_2 = 2 - 5/e + [1 - y_m^{1-p}]/[e(p-1)]$, and $\mathcal{F}(w)$ is a dimensionless spectral function given by

$$\mathcal{F}(w) \equiv \int_0^1 \mathrm{y}^2 \mathrm{e}^{-\mathrm{y}} \mathrm{F}'\left(\frac{\mathrm{w}}{\mathrm{y}^2}\right) \mathrm{dy} + \frac{1}{\mathrm{e}} \int_1^{\mathrm{y_m}} \mathrm{y}^{-\mathrm{p}} \mathrm{F}'\left(\frac{\mathrm{w}}{\mathrm{y}^2}\right) \mathrm{dy} \tag{3.4}$$

where we denoted

$$w = \nu/(\nu^*_c \sin\alpha), \quad y = \gamma/\gamma_*, \quad y_m = \gamma_m/\gamma_* \tag{3.5}$$

with

$$F'(x) \equiv x \int_x^\infty K_{5/3}(x')\, dx' \tag{3.6}$$

the synchrotron spectral function, and $K_{5/3}(x')$ is the modified Bessel function of order 5/3. The differential proper intensity in the shock comoving frame (proper intensity) I^S_ν is obtained after an integration of J^S_ν over the solid angle $d\Omega(\alpha)$ and emission volume dV

$$I^S_\nu = \int\int J^s_\nu(\alpha)\, d\Omega(\alpha)\, dV \tag{3.7}$$

The observed flux F^S_ν can be obtained from the proper intensity I^S_ν by dividing by the square of the source distance D, and by taking into account the possible effect of relativistic beaming and possible cosmological effects.

In this SSM, $E_{\rm peak}$ corresponds to the synchrotron critical frequency $\nu_c = 3\gamma_*^2 e\, B\, \sin\alpha/(4\pi mc)$. The electron spectral index p has to be less than 3 for $E_{\rm peak}$ to be the synchrotron critical frequency (figure 3.2).

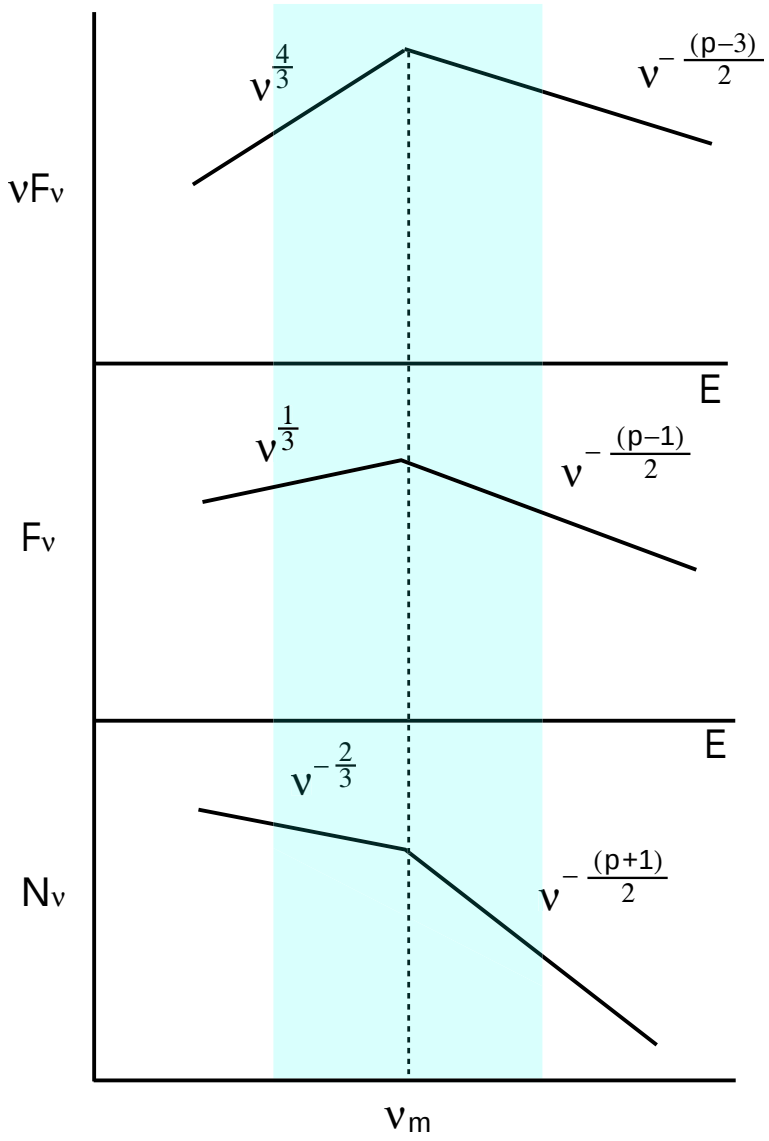

Figure 3.2: The spectrum calculated by synchrotron shock model proposed by Tavani. The spectral shape is the same as "classical" synchrotron radiation with a slope change at the synchrotron critical frequency ν_m. The light blue region is the observing energy band of GRBs.

3.1.2 SSM with synchrotron cooling

There are several reasons that the simple SSM [100] is not the appropriate model for GRB prompt emission. First, as seen in figure 3.2, the low energy photon index α is constant value $-2/3$, so the observed α value should be narrow distribution around $-2/3$. However, according to the BATSE results, α is scattered from -2 to 0 (see figure 2.2). Second, since $E_{\rm peak}$ is concentrated around 250 keV in BATSE data, magnetic fields will be 10^7 G if we use the typical value for electron Lorentz factor $\gamma \sim 100$ and bulk Lorentz factor $\Gamma \sim 100$. Then, the synchrotron cooling time $t_{\rm cool}$ at the observer's frame is $t_{\rm cool} \sim (1 + z) / (\Gamma\gamma B^2) \leq 10^{-6}$ s. So the synchrotron loss effects should be apparent in the GRB spectrum.

Sari et al. [84] proposed a SSM taking into account the effect of synchrotron cooling. They consider two possibilities depending on the cooling timescale $t_{\rm cool}$ and the hydrodynamic timescale of the expanding shell $t_{\rm hyd}$. The total duration of the burst is the time to convert the bulk of the kinetic energy of expanding shell into thermal energy via shocks; on the other hand, the individual peaks of GRBs are due to shotlike thermalization. The width of the individual peaks represents the cooling time scale. So, a burst having a complicated time structure is the case where $t_{\rm hyd} > t_{\rm cool}$ (so called "fast cooling"). In $t_{\rm hyd} < t_{\rm cool}$ (so called "slow cooling"), the kinetic energy of the shell is turned rapidly into thermal energy, but the electrons lose their energy via radiation on a much longer timescale. This regime can create a burst with a smooth single-hump and afterglow emission.

Sari et al. [85] calculated the spectrum in the SSM model including the effect of cooling. Assuming an electron distribution of $N(\gamma) \propto \gamma^{-p}$, the spectrum has three characteristic frequencies; the synchrotron self absorption frequency $\nu_{\rm a}$, the synchrotron critical frequency for electrons with the minimum Lorentz factor $\nu_{\rm m}$, and the synchrotron cooling frequency $\nu_{\rm c}$ (figure 3.3). The lower and higher end of the spectrum is the same for both the "fast cooling" and the "slow cooling" processes. In the higher frequency range ($\nu > \nu_{\rm m}$ for "fast cooling" and $\nu > \nu_{\rm c}$ for "slow cooling"), the number of electrons with Lorentz factor of $\sim \gamma$ is proportional to γ^{1-p} due to the power-law assumption of the electron distribution. Their energy is proportional to γ^{2-p}. As the electrons cool, they deposit most of their energy into a frequency range ν_{syn} $(\gamma) \propto \gamma^2$, hence $F_\nu \propto \gamma^{-p} \propto \nu^{-p/2}$. On the other hand, at frequencies below ν_a, the spectrum is the Rayleigh-Jeans portion of the blackbody spectrum $F_\nu \propto \nu^2\gamma(\nu_{typ})$ where $\gamma(\nu_{typ})$ is the typical Lorentz factor of the electrons. If we assume that $\gamma(\nu_{typ}) \propto \nu^0$, $F_\nu \propto \nu^2$. In the range of $\nu_{\rm c} < \nu < \nu_{\rm m}$ in the "fast cooling" spectrum, all the electrons cool down on the dynamical timescale t_{dyn}. Since the energy of an electron is $\propto \gamma$ and its typical frequency is $\nu_{syn} \propto \gamma^2$, F_ν

$\propto \gamma^{-1} \propto \nu^{-1/2}$. The spectral shapes in other frequency ranges are same as the Tavani's simple SSM (this argument refers to Granot et al. [29]).

In this cooling SSM, the prompt emission is in the "fast cooling" phase, and peak energy in νFν spectrum corresponds to $\nu_{\rm m}$. Whether Tavani's SSM or Sari's SSM, $E_{\rm peak}$ is at the synchrotron critical frequency of Lorentz factor of $\gamma_{\rm m}$.

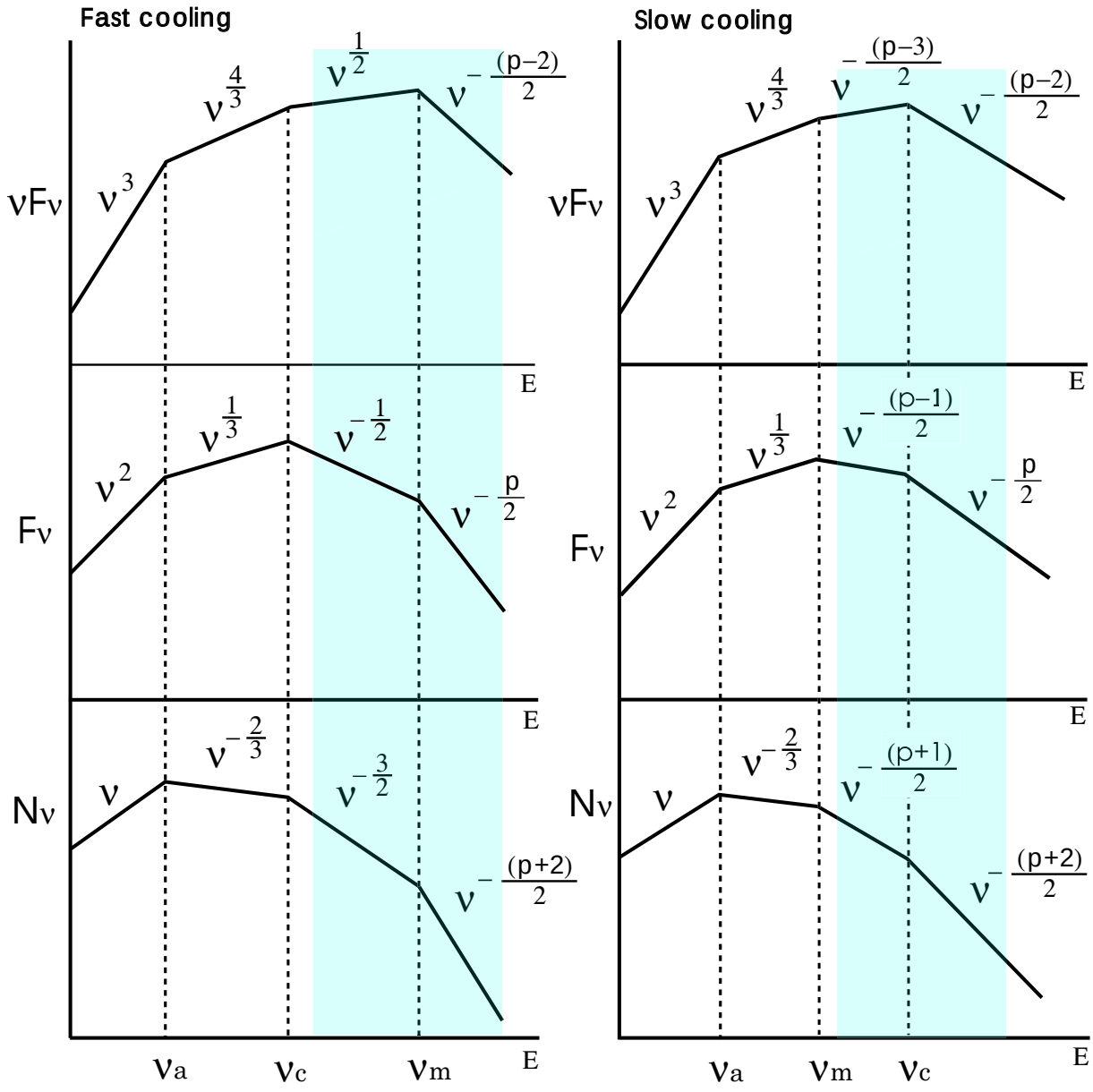

Figure 3.3: The synchrotron cooling spectrum proposed by Sari et al. [85]. There are two phases, fast cooling and slow cooling, whether $\nu_c < \nu_m$ or $\nu_c > \nu_m$. The light blue region is the observing energy band of GRBs.

3.2 Theoretical models for XRF

There are key phenomena which could be a breakthrough in our understanding of the prompt emission of GRBs. They are X-ray flash (XRF) and X-ray rich GRBs. XRFs and X-ray rich GRBs are GRBs with a high fluence in the X-ray range. We review several theoretical models of XRF which attempt to explain in the unified physical picture from XRFs to ordinary GRBs.

3.2.1 Off-axis jet model

Yamazaki et al. [112] proposed a model for XRF in which the viewing angle is much larger than the collimation angle of the jet (left panel of figure 3.4). In this model, the high X-ray to γ-ray fluence ratio is due to the relativistic beaming factor $\delta \equiv \Gamma[1 - \beta\cos(\theta_v - \Delta\theta)]$ changing as a function of off-axis angle (right panel of figure 3.4). Both the peak flux ratio and the fluence ratio increase as the viewing angle increases.

According to the model, $E_{\rm peak}$ energy of GRB ($\sim$ 250 keV) is shifted to low energies because of the smaller relativistic beaming effect. So $E_{\rm peak}$ can be estimated as $\sim \nu'_0$ / δ, where $\delta \equiv \Gamma[1 - \beta\cos(\theta_v - \Delta\theta)] \simeq [1 + \Gamma^2(\theta_v - \Delta\theta)^2)]/2\Gamma$ and $\theta_v > \Delta\theta$. $E_{\rm peak}$ of XRF as a function of the viewing angle is plotted in figure 3.5 assuming a GRB $E_{\rm peak}$ energy of 300 keV and a bulk Lorentz factor of 100. A value of $E_{\rm peak}$ energy of a few keV could be achieved at viewing angles larger than 5° in the case where the half opening angle of the jet $\sim 1°$.

In this original model, since the fluence at the $E_{\rm peak}$ is proportional to δ^{-3}, XRFs should not be at high redshift. However, the *Beppo*SAX team revisited the XRF data and updated the value of $< V/V_{\rm max} >$ from 0.56 to 0.27. This number is very close to $< V/V_{\rm max} >$ for classical GRBs: this suggests that XRFs could be at large cosmological distances. Yamazaki et al. [113] changed some model parameters of their off-axis model and find that a hard GRB at a viewing angle of 0.05 radian ($\sim 2.9°$) with a half opening angle of 0.03 radian ($\sim 1.7°$) could be an XRF with a redshift of 1.5.

3.2.2 Photosphere-dominated fireball

Mészáros et al. [51] studied the photosphere at smaller radius than the radius where the internal shock is occurring ($10^{12}-10^{14}$ cm). The flow starts from a minimum radius $\mathrm{r}_0 = \mathrm{ct}_{v,min} = 10^7 \mathrm{r}_{0,7}$ cm, and the Lorentz factor accelerates as $\Gamma \propto \mathrm{r}$ up to a coasting (or saturation) radius $\mathrm{r}_c \sim \mathrm{r}_0\Gamma_f$. The shells with Lorentz factors of Γ_M and Γ_m eject from a starting radius r_0 and collide at radius r_{sh}. The energy radiated in the shock by these merged shells can be enough to create

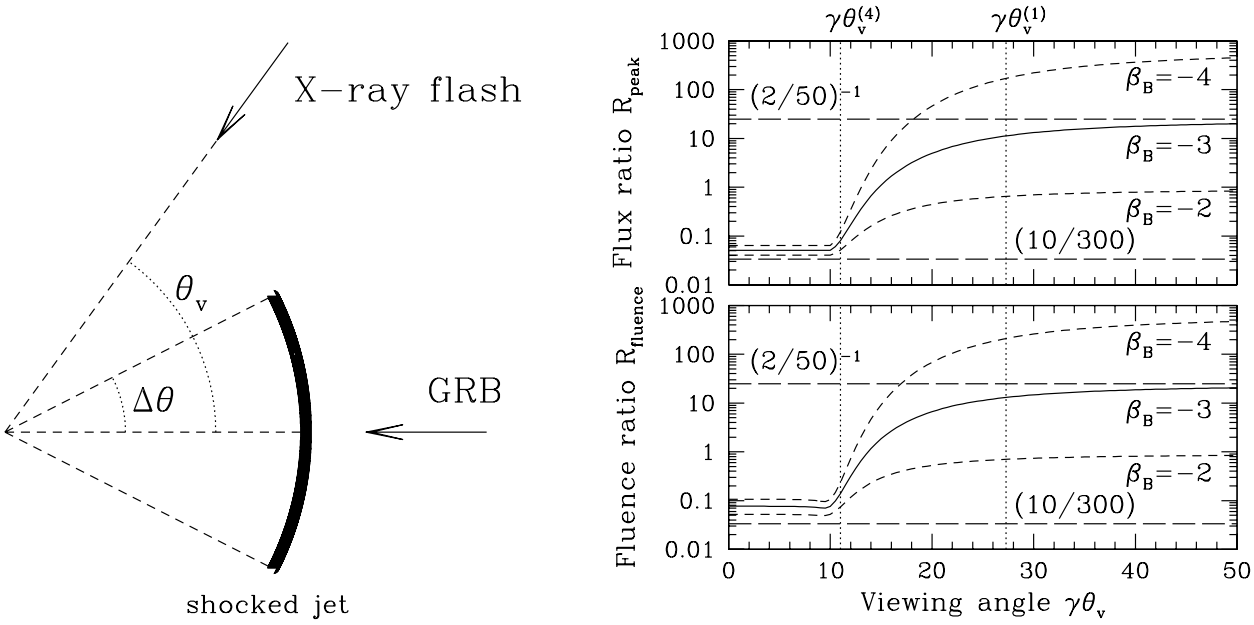

Figure 3.4: Left: The schematic figure of the off-axis GRB model. An XRF is a hard GRB observed at a large viewing angle. Right: The peak flux ratio (upper panel) and fluence ratio (lower panel) of 2–10 keV to 50–300 keV as a function of viewing angle (see Yamazaki et al. [112] for details).

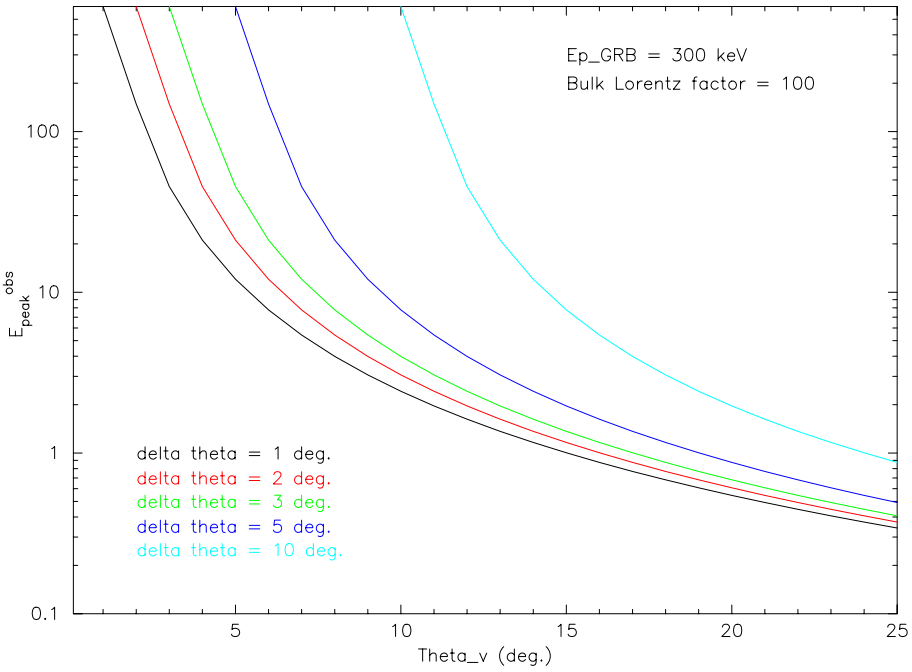

Figure 3.5: The observed $E_{\rm peak}$ energy as a function of viewing angle assuming a GRB $E_{\rm peak}$ of 300 keV and a bulk Lorentz factor of 100. The solid lines corresponding to the half opening angle of the jet are 1° (black), 2° (red), 3° (green), 5° (blue), and 10° (sky blue).

pairs optically thick to Thomson scattering. The radius $r_{\pm}$ is defined as that where the pair comoving scattering depth $\tau \sim 1$.

For shocks occurring at $r_{sh} < r_{\pm}$, the scattering optical depth of the shocked shells can become $\tau' \geq 1$ (the prime corresponds to the value at the rest frame). It is expected that pair-production acts as a thermostat, and for comoving compactness parameters (parameter for judging whether the source is optically thick for $\gamma\gamma$ interaction or not) $10 - 10^3$, the comoving pair temperature $T'_{\pm}$ is 3 – 30 keV. For a center of mass bulk Lorentz factor $\Gamma_c = (\Gamma_M \Gamma_m)^{1/2}$ $= 300\Gamma_{c,2.5}$, the observer-frame pair-producing shock radiation peak is at

$$h\nu_{x,sh} \sim 100\, T'_{\pm,10} \tau'^{-2}_{\pm,3} \zeta_{0.2} \Gamma_{c,2.5} [2/(1+z)]\, {\rm keV}. \tag{3.8}$$

Since the term $\Gamma_c[2/(1+z)]$ depend on z and Γ, the typical peak energy is 20 – 100 keV. Note that because the pair-production is needed in this model, Γ_c can not be too low. Therefore a peak energy of $\sim$ 20 keV could be achieved in the case of a very high redshift (z$\sim$ 10).

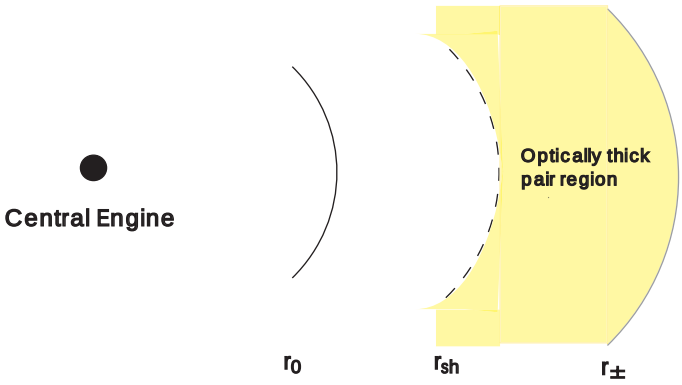

Figure 3.6: Schematic drawing of the photosphere-dominated fireball. r_{sh} is the radius of the collision of the two shells. $r_{\pm}$ is the radius of the optical depth of the pair-production $\tau_{\pm} \sim 1$. When $r_{sh} < r_{\pm}$, the optically thick pair-production region exists from r_{sh} to $r_{\pm}$. This region could produce X-ray excess GRBs.

3.2.3 Dirty fireball model

The small bulk Lorentz factor GRBs called dirty fireball model [16] could produce XRFs. Hard GRBs observed by BATSE have a bulk Lorentz factor from 100 to 1000 (the authors called these "clean fireballs" as $\Gamma_0 \gg 300$). On the other hand, the dirty fireball has a bulk Lorentz factor $\Gamma_0 \ll 300$. In their model, the spectrum is extremely sensitive to Γ_0. Since the peak energy is $\propto \Gamma_0^4$, it changes by 8 orders of magnitude between $\Gamma_0 = 3000$ and $\Gamma_0 = 30$. The duration of peak power output is just the deceleration timescale which is $\propto \Gamma_0^{-8/3}$. The dirty fireball produces transient emissions that are longer lasting and most luminous at X-ray energies and below (figure 3.7).

3.2.4 Structure jet model

Rossi et al. [79] investigated the jet which has a beam pattern where the luminosity per unit solid angle decreases smoothly away from the axis (figure 3.8). Both the energy per unit solid angle (ϵ) and the bulk Lorentz factor (Γ) depend as power laws:

$$\epsilon = \begin{cases} \epsilon_c & 0 \le \theta \le \theta_c \\ \epsilon_c (\frac{\theta}{\theta_c})^{-2} & \theta_c \le \theta \le \theta_j \end{cases} \tag{3.9}$$

and

$$\Gamma = \begin{cases} \Gamma_c & 0 \le \theta \le \theta_c \\ \Gamma_c (\frac{\theta}{\theta_c})^{-\alpha\Gamma}, \quad \alpha\Gamma > 0 & \theta_c \le \theta \le \theta_j \end{cases} \tag{3.10}$$

where θ_j is the opening angle of the jet, θ_c is introduced to avoid a divergence at $\theta = 0$. The power-law index of -2 is assumed in this model; however, this is not a necessary ingredient of

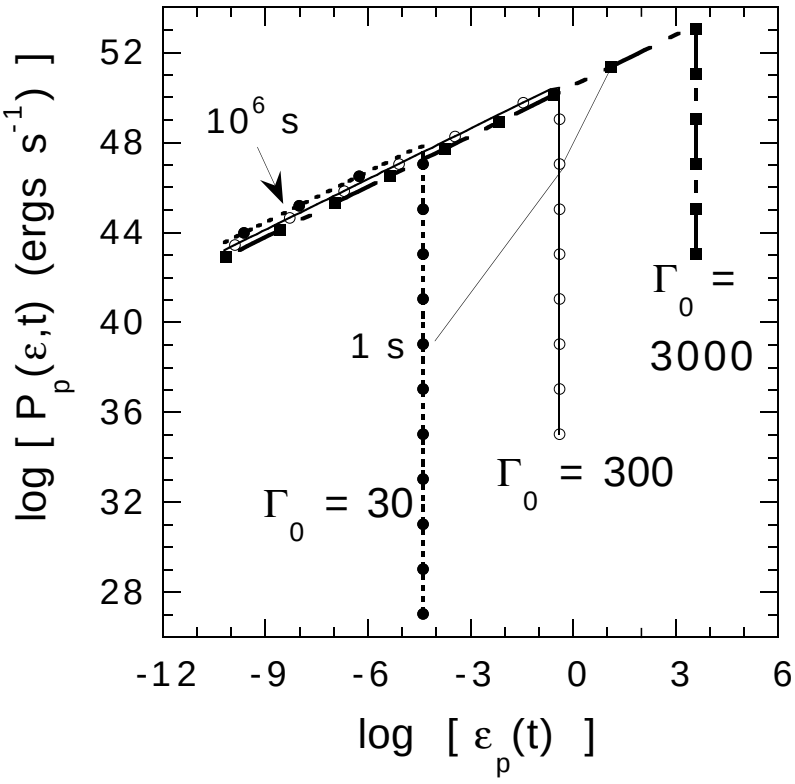

Figure 3.7: The plot of the photon energy ϵ in the unit of m_e vs. the spectral power P(t). The lines correspond to the different values of bulk Lorentz factors. The peak photon energy ϵ_p will decrease and the duration will increase when the Lorentz factor goes down [16].

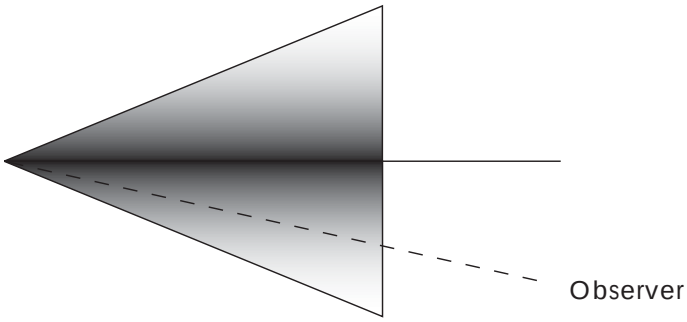

Figure 3.8: Schematic drawing of jet which has an axisymmetric energy distribution.

the model.

In this model, Γ tends to be lower when the viewing angle increases. This kind of "structured" jet is predicted by the Collapsar model [116] and XRF could be the off-axis viewing of the structure jet.

3.2.5 Relativistic wind with a small contrast of high Lorentz factor

Mochkovitch et al. [54] investigated the internal shock model which a central engine generates a relativistic wind with a non-uniform distribution of Lorentz factor. In their two-shell toy model, $E_{\rm peak}$ can be express as,

$$E_{\rm p} \propto \frac{\dot{E}^x \varphi_{xy}(\kappa)}{\tau^{2x} \bar{\Gamma}^{6x-1}}, \tag{3.11}$$

where $\dot{E}$ is the average injection power into the wind, κ is the ratio of Lorentz factor of 1st (Γ_1) and 2nd (Γ_2) shell ($\kappa = \Gamma_2/\Gamma_1$), τ is the time difference between 1st and 2nd shell, $\bar{\Gamma}$ is the average Lorentz factor ($\bar{\Gamma} = (\Gamma_1 + \Gamma_2)/2$), and $\varphi_{xy}(\kappa)$ is an increasing function of κ for all reasonable value of x and y. According to this equation, $E_{\rm peak}$ is a decreasing function of $\bar{\Gamma}$ as long as $x > 1/6$. XRFs are obtained with "clean fireballs" (large $\bar{\Gamma}$) while winds with large baryon loads ("dirty fireballs") lead to a harder spectrum because internal shocks occur closer to the source at a higher density.

The excellent agreement with the observed $E_{\rm peak}$ distribution could be achieved in the case of $x = y = 1/4$ (figure 3.9 left). According to Mochkovitch et al. [54]; 1) the redshift distribution of XRFs is identical to that of hard GRBs, 2) the duration and injected power are not very different for XRFs and hard GRBs, and 3) the most effective way of producing XRFs is a reduction of the constant $\kappa = \Gamma_2/\Gamma_1$ and an increase of the average Lorentz factor $\bar{\Gamma}$.

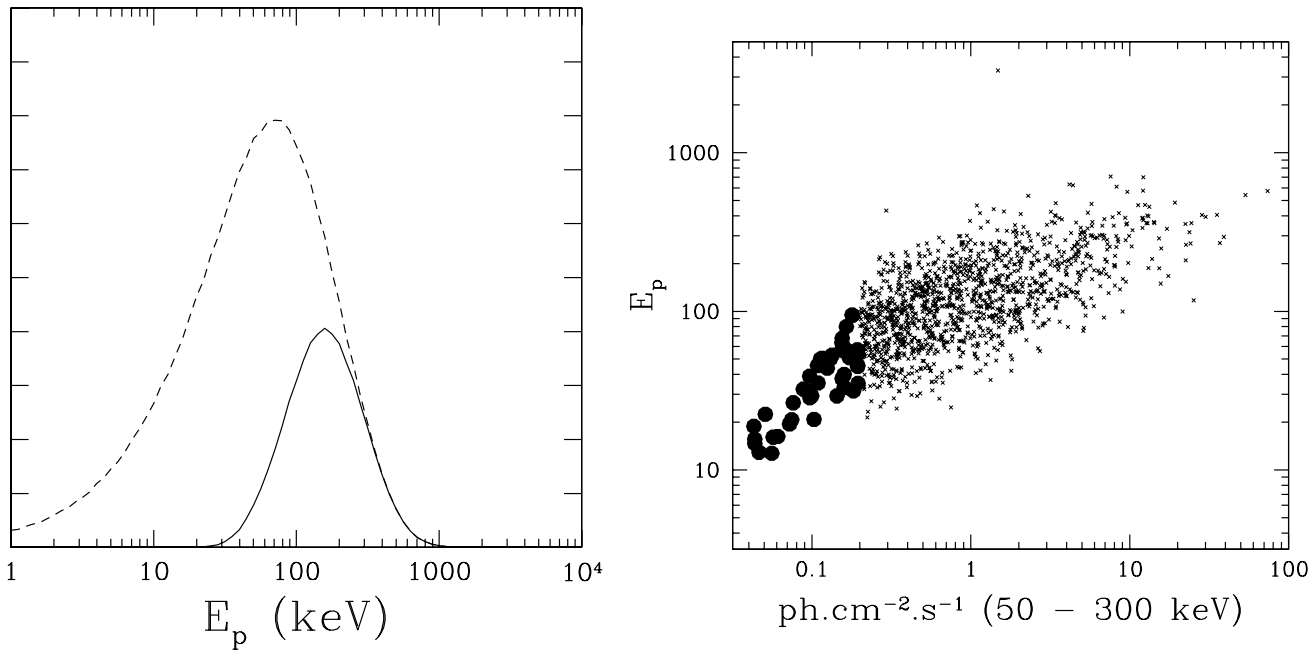

Figure 3.9: Left: The $E_{\rm peak}$ distribution in the case of x=y=1/4. The dashed line represents the whole population and the solid line is those bursts which can be detected by BATSE. Right: Simulated results of $E_{\rm peak}$ vs. peak flux [54].

3.2.6 High redshift GRB

Heise et al. [36] proposed that XRFs could be GRBs at the high redshift. According to Lamb and Reichart [46], if many GRBs are produced by the collapse of massive stars and/or the neutron star margers and their evolution rate is proportional to the star formation rate ([101], [102]), GRBs could occur out to at least z $\sim$ 10, and possibly to z $\sim$ 15–20. If this is the case for XRFs, the observed spectrum of the prompt emission is highly redshifted. For example, the $E_{\rm peak}$ energy of 300 keV at the source frame is observed as $\sim$ 30 keV in the case of redshift of 10. However, there are several observational evidences that the XRFs are not at a very high redshift (e.g. GRB011030, GRB020427 [10], GRB020903 [95] and so on).

Chapter 4

Instruments

4.1 HETE-2 Satellite

The High Energy Transient Explorer 2 (*HETE-2*; [78]) is the first astronomical satellite dedicated to observe GRBs. The *HETE-2* (hereafter *HETE*) satellite was successfully launched on October 9, 2000 using a Pegasus rocket. There are two unique features to *HETE*. First, *HETE* can provide the location of GRBs with localizations of a few tens of arcminutes to a few tens of arcseconds, with delay times of 10 s to a few hours, to the ground observers. This capability gives us the opportunity to observe GRB afterglows in multi-wavelengths from a very early phase. Second, broad-band spectroscopy (2–400 keV) of GRBs are possible with the combination of the X-ray and γ-ray instruments. This not only allows us to detect the various classes of GRBs, but also to determine the spectral parameters of the prompt emission. The information about the prompt emission is essential for study of the central engine, since even excellent observations of the afterglows only provide limited information.

The three scientific instruments on-board *HETE* are: the FREnch GAmma TElescope (FREGATE; [4]), which gives the trigger to GRBs; the Wide-field X-ray Monitor (WXM; [41], which is the key instrument to localize GRBs to $\sim 10'$ accuracy within a few tens of seconds; and the Soft X-ray Camera (SXC; [109], [55]), which localizes GRBs to a few arcseconds accuracy. The details about each instruments are described in the next section.

There are three primary ground stations (PGS; [13]); these are located at Singapore, at the Kwajalein Atoll in the Republic of the Marshall Islands, and at Cayenne, French Guinea. The commanding and the data downloads are performed with these three PGSs. These stations operate at S-band frequencies, with data rates of 31.25 kbps for uplink and 250 kbps for downlink.

Table 4.1: HETE satellite

Mass	124 kg
Envelope	89 cm × 66 cm
Orbit	625 km circular, 0-2 degree inclination
Mission Life	> 2 years
Attitude	Instruments are pointing at the anti-solar direction
Data Processing	4 T805 transputers, 8 DSP56001
Downlink	S-band (2.272 GHz) 250 kbps
	VHF (137.96 MHz) 300 bps
Uplink	S-band (2.092 GHz) 31 kbps

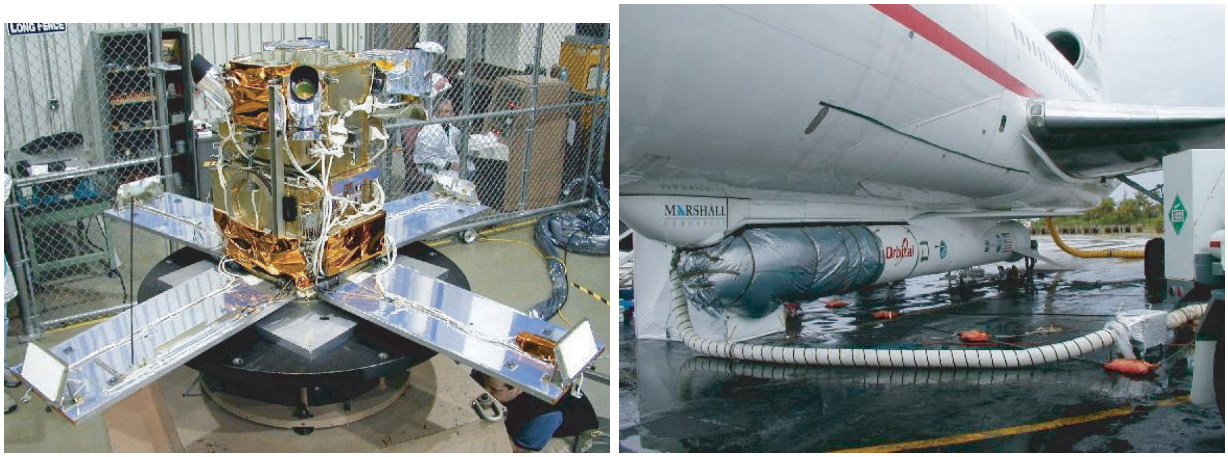

Figure 4.1: Left: HETE-2 spacecraft under a ground testing. Right: The Pegasus rocket on the bottom of the airplane.

The burst alert network (BAN) consists of fourteen burst alert stations ([14]; [108]; figure 4.4). Information about GRBs detected by *HETE* is transmitted to the BAN in real time at a frequency of 137.96 MHz 300 bps, immediately relayed to the *HETE* Mission Control Center at MIT, and then sent to the GRB Coordinates Distribution Network (GCN). The GCN then sends the information in the various forms (email, pager and/or internet socket messages) to the observers around the world (figure 4.3).

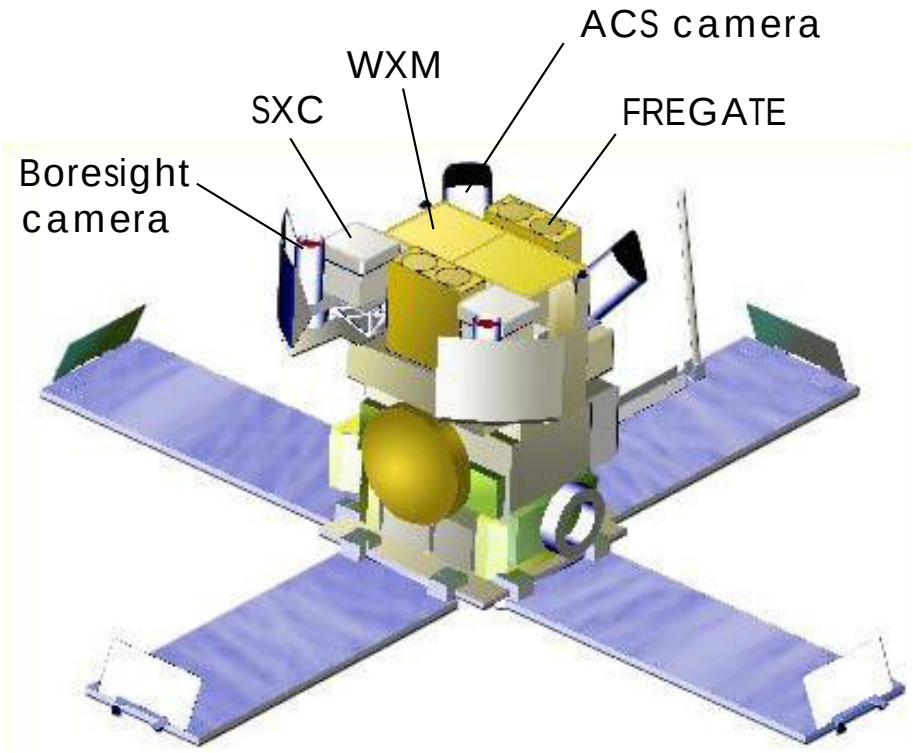

Figure 4.2: Schematic drawing of the HETE-2 spacecraft.

4.2 FREGATE

The french gamma telescope (FREGATE) plays an essential role by initiating HETE activity for each GRB triggered event.

Thanks to its wide energy coverage, FREGATE is also a key instrument for the spectroscopic study of GRB prompt emission. Due to its larger solid angle coverage, bursts outside the WXM field of view can be studied by FREGATE, and their positions can be determined the IPN collaboration.

The FREGATE detector consists of a cleaved NaI crystal (a cylinder 10 mm thick and 71 mm in diameter) read by a photomultiplier (Hamamatsu 1848, figure 4.5). The cleaved crystals have no dead layer, and are used to extend the spectral coverage in the low energy band ($\sim$ 6 keV), together with the beryllium window in front of the crystal. The geometric area of the sum of four detectors is $\sim$ 160 cm^2. To monitor the gain of the detector, the two radioactive sources of ^{133} Ba are placed outside of the detector. The effective area curve at several incident angles is shown in figure 4.6

The detectors are guarded by a graded shield made of lead, tantalum, tin, copper, and aluminum which block photons originating from outside the nominal field of view of the instrument

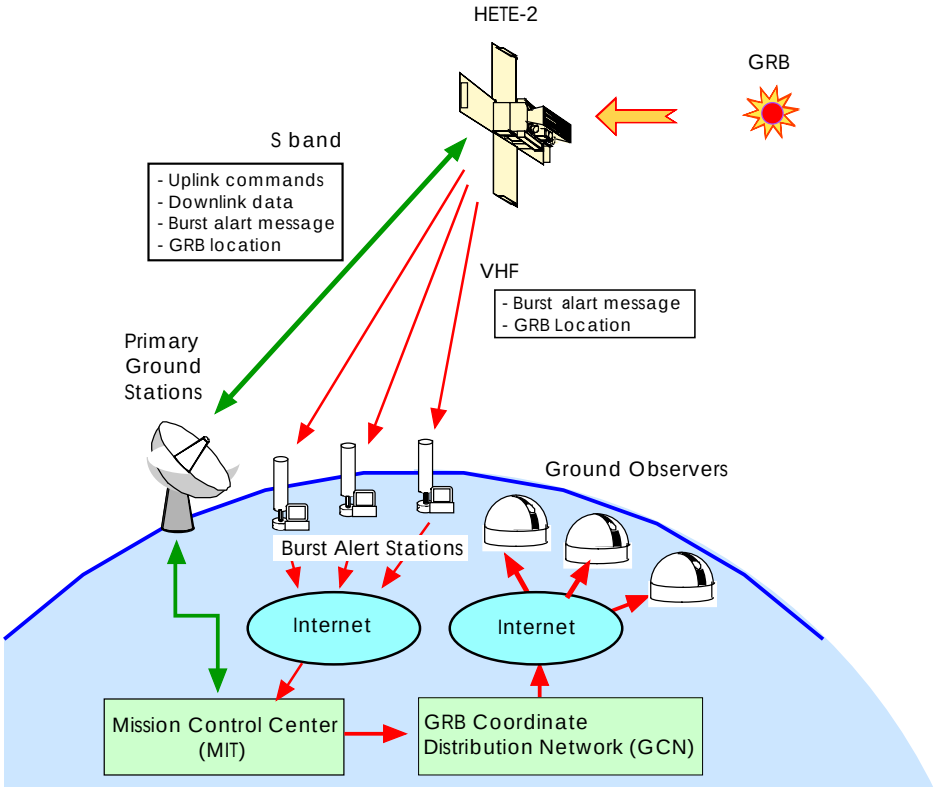

Figure 4.3: Burst alert network

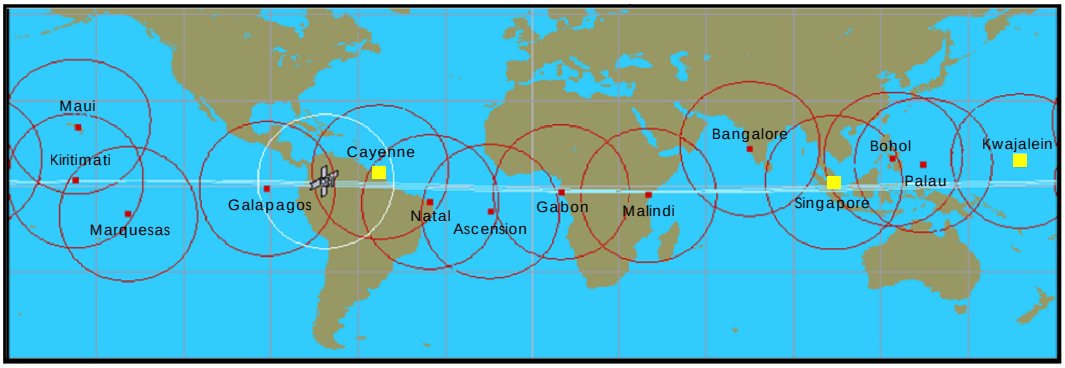

Figure 4.4: SGS status

Table 4.2: FREGATE performance

Energy range	6–400 keV
Effective area (4 detectors, on axis)	160 cm^2
Field of view	70°
Energy Resolution	$\sim$ 12 % @122 keV

Table 4.3: FREGATE data type

Data type	time resolution	description
HK	–	The house keeping data. Available for all time.
TH	0.16 s / 0.32 s	The time history data in 4 energy bands (approximately 6–40 keV, 6–80 keV, 32-400 keV, and > 400 keV) for each detectors.
SP	5 s / 10 s	128 channel energy spectral data for each detectors.
PH	6.4 μs	The photon data available when triggered the event. The time and 256 channel energy spectrum information is available for every photons.

(e.g. the diffuse X-ray background).

The data product of FREGATE is summarized in table 4.3. There are two types of data, similar to the WXM. One is the survey data (TH and SP) which is always available when the high voltage is on, and the other is the burst photon data (PH) which is only produced when the trigger occurred.

The energy response matrix of FREGATE was calculated using the GEANT Monte Carlo package [57]. More than 50 parts of the detector components are included in the simulation. This simulation code is examined before launch with the ground calibrations using a large set of radioactive sources and various incident angles. In-orbit calibration of the FREGATE response matrix is performed using the Crab data occulted by the earth. It successfully represents the Crab nebula spectrum with the photon index of (2.16 ± 0.03) ($\chi^2_\nu = 1.19$ / 84 D.O.F.). Details about the cross calibration of WXM and FREGATE response matrix is in Appendix A.

4.3 WXM

The wide-field camera (WXM) is located in the center of the spacecraft and the key instrument for localizing the GRBs. The WXM consists of the one-dimensional position sensitive proportional counters (PSPC) and the coded mask aperture. The one-dimensional coded mask is

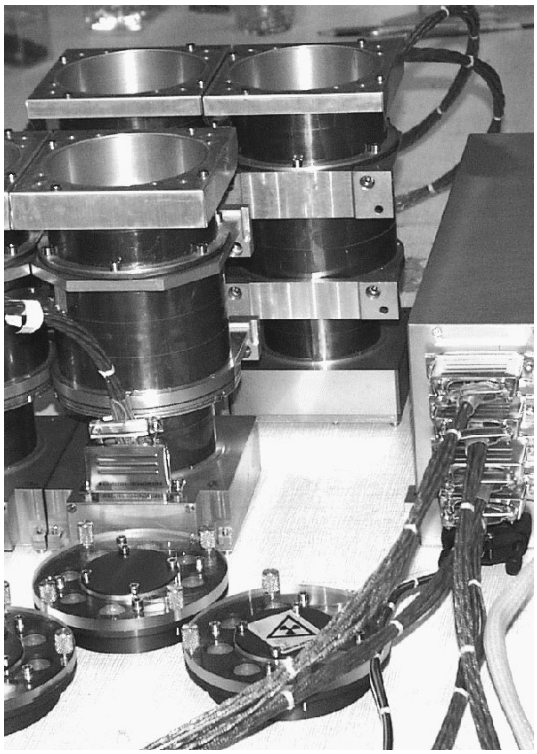

(a) Picture of the FREGATE detector

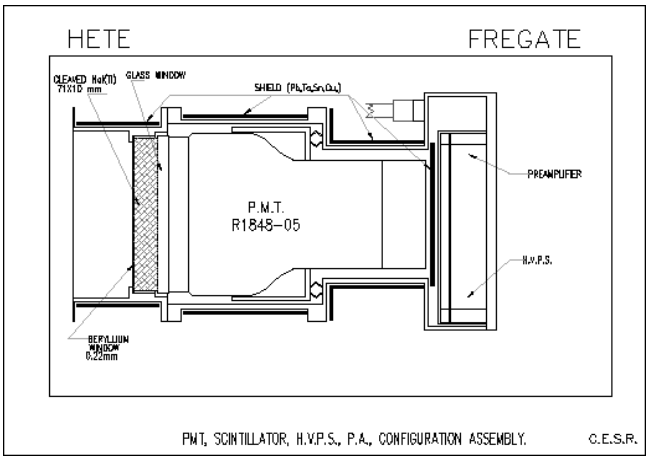

(b) The cross-section of the FREGATE detector.

Figure 4.5: The picture of the FREGATE detectors before the integration on the spacecraft (figure (a)). The cross-section view of the one FREGATE detector (figure (b)).

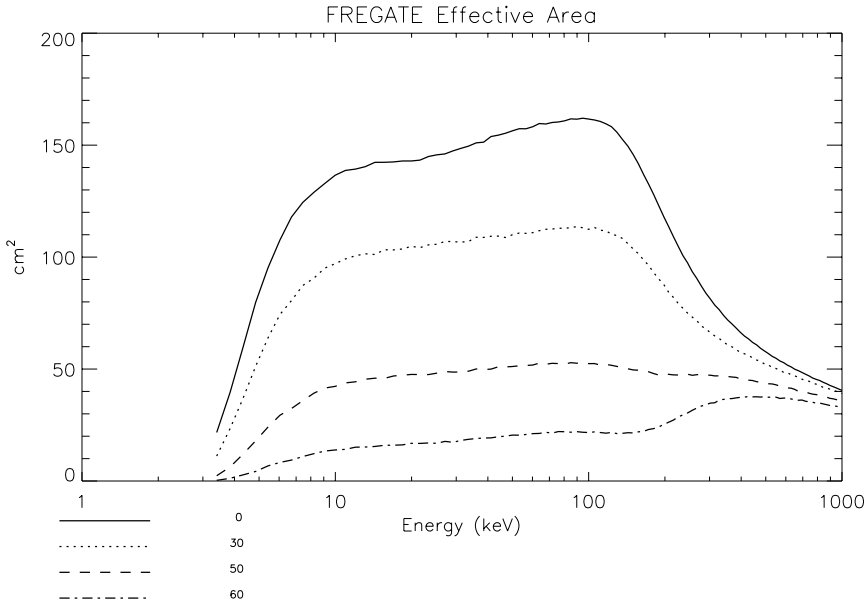

Figure 4.6: FREGATE effective area of the incident angle in 0°, 30°, 50° and 60°.

located 187 mm above the PSPCs (figure 4.8). There are two units of counters called X-camera and Y-camera. Each camera has two PSPCs; the PSPCs in the X-camera are referred to as XA and XB, while those in the Y-camera are referred to as YA and YB. The orientation of the X-camera is perpendicular to the Y-camera, and the X and Y locations of GRBs are determined separately (see figure 4.7).

The area of each coded mask is twice that of the total detector area, to ensure a wide field of view. The masks are supported by an aluminum support structure. The mask is composed of a plate of aluminum (0.5 mm thickness) plated with gold (50.8 μm). The width of the slits are randomly varying integer multiples of 2 mm (figure 4.7). The open fraction of the mask is 0.33. A 7.6 μm thickness aluminum-coated kapton foil is placed in front of the mask, as a thermal shield. The location of the GRB is calculated from the shift distance of the mask shadow on the X and Y camera independently.

The cross-section view of PSPC is shown in figure 4.9. The PSPC has three anode wires which are composed of carbon fibers 10 μm in diameter and 120 mm in length. The counter is divided into an upper layer with three anode cells and a lower veto layer. The veto layer is to distinguish the charged particles from the X-ray photons. The counters are filled with xenon (97%) and carbon dioxide (3%) at 1.4 atm pressure at room temperature. The beryllium windows of 100 μm thickness is placed at the front of the detector. The detector body is made of titanium. The geometrical area of the entrance window is 88 cm^2. The effective area curve of WXM is shown in figure 4.10 in the case of the boresight incident angle. The ^{55}Fe radioisotopes are attached at the top of the support structure of the coded mask. The radioisotope is contained in a slit case and both sides of each counter at 40 mm distance from the center of the counter are irradiated.

One of the key features of WXM is on-board triggering and localization of GRBs. There are 68 trigger criteria with time scales from 80 ms to 27 s, and the threshold levels from 4.7 to 8.0 sigma depending on their time scales. There are also "bracket-type" triggers which have two background regions taken before and after the foreground region. This trigger reduces the number of false triggers due to increase of the background. As of November 2003, 32 on-board triggers are working. When a GRB triggers WXM or FREGATE, the position histograms of the X and Y cameras for the optimized foreground and background regions are extracted from the memory, and the histogram is cross-correlated with the templates for all the incidence angles. As each localization is completed, the trigger process continues to search for better time intervals based on the signal-to-noise ratio, and localization is performed for each updated foreground and background regions. The cross-correlation scores between the position histogram data

Table 4.4: WXM performance

Energy range	2–25 keV
Effective area (1 PSPC, without coded mask, on axis)	~ 80 cm^2
Position Resolution	~ 1 mm @ 8 keV
Energy Resolution (FWHM)	~ 20 % @ 8 keV
Angular Resolution	$\sim 10'$

Table 4.5: Data products of WXM

Data type	Time resolution	Description
HK	4 s	House Keeping data. Power status, HV setting temperatures of an electronic board and the wall of the support structure.
RAW	1 μ s	The unprocessed photon data. This data is used as the health check of the instrument and the calibration of the energy response.
TH	1.2 s	The time history data for 4 energy bands (approximately 2–5 keV, 5–10 keV, 10–17 keV and 17–25 keV) and for 4 counters.
POS	6.6 s	The position histogram data in two energy bands (approximately 2–7 keV and 7–25 keV).
PHA	4.9 s	4.9 s time-binned energy spectrum. Available for each anode wires. The position information is not available.
TAG	256 μs	This data is generated when the trigger is occurred. The photon data with the information of time, position, energy and wire ID are available.

and the Monte Carlo simulated templates of various incident angles are calculated to find the template which matches best with the data. The GRB location in the WXM detector coordinate is converted to the celestial coordinate using the aspect information of the spacecraft. A conservative error (90% confidence radius) is $30'$ in flight. More sophisticated ground analysis gives $\sim 10'$ accuracy.

Details about the WXM characteristics and the energy response matrix are in Appendix A.

The data products of WXM are summarized in table 4.5. The data using for the scientific study are TAG, POS, TH and PHA.

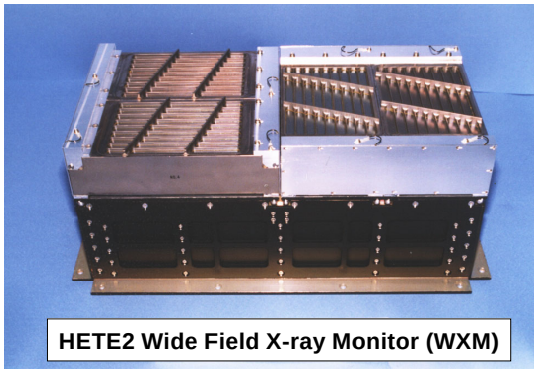

(a) The WXM detector. The left side is the X camera, while the right side is the Y camera.

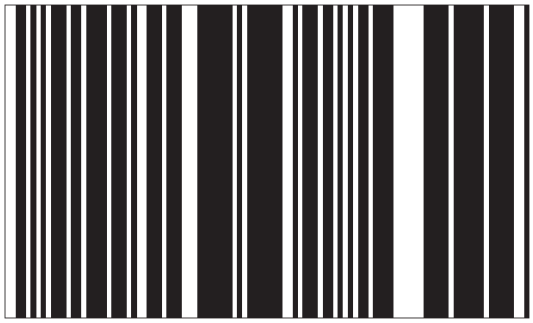

(b) The coded aperture of WXM.

Figure 4.7: The photograph of the WXM detector part (figure a) and the coded aperture of one direction (figure b).

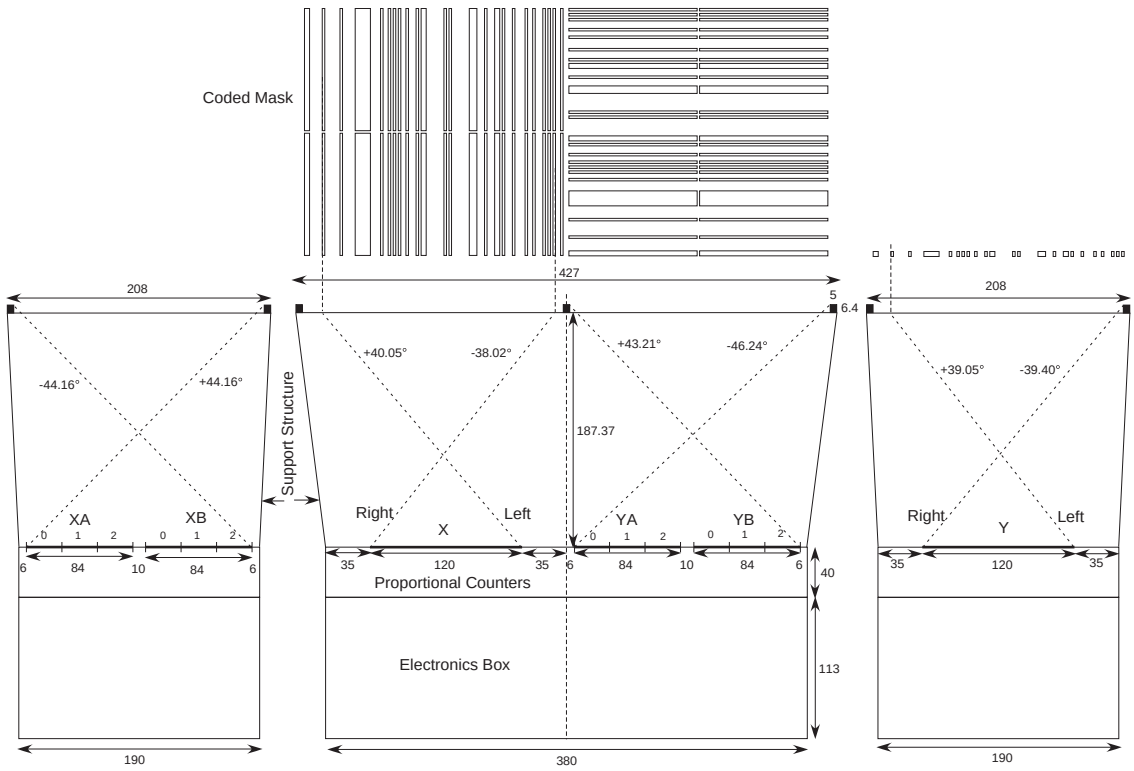

Figure 4.8: The dimension of the whole WXM system.

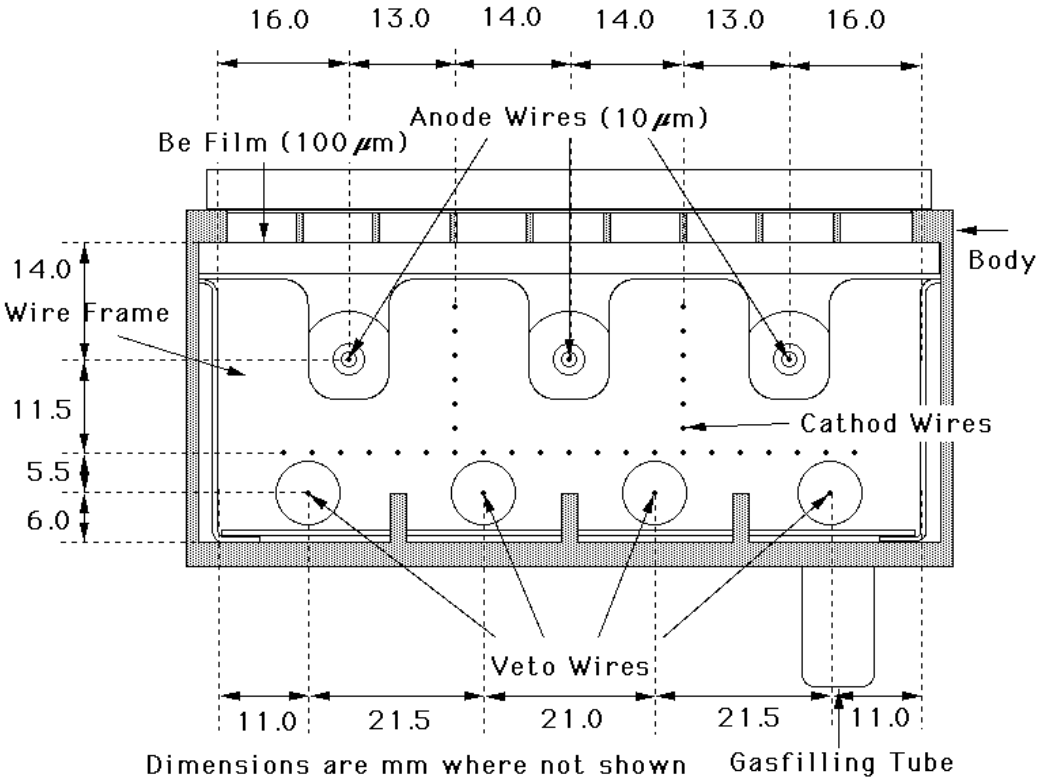

Figure 4.9: The cross section of one PSPC.

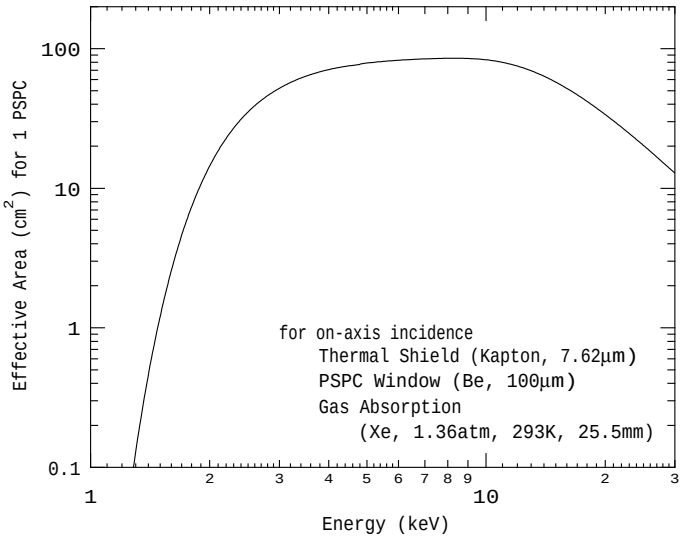

Figure 4.10: The effective area of one PSPC for the boresight incidence.

Table 4.6: SXC performance

Energy range	2–14 keV
Effective area	7.4 cm^2 per SXC
Field of view	0.91 sr
Energy Resolution	46 eV @ 525 eV, 129 eV @ 5.9 keV

4.4 SXC

The soft X-ray camera (SXC) is designed to provide a few arcsecond location of the GRB. SXC consists of X-ray CCDs and a fine coded mask. The coded mask is located 95 mm above the CCD chips with the mask element size of 45 μm. This corresponds to the characteristic angular resolution of 96″.

The size of the SXC coded mask is 10 cm × 10 cm. The deviations of the slit edges of the mask is less than 5 μm rms and this is an ideal performance to achieve the SXC angular resolution. The pattern consisted of 2100 coded elements. The open fraction of the mask is $\sim$ 0.2.

The X-ray CCDs are front-side CCID-20 2048 × 4096 arrays (15 × 15 μm pixels; 6.1 cm × 3.1 cm size) fabricated at MIT Lincoln Labs. The device operates as a collection of 2048 long and narrow detectors. The integration time is 1.2 s. To minimize the power consumption, the CCDs are passively cooled to -50°C in flight using a radiator plate attached to the baseplate.

Two optical blocking filters (OBF) were mounted on the SXC. The OBFs were intended to prevent non X-ray photons like moonlight from reaching the CCDs. The outer OBF is made of a 0.05 μm aluminized polyimide film, covering the whole aperture. The inner OBF is made of a 25 μm Be foil, covering one half of the CCD area. Unfortunately, due to the increase of the density of atomic oxygen by the intense solar flares in the period of the late year 2000 to the early year 2001, the outer OBFs were lost. The polyimide was eroded by unexpected high flux of atomic oxygen. Since then, the SXC is not operated at the bright moon phases.

To monitor the gain variation in orbit, ^{55}Fe radioactive source is attached to the mask frame.

The localization procedure of SXC is restricted for the search region to $\pm$ 1° of the best WXM location to avoid the false localization. With this restriction, there is only a 1% chance that the location is a false detection. Empirical measurements show a 20″ radius RMS localization accuracy in the X and Y directions. This corresponds to a 90% confidence, two-dimensional error circle of 43″ radius [55].

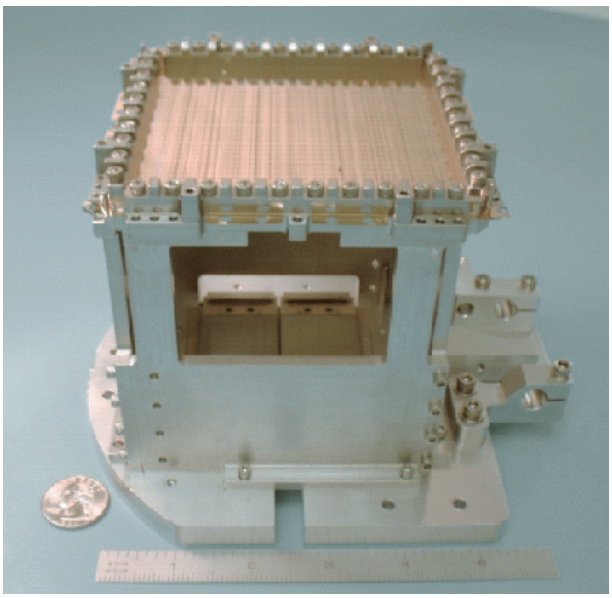

Figure 4.11: The picture of SXC.

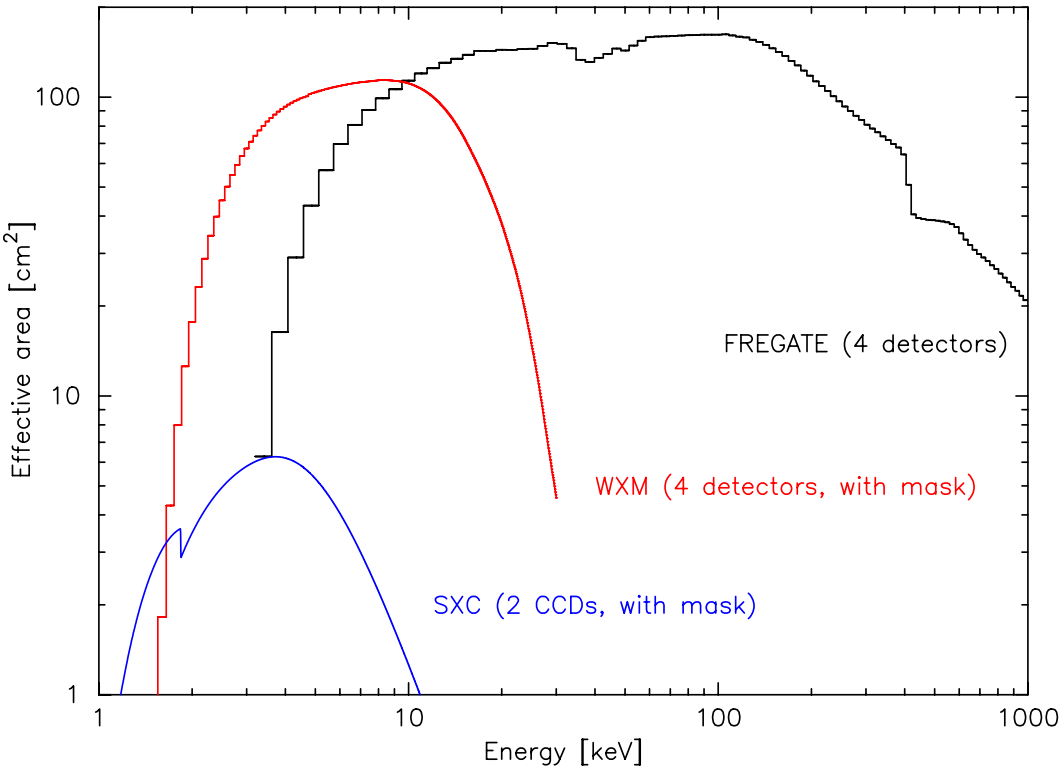

Figure 4.12: Effective area curve for three instruments as a summary.

Chapter 5

Analysis

5.1 Data reduction of the WXM data

In the spectral analysis of WXM, we used the photons within the wire range of ± 50 mm (full wire range is ± 60 mm) when the WXM photon data (TAG data) are available in order to avoid the gain variations of the both ends of the wires (see Appendix A, "∼" curve). Since the position information is not available in the spectral survey data (PHA data), this reduction is only applied to the TAG data.

The WXM spectrum is constructed by the summing the photons of the wires illuminated by the source using a FTOOLS command *mathpha*.

5.2 Spectral models

Three spectral models are used in fitting the GRB spectrum. The first model is the power-law model:

$$f_{\rm GRB}(E) = A(E/15)^{\alpha}, \tag{5.1}$$

where the normalization A in photons $\rm cm^{-2}$ $\rm s^{-1}$ $\rm keV^{-1}$, and the photon index α. The normalization is selected to be at 15 keV, because both the WXM and FREGATE spectra are overlapped at this energy.

The second model is the cutoff power-law model:

$$f_{\rm GRB}(E) = A(E/15)^{\alpha}\exp(-E(2+\alpha)/E_{\rm peak}), \tag{5.2}$$

where the normalization A, the photon index α, and the peak energy in νF_{ν} spectrum $E_{\rm peak}$.

The third model is the Band function [63]:

$$f_{\rm GRB}(E) = A(E/15)^{\alpha}\exp(-E(2+\alpha)/E_{\rm peak})$$

if $$E < (\alpha-\beta)E_{\rm peak}/(2+\alpha) \equiv E_{\rm break},$$

and $$f(E) = A(\alpha-\beta)E_{\rm peak}/[15(2+\alpha)]^{\alpha-\beta}\exp(\beta-\alpha)(E/15)^{\beta}$$

if $$E \geq (\alpha-\beta)E_{\rm peak}/(2+\alpha), \tag{5.3}$$

where the four parameters are the normalization A, a low-energy spectral index α, a high-energy spectral index β, and a peak energy $E_{\rm peak}$ in νF_{ν} spectrum.

All the spectral analyses are performed in XSPEC v11.2.0 software package.

5.3 Selected TAG data

Due to the coded aperture, the signal to noise ratio (SNR) of the WXM data are usually low (the open fraction of the mask is $\sim 30\%$ at the boresight incident angle). However, it is possible to increase the SNR of the WXM data using its imaging capability. We apply the following steps to maximize the SNR of the WXM data:

1. Simulate positional distribution of the burst photons due to the mask shadows.
2. Sort the position bins according to the simulated counts in decreasing order.
3. Find the foreground/background time regions which maximize the SNR (They usually agree with the foreground/background time regions used in the localization of the burst).
4. Cumulate the foreground/background counts and compute the SNR for the position bins.
5. Choose N which shows the highest SNR.
6. Select the wire-position pairs from 1 to N.

The new data set created in this method called "selected TAG data." The resulting improvement of SNR is demonstrated in figure 5.1. All the bursts which the TAG data are available, are creating the selected TAG data. The selected TAG data are using in both the temporal and the spectral analysis. Note that since the selected TAG data are "artificially" selecting the illuminated position bins from the burst, we have to correct the effective area for the spectral analysis. We are multipling the fraction to the response matrix of each wires defined as (simulated counts of selected bins)/(total simulated counts).

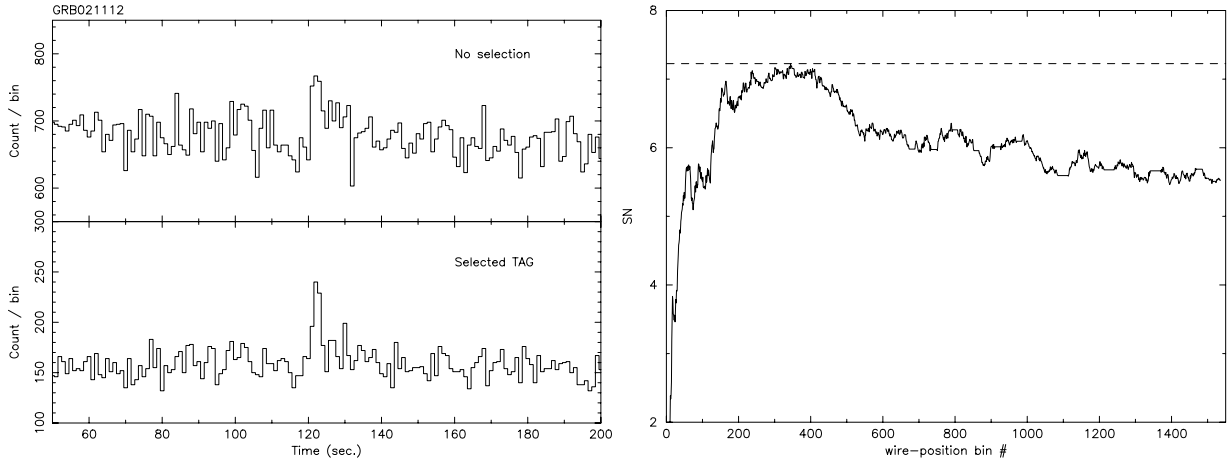

Figure 5.1: Left: Example of the light curves (GRB021112) using the normal TAG data (above) and the selected TAG data (bottom). Right: The wire-position pairs vs. the cumulated signal to noise ratio. The dashed line corresponds to the maximum SNR.

5.4 Definition of X-ray flash, X-ray-rich GRB, and hard GRB

Our definitions of X-ray-flash, X-ray-rich GRB, and hard GRB [1] are:

$$\begin{array}{cc} \log(S_{\rm X}/S_\gamma) > 0 & \text{X-ray flash} \\ -0.5 < \log(S_{\rm X}/S_\gamma) \leq 0 & \text{X-ray-rich GRB} \\ \log(S_{\rm X}/S_\gamma) \leq -0.5 & \text{hard GRB} \end{array}$$

where $S_{\rm X}$ and S_γ are the fluence of 2–30 keV and 30–400 keV in the best fit spectral model respectively.

5.5 "Constrained" Band function

In some XRFs, we confronted by the difficulty of determining the four spectral parameters in the Band function due to the low statistics. Moreover, since XRFs are intrinsically weak and the break energy is close to the lower boundary of the observable energy band of *HETE*, the simple power-law will be the acceptable model for many cases. If we assume that XRF has the similar spectrum as hard GRB, the power-law index < -2 is the high energy photon index β of the Band function. The break energy $E_{\rm break} = (\alpha - \beta)E_0$ which separates the low and high energy part of the Band function is near or below the lower boundary of the energy range of a

[1] We call the BATSE-like GRBs as "hard GRBs" for the clarification.

detector.

When we try to fit this kind of XRF spectrum with the Band function, a problem arises. Since the Band function is a combination of the two power-law spectrum, both the low energy index α and the high energy index β can make the pure power-law spectrum.

To handle this situation, we develop the new spectral model called a *constrained* Band function. The *constrained* Band function has three spectral parameters (β, $E_{\rm peak}$, and A) and one fixed parameter $E_{\rm pivot}$. The *constrained* Band function is perfectly able to make both pure power-law spectra and the cutoff power-law spectra of the required curvature in the detector range. And only the high-energy part of the Band function is allowed to produce a pure power-law spectrum. We described this model in detail at Appendix D.

Chapter 6

HETE X-ray Flashes and X-ray-rich GRBs

In this chapter, we provide the detailed spectral and temporal analysis of 18 X-ray flashes (XRF) and X-ray rich GRBs (XRR). The selection criterion for these events is that their X-ray to γ-ray fluence ratios are larger than 0.75[1]. Each section consists of a brief summary of the event, afterglow status, temporal characteristics, and spectral characteristics. From these detailed studies of the individual properties of XRFs and XRRs, we found 1) the durations of the XRFs and XRRs are similar to those of hard GRBs, 2) most XRFs and XRRs show complex time-structures similar to those of hard GRBs, 3) spectral softening is seen during the burst for most XRFs and XRRs, 4) the $E_{\rm peak}$ energies of XRFs and XRRs are generally lower than those of hard GRBs, 5) six events in the sample had $E_{\rm peak}$ energies as low as a few keV, and 6) afterglows were found only for a few XRF, which may imply that the afterglows of XRFs are generally very faint.

6.1 GRB010213

The bright X-ray flash was detected on 13 February 2001 at 12:35:35 UTC [69]. Since *HETE* was in the performance verification phase at that period, the localization was performed by the ground analysis. The celestial coordinate of this source is (R.A., Dec.) = ($10^{\rm h}31^{\rm m}36^{\rm s}$, $5^\circ30'30''$) (J2000) with a 95% error radius of $30'$. This large uncertainty is due to the unstable attitude

[1]GRB020625, which has an X-ray to γ-ray fluence ratio of 20.5, is not included in this study, because this fluence ratio value is derived from the possible second peak of the burst and might not be the "actual" fluence ratio for this event.

of the spacecraft.

The status of the afterglow search of this X-ray flash is summarized in table 6.1. No afterglow candidate has been found for GRB010213.

Table 6.1: The afterglow search for GRB010213

Time[a]	Telescope & Instruments	OT	Lim. Mag.[b]	GCN
1.48 days	HETE GCN notice			#934
38 hours	Automatic 25 cm telescope TAROT (Nice, France)	N	17 mag. (USNO A2.0)	Boer et al. (#936)
1.57 days	0.57m f/5.2 Telescope (unfiltered) Klet Observatory (Czech Republic)	N	$\sim$ 20.5 mag. (DSS2)	Hudec et al. (#941)
1.89 days	ASTROCAM IR camera USNOFS[c] 1.55 m	N	POSS-IIF limit	Henden et al. (#940)
1.90 days	VLA[d] (1.43 GHz)	N[e]		Berger et al. (#945)
2 days	BAO[f] 0.6 m Schmit Telescope (BATC-i filter)	N	$\sim$ 22 mag.	Zhu et al. (#946)

[a] Time after the trigger

[b] Limiting magnitude

[c] U.S. Naval Observatory Flagstaff Station (Arizona, USA)

[d] Very Large Array (New Mexico, USA)

[e] Berger et al. reported the afterglow candidate in GCN #945, however, they rejected in GCN #947.

[f] Beijing Astronomical Observatory

6.1.1 Light curve

As seen in Figure 6.1, two peaks are observed in the WXM energy range. The first peak is visible for all four WXM energy bands. On the other hand, the second peak is only existed in the energy range below 10 keV. The double peak structure is also seen in the FREGATE 6-40 keV light curve. There is no significant excess in the FREGATE 32–400 keV band. The duration in 2–25 keV is $\sim$ 40 seconds.

6.1.2 Spectrum

The spectral analysis is performed for the four time intervals including the whole burst region (Fig. 6.1). The fluxes and fluences derived from the Band function are summarized in table 6.2.

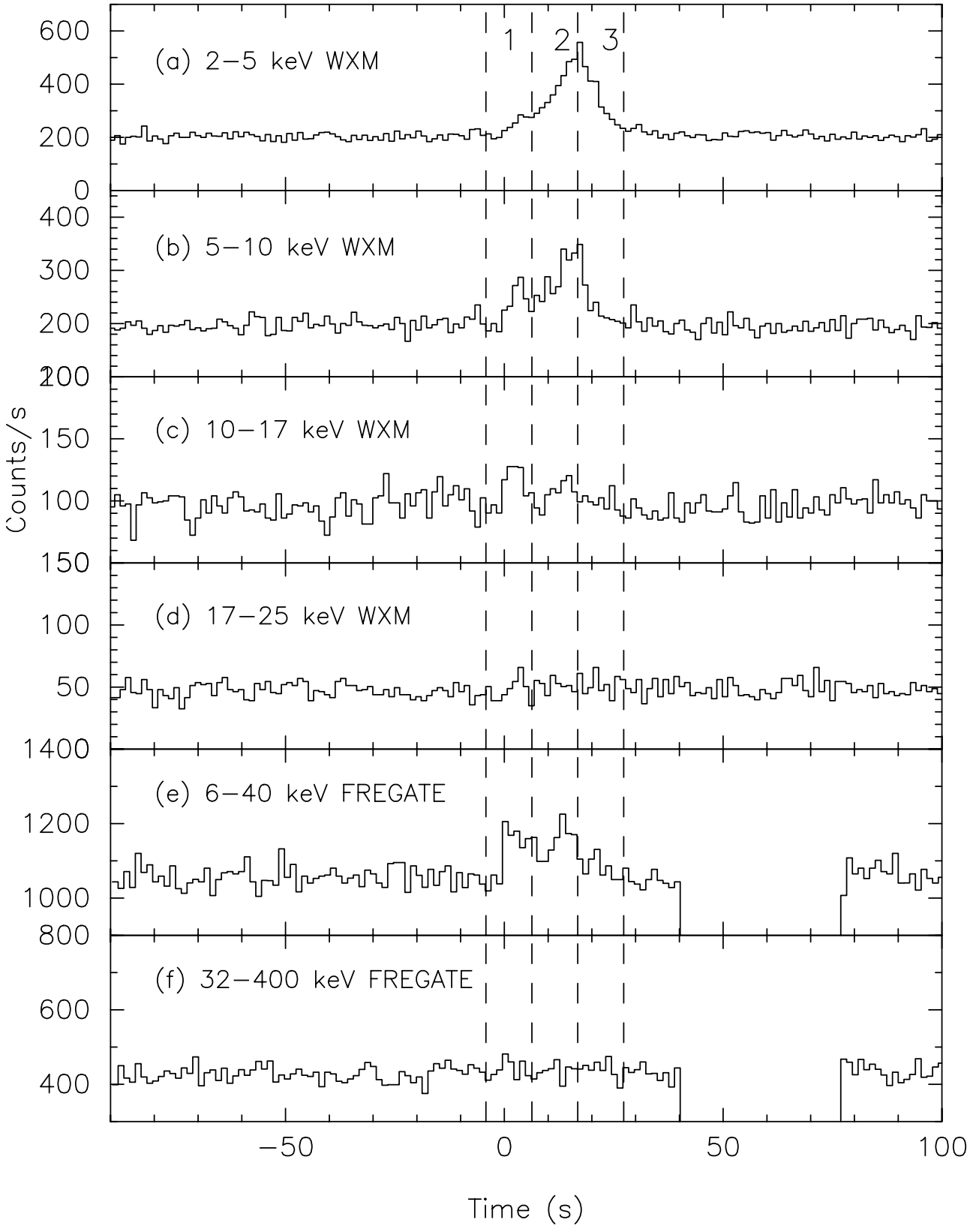

Figure 6.1: The energy resolved light curves of GRB010213 in 1.23 seconds time resolution. The three spectral regions are shown in the dotted lines. There is a data gap in the FREGATE light curves from 40 to 80 seconds from the onset.

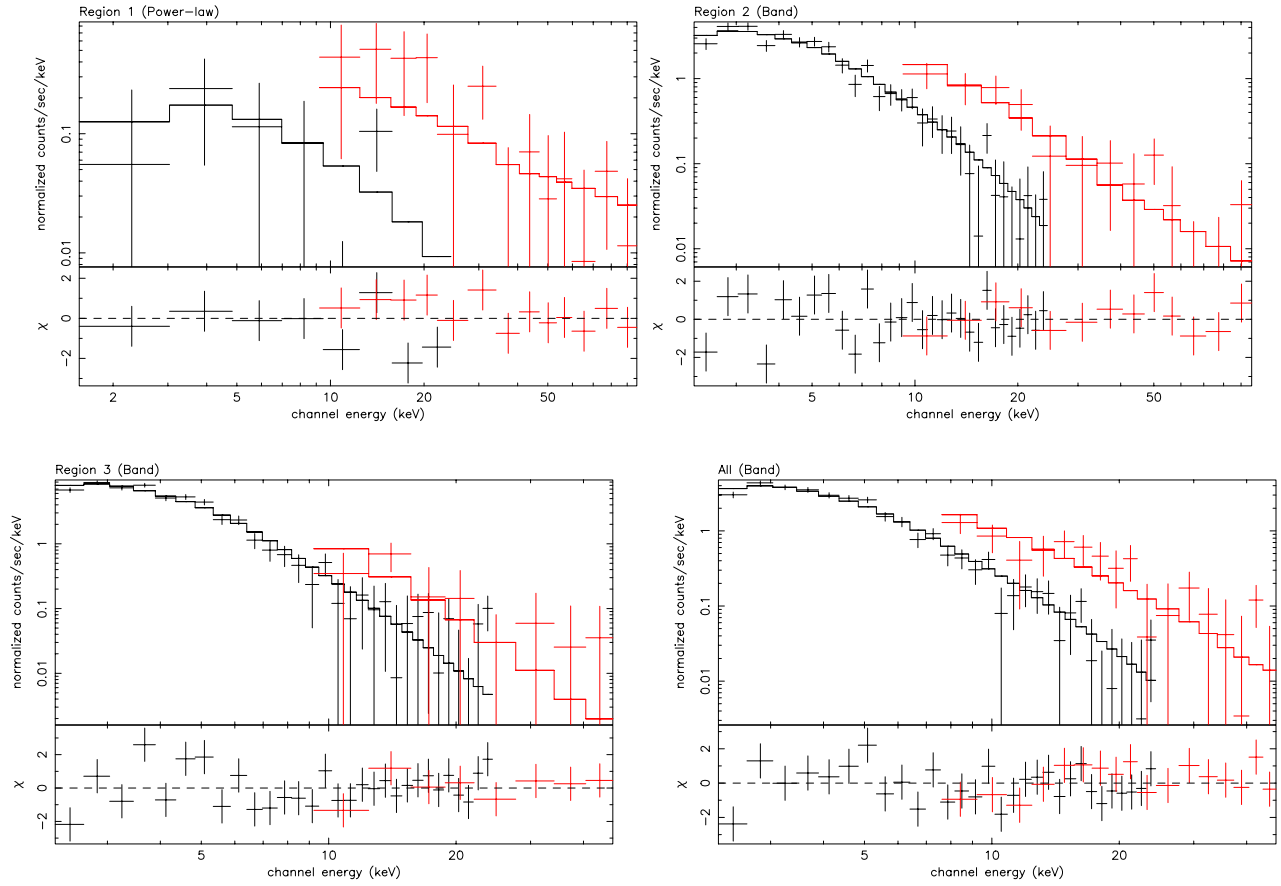

Figure 6.2: The WXM and FREGATE spectra of GRB010213. The spectra of region 1, region 2, region 3 and the whole time region are shown. The model spectrum is the Band function for region 2, region 3, and the whole time region, whereas region 1 is the power-law model.

The energy fluence ratio of 2–30 keV to 30–400 keV is 11.4, qualifying this event as an X-ray flash in our definition. The spectra for the second, the third, and the whole region apparently require a break within the observed energy range. For the first region, however, a simple power-law model provides an acceptable fit. The outstanding characteristics of the prompt emission of GRB010213 is the low $E_{\rm peak}$ energy (a few keV) for the second and the third time intervals. Softening of $E_{\rm peak}$ is observed between these two time intervals.

We investigate the spectral evolution during the burst with the hardness ratio between 5–10 keV and 2–5 keV energy band. As seen in figure 6.3, the spectral softening started just after the first peak at t = 5 sec.

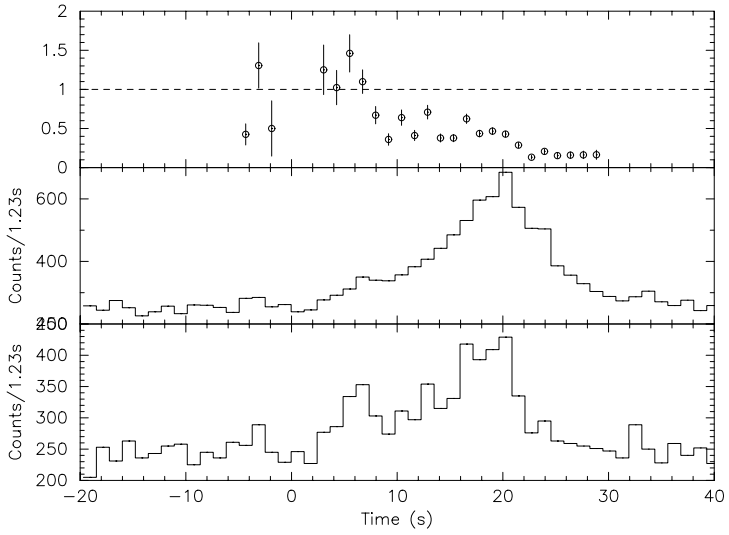

Figure 6.3: The hardness ratio between the 5–10 keV and 2–5 keV bands. The upper panel is the hardness ratio plot, and the middle and the bottom panels are the light curves in the 2–5 keV and 5–10 keV bands respectively.

Table 6.2: The fluxes and fluence of GRB010213 in the Band function.

	energy range [keV]	region 1	region 2	region 3	all
Duration [sec.]		10.5	10.5	10.5	31.5
Photon flux	2 – 10	1.8±1.6	30.1±2.0	59.8±3.0	30.4±1.5
[10^{-1} ph cm^{-2} s^{-1}]	2 – 30	2.7±1.9	33.4±2.2	61.0±3.0	32.3±1.5
	30 – 400	1.4±1.2	$0.7^{+0.5}_{-0.1}$	(31.7±17.9) × 10^{-3}	0.2±0.1
	2 – 400	4.1±2.2	34.1±2.3	61.0±3.0	32.5±1.6
Energy flux	2 – 10	1.4±1.1	19.6±1.3	33.5±1.7	18.4±0.8
[10^{-9} erg cm^{-2} s^{-1}]	2 – 30	4.0±2.3	27.9±2.3	35.8±2.3	$22.9^{+0.7}_{-1.6}$
	30 – 400	$14.7^{+14.4}_{-10.7}$	$6.7^{+6.1}_{-4.7}$	$(1.3^{+2.0}_{-0.6}) \times 10^{-1}$	$2.0^{+1.7}_{-0.9}$
	2 – 400	$32.3^{+39.2}_{-23.4}$	$34.6^{+7.8}_{-6.6}$	35.9±2.6	24.9±2.8
Photon fluence	2 – 10	$1.9^{+1.8}_{-1.5}$	31.7±2.8	62.8±3.1	95.9±4.5
[ph cm^{-2}]	2 – 30	2.9±2.0	35.1±2.2	64.0±3.1	101.8±4.7
	30 – 400	$1.5^{+1.4}_{-1.1}$	$0.7^{+0.5}_{-0.1}$	(3.3±1.9) × 10^{-2}	$0.7^{+0.5}_{-0.3}$
	2 – 400	4.3±2.3	35.8±2.4	64.1±3.1	102.5±4.8
Energy fluecne	2 – 10	$1.5^{+1.2}_{-1.1}$	20.6±1.3	35.2±1.7	58.0±2.6
[10^{-8} erg cm^{-2}]	2 – 30	4.2±2.4	29.3±2.4	37.6±2.4	$72.2^{+2.2}_{-5.0}$
	30 – 400	$15.4^{+15.1}_{-11.2}$	$7.1^{+6.4}_{-5.0}$	$1.3^{+2.1}_{-0.6} \times 10^{-1}$	$6.3^{+5.3}_{-2.9}$
	2 – 400	$33.9^{+41.2}_{-24.6}$	$36.4^{+8.2}_{-7.0}$	37.7±2.7	$78.5^{+9.2}_{-8.6}$

Table 6.3: The spectral parameters of GRB010213 for the power-law model (PL), the cutoff power-law model (Cutoff PL), and the Band function (Band).

Model	parameters	region 1	region 2	region 3	all
PL	α	$-1.23^{+0.54}_{-0.51}$	$-2.19^{+0.10}_{-0.10}$	-2.89	$-2.47^{+0.08}_{-0.09}$
	$K_{15}{}^{a}$	$5.65^{+2.99}_{-3.19}\times10^{-3}$	$2.64^{+0.35}_{-0.34}\times10^{-2}$	1.85×10^{-2}	$1.75^{+0.23}_{-0.21}\times10^{-2}$
	χ^2_ν/DOF	0.964/19	1.293/41	2.363/36	1.561/45
Cutoff PL	α		-1.00 (fixed)	-1.00 (fixed)	-1.00 (fixed)
	E_{peak} [keV]		$5.45^{+0.82}_{-0.69}$	$2.57^{+0.22}_{-0.21}$	$3.60^{+0.34}_{-0.31}$
	K_{15}		$0.29^{+0.04}_{-0.04}$	$1.26^{+0.18}_{-0.17}$	$0.42^{+0.06}_{-0.05}$
	χ^2_ν/DOF		1.057/41	1.114/36	1.144/45
Band	α		-1.00 (fixed)	-1.00 (fixed)	-1.00 (fixed)
	β		$-2.55^{+0.22}_{-0.60}$	< -3.61	$-2.96^{+0.23}_{-0.53}$
	E_{peak} [keV]		$4.81^{+1.06}_{-0.78}$	$2.56^{+0.22}_{-0.23}$	$3.41^{+0.35}_{-0.40}$
	K_{15}		$0.32^{+0.06}_{-0.06}$	$1.26^{+0.21}_{-0.15}$	$0.45^{+0.07}_{-0.06}$
	χ^2_ν/DOF		0.949/40	1.120/35	0.940/44

[a] Normalization at 15 keV in the unit of photon cm^{-2} s^{-1} keV^{-1}

6.2 GRB010225

The trigger for this event came from the FREGATE instrument, on 25 February 2001 at 16:52:11.2 UTC. The trigger occurred in the 5–120 keV band, on the 1.3-second time scale. Since the attitude control camera was not operational, the celestial coordinates of this burst were not distributed to the GRB community.

The WXM photon (i.e. TAG) data are not available due to data corruption. The TH (time resolution of 1.2 s) and PHA (time resolution of 5.6 s) survey data are used in the temporal and the spectral analysis instead.

6.2.1 Light curve

A burst consisting of a single peak is visible below 85 keV. The duration of the burst is $\sim$ 10 seconds. A fast rise and exponential decay (FRED) -like temporal structure is seen in the FREGATE lower energy bands. The peak width decreases with increasing energy. The same trend has been noted in many long bright GRBs detected by BATSE [19].

6.2.2 Spectrum

The spectrum is investigated using data from the entire burst duration. The spectral parameters, fluxes and fluence are summarized in table 6.4 and in table 6.5. The X-ray to γ-ray fluence ratio of this burst is 1.4. We therefore classify as an X-ray flash.

When fitting a simple power-law model to the spectrum, we obtained a best-fit χ^2 of 43.9 for 40 d.o.f., which is formally acceptable. However, with the addition of one parameter, a cutoff power-law model fit yielded a χ^2 of 36.1 for 39 d.o.f.. The F-test probability for this improvement is 6.06×10^{-3}. The Band function fit also provides a significant improvement over the simple power-law model fit, but it is no better than the cutoff power-law model, and the addition of two parameters is not justified. For this reason, we decided that the cutoff power-law model is the best representative model for this burst. The $E_{\rm peak}$ energy is around 30 keV. This value lies in the low-energy tail of the BATSE $E_{\rm peak}$ distribution [63] (see also figure 2.1).

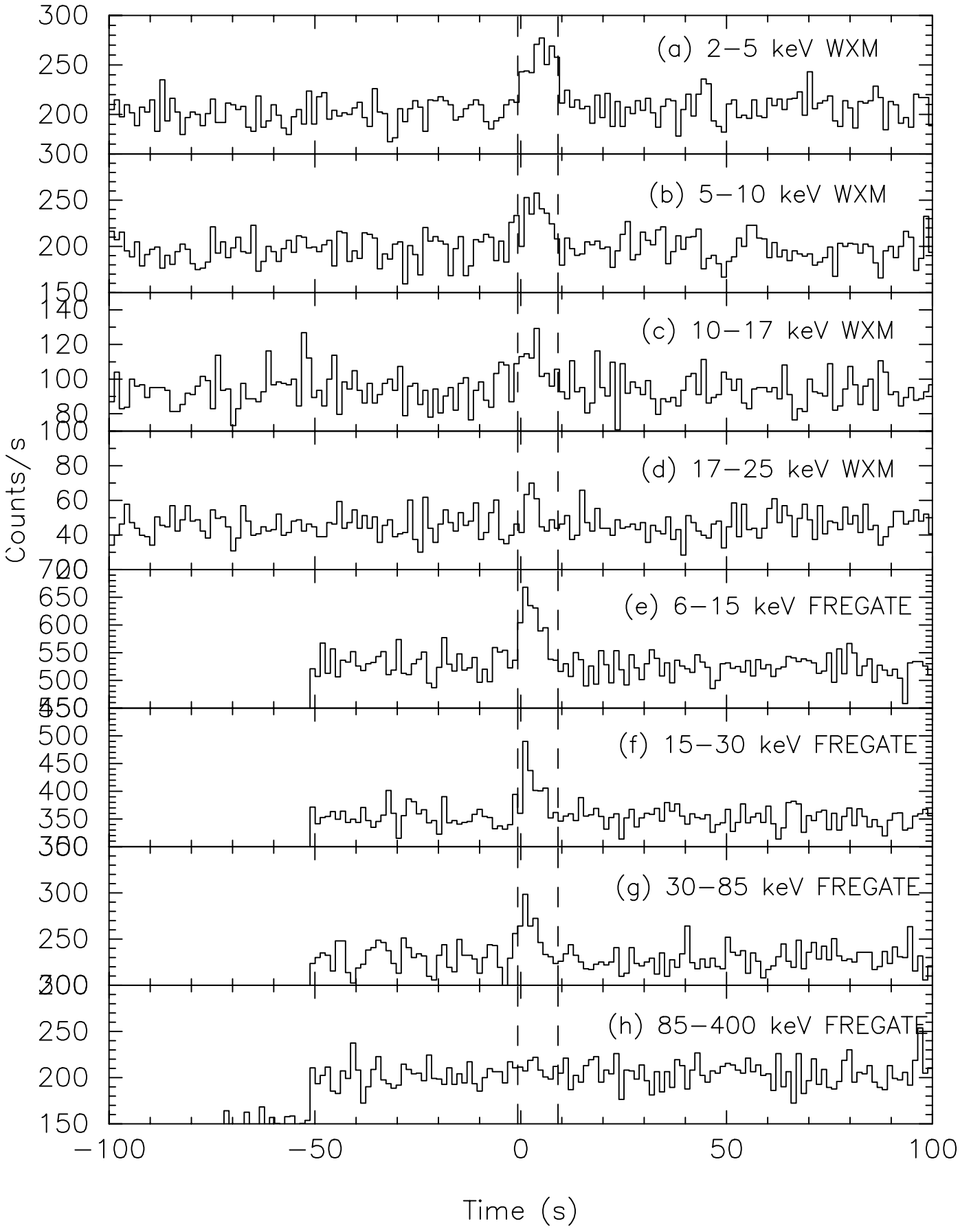

Figure 6.4: The energy-resolved light curves of GRB010225. The dotted lines indicate the time regions used as the foreground to construct the spectrum.

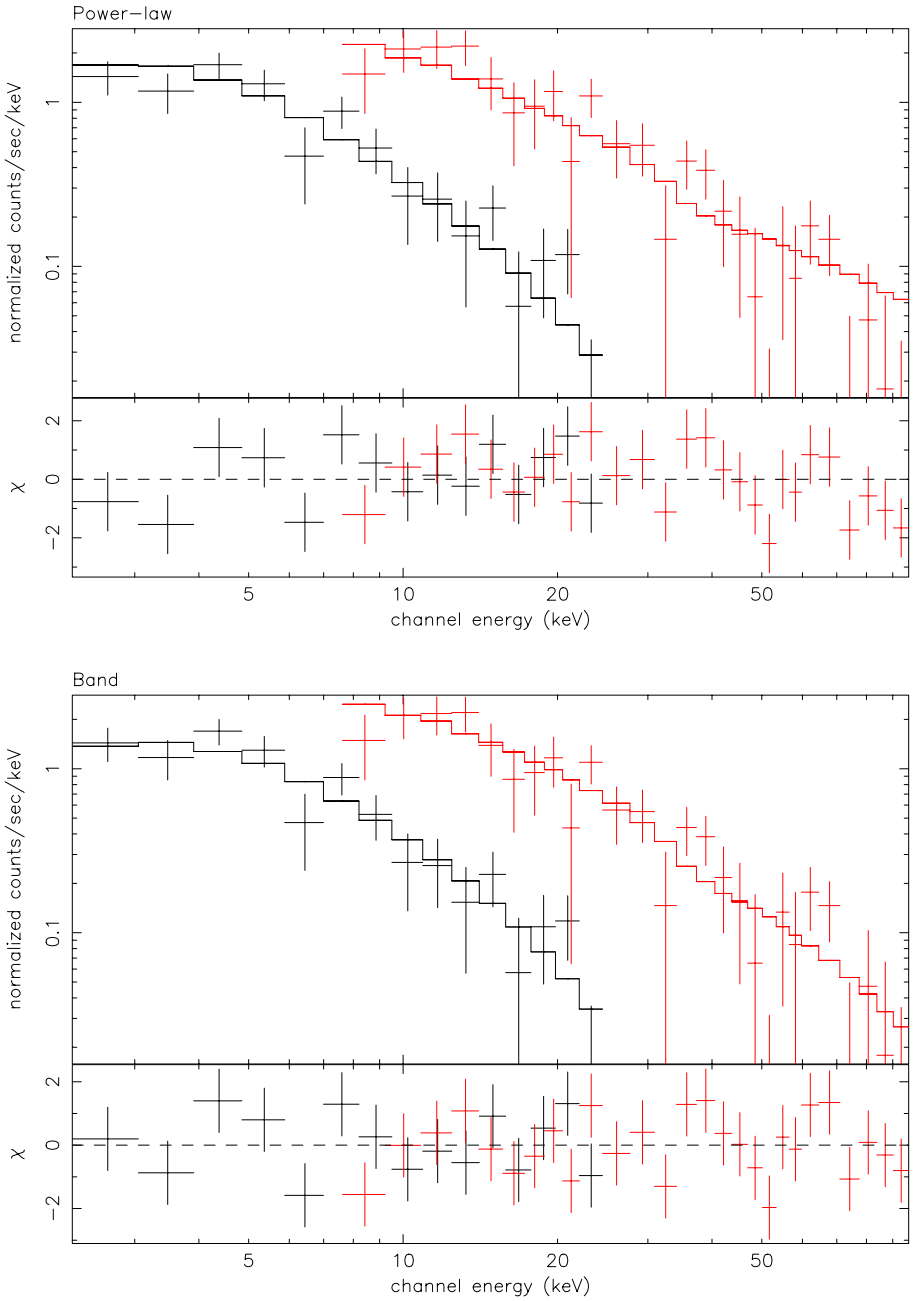

Figure 6.5: The WXM and FREGATE spectra of GRB010225. The spectra with the power-law model (top) and Band function (bottom) are shown.

Table 6.4: The fluxes and fluence of GRB010225 in the cutoff power-law model.

	energy range [keV]	
Duration [sec.]		9.8
Photon flux	2 – 10	2.2±0.4
[ph cm^{-2} s^{-1}]	2 – 30	2.9±0.4
	30 – 400	0.3±0.1
	2 – 400	3.2±0.4
Energy flux	2 – 10	1.6±0.2
[10^{-8} erg cm^{-2} s^{-1}]	2 – 30	3.6±0.4
	30 – 400	$2.5^{+1.8}_{-1.0}$
	2 – 400	$6.0^{+1.7}_{-1.1}$
Photon fluence	2 – 10	21.1±3.7
[ph cm^{-2}]	2 – 30	28.3±3.8
	30 – 400	$2.7^{+1.0}_{-0.8}$
	2 – 400	31.0±3.9
Energy fluecne	2 – 10	15.4±2.2
[10^{-8} erg cm^{-2}]	2 – 30	34.8±3.6
	30 – 400	$24.0^{+17.2}_{-9.5}$
	2 – 400	$58.8^{+16.9}_{-10.6}$

Table 6.5: The spectral parameters of GRB010225 in the power-law, the cutoff power-law, and the Band function.

Model	parameters	
PL	α	-1.71 ± 0.1
	K_{15}[a]	$(4.05 \pm0.45) \times 10^{-3}$
	χ^2_ν/DOF	1.098/40
Cutoff PL[2]	α	$-1.31^{0.30}_{-0.26}$
	E_{peak} [keV]	$31.57^{+26.50}_{-9.17}$
	K_{15}	$6.75^{+2.93}_{-1.87} \times 10^{-2}$
	χ^2_ν/DOF	0.925/39
Band	α	$-1.31^{+0.30}_{-0.26}$
	β	$-9.21^{+7.31}_{-0.79}$
	E_{peak} [keV]	$31.55^{+26.65}_{-9.07}$
	K_{15}	$6.72^{+2.93}_{-1.87} \times 10^{-2}$
	χ^2_ν/DOF	0.950/38

[a] Normalization at 15 keV in the unit of photon cm^{-2} s^{-1} keV^{-1}

6.3 GRB010326B

The trigger for this event came from the FREGATE instrument in the 6–120 keV band on the timescale of 160 ms on 26 March 2001 at 08:33:12 UTC [70]. The celestial coordinates of the burst are R.A. = $11^{\rm h}24^{\rm m}23.36^{\rm s}$, Dec. = $-11°09'57''$ (J2000) with the 90% error radius of $21'$ which includes statistical and systematic errors.

Although the optical observation of this error field was performed at 6 hours after the trigger with the robotic 50-inch telescope at Mount Stromlo Observatory, no optical transient was found in the comparison with the DSS-2 plates [65].

6.3.1 Light curve

The burst signal is visible in the all energy bands. The spiky structures are clearly seen at the FREGATE light curve. There are at least three peaks. The middle peak is the hardest, and the first and the third peaks are softer. The duration of the burst is > 3 seconds and it is a long burst.

6.3.2 Spectrum

The results of the spectral analysis of the time average spectrum are summarized in table 6.6 and 6.7. For some unknown reason, we have to multiply the normalization to the model function for WXM by a constant factor 0.47 to fit simultaneously with the WXM and the FREGATE spectrum. When fitting the spectrum in a simple power-law model, we obtained a χ^2 of 120.3 for d.o.f. of 112, which is fairly acceptable. However, with the one additional parameter, the cutoff power-law model yielded a χ^2 of 95.0 for d.o.f. 111. The F-test probability for this improvement is 3.5×10^{-7}. Although the Band function also provides a significant improvement over the simple power-law model, it is not better than the cutoff power-law model. We decided the cutoff power-law model is the best representative model for this burst. The X-ray to γ-ray fluence ratio is 0.75 which qualifies this event as an X-ray rich GRB.

To investigate the spectral evolution during the burst, the hardness ratio between the FREGATE band C (32–400 keV) and band A (6–40 keV) are plotted in figure 6.8. The gradual softening is seen after the sharp peak of the band C. The highest peak at band A is very soft. The photons at the one second before the trigger are the relatively soft. The hard to soft spectral evolution is observed at the prompt emission of GRB010326B.

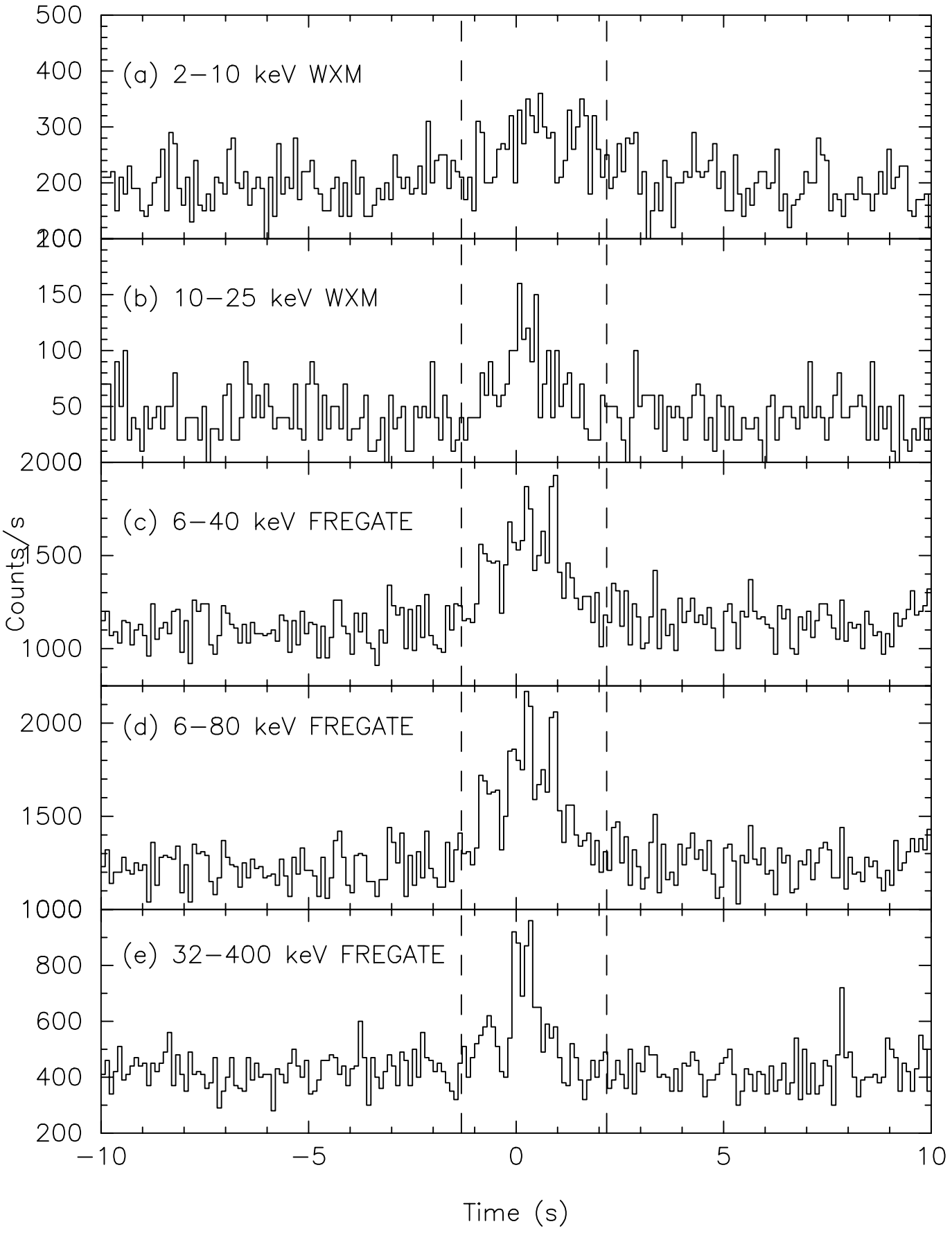

Figure 6.6: The energy resolved light curves of GRB010326B at 0.1 s time bin. The dotted lines correspond to the foreground interval used for accumulating the spectrum.

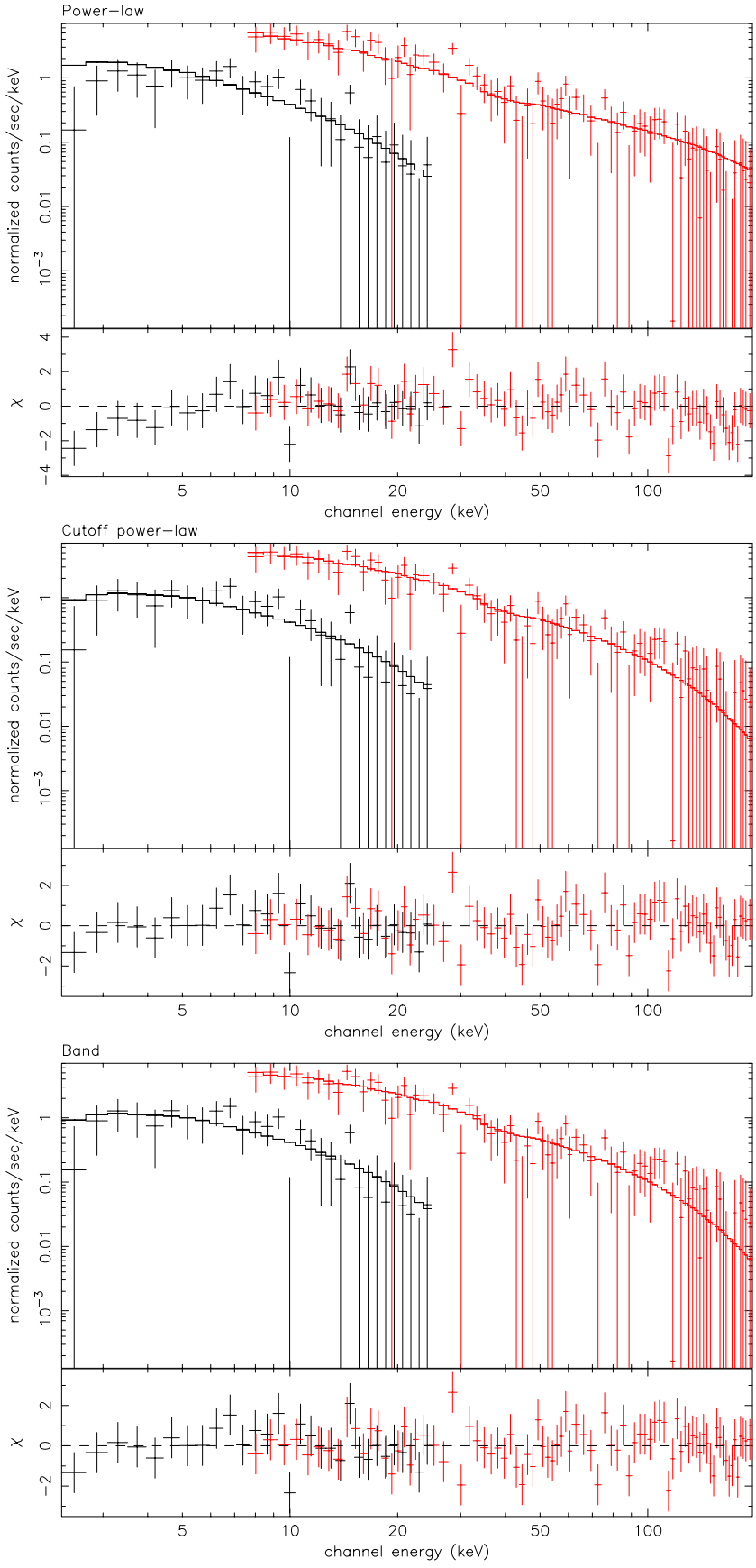

Figure 6.7: The WXM and FREGATE spectra of GRB010326B. The model spectrum are the power-law model, the cutoff power-law model and the Band function from top to bottom.

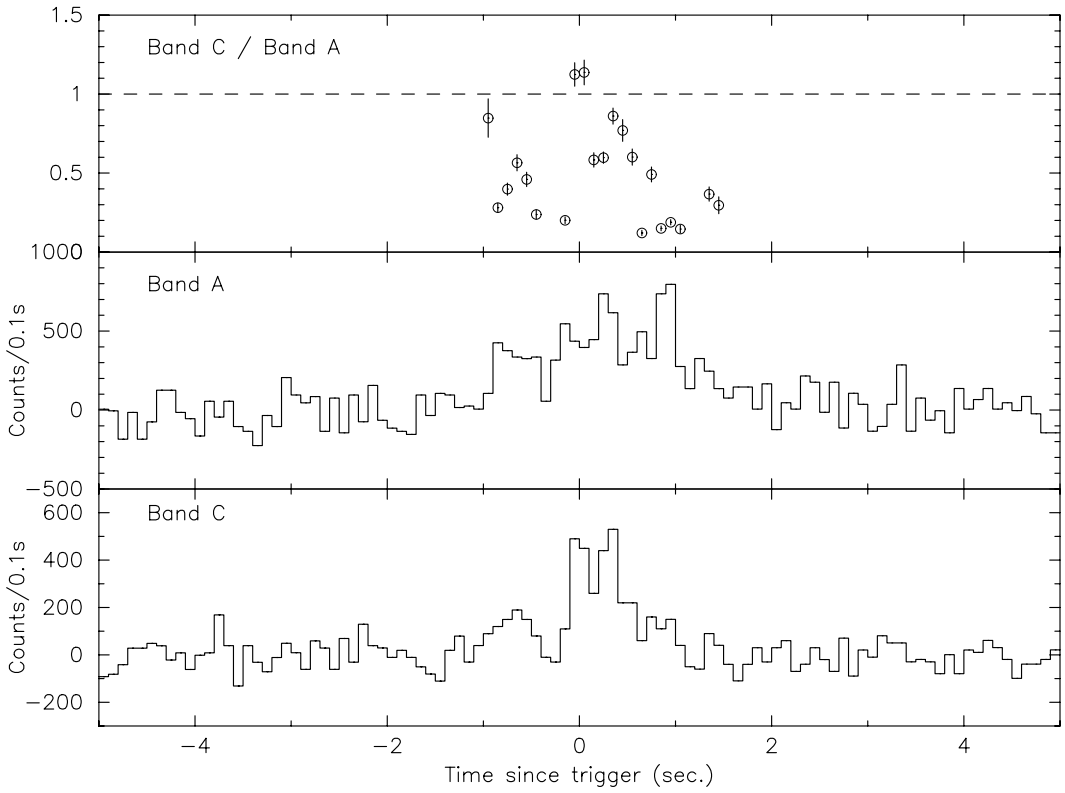

Figure 6.8: The hardness ratio between the FREGATE band C (32–400 keV) and the band A (6–40 keV). The top panel is the harness ratio. The middle and the bottom panels are the FREGATE light curves of band A and C respectively.

Table 6.6: The fluxes and fluence of GRB010326B in the cutoff power-law model.

	energy range [keV]	
Duration [sec.]		3.5
Photon flux	2 – 10	3.2±0.7
[ph cm^{-2} s^{-1}]	2 – 30	4.8±0.8
	30 – 400	0.9±0.2
	2 – 400	5.7±0.8
Energy flux	2 – 10	2.5±0.5
[10^{-8} erg cm^{-2} s^{-1}]	2 – 30	6.9±0.8
	30 – 400	$9.2^{+2.6}_{-2.2}$
	2 – 400	$16.1^{+2.7}_{-2.3}$
Photon fluence	2 – 10	11.3±2.6
[ph cm^{-2}]	2 – 30	16.8±2.8
	30 – 400	3.2±0.5
	2 – 400	20.0±2.8
Energy fluecne	2 – 10	8.7±1.7
[10^{-8} erg cm^{-2}]	2 – 30	24.0±2.7
	30 – 400	$32.2^{+9.2}_{-7.6}$
	2 – 400	$56.2^{+9.5}_{-8.9}$

Table 6.7: The spectral parameters of GRB010326B in the power-law model (PL), the cutoff power-law model (Cutoff PL), and Band function (Band).

Model	parameters	
PL	α	-1.62 ± 0.07
	K_{15}[a]	$(8.23\pm0.84)\times10^{-2}$
	C[b] (WXM)	0.47 (fixed)
	χ^2_ν/DOF	1.073/112
Cutoff PL	α	$-1.08^{+0.25}_{-0.22}$
	E_{peak} [keV]	$51.8^{+18.61}_{-11.25}$
	K_{15}	$1.32^{+0.31}_{-0.23}\times10^{-1}$
	C (WXM)	0.47 (fixed)
	χ^2_ν/DOF	0.856/111
Band	α	$-1.08^{+0.23}_{-0.19}$
	β	$-9.33^{+7.35}_{-0.67}$
	E_{peak} [keV]	$51.70^{+12.59}_{-10.98}$
	K_{15}	$(1.32\pm0.18)\times10^{-1}$
	C (WXM)	0.47 (fixed)
	χ^2_ν/DOF	0.864/110

[a] Normalization at 15 keV in the unit of photon cm^{-2} s^{-1} keV^{-1}

[b] Constant parameter of WXM. The constant parameter of FREGATE is fixed to 1.

6.4 GRB010629B

The WXM and FREGATE instruments detected this event on 29 June 2001 at 12:21:08 UTC [71]. The position of the burst is R.A. = $16^{h}32^{m}38.3^{s}$, Dec. = $-18°43'24''$ (J2000) with the 90% error radius of $15'$. This event was also observed by *Ulysses* and the *Beppo*SAX GRBM [38].

The status of the afterglow search is summarized in table 6.8. No afterglow was found for GRB010629B.

Table 6.8: The afterglow search for GRB010629B

Time[a]	Telescope & Instruments	OT	Lim. Mag.[b]	GCN
8.95 hours	HETE GCN notice			#1075
11.68 hours	DFOSC[c] 1.54 m Telescope La Silla Observatory (Chile)	N	20.5 mag. (I band)	Andersen et al. (#1080)
15.2 hours	1.3 m Telescope (R band) MDM Observatory (Arizona, USA)	N	deeper than DSS	Halpern et al. (#1079)
19 hours	USNOFS[d] 1.0 m Telescope (Arizona, USA)	N	19 mag. (I band)	Henden et al. (#1077)

[a] Time after the trigger

[b] Limiting magnitude

[c] Danish Faint Object Spectrograph and Camera

[d] U.S. Naval Observatory Flagstaff Station

6.4.1 Light curve

The two peaks are visible in all the energy bands (figure 6.9). The both peaks are the fast-rise and the exponential decay (FRED) - like temporal structures in the FREGATE band B and C. The duration of the burst is shorter in the high energy band. The second peak seems to be much softer than the first peak.

6.4.2 Spectrum

The prompt emission of GRB010629 is studied with the spectra of individual peaks and that of the whole burst region. Due to the corruption of the burst data in WXM, PHA data are used for the analysis.

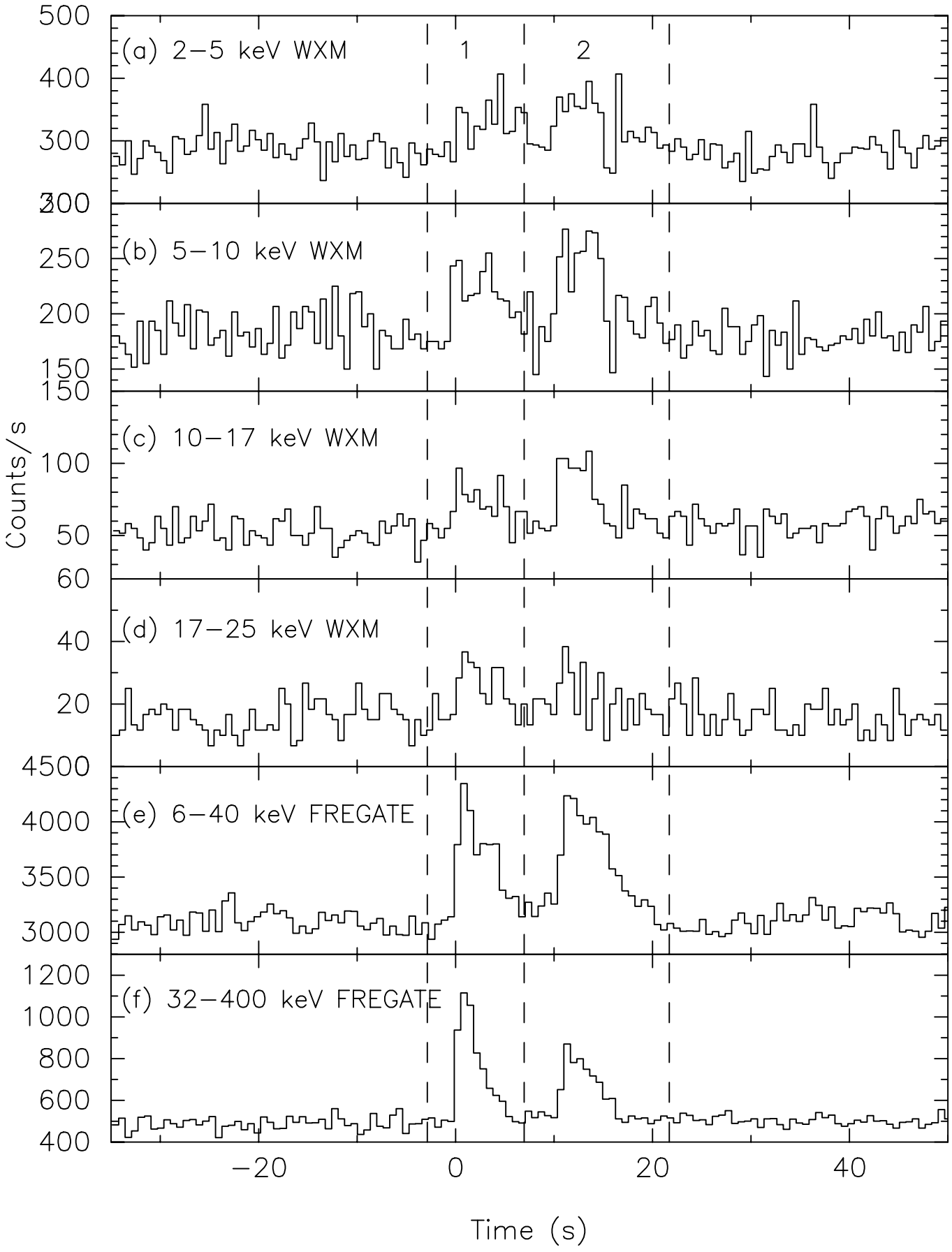

Figure 6.9: The energy resolved light curves of GRB010629B at 1.23 s time bin. The dotted lines correspond to the two foreground intervals used for creating the spectra.

The time-averaged fluxes and fluences in the various energy bands are summarized in table 6.9. The fluence ratio of 2–30 keV to 30–400 keV is 0.9 which qualifies this event as an X-ray rich GRB. The fluence in the 30–400 keV band decreases from region 1 to region 2, while that in the 2–30 keV band increases, indicating the spectral softening during the burst.

The spectral parameters are shown in table 6.10. The power-law model is rejected for the region 1 and for the whole burst region with the null hypothesis probability of 1.2×10^{-10} and 1.7×10^{-8} respectively. For the region 2, the F test probability is 1.9×10^{-9} from the improvement of the cutoff power-law model over the power-law model. There was no improvement in χ^2 to justify the Band function over the cutoff power-law model. Thus, the spectra of all spectral regions require the break in the power-law spectrum. Since the high energy photon index β is not well determined for all spectral regions, we decided that the cutoff power-law model is the best representative model for GRB010629B.

The hard to soft spectral evolution is observed from region 1 to region 2. The low energy power-law slope becomes steeper, and $E_{\rm peak}$ becomes softer between these two intervals. The $E_{\rm peak}$ energy of the time-averaged spectrum is $\sim$ 45 keV.

Table 6.9: The fluxes and fluences of GRB010629B. The spectral model is the cutoff power-law model.

	energy range [keV]	region 1	region 2	all
Duration [sec.]		9.8	14.7	24.5
Photon flux	2–10	$2.5^{+0.8}_{-0.7}$	7.5±1.4	5.1±0.8
[ph cm^{-2} s^{-1}]	2–30	$4.6^{+0.9}_{-0.8}$	9.9±1.4	7.4±0.8
	30–400	1.6±0.1	0.9±0.1	1.2±0.1
	2–400	$6.2^{+0.9}_{-0.8}$	10.9±1.4	8.7±0.9
Energy flux	2–10	$2.1^{+0.6}_{-0.5}$	$5.6^{+0.7}_{-1.0}$	3.9±0.5
[10^{-8} erg cm^{-2} s^{-1}]	2–30	8.0±0.9	12.1±1.0	10.3±0.7
	30–400	$16.3^{+1.9}_{-1.7}$	$8.2^{1.5}_{-1.2}$	11.6±1.0
	2–400	24.3±2.1	$20.3^{+1.9}_{-1.6}$	22.0±1.3
Photon fluence	2–10	$24.9^{+8.0}_{-6.8}$	$110.5^{+20.9}_{-19.8}$	$126.2^{+20.1}_{-18.9}$
[ph cm^{-2}]	2–30	$44.8^{+9.2}_{-8.1}$	$146.5^{+21.3}_{-20.3}$	$182.9^{+21.3}_{-20.3}$
	30–400	$16.3^{+1.8}_{-1.7}$	13.8±1.4	30.0±1.7
	2–400	$60.8^{+9.2}_{-8.2}$	$160.4^{+21.4}_{-20.5}$	$212.9^{+21.3}_{-20.3}$
Energy fluecne	2–10	$2.1^{+0.6}_{-0.5}$	$8.2^{+1.0}_{-1.4}$	9.6±1.3
[10^{-7} erg cm^{-2}]	2–30	7.8±0.9	17.8±1.4	25.4±1.7
	30–400	$16.1^{+1.8}_{-1.6}$	$12.1^{+2.3}_{-1.7}$	$28.6^{+2.7}_{-2.5}$
	2–400	23.9±2.1	$29.9^{+2.8}_{-2.4}$	$54.0^{+3.3}_{-3.1}$

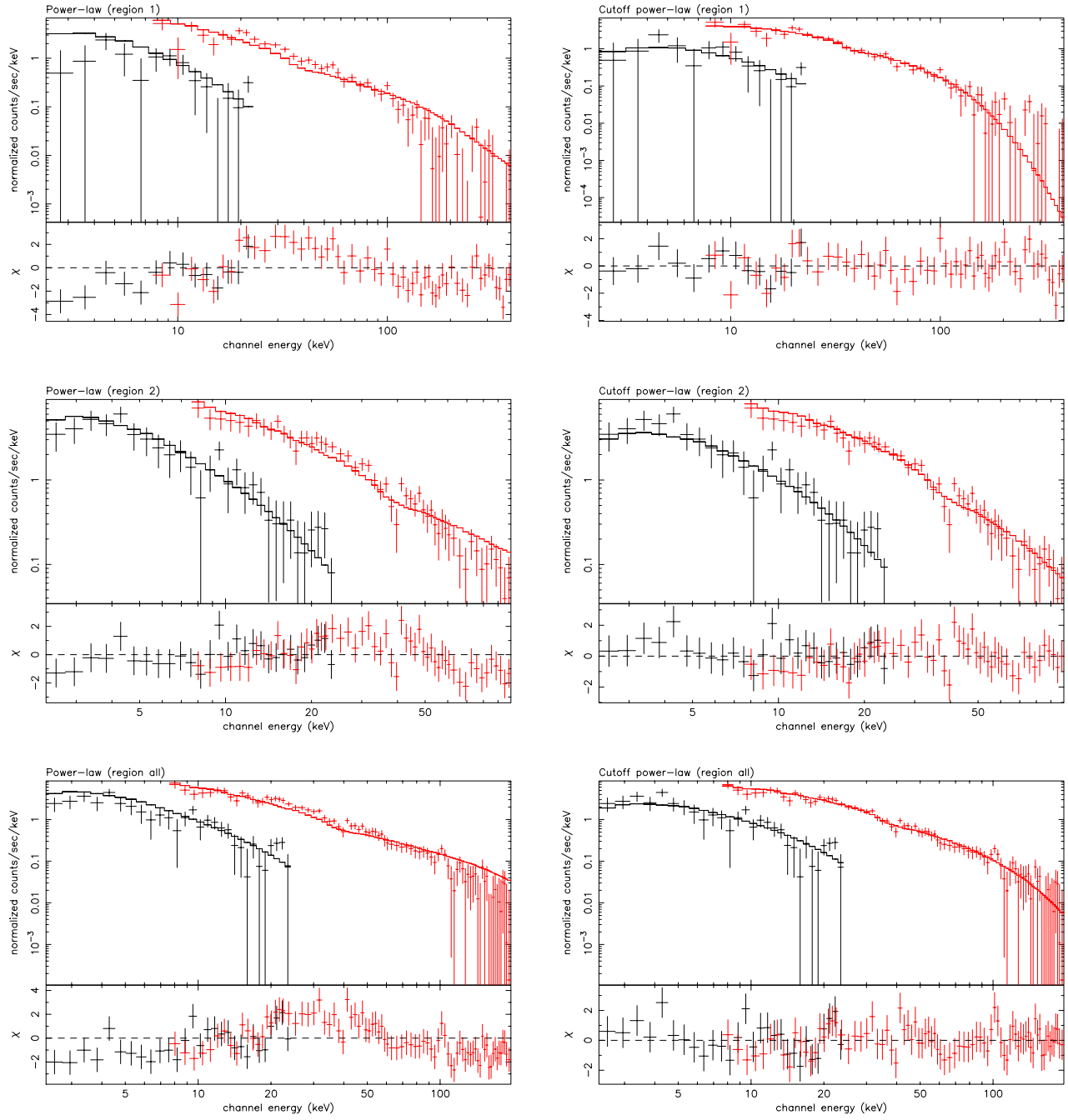

Figure 6.10: The WXM and FREGATE spectra of GRB010629B. The spectra of region 1, region 2, and all region are shown from top to bottom. The left and right plots are fitting with the power-law model and cutoff power-law model, respectively.

Table 6.10: The spectral parameters of GRB010629B in the power-law (PL), the cutoff power-law (Cutoff PL), and the Band function (Band).

Model	Parameters	Region 1	Region 2	All
PL	α	-1.63	-1.87 ± 0.05	-1.79 ± 0.03
	$K_{15}{}^{a}$	0.13	0.14 ± 0.01	0.14 ± 0.01
	χ^2_ν/DOF	2.481/69	1.112/82	1.924/111
Cutoff PL	α	$-0.66^{+0.26}_{-0.22}$	$-1.35^{+0.21}_{-0.18}$	$-1.13^{+0.14}_{-0.13}$
	E_{peak} [keV]	$60.47^{+7.81}_{-6.11}$	$31.29^{+5.22}_{-3.90}$	$45.57^{+4.61}_{-3.84}$
	K_{15}	0.18 ± 0.02	$0.22^{+0.04}_{-0.03}$	0.20 ± 0.02
	χ^2_ν/DOF	1.006/68	0.719/81	0.817/110
Band	α	$-0.52^{+0.61}_{-0.33}$	$-1.35^{+0.21}_{-0.18}$	$-1.13^{+0.20}_{-0.13}$
	β	$-2.80^{+0.52}_{-7.20}$	$-9.35^{+6.96}_{-0.65}$	$-4.84^{+2.31}_{-5.16}$
	E_{peak} [keV]	$55.47^{+11.14}_{-11.98}$	$31.39^{+5.12}_{-4.02}$	$45.56^{+4.59}_{-6.39}$
	K_{15}	$0.19^{+0.06}_{-0.03}$	$0.22^{+0.04}_{-0.03}$	0.20 ± 0.02
	χ^2_ν/DOF	1.008/67	0.730/80	0.825/109

[a] Normalization at 15 keV in the unit of photon cm^{-2} s^{-1} keV^{-1}

6.5 GRB011019

The faint GRB was observed on 19 October 2001 at 8:42:50 UT [72]. The burst position was R.A.= $00^{\rm h}42^{\rm m}50.23^{\rm s}$, Dec. $= -12°26'58''$ (J2000) . One sigma uncertainty radius for this location was $21'$ ($7.5'$ statistical error combined in quadrature with $19.8'$ systematic error). This relatively large systematic error is due to the uncertainty of the spacecraft aspect because of the irradiation of ACS camera by the bright earth at the burst time. This burst was an untriggered event.

The status of the afterglow search is summarized in table 6.11. No afterglow was found for this burst.

Table 6.11: The afterglow search for GRB011019

Time[a]	Telescope & Instruments	OT	Lim. Mag.[b]	GCN
12.12 hours	HETE GCN circular			#1109
13.3 hours	automated 600 mm telescope Kosmoten Observatory (Russia)	N	15.5 mag. (R)	Bondar et al. (#1130)
17.6 hours	ROTSE-III (0.45 m) (New Mexico, USA)	N	19.5 mag. (R)	Akerlof et al. (#1115)
20.9 hours	NOFS[c] 1.0 m telescope (Arizona, USA) V band	N	deeper than DSS	Henden et al. (#1110)
1.03 days	50 inch robotic telescope Mount Stromlo Observatory[d]	N	19.5 mag. (R)	Price et al. (#1112)
1.06 days	Subaru 8.2 m telescope SuprimeCam	N	22.5[e] mag. (R) 25.0[f] mag. (R)	Komiyama et al. (#1128)
1.85 days	48 inch NEAT automated telescope Mt. Palomar Observatory[g]	N	19.5 mag. (R)	Fox et al. (#1116)

[a] Time after the trigger

[b] Limiting magnitude

[c] U.S. Naval Observatory Flagstaff Station

[d] Australia [e] limiting magnitude of the first exposure

[f] limiting magnitude of the second exposure

[g] California, USA

6.5.1 Light curve

The energy resolved light curves of WXM and FREGATE are shown in figure 6.11. The burst signal is observed in only below 10 keV in WXM. There is no signal in the FREGATE 32-400

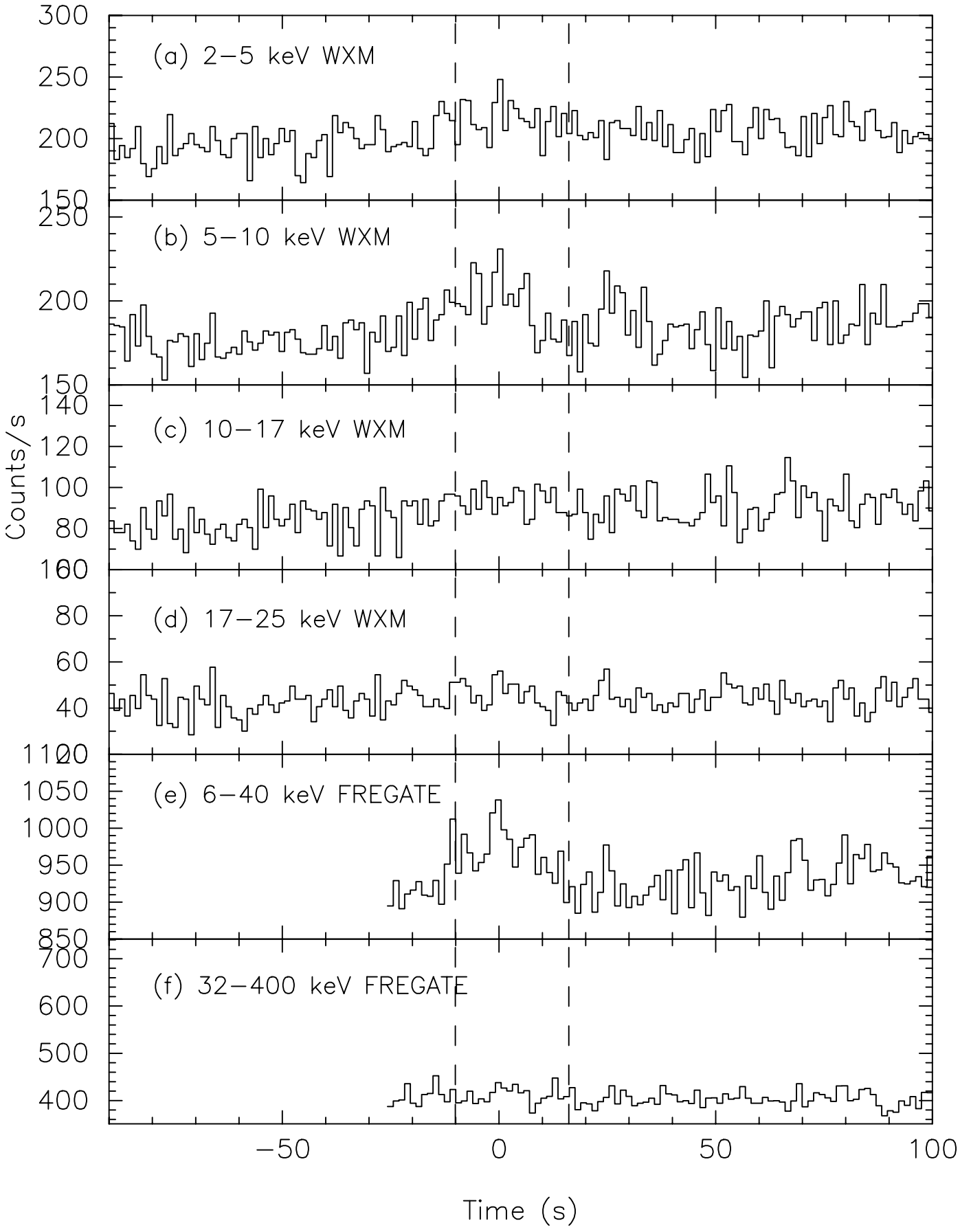

Figure 6.11: The energy resolved light curves of GRB011019 at 1.23 s time bin. The dotted lines correspond to the foreground spectral region.

Table 6.12: The fluences of GRB011019 in the cutoff power-law.

	Energy range [keV]	All
Duration [sec.]		26.2
Photon flux	2–10	0.9±0.2
[ph cm^{-2} s^{-1}]	2–30	1.1±0.2
	30–400	$5.7^{+5.0}_{-3.6}$ $\times 10^{-2}$
	2–400	1.2±0.26
Energy flux	2–10	0.6±0.1
[10^{-8} erg cm^{-2} s^{-1}]	2–30	1.2±0.2
	30–400	$0.4^{+0.6}_{-0.3}$
	2–400	$1.7^{+0.6}_{-0.5}$
Photon fluence	2–10	$21.9^{+5.2}_{-4.8}$
[ph cm^{-2}]	2–30	$27.5^{+5.7}_{-5.6}$
	30–400	$1.4^{+1.2}_{-0.9}$
	2–400	29.0±5.6
Energy fluecne	2–10	1.5±0.3
[10^{-7} erg cm^{-2}]	2–30	3.0±0.6
	30–400	$1.1^{+1.4}_{-0.7}$
	2–400	$4.1^{+1.5}_{-1.1}$

keV band which is the typical energy band for hard GRBs.

6.5.2 Spectrum

The time-averaged spectrum is investigated for this burst. Although a simple power-law model provides an acceptable fit, a χ^2 improves by $\Delta\chi^2 = 4.6$ with 1 additional parameter in the cutoff power-law model . The F test probability of this improvement is 2.3 $\times 10^{-2}$. From this statistical test, we decided the cutoff power-law model is the best representative model for this burst. The fluxes and fluences in the cutoff power-law model are summarized in table 6.12. The fluence ratio of 2–30 keV and 30–400 keV of 2.7 qualifies this event as an X-ray flash. The $E_{\rm peak}$ energy is $\sim$ 20 keV.

Table 6.13: The spectral parameters of GRB011019 in the power-law (PL) and the cutoff power-law model (Cutoff PL).

Model	Parameters	
PL	α	$-1.93^{+0.18}_{-0.21}$
	$K_{15}{}^{a}$	$1.23^{+0.28}_{-0.29}$
	χ^2_ν/DOF	0.909/68
Cutoff PL	α	-1.43 (fixed)
	E_{peak} [keV]	$18.71^{+18.33}_{-8.72}$
	K_{15}	$2.46^{0.82}_{-0.63}$
	χ^2_ν/DOF	0.854/68

[a] Normalization at 15 keV in the unit of 10^{-2} photon cm^{-2} s^{-1} keV^{-1}

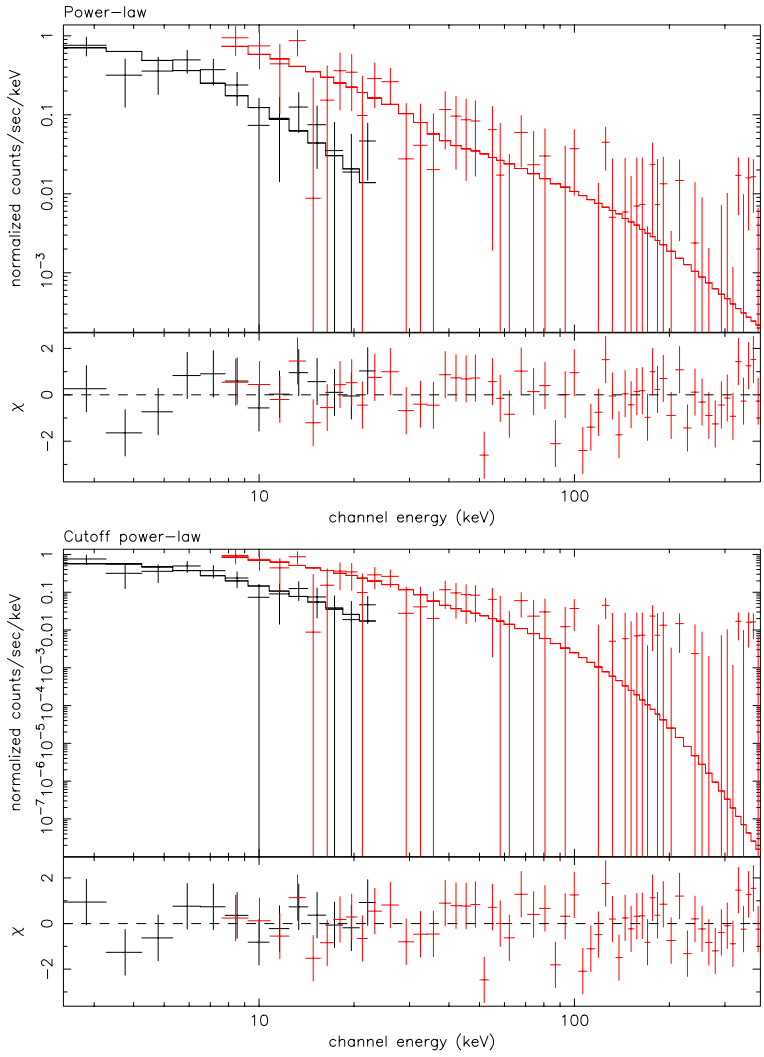

Figure 6.12: The WXM and FREGATE spectra of GRB011019. The spectral model is the power-law (top) and the cutoff power-law (bottom).

6.6 GRB011130

The WXM observed the GRB at 6:19:35 on 30 November 2001. This event occurred just before the orbital dusk, and the uncertainty of spacecraft aspect is larger than usual. The celestial coordinates of this burst were R.A. = $02^{\rm h}58^{\rm m}09.1^{\rm s}$, Dec. = $07°24'40''$ (J2000) with 90% error radius of $60'$ including the statistical and the systematic error [73]. The revised WXM localization is R.A. = $03^{\rm h}05^{\rm m}36.45^{\rm s}$, Dec. = $3°48'\ 37''$ (J2000) with 90% error radius of $8.0'$ [74].

The status of the afterglow search is summarized in table 6.14. Although there was the afterglow candidate which was found by VLA, this source might be an AGN. The Chandra observed the HETE error circle and found 43 X-ray sources. The Chandra observation of the 2nd epoch (about two months after the trigger) found that two X-ray sources faded to the background level. Further investigation of these X-ray sources has not been reported in GCN and their nature is still unknown.

6.6.1 Light curve

The light curve shows the double peak structure with no signal above 10 keV. The duration of the burst is $\sim$ 50 seconds in the 2–5 keV band.

6.6.2 Spectrum

The prompt emission of GRB011130 is investigated for the three time intervals; the first peak, the second peak and the whole burst. The fluxes and fluences at the several energy bands are shown in table 6.15. Since the fluence ratio of 2–30 keV to 30–400 keV is 5.8, this event is classified as an X-ray flash.

The spectral parameters are summarized in table 6.16. A simple power-law model gives an acceptable fit for all intervals. The photon index becomes steeper from region 1 to region 2, however, this trend is not statistically significant.

If there is a spectral break (peak energy at νF_ν spectrum) within or below the WXM energy band, the photon index of power-law model must be < -2. The data suggest that the photon index of the power-law model is < -2 for all regions. This is the solid evidence that WXM and FREGATE are observing the high-energy photon index β of the Band function. Following this argument, we tried to constrain the time-average $E_{\rm peak}$ energy using the *constrained* Band function (see appendix D). The posterior probability density distribution as a function of $E_{\rm peak}$

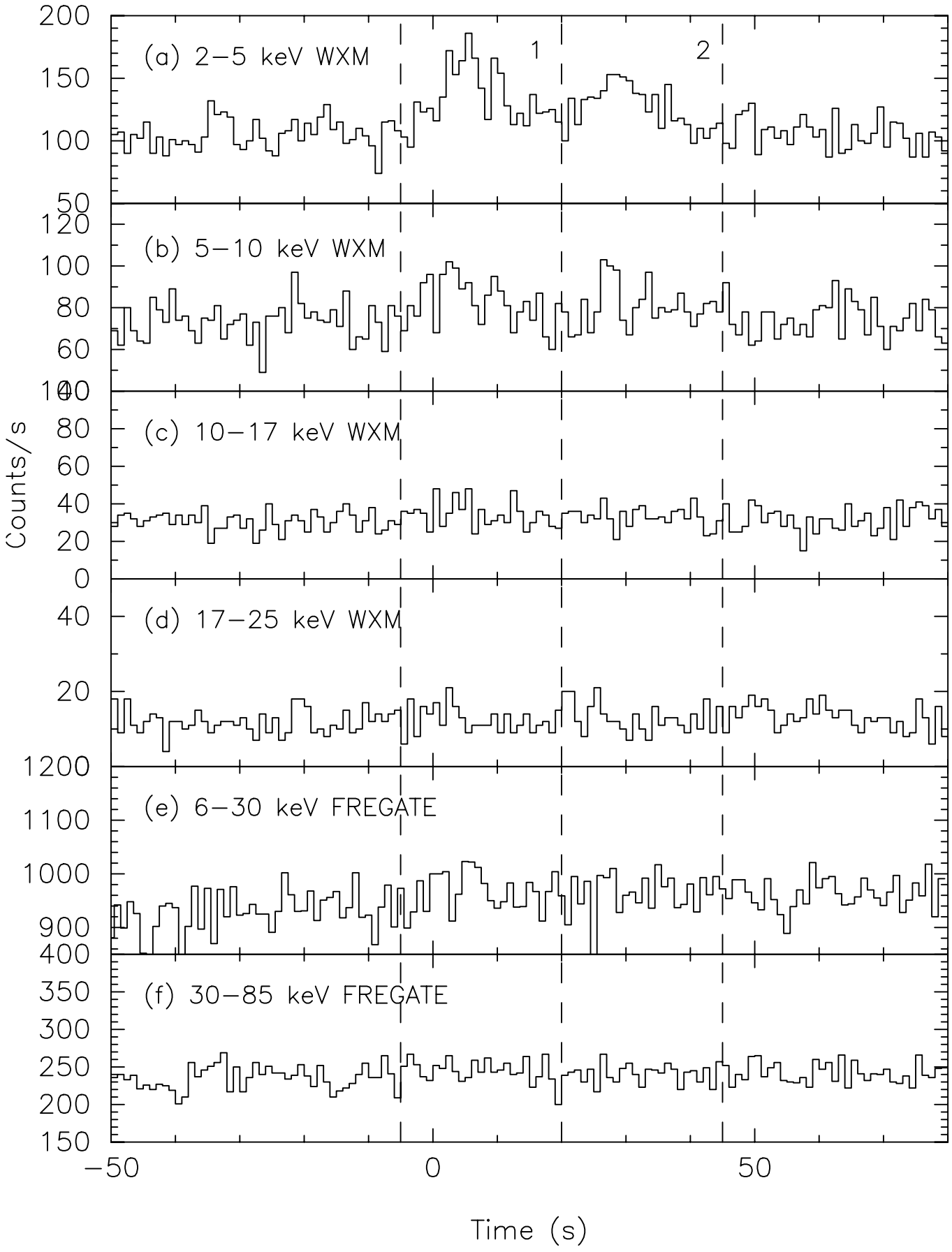

Figure 6.13: The energy resolved light curves of GRB011130 at 1 s time bin. The dotted lines correspond to the foreground regions of the spectra.

is shown in figure 6.15. The 68% confidence range is $0.6 < E_{\rm peak} < 3.5$ keV. The 95% and 99.7% upper limit is 4.1 keV and 4.9 keV respectively.

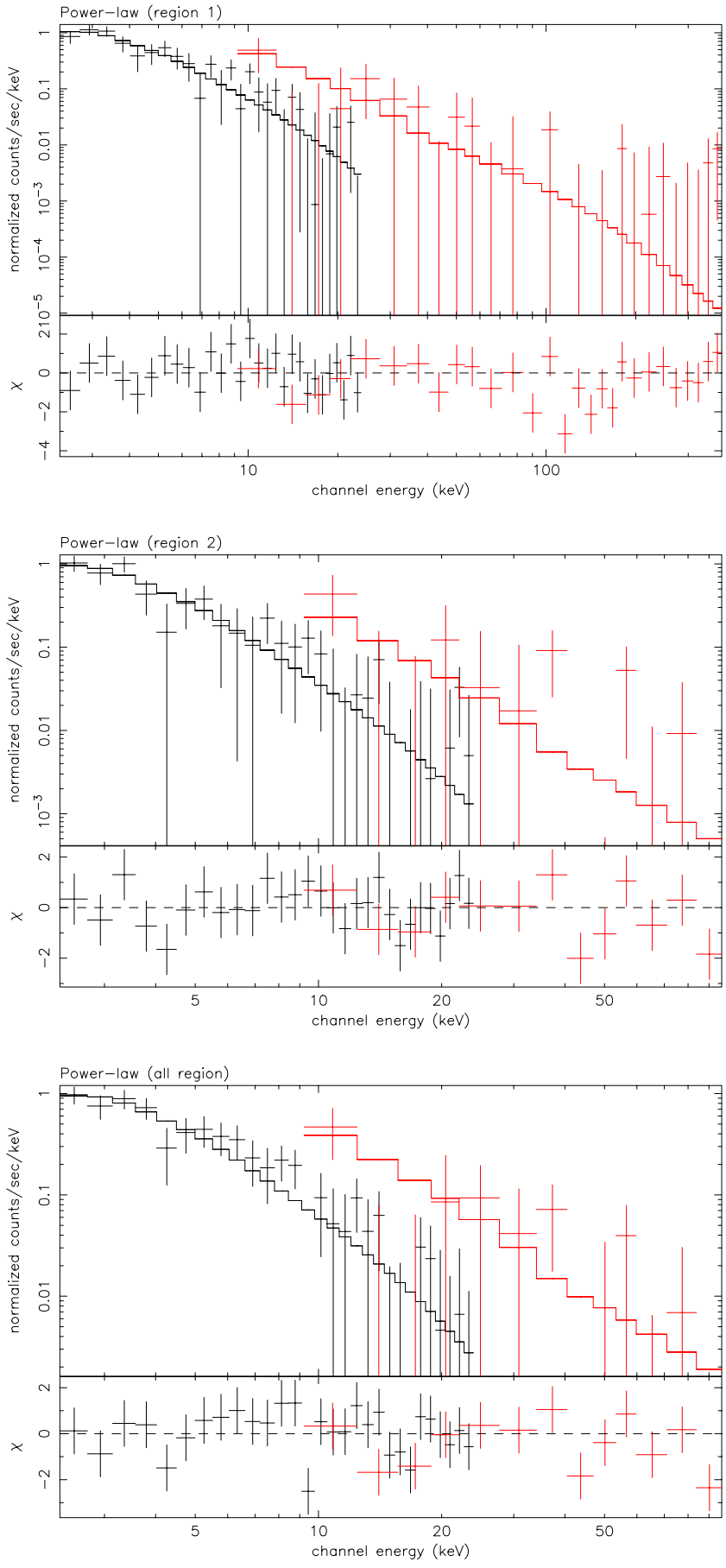

Figure 6.14: The WXM and FREGATE spectra of XRF011130. The spectra of region 1, region 2, and all region are shown from top to bottom. The spectral model is the power-law.

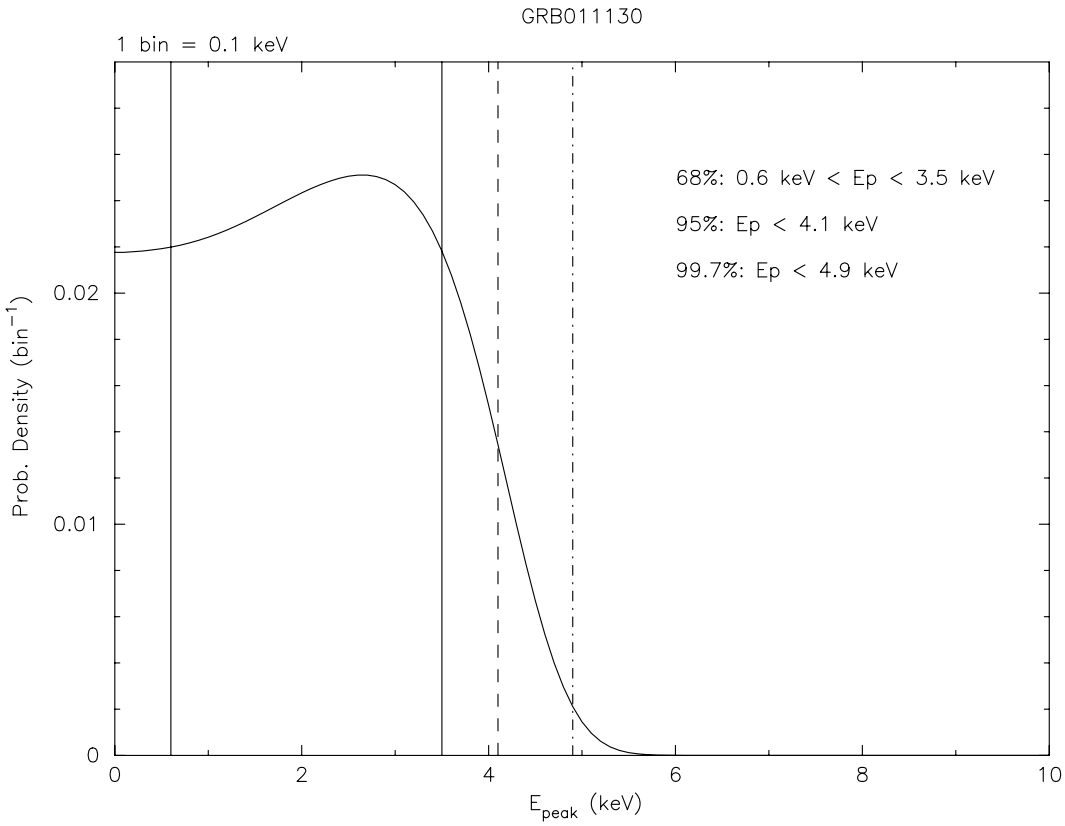

Figure 6.15: The posterior probability density distribution as a function of $E_{\rm peak}$ ($E_{\rm pivot} = 3.4$ keV). The highest probability is 2.7 keV. The solid line, the dashed line and the dashed-dotted line correspond to the 68%, 95% and 99.7% confidence region respectively.

Table 6.14: The afterglow search for GRB011130

Time[a]	Telescope & Instruments	OT	Lim. Mag.[b]	GCN
5.71 hours	HETE GCN circular			#1165
16.5 hours	1.23 telescope (R&I band) Calar Alto Observatory (Spain)	N	18.5–19 mag. (R&I)	Greiner et al. (#1171)
18.78 hours	HETE GCN circular (2nd)			#1169
23.45 hours	48 inch NEAT automated telescope Mt. Palomar Observatory[c]	N	18.5 mag. (R)	Fox et al. (#1170)
3.47 days	VLA[d] (4.86 GHz)	Y(N)[e]		Berger et al. (#1173)
1.13 days	Wide-Field Infrared Camera Palomar Hale Telescope	N	18.5 (K')	Fox et al. (#1174)
1.94 days	SDSS[f] 0.5 m Photometric Telescope at APO[g]	VLA src.	20.5±0.5 (i*)	Lee et al. (#1175)
2.04 days	1.3 m Telescope MDM Observatiory[h]	VLA src.	note[i]	Mirabal et al. (#1177)
4.97 days	Magellan 6.5 m Baade Telescope Las Campanas Observatory[j]	VLA src.	22.8 (R)	Jha et al. (#1179)
5.11 days	3.0 m telescope NASA IRTF[k] + NSFCAM	VLA src.	18.1 (K)	Rhods et al. (#1180)
5.73 days	HETE GCN circular (3rd)			#1178
5.89 days	Magellan 6.5 m Baade Telescope Las Campanas Observatory	VLA src.	23.0 (R)	Garnavitch et al. (#1181)
6.89 days	Magellan 6.5 m Baade Telescope Las Campanas Observatory	VLA src.	z=0.5[l]	Jha et al. (#1183)
9.76 days	Chandra ACIS-I (1st)	20 src.		Ricker et al. (#1185)
5.92 days 6.98 days 9.01 days	1.3 m telescope MDM Observatory	note[m]		Mirabal et al. (#1186)
Feb. 20	Chandra (2nd)	two src.		Butler et al. (#1227)
	Milagro GeV/TeV Telescope	note[n]		McEnery et al. (#1212)

[a] Time after the trigger

[b] Limiting magnitude

[c] California, USA

[d] Very Large Array (New Mexico, USA)

[e] They reported the unknown source at R.A. = $03^h05^m24.71^s$, Dec. = $03°46'13.1''$. However, this source might be an AGN with a flat spectrum (#1207). Here after this source called "VLA src.".

[f] Sloan Digital Sky Survey

[g] Apache Point Observatory (New Mexico, USA)

[h] Arizona, USA

[i] OT reported on #1175 has the offset of $4.5''$ from the VLA source.

[j] Carro Las Campanas, Chile

[k] NASA Infrared Telescope Facility (Hawai, USA)

[l] Strong calcium break (600 nm). No significant [OII].

[m] No optical counter part for CXOU J0306458+034702.

[n] The upper limit: J(E > 2 TeV) < 6×10^{-7} erg cm^{-2}, J(100–150 GeV) < 5×10^{-4} erg cm^{-2}

Table 6.15: The fluxes and fluences of GRB011130. The spectral model is the power-law model.

	energy range [keV]	region 1	region 2	all
Duration [sec.]		25.0	25.0	50.0
Photon flux	2–10	1.8±0.3	1.5±0.3	1.6±0.3
[ph cm^{-2} s^{-1}]	2–30	1.9±0.3	1.6±0.3	1.7±0.3
	30–400	$2.1^{+2.1}_{-1.2}$ $\times10^{-2}$	$6.4^{+14.4}_{-5.3}$ $\times10^{-3}$	$2.0^{+1.9}_{-1.1}$ $\times10^{-2}$
	2–400	1.9±0.3	1.6±0.3	1.7±0.26
Energy flux	2–10	1.0±0.2	0.8±0.1	0.9±0.1
[10^{-8} erg cm^{-2} s^{-1}]	2–30	1.3±0.2	0.9±0.2	1.2±0.2
	30–400	$2.1^{+2.6}_{-1.4}$ $\times10^{-1}$	$5.7^{+15.9}_{-4.9}$ $\times10^{-2}$	$0.2^{+0.2}_{-0.1}$
	2–400	$1.5^{+0.4}_{-0.3}$	$1.0^{+0.3}_{-0.2}$	$1.4^{+0.4}_{-0.3}$
Photon fluence	2–10	44.5±7.2	$37.6^{+7.6}_{-7.4}$	80.9±12.8
[ph cm^{-2}]	2–30	47.3±7.2	$38.9^{+7.5}_{-7.4}$	86.0±12.8
	30–400	$5.3^{+5.2}_{-3.1}$ $\times10^{-1}$	$1.6^{+3.6}_{-1.3}$ $\times10^{-1}$	$1.0^{+0.9}_{-0.6}$
	2–400	47.8±7.2	$39.0^{+7.5}_{-7.4}$	86.9±12.8
Energy fluecne	2–10	2.5±0.4	2.0±0.4	4.6±0.6
[10^{-7} erg cm^{-2}]	2–30	3.2±0.6	2.3±0.5	5.8±1.0
	30–400	$5.3^{+6.4}_{-3.4}$ $\times10^{-1}$	$1.4^{+4.0}_{-1.2}$ $\times10^{-1}$	$1.0^{+1.2}_{-0.6}$
	2–400	$3.7^{+1.1}_{-0.8}$	$2.5^{+0.8}_{-0.6}$	$6.8^{+1.9}_{-1.5}$

Table 6.16: The spectral parameters of GRB011130 in the power-law model (PL).

Model	Parameters	Region 1	Region 2	All
PL	α	$-2.66^{+0.27}_{-0.34}$	$-3.01^{+0.44}_{-0.68}$	$-2.65^{+0.26}_{-0.33}$
	K_{15}[a]	$7.48^{+3.25}_{-2.93}$ $\times$ 10^{-3}	$3.64^{+3.11}_{-2.36}$ $\times$ 10^{-3}	$6.86^{+2.92}_{-2.64}$ $\times$ 10^{-3}
	χ^2_ν/DOF	1.000/55	0.779/40	1.016/40

[a] Normalization at 15 keV in the unit of photon cm^{-2} s^{-1} keV^{-1}

6.7 GRB011212

The WXM and FREGATE instruments observed the burst on 12 December 2001 at 04:04:02 UT [75]. The position of the burst was reported to be R.A. = $05^{\rm h}00^{\rm m}05^{\rm s}$, Dec. = $32°07'39''$ (J2000) with a 90% total error radius of $11'$. This event is also detected by *RXTE* ASM. The error box corners combining the *RXTE* ASM and *HETE* WXM is (R.A., Dec.) = ($05^{\rm h}00^{\rm m}00^{\rm s}$, $31°55'48''$), ($05^{\rm h}00^{\rm m}05^{\rm s}$, $32°08'24''$), ($04^{\rm h}59^{\rm m}43^{\rm s}$, $32°22'48''$), and ($04^{\rm h}59^{\rm m}22^{\rm s}$, $32°13'12''$) (J2000). This event was an untriggerd event.

The status of the afterglow search of GRB011212 is summarized on table 6.17. The Magellan 6.5 m telescope and the 2.2 m telescope on Maunakea observed the four fading sources, however, the further observations have not been reported.

Table 6.17: The afterglow search for GRB011212

Time[a]	Telescope & Instruments	OT	Lim. Mag.[b]	GCN
8.3 hours	HETE GCN Position Notice			
9.1 hours 1.4 days	1.5 m Telescope (R) Gunma Astronomical Observatory	N	20.5 mag. (R)	Kinugasa et al. (#1210)
14.7 hours	RXTE ASM Position Notice			
0.7 days	0.25 m F/4.2 Telescope	N	18.5 mag. (R)	Trondal et al. (#1201)
0.7 days	2 m Telescope Peak Terskal Observatory (Russia)	N	21.5 mag. (R)	Sergeev et al. (#1206)
1.0 days	Mt. Ekar 1.8 m Telescope Asiago Observatory[c]	N	22.7 mag. (R)	Saracco et al. (#1205)
1.2 days	1.3 m Telescope (Ic) USNO Flagstaff Station	N	20.0-20.1 mag. (R) [d]	Vrab et al. (#1216)
2.0 days 3.0 days 4.2 days 5.2 days	Magellan 6.5 m Baade Telescope Las Campanas Observatory[j] 2.2 m on Maunakea (VR) U. of Hawai	Y	4 sources[e]	Dullighan et al. (#1324))

[a] Time after the trigger

[b] Limiting magnitude

[c] Cima Ekar-Asiago, Italy

[d] extinction-corrected magnitude

[e] 4 fading sources

	RA	Dec	Epoch 1 m(R)	Epoch 2 m(R)	Epoch 3 m(VR)
1	4:59:58.1	+32:02:57	23.14 +/- 0.12	23.89 +/- 0.22	24.08 +/-0.24
2	4:59:59.4	+32:03:43	23.80 +/- 0.18	24.65 +/- 0.39	> 24.5
3	4:59:59.0	+32:09:04	23.75 +/- 0.18	24.80 +/- 0.48	> 24.5
4	4:59:39.5	+32:08:34	23.38 +/- 0.12	24.41 +/- 0.38	> 24.5

6.7.1 Light curve

The duration of this burst is > 60 seconds in 2–5 keV band. Some structures in the light curve might be visible in the WXM 2–5 keV energy band. The burst signal is not seen above 17 keV.

6.7.2 Spectrum

The fluence ratio of 2–30 keV to 30–400 keV is 1.2 qualifying this burst as an X-ray flash. The prompt emission is well fitted in a simple power-law model with the photon index of ~ -2. However, it is not possible to reject that the photon index is flatter than -2 in a high significance (i.e. the peak energy $E_{\rm peak}$ cannot determined reliably). Thus, it is not possible to fit the spectrum with the *constrained* Band function to calculate the $E_{\rm peak}$ energy.

Table 6.18: The fluxes and fluences of GRB011212. The spectral model is the power-law model.

	energy range [keV]	
Duration [sec.]		57.6
Photon flux	2–10	7.1 ± 1.2
[10^{-1} ph cm^{-2}]	2–30	8.2 ± 1.2
	30–400	$0.4^{+0.3}_{-0.2}$
	2–400	8.7 ± 1.2
Energy flux	2–10	4.5 ± 0.7
[10^{-9} erg cm^{-2}]	2–30	7.3 ± 1.1
	30–400	$5.8^{+4.4}_{-2.9}$
	2–400	$13.2^{+5.0}_{-3.7}$
Photon fluence	2–10	41.1 ± 6.8
[ph cm^{-2}]	2–30	47.3 ± 7.0
	30–400	$2.6^{+1.5}_{-1.1}$
	2–400	49.9 ± 7.0
Energy fluecne	2–10	2.6 ± 0.4
[10^{-7} erg cm^{-2}]	2–30	4.2 ± 0.6
	30–400	$3.4^{+2.5}_{-1.7}$
	2–400	$7.6^{+2.9}_{-2.2}$

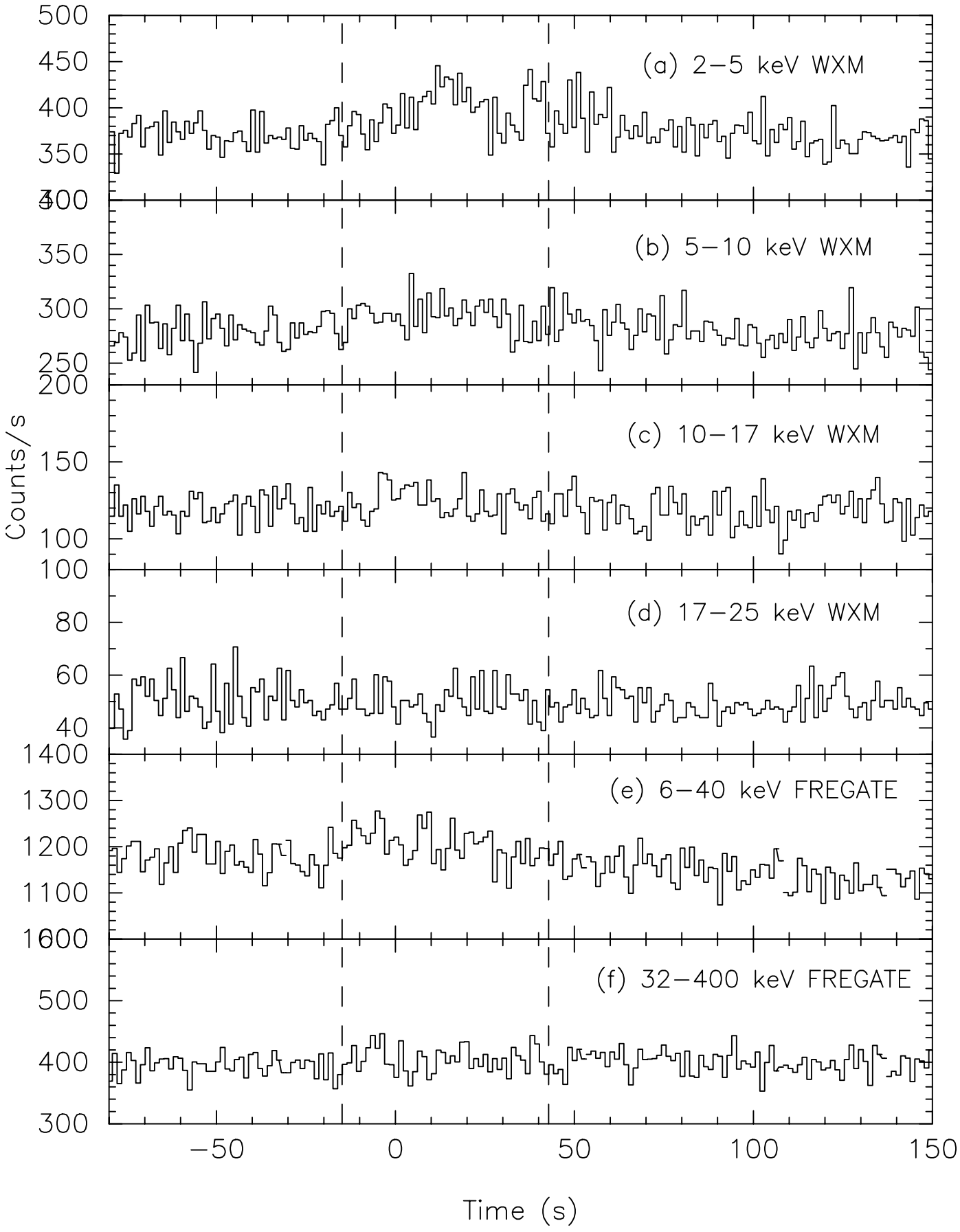

Figure 6.16: The energy resolved light curves of GRB011212 at 1.23 s time bin. The dotted lines represent the foreground region of the spectrum.

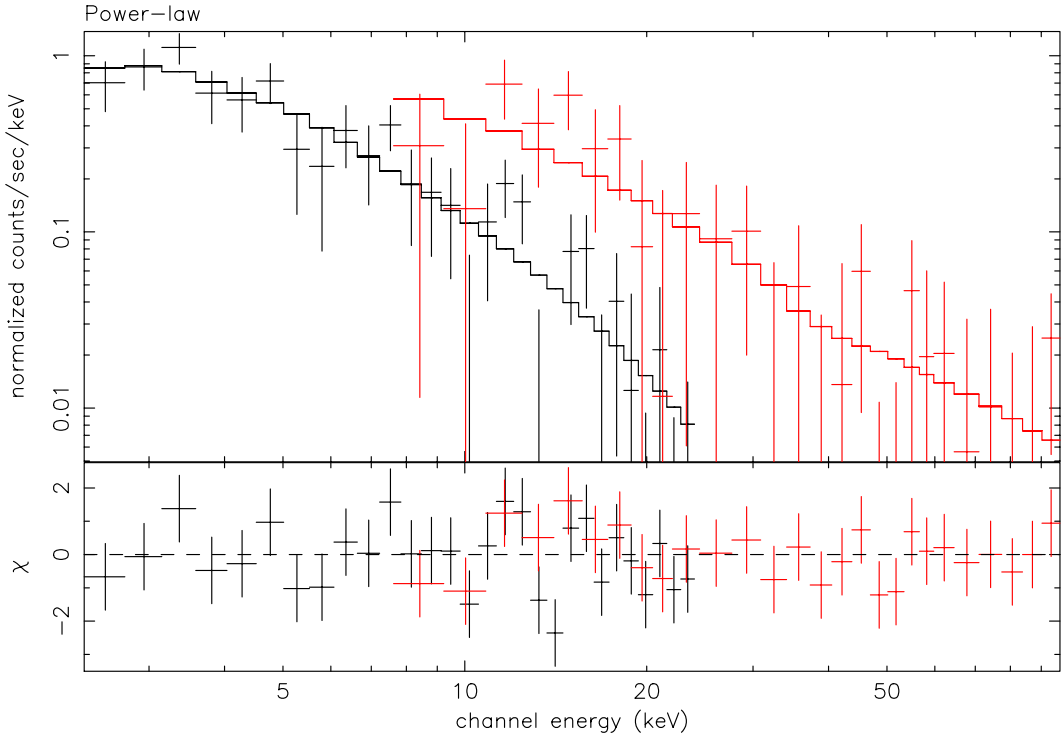

Figure 6.17: The WXM and FREGATE spectrum of XRF011212. The spectral model is the power-law.

Table 6.19: The spectral parameters of GRB011212 in the power-law model (PL).

Model	Parameters	
PL	α	$-2.07^{+0.19}_{-0.22}$
	$K_{15}{}^{a}$	$7.18^{+1.74}_{-1.78} \times 10^{-3}$
	χ^2_ν/DOF	0.795/54

[a] Normalization at 15 keV in the unit of photon cm^{-2} s^{-1} keV^{-1}

6.8 GRB020317

The GRB was observed by WXM and FREGATE on 17 March 2002 at 18:15:31.4 UT [76]. According to the ground analysis, the position of the source is R.A. = $10^{\rm h}23^{\rm m}21^{\rm s}$, Dec. = $12°44'38''$ (J2000) with a 90% total error radius of $18'$.

The afterglow search for GRB020317 is summarized in table 6.20. The first two reports (GCN #1277 and #1278) about the suspicious object could be just minor planets which are not in the DSS-2 image (GCN #1282). The nature of four suspicious sources reported by the KISO observatory are still unknown.

Table 6.20: The afterglow search for GRB020317

Time[a]	Telescope & Instruments	OT	Lim. Mag.[b]	GCN
52 minutes	HETE GCN Position Notice			
57.8 minutes	BART robotic telescope	Y(?)[c]	15.5 mag. (R)	Jelinek et al. (#1278)
2 hours	0.38 m Cassegrain telescope	Y(?)[d]	18.2±0.3	Pavlenko et al. (#1277)
0.77 days 0.96 days	1.05 m telescope (R) KISO observatory	4 src.[e]	20.8 mag. (R) 18.1 mag. (R)	Tomita et al. (#1282)
1.15 days	1.52 m telescope (R)	N	18.7/17.0 mag. (R)	Guarnierie al. (#1287)
1.93 days	1.2 m telescope (IR) Mt. Abu IR Observatory[f]	N	not reported	Baliyan et al. (#1297)

[a] Time after the trigger

[b] Limiting magnitude

[c] Position is RA.(J2000) = $10^h23^m25^s$, Dec. (J2000) = $12°51'36''$. Could be a minor planet reported by GCN #1282.

[d] Position is RA.(J2000) = $10^h24^m27.99^s$, Dec. (J2000) = $12°36'5.6''$. Could be a minor planet reported by GCN #1282.

[e] 6 suspicious sources are reported including the two minor planets.

	RA	Dec	Mag. (R)
1	10:24:25	+12:51:55	18.0 (minor planet)
2	10:24:09	+12:48:33	17.3 (minor planet)
3	10:23:10	+12:33:17	19.6
4	10:22:40	+12:32:02	18.5
5	10:22:39	+12:44:02	19.0
6	10:22:20	+12:36:55	19.1

f MIRO, operated by the Physical Reaserch Laboratory, Ahmedabad, India

6.8.1 Light curve

The energy resolved light curves are shown in figure 6.18. The duration of the burst is around $\sim$ 10 seconds.

6.8.2 Spectrum

The fluence ratio of 2–30 keV to 30–400 keV in the cutoff power-law model is 1.8. This burst is classified as an X-ray flash. The cutoff power-law model with the $E_{\rm peak}$ energy $\sim$ 30 keV is the acceptable model for the time-average spectrum.

The spectral evolution of the burst is investigated by the hardness ratio between 10–25 keV and 2–10 keV. As seen in the figure 6.20, there is a global trend of the softening during the burst. And also it is possible to see the hard-to-soft spectral evolution for the individual pulses.

Table 6.21: The fluxes and fluences of GRB020317. The spectral model is the cutoff power-law model.

	energy range [keV]	
Duration [sec.]		7.3
Photon flux	2–10	1.1±0.3
[ph cm^{-2} s^{-1}]	2–30	1.8±0.3
	30–400	0.2±0.1
	2–400	2.0±0.4
Energy flux	2–10	0.9±0.2
[10^{-8} erg cm^{-2} s^{-1}]	2–30	2.8±0.4
	30–400	$1.6^{+1.2}_{-0.9}$
	2–400	$4.4^{+1.2}_{-1.0}$
Photon fluence	2–10	8.2±2.2
[ph cm^{-2}]	2–30	13.2±2.4
	30–400	1.6±0.8
	2–400	14.8±2.6
Energy fluecne	2–10	0.7±0.2
[10^{-7} erg cm^{-2}]	2–30	2.1±0.3
	30–400	$1.2^{+0.8}_{-0.7}$
	2–400	$3.2^{+0.9}_{-0.8}$

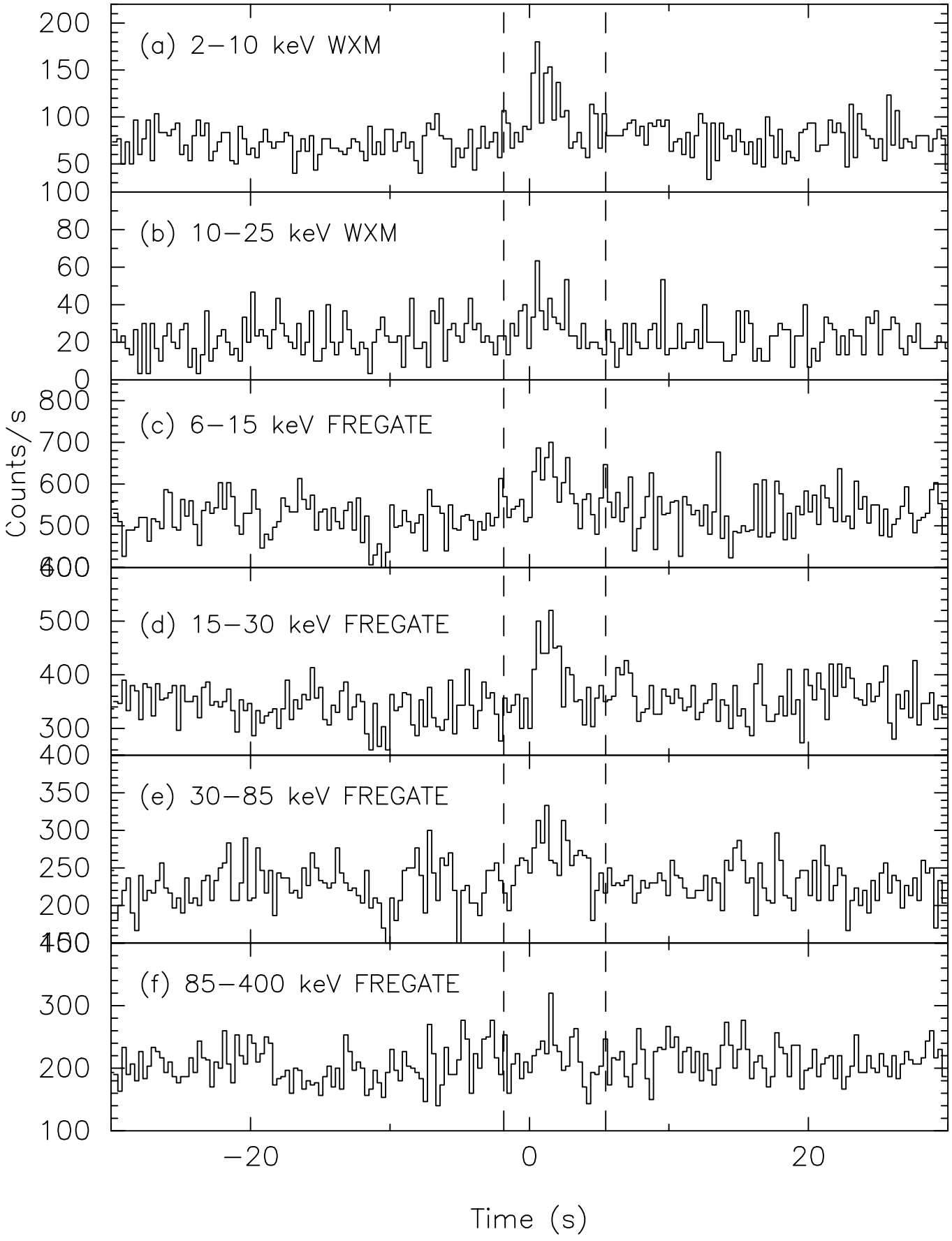

Figure 6.18: The energy resolved light curves of GRB020317 at 0.3 s time bin. The dotted lines represent the foreground region of the spectrum.

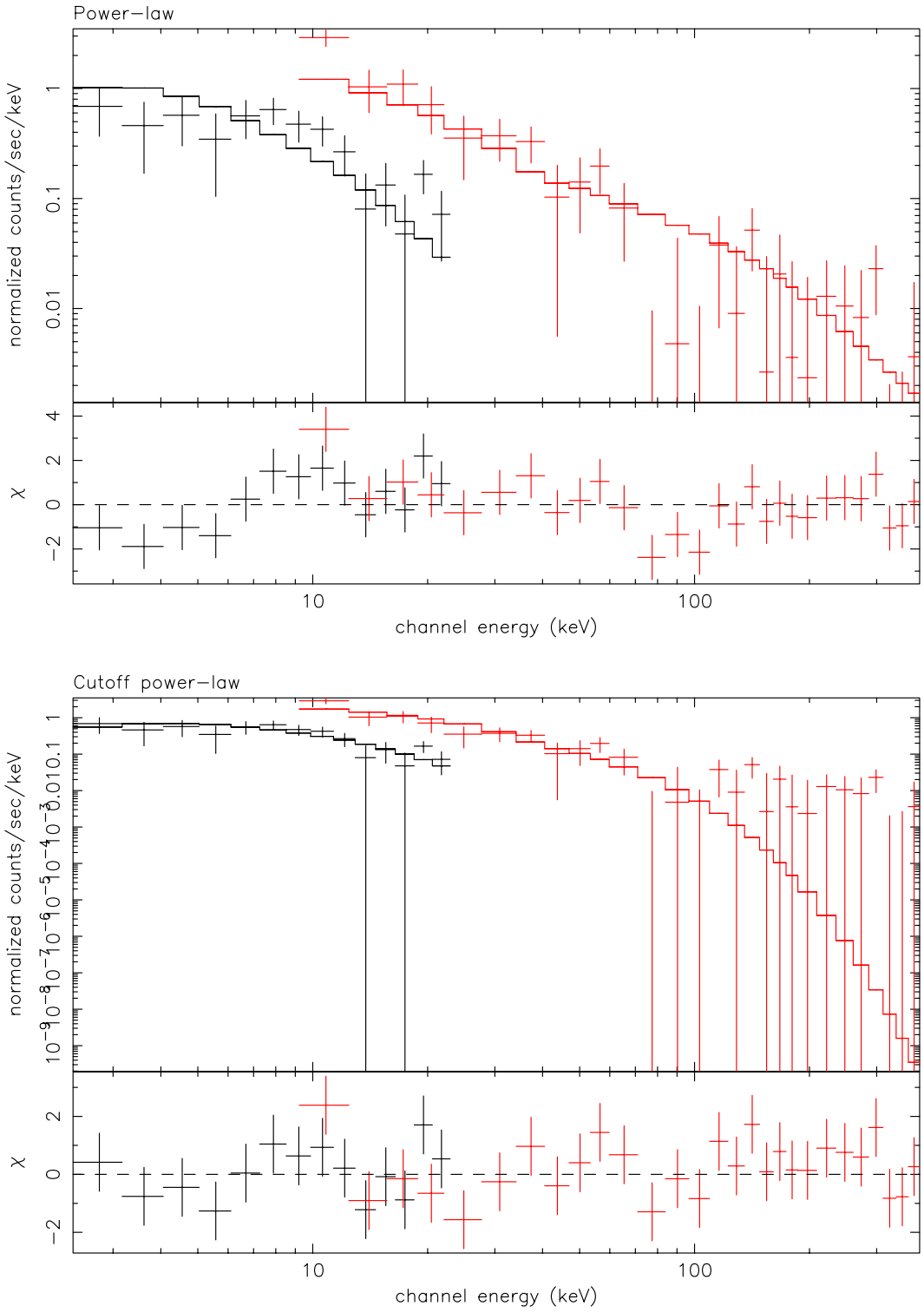

Figure 6.19: The WXM and FREGATE spectra of GRB020317. The spectra of the whole burst region with a spectral model of the power-law (top) and the cutoff power-law (bottom) are shown.

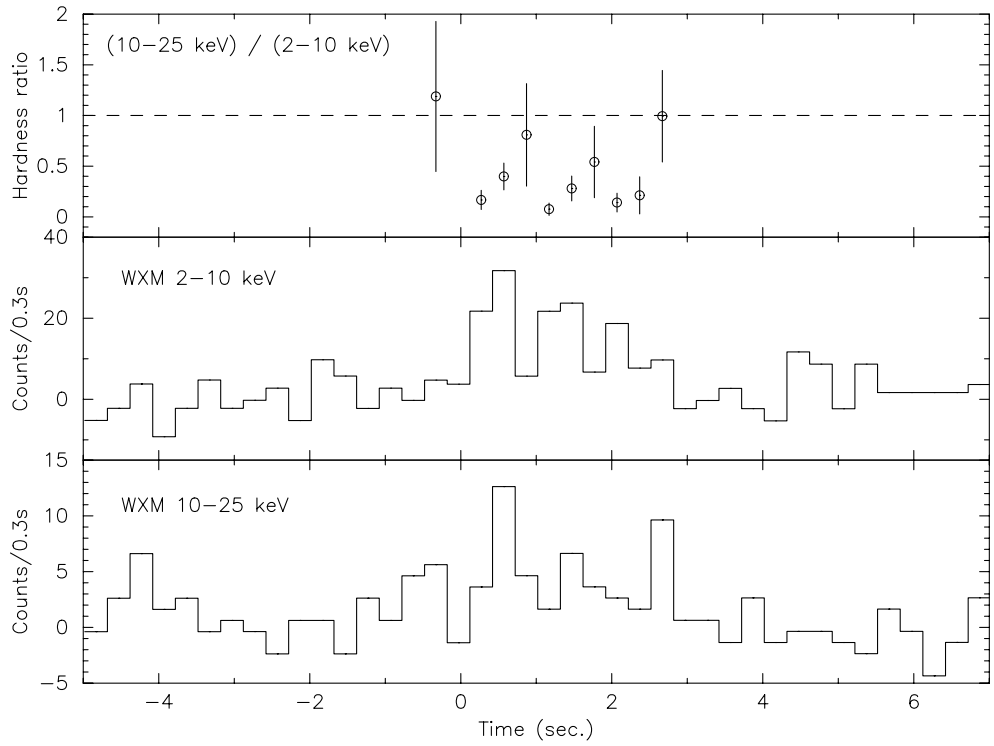

Figure 6.20: The hardness ratio between WXM 10–25 keV and 2–10 keV is in the top panel. The second and the third panels are the WXM light curves of 2–10 keV and 10-25 keV respectively.

Table 6.22: The spectral parameters of GRB020317 in the power-law model (PL) and the cutoff power-law model (Cutoff PL).

Model	Parameters	all
PL	α	-1.60 ± 0.11
	K_{15}[a]	$(2.86\pm0.44) \times 10^{-2}$
	χ^2_ν/DOF	1.420/40
Cutoff PL	α	$-0.56^{+0.56}_{-0.45}$
	E_{peak} [keV]	$27.3^{+12.0}_{-7.7}$
	K_{15}	$10.22^{+12.6}_{-4.26} \times 10^{-2}$
	χ^2_ν/DOF	0.944/39

[a] Normalization at 15 keV in the unit of photon cm^{-2} s^{-1} keV^{-1}

6.9 GRB020903

This event was detected by WXM and SXC at 10:05:37.96 UT on 2002 September 3 [77]. Although the WXM flight location was correct, it was not sent to the GCN, because *HETE* was pointed to the Galactic Bulge region at this time and the automatic transmission of the flight location was turned off at that time. The WXM location, which was sent to GCN 3.8 hours after the trigger, based on the ground analysis can be express as a 90% confidence circle that is 16.6° in radius and is centered at (R.A., Dec.) = ($22^h49^m25^s$, $-20°53'59''$) (J2000). The one-dimensional localization was possible using the SXC data. The combined the SXC and the WXM localization, which was sent to GCN 6.9 hours after the trigger, can be described as a 90% confidence quadrilateral that is $4'$ in width and $\sim 31'$ in length. It is centered at R.A. = $22^h49^m01^s$, Dec. = $-20°55'47''$ (J2000), and its four corners lie at (R.A., Dec.) = ($22^h48^m48.00^s$, $-20°39'36.0''$), ($22^h48^m33.60^s$, $-20°42'36.0''$), ($22^h49^m10.80^s$, $-21°10'12.0''$), and ($22^h49^m30.00^s$, $-21°10'48.0''$) (J2000).

Detection of the optical and radio afterglow, and the host galaxy have been reported by several authors (table 6.23). Soderberg et al. [95] discovered an optical transient within the HETE-2 SXC + WXM localization region at R.A. = $22^h48^m42.34^s$, Dec = $-20°46'09.3''$ (J2000), using the Palomar 200-inch telescope. They report that the optical transient brightened by $\sim 0.3 - 0.4$ magnitudes between about 7 and 24 days after the XRF, and suggest that the re-brightening might be due to an associated supernova. However, the optical transient apparently faded by over a magnitude only three days later. Spectroscopic observations of the optical transient, using the Magellan 6.5 m Baade and Clay telescopes, detected narrow emission lines from an underlying galaxy at a redshift $z = 0.25 \pm 0.01$, suggesting that the host galaxy of the optical transient is a star-forming galaxy. A fading bright radio source at the position of optical transient was detected using the Very Large Array. Hubble Space telescope observations of the GRB 020903 field reveal the optical transient and show that its host galaxy is an irregular galaxy, possibly with four interacting components. These detections likely represent the first discoveries of the optical and radio afterglows, together with the host galaxy, of an XRF.

6.9.1 Light curve

The energy resolved light curves are shown in figure 6.22. There is no signal above 10 keV. The double peak structure is visible in the light curve.

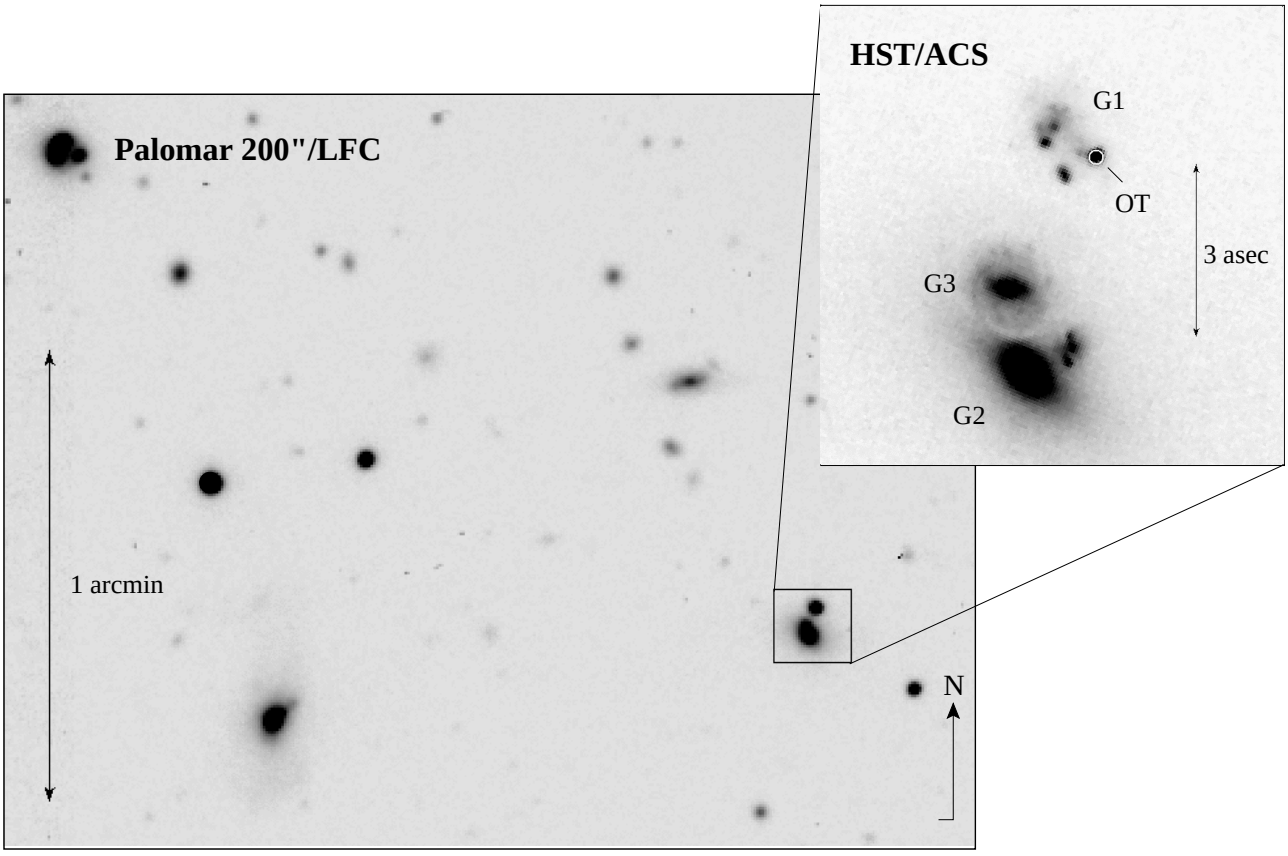

Figure 6.21: The Palomar and HST images of the transient (label OT) discovered within the error-box of GRB020903. The HST image reveals a complicated galaxy morphology for G1, suggesting a system of at least four interacting galaxies [95].

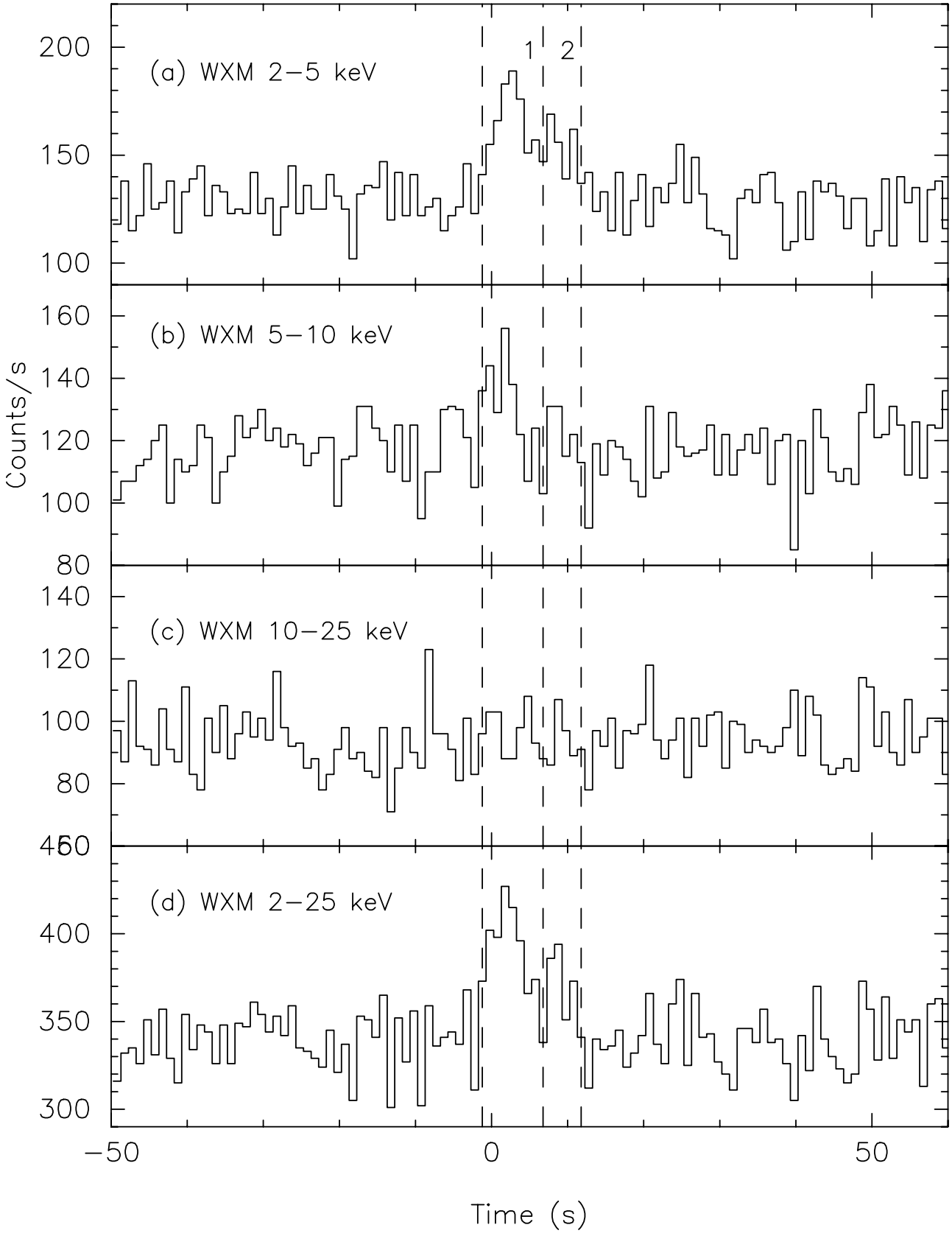

Figure 6.22: The energy resolved light curves of GRB020903 in 1.0 second resolution. The two spectral regions are shown in the dotted lines.

6.9.2 Spectrum

The X-ray to the γ-ray fluence ratio of 5.6 qualifies this burst as an X-ray flash. Although the power-law model is the acceptable model for the prompt emission, the photon index is < -2 in a high significance (99% confidence level). If we assume that this XRF has the same spectral shape as ordinary GRBs, WXM and FREGATE observed the high energy portion of the Band function (photon index β). We applied the *constrained* Band function to calculate the upper limit of the $E_{\rm peak}$ energy. The posterior probability density distribution is shown in the figure 6.24. We find a best-fit value $E_{\rm peak} = 2.7$ keV, and the confidence limits of 1.1 keV $< E_{\rm peak}$ < 3.6 keV with 68% probability, and that $E_{\rm peak} < 4.1$ keV with 95% and 5.0 keV with 99.7% probabilities.

There is evidence of spectral softening between the first and second time intervals. To investigate the spectral evolution, we perform the spectral analysis for the first and the second peaks which are seen in the WXM 2–5 keV band (see figure 6.22). We treat each individual WXM wires separately in order to extract the strongest possible constraints on the spectral parameters. A power-law fit to the sum of the first time interval gives $\alpha_1 = -2.4^{+0.5}_{-0.6}$ and $\chi^2_{\rm min,1} = 75.1$, while a power-law fit to the second time interval gives $\alpha_2 = -4.2^{+1.1}_{-3.7}$ and $\chi^2_{\rm min,2} = 71.1$. In contrast, a power-law fit to the first and second time intervals, gives $\alpha = -2.86^{+0.44}_{-0.82}$ and $\chi^2_{\rm min} = 152.2$. The first (more complicated) model includes the second model as a special case. Comparing $\chi^2_{\rm min}$ for the two models, we find that $\Delta\chi^2 = 6.0$ for one additional parameter. Thus, there is evidence of spectral softening at the 98.6% confidence level.

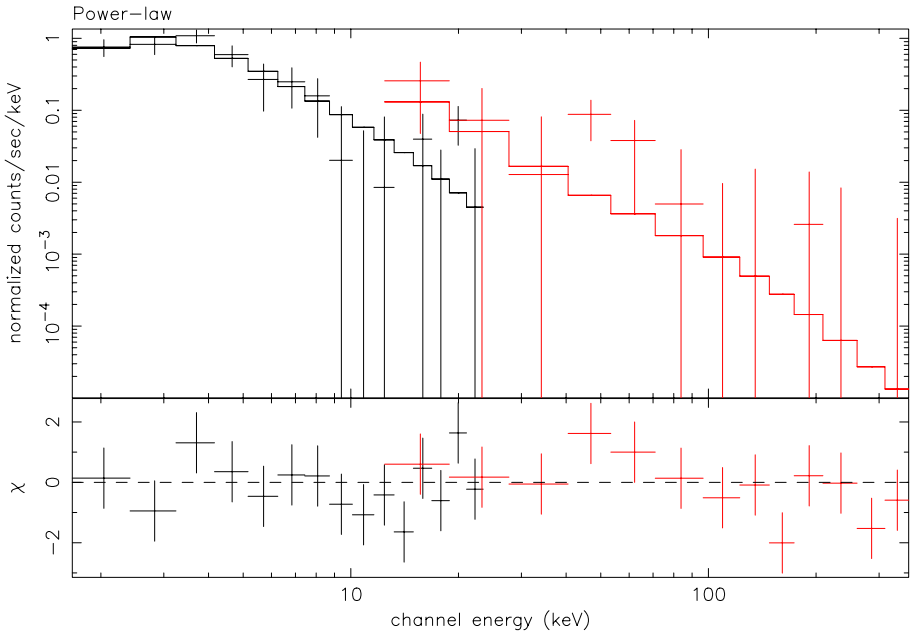

Figure 6.23: The time-average spectrum of GRB020903.

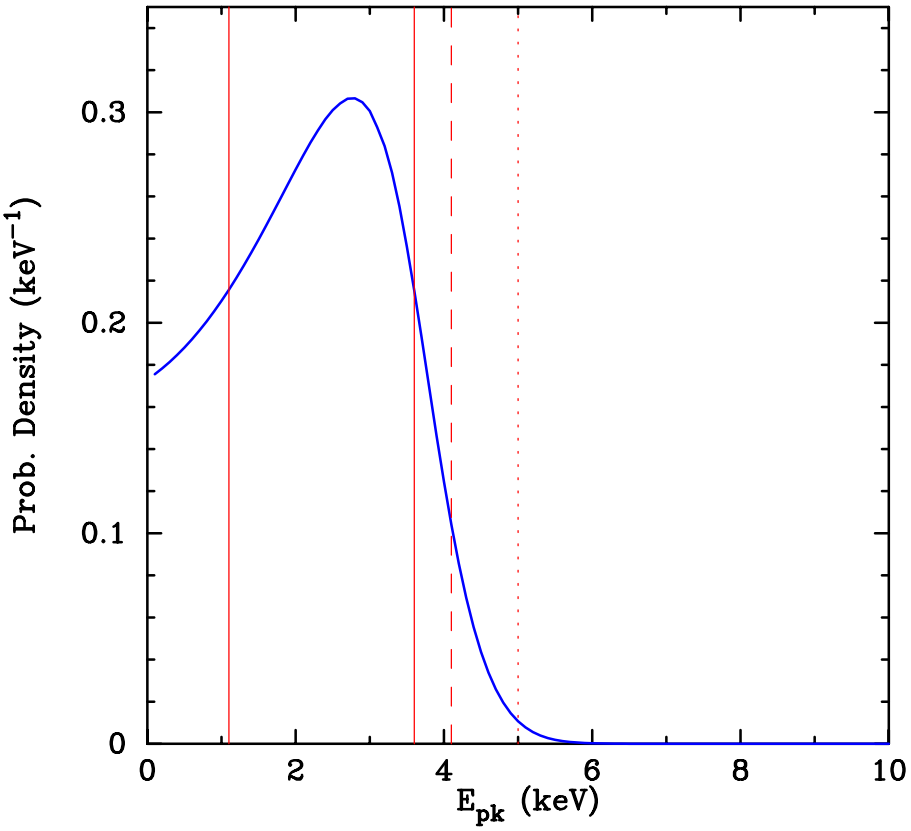

Figure 6.24: The posterior probability density distribution as a function of $E_{\rm peak}$. The solid lines define the 68% probability interval for $E_{\rm peak}$, while the dashed and dotted lines show the 95% and 99.7% probability upper limits on $E_{\rm peak}$.

Table 6.23: The afterglow search for GRB020903

Time[a]	Telescope & Instruments	OT	Lim. Mag.[b]	GCN
3.84 hours	HETE GCN position notice (WXM)			
6.91 hours	HETE GCN position notice (SXC)			
4.15 hours	0.6 m (wide B and wide R) Mt. John Obs.[c]	N	DSS-2 lim.	#1531 Tristram et al.
1 day	50-inch Telescope (R-MACHO) Mount Stromlo Obs.[d]	N	R∼19.8	#1533 Price et al.
12.46 hours	0.38 m Cassegrain Telescope Crimean Astrophysical Obs.[e]	N	R∼17.4	#1535 Pavlenko et al.
4.18 hours	25 cm Telescope Kyoto University	N	R∼17.5	#1537 Uemura et al.
0.88 days 6.88 days 24.9 days 24.7 days	5 m Telescope + LFC[f] (R) Palomar Obs.[h] MDM[i] 1.3 m Telescope (R) Magellan[j] 6.5 m (spectroscopy)	Y[g] host 	 z=0.25±0.02	#1554 Soderberg et al.
23.8 days 25.7 days	VLA (8.46 GHz)	Y	1.1 mJy 0.7 mJy	#1555 Berger et al.
16.3 hours 5.68 days	CTIO[k] 4 m Telescope (BRI) (R only)	Y	 ↘ 0.2 mag.	#1557 Fruchter et al.
26.5 days	182 cm Telescope (VRI) Cima Ekar Observatory[m]	Y	18.6±0.2[l]	#1561 Stefanon et al.
5.45 hours	0.25 cm Telescope RIKEN	N	unresolved obj.	#1562 Torii et al.
28.5 days	3.5 m TNG[n] Telescope (BVRI) ORM[o]	Y	↘ 0.2 mag. (VRI)	#1563 Covino et al.
34.6 days	Keck I 10 m Telescope	host[p]		#1609 Chornock et al.
36.8 days	1.54 m Danish Telescope (BVR) La Silla Obs.[r]	Y	note[q]	#1631 Gorosabel et al.
3 months	HST/ACS F606W	host		#1761 Levan et al.

[a]Time after the trigger [b]Limiting magnitude [c]Lake Tekapo, New Zealand

[d]Weston, Australia [e]Ukraine [f] Large Format Camera

[g] The position of OT is (R.A., Dec.) = $(22^h48^m42.34^s, -20°46'09.3'')$ (J2000)

[h]San Diego, CA [i]MDM Observatory, Tucson, AZ

[j]Las Campanas Observatory, Cerro Las Campanas, Chile

[k]Cerro Tololo Inter-American Observatory, La Serena, Chile

[l]re-brightening m Cima Ekar-Asiago, Italy

[n]Telescopio Nazionale Galileo

[o]Observatorio del Roque de los Muchachos, Palma, Italy

[p]low metallicity, high excitation starburst galaxy

[q]same magnitude as #1563 r La Silla, Chile

Table 6.24: The fluxes and fluences of GRB020903. The spectral model is the power-law model.

energy range [keV]		
Duration [sec.]		13.0
Photon flux	2–10	9.3±1.9
[10^{-1} ph cm^{-2} s^{-1}]	2–30	9.9±2.0
	30–400	$1.2^{+2.6}_{-1.0}$ $\times 10^{-1}$
	2–400	10.0±2.1
Energy flux	2–10	5.3±1.5
[10^{-9} erg cm^{-2} s^{-1}]	2–30	6.8±2.0
	30–400	$1.3^{+3.4}_{-1.0}$
	2–400	$8.1^{+5.1}_{-2.9}$
Photon fluence	2–10	12.1±2.5
[ph cm^{-2}]	2–30	12.9±2.7
	30–400	$1.6^{+3.3}_{-1.3}$ $\times 10^{-1}$
	2–400	13.0±2.7
Energy fluecne	2–10	6.9±1.5
[10^{-8} erg cm^{-2}]	2–30	8.9±2.7
	30–400	$1.6^{+4.4}_{-1.4}$
	2–400	$10.5^{+6.7}_{-3.8}$

Table 6.25: The time-average spectral parameters of GRB020903.

Model	Parameters	all (WXM+FREGATE)
PL	α	$-2.62^{+0.42}_{-0.55}$
	$K_{15}{}^{a}$	$4.14^{+3.40}_{-2.47} \times 10^{-3}$
	χ^2_ν/DOF	0.845/26

[a] Normalization at 15 keV in the unit of photon cm^{-2} s^{-1} keV^{-1}

6.10 GRB021021

WXM and FREGATE detected a faint burst on 21 Oct 2002 at 18:43:00.00 UTC [81]. This burst was an untriggered event. The ground localization result was distributed 16 hours after the event. The WXM location can be expressed as a 90% confidence circle that is $20'$ in radius and is centered at (R.A., Dec.) = $(00^{\rm h}17^{\rm m}23^{\rm s}, -01^\circ 37' 00'')$ (J2000). There is no report about the afterglow search for this burst.

6.10.1 Light curve

As seen in the figure 6.25, there is no obvious signal in the typical GRB energy band 32–400 keV. Although the signal to noise ratio is quite low, the burst seems to be lasting for $\sim$ 50 seconds.

6.10.2 Spectrum

The calculated fluxes, fluences and the spectral parameters are shown in table 6.26 and 6.27. The X-ray to γ-ray fluence ratio is 4.0, so this event is classified as an X-ray flash. The cutoff power-law model provides a better fit to the spectrum than a simple power-law model. The F-test probability for the improvement at the cutoff power-law model against the simple power-law model is 4.46×10^{-2}.

To constrain the $E_{\rm peak}$ energy in the cutoff power-law model, the photon index α is fixed to the best fit value -1.33. The $E_{\rm peak}$ energy is 15.4 keV.

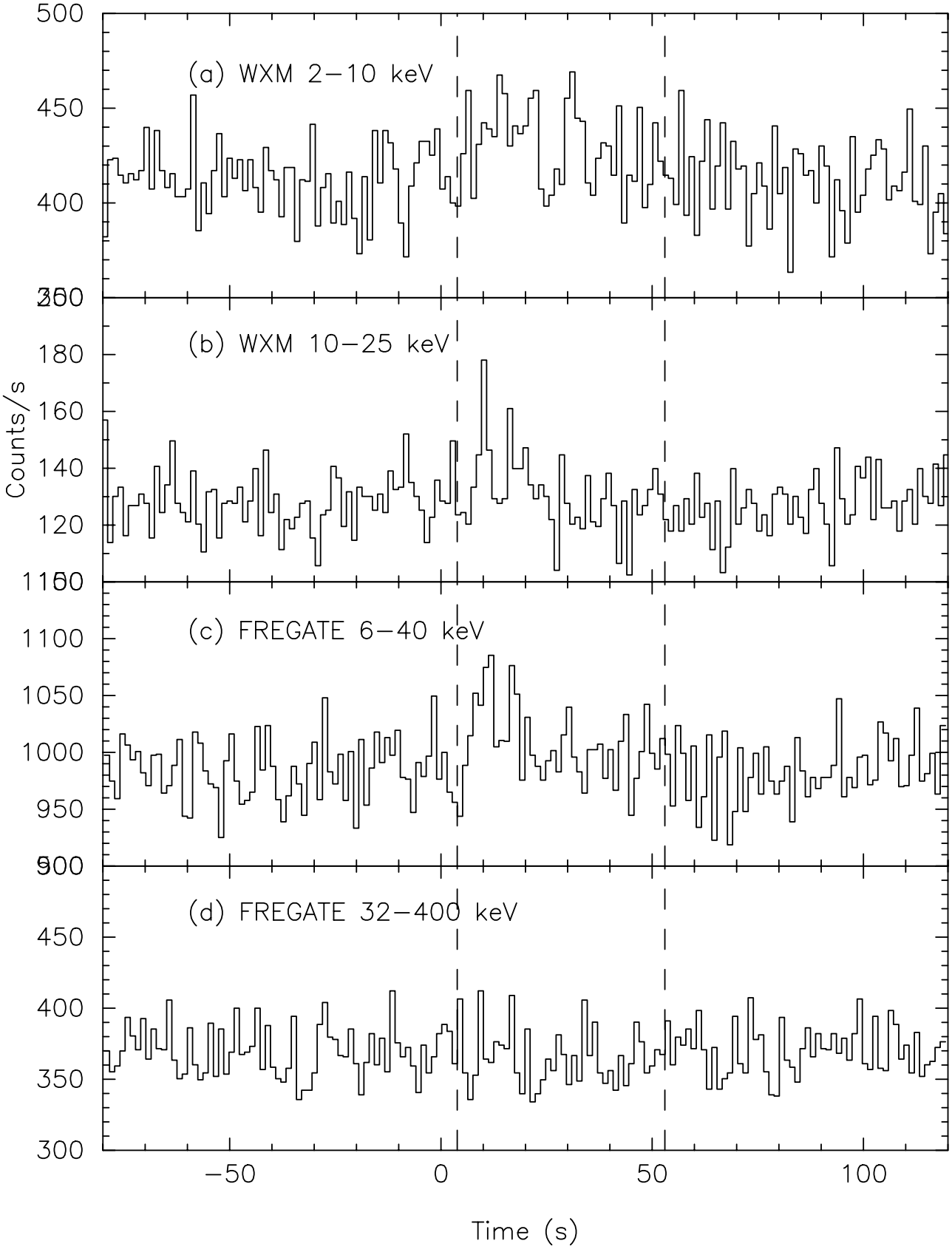

Figure 6.25: The energy resolved light curves of GRB021021 in 1.23 second time-bins.

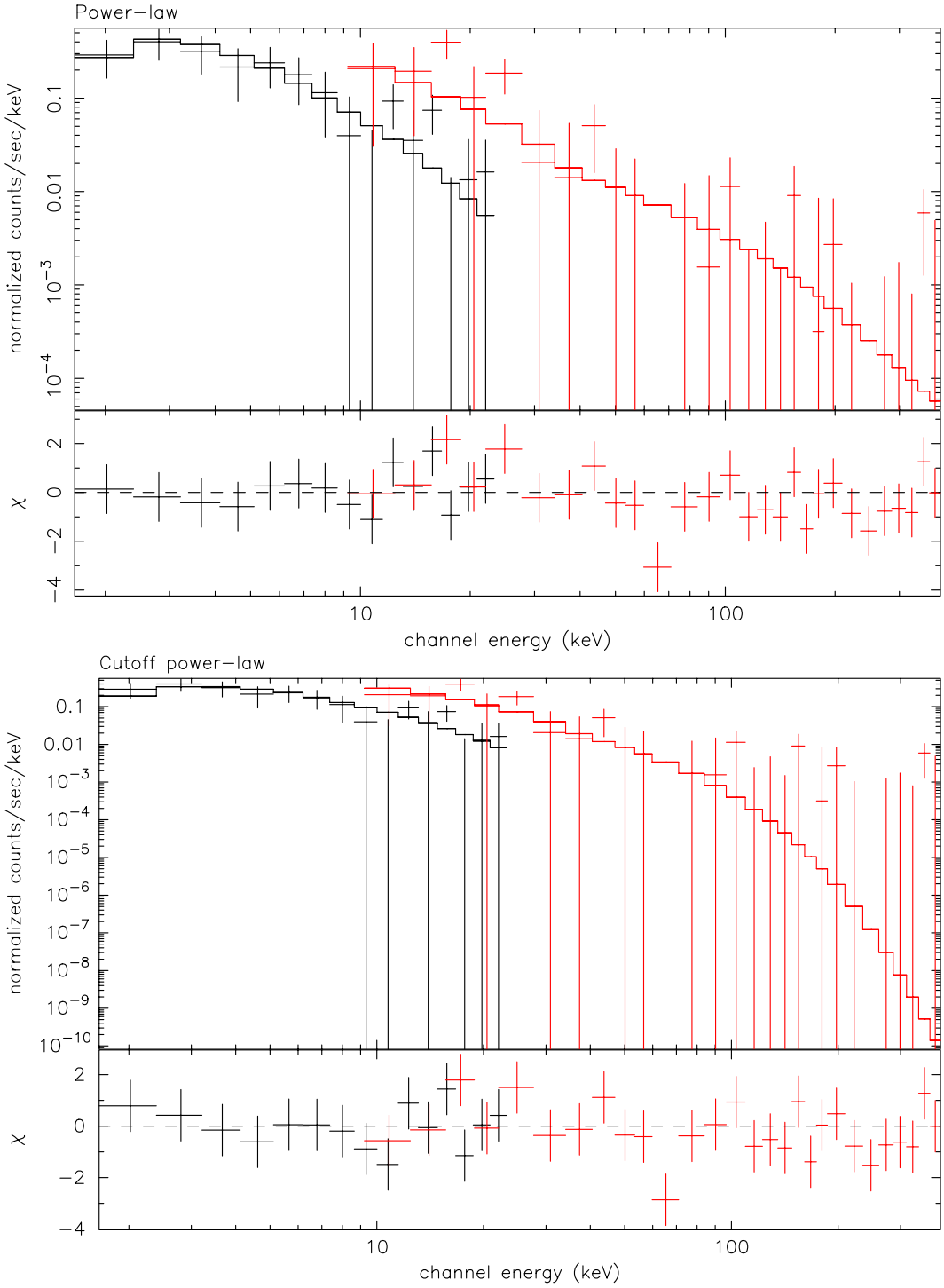

Figure 6.26: The time-average spectra of GRB021021 in the power-law model (upper) and the cutoff power-law model (bottom).

Table 6.26: The fluxes and fluences of GRB021021. The spectral model is the cutoff-law power-law model.

energy range [keV]		
Duration [sec.]		49.2
Photon flux	2–10	3.8±1.0
[10^{-1} ph cm^{-2} s^{-1}]	2–30	4.7±1.1
	30–400	$1.8^{+2.3}_{-1.4}$ $\times 10^{-1}$
	2–400	4.9.0±1.2
Energy flux	2–10	2.7±0.7
[10^{-9} erg cm^{-2} s^{-1}]	2–30	5.1±1.3
	30–400	$1.3^{+2.2}_{-1.0}$
	2–400	$6.4^{+2.8}_{-2.2}$
Photon fluence	2–10	18.6±4.9
[ph cm^{-2}]	2–30	23.1±5.6
	30–400	$8.8^{+11.1}_{-6.7}$ $\times 10^{-1}$
	2–400	24.0±5.7
Energy fluecne	2–10	13.0±3.3
[10^{-8} erg cm^{-2}]	2–30	25.1±6.3
	30–400	$6.2^{+10.6}_{-4.9}$
	2–400	$31.3^{+13.9}_{-10.6}$

Table 6.27: The time-average spectral parameters of GRB020903.

Model	Parameters	
PL	α	$-2.04^{+0.24}_{-0.34}$
	K_{15}[a]	$4.30^{+1.63}_{-1.71} \times 10^{-3}$
	χ^2_ν/DOF	0.974/41
Cutoff PL	α	-1.33 (fixed)
	$E_{\rm peak}$ [keV]	$15.38^{+14.24}_{-7.47}$
	K_{15}[a]	$1.24^{+0.50}_{-0.37} \times 10^{-2}$
	χ^2_ν/DOF	0.879/41

[a]Normalization at 15 keV in the unit of photon cm^{-2} s^{-1} keV^{-1}

6.11 GRB021104

At 07:01:02.9 UTC on 4 Nov 2002, FREGATE and WXM detected the burst [98]. The signal to noise ratio in WXM was ~ 5. The position of the burst can be expressed as a 90% confidence rectangle that is approximately $24'$ in width and $42'$ in length. The four corners of the rectangle are (R.A., Dec.) = ($3^h52^m40.3^s$, $38°19'26''$), ($3^h54^m44.6^s$, $38°17'10''$), ($3^h54^m56.2^s$, $37°34'59''$), and ($3^h52^m52.6^s$, $37°37'12''$) (J2000). Although the afterglow was searched by several observers within 4 hours after the trigger (see table 6.28), no optical transient has been found for GRB021104.

Table 6.28: The afterglow search for GRB021104

Time[a]	Telescope & Instruments	OT	Lim. Mag.[b]	GCN
2.76 hours	HETE GCN position notice			
2.78 hours	Automatic 0.76 m telescope KAIT[c]	N[d]		Li et al. (#1668)
2.78 hours	1.2 m Telescope (unfiltered) Oschin NEAT camera[e]	N	$\sim$ 21 mag.	Fox et al. (#1671)
3.93 hours	Automatic 0.6 m telescope Super-LOTIS[f]	N	DSS limit	Bradshaw et al. (#1677)
	Milagro GeV/TeV Telescope	N	conf.[g]	McEnery et al. (#1724)

[a] Time after the trigger

[b] Limiting magnitude

[c] Katzman Automatic Imaging Telescope, Lick Observatory, San Jose, CA

[d] They reported the candidate of OT, however, this source is seen in DSS2 plate (#1669, #1670).

[e] Mt. Palomar, San Diego, CA

[f] Livermore Optical Transient Imaging System, located on Kitt Peak National Observatory (Tucson, AZ)

[g] J(0.2-20 TeV) $< 3.4 \times 10^{-6}$ erg cm^{-2}

6.11.1 Light curve

The energy resolved light curves are shown in figure 6.27. The duration is ~ 30 seconds. In 2–10 keV band, the burst might have a longer duration. Due to the low signal to noise ratio, it is hard to say about the structure of the time profile.

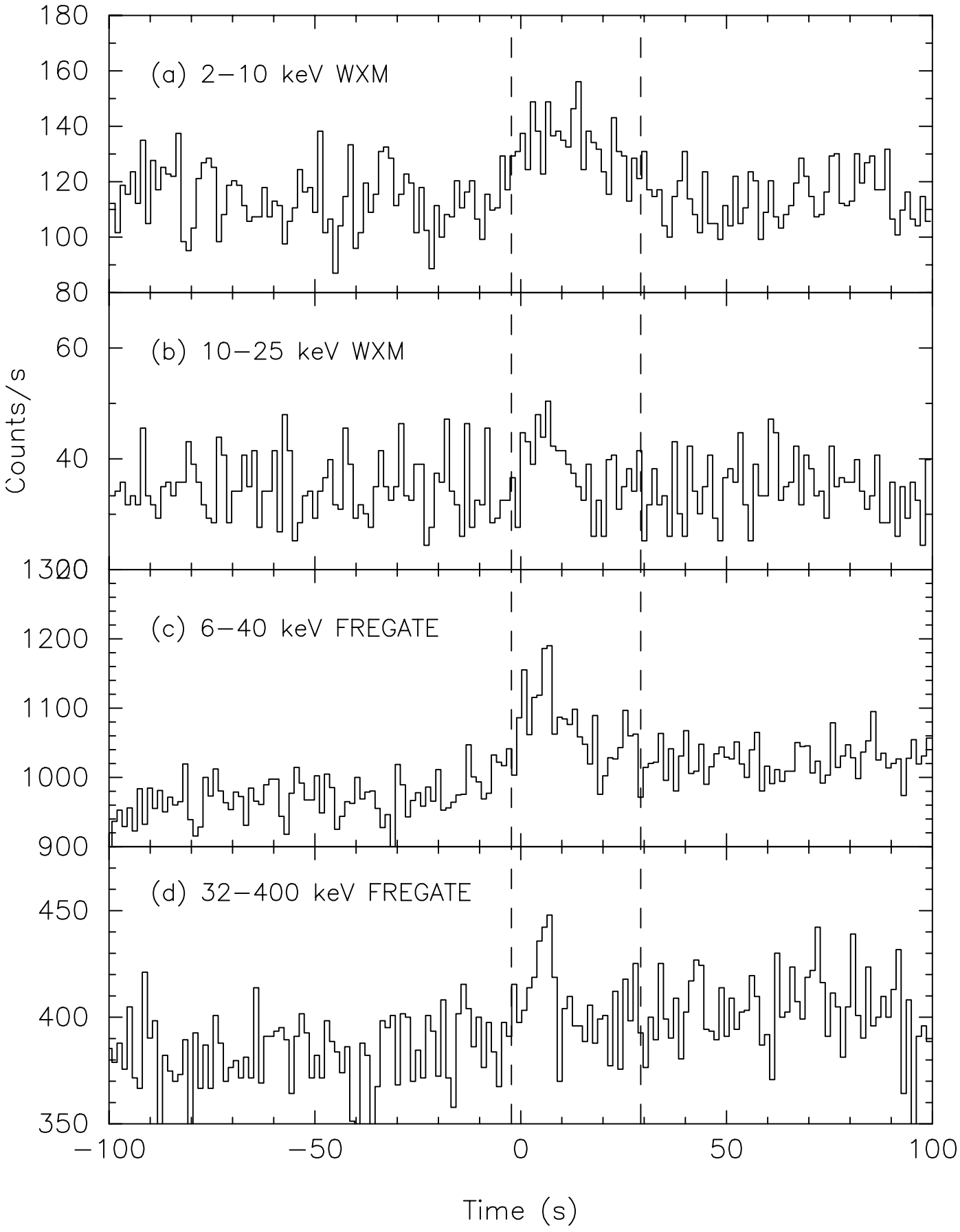

Figure 6.27: The energy resolved light curves of GRB021104 at 1.23 s time bin. The dotted lines represent the foreground region of the spectrum.

6.11.2 Spectrum

The X-ray to γ-ray fluence ratio of 1.7 qualifies this burst as an X-ray flash. Although the simple power-law model shows an acceptable fit to the time-average spectrum, the χ^2 value improves in the cutoff power-law model fit. $\Delta\chi^2$ is 6.62 for one extra degree of freedom (F test probability of 5.78×10^{-3}) in the cutoff power-law model against the simple power-law model. Hence, the model with a spectral break is requested from the data. We decided that the cutoff power-law model is the best representative model for the prompt emission. $E_{\rm peak}$ lies around 30 keV.

Table 6.29: The fluxes and fluences of GRB021104. The spectral model is the cutoff power-law model.

	energy range [keV]	
Duration [sec.]		31.4
photon flux	2–10	$1.8^{+0.9}_{-0.6}$
[ph cm^{-2} s^{-1}]	2–30	$2.5^{+1.0}_{-0.7}$
	30–400	$2.4\pm1.0 \times10^{-1}$
	2–400	$2.7^{+1.0}_{-0.7}$
Energy flux	2–10	1.4 ± 0.5
[10^{-8} erg cm^{-2} s^{-1}]	2–30	3.3 ± 0.7
	30–400	$2.0^{+1.4}_{-0.9}$
	2–400	$5.2^{+1.6}_{-1.1}$
Photon fluence	2–10	$56.5^{+29.2}_{-19.6}$
[ph cm^{-2}]	2–30	$78.7^{+29.9}_{-20.9}$
	30–400	$7.5^{+3.0}_{-2.6}$
	2–400	$86.3^{+30.4}_{-21.3}$
Energy fluecne	2–10	$4.3^{+1.8}_{-1.3}$
[10^{-7} erg cm^{-2}]	2–30	$10.3^{+2.1}_{-1.8}$
	30–400	$6.1^{+4.4}_{-2.7}$
	2–400	$16.4^{+5.0}_{-3.3}$

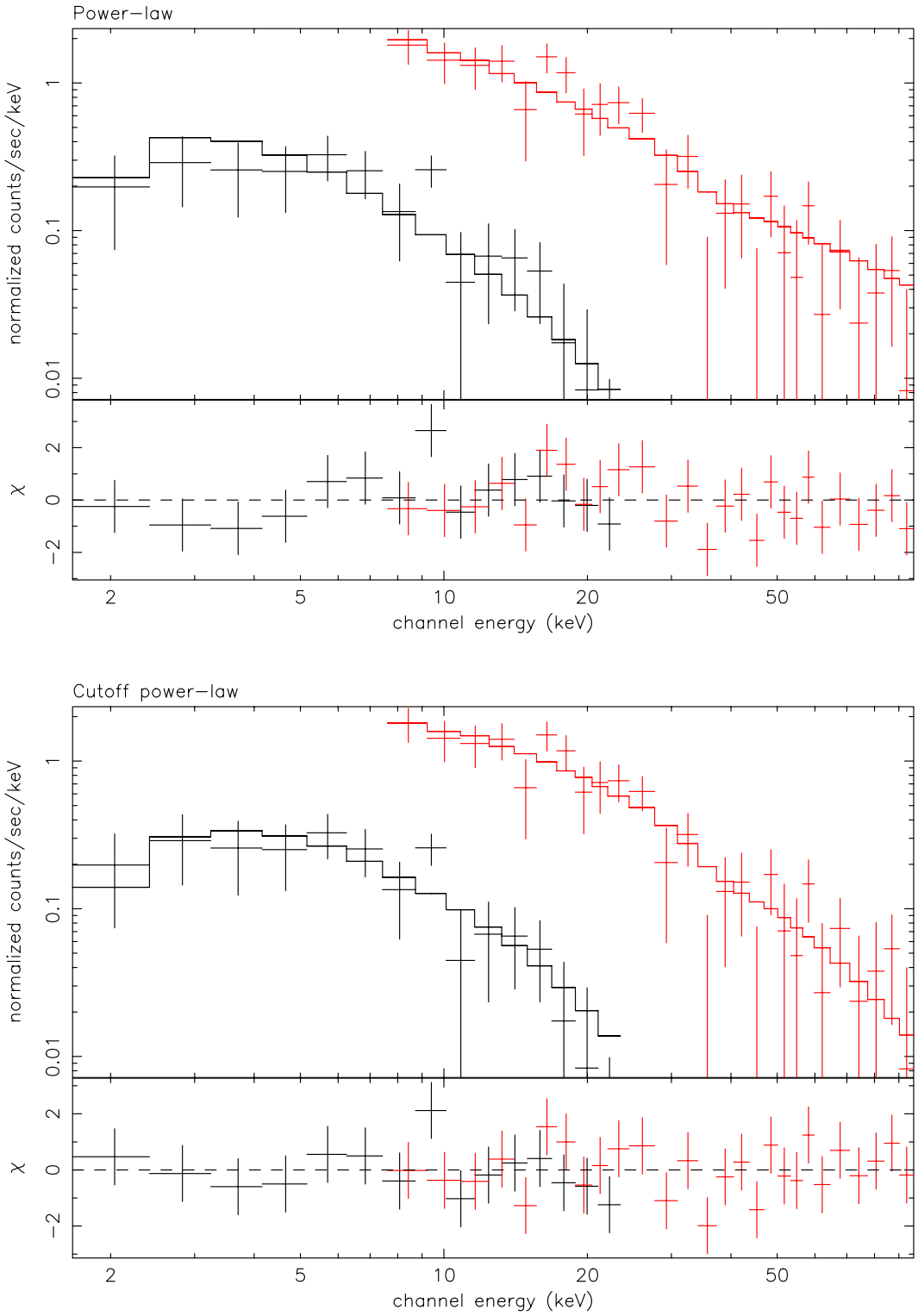

Figure 6.28: The WXM and FREGATE spectra of GRB021104. The top and bottom figures are fitting with the power-law model and the cutoff power-law model, respectively.

Table 6.30: The spectral parameters of GRB021104.

Model	Parameters	
PL	α	-1.82 ± 0.18
	K_{15}[a]	$(4.19\pm0.66) \times 10^{-2}$
	C[b] (WXM)	$0.34^{+0.16}_{-0.11}$
	χ^2_ν/DOF	0.924/39
Cutoff PL	α	$-1.11^{+0.54}_{-0.46}$
	E_{peak} [keV]	$28.2^{+17.4}_{-7.9}$
	K_{15}	$7.59^{+5.31}_{-2.55} \times 10^{-2}$
	C (WXM)	$0.48^{+0.20}_{-0.15}$
	χ^2_ν/DOF	0.774/38

[a]Normalization at 15 keV in the unit of photon cm^{-2} s^{-1} keV^{-1}

[b]Constant parameter of WXM. The constant parameter of FREGATE is fixed to 1.

6.12 GRB030416

At 11:03:59.00 UTC on 16 Apr 2003, FREGATE and WXM observed the untriggered burst [40]. Since the trigger process of WXM and the FREGATE 6–80 keV band had been turned off in order to avoid false triggers by Sco X-1, *HETE* did not trigger this event. The position of the burst by the ground analysis is centered at (R.A., Dec.) = ($11^{\rm h}06^{\rm m}51^{\rm s}$, $-02^\circ52'\ 58''$) (J2000) with a 90% radius of $7'$.

There are two reports about the afterglow search for this event (table 6.31). However, no afterglow has been found.

Table 6.31: The afterglow search for GRB030416

Time[a]	Telescope & Instruments	OT	Lim. Mag.[b]	GCN
15.74 hours	HETE GCN position notice			
15.4 hours	USNO	N	BVRcIc[c]	Henden et al. (#2250)
1.38 days	0.23 m Telescope MASTER system[d]	N	$\sim$ 15.0 mag. (R)	Lipunov et al. (#2154)

[a]Time after the trigger

[b]Limiting magnitude

[c]Limiting magnitude:

Start Date	Start Time Since GRB (hours)	Filter	Integration Time (sec) x Pointings	Limiting Magnitude (3 sigma)	Telescope	Calibration Catalog
Apr 17.103	15.391	Rc	6000 x 1	19.8	0.6-m RBO*	USNO A2.0
Apr 17.143	16.361	B	300 x 1	20.1	1.3-m USNO	USNO A2.0
Apr 17.149	16.502	V	300 x 1	20.9	1.3-m USNO	ACT
Apr 17.155	16.643	Rc	300 x 1	20.4	1.3-m USNO	USNO A2.0
Apr 17.160	16.784	Ic	300 x 1	19.9	1.3-m USNO	USNO B1.0
Apr 20.143	88.454	Rc	2160 x 1	22.3	1.3-m USNO	USNO A2.0

* RBO = Red Buttes Observatory

[d]Alexander Kryolov Observatory, Moscow, Russia

6.12.1 Light curve

The duration is $\sim$ 80 seconds in the WXM 2–5 keV energy band. The gradual excess of the signal is lasting about 30 seconds. The high flux part continues about 20 seconds, and then the

signal decreases in 30 seconds. The burst signal is very weak in the WXM 17–25 keV band.

6.12.2 Spectrum

The time-average fluxes and the fluences are summarized in table 6.32. Since the X-ray to γ-ray fluence ratio is 2.4, this burst is classified as X-ray flash.

Table 6.32: The time-average fluxes and fluences of GRB030416. The spectral model is the power-law model.

	energy range [keV]	
Duration [sec.]		78.6
Photon flux	2–10	1.3±0.1
[ph cm^{-2} s^{-1}]	2–30	1.4±0.1
	30–400	$4.1^{+1.7}_{-1.3}$ $\times 10^{-2}$
	2–400	1.5±0.1
Energy flux	2–10	7.9±0.7
[10^{-9} erg cm^{-2} s^{-1}]	2-30	11.4±1.1
	30–400	$4.7^{+2.4}_{-1.7}$
	2–400	$16.1^{+3.1}_{-2.6}$
Photon fluence	2–10	102.9±9.8
[ph cm^{-2}]	2–30	113.7±10.0
	30–400	3.2±1.3
	2–400	116.9±10.1
Energy fluecne	2–10	6.2±0.5
[10^{-7} erg cm^{-2}]	2–30	9.0±0.9
	30–400	$3.7^{+1.9}_{-1.4}$
	2–400	$12.7^{+2.5}_{-2.1}$

The simple power-law model is acceptable for the time-averaged spectrum of GRB030416. Since the photon index is well steeper than < -2, the *constrained* Band function is applied to constrain the $E_{\rm peak}$ of this event. The probability density distribution as a function of $E_{\rm peak}$ is shown in figure 6.31. The 68%, 95% and 99.7% upper limit of $E_{\rm peak}$ are 3.1, 3.3 and 3.8 keV respectively.

To investigate the spectral evolution, the hardness ratio between 5–25 keV and 2–5 keV is plotted in figure 6.32. It is possible to see two hard-to-soft evolutions during the burst. The first part is from T_0 + 10 s to T_0 + 20 s, and the second part is from T_0 + 20 s to T_0 + 35 s (T_0 is the trigger time). The soft tail is lasting for T_0 + 60s.

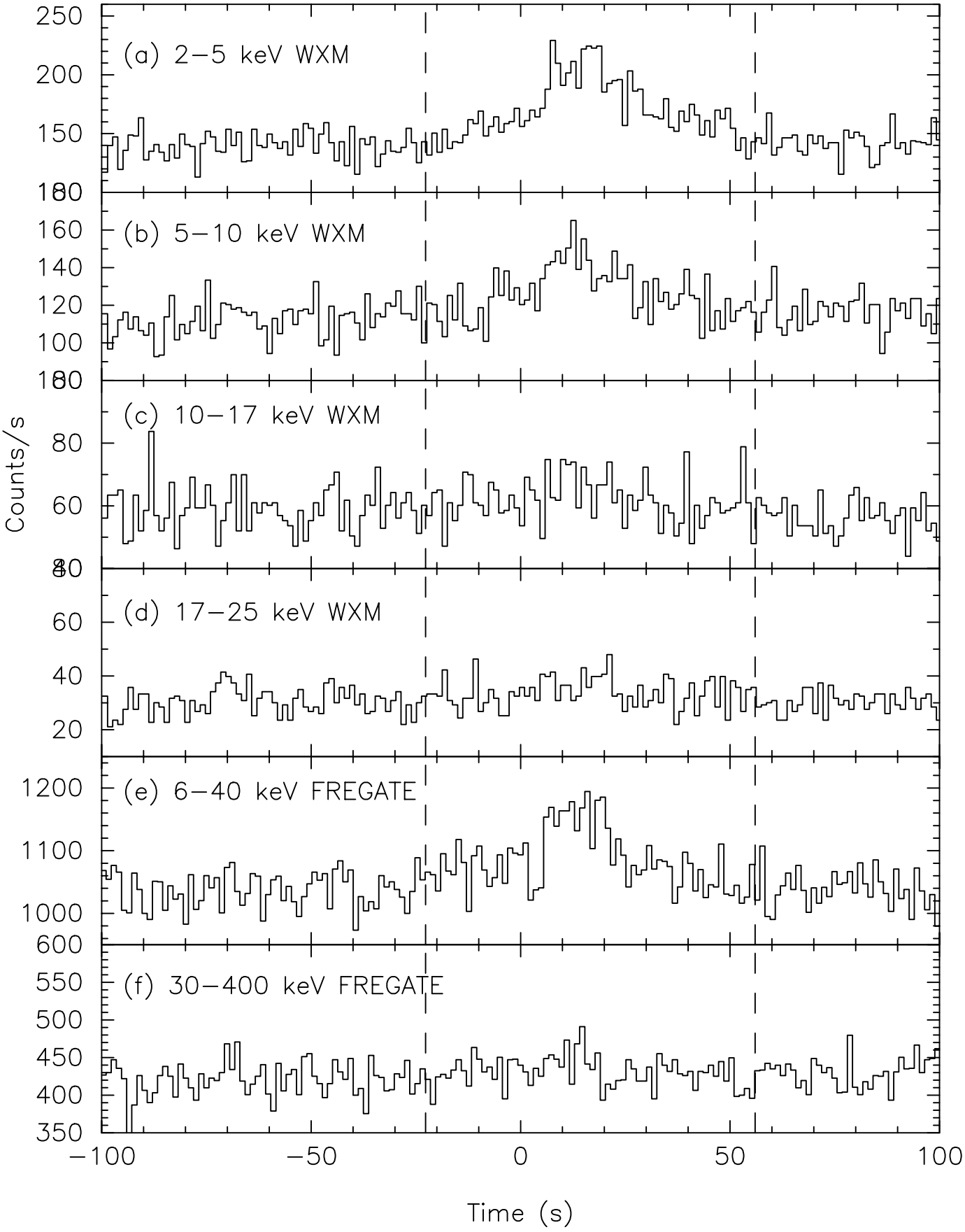

Figure 6.29: The energy resolved light curves of GRB030416 at 1.23 s time bin. The dotted lines represent the foreground region of the spectrum.

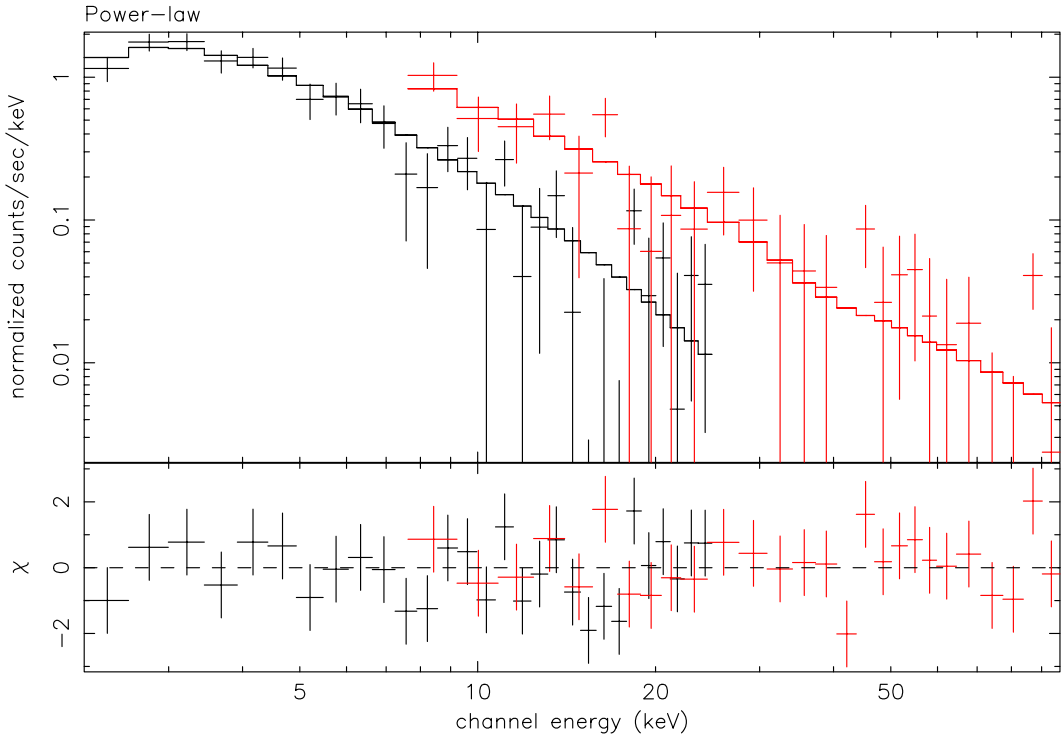

Figure 6.30: The time-average spectrum of GRB030416.

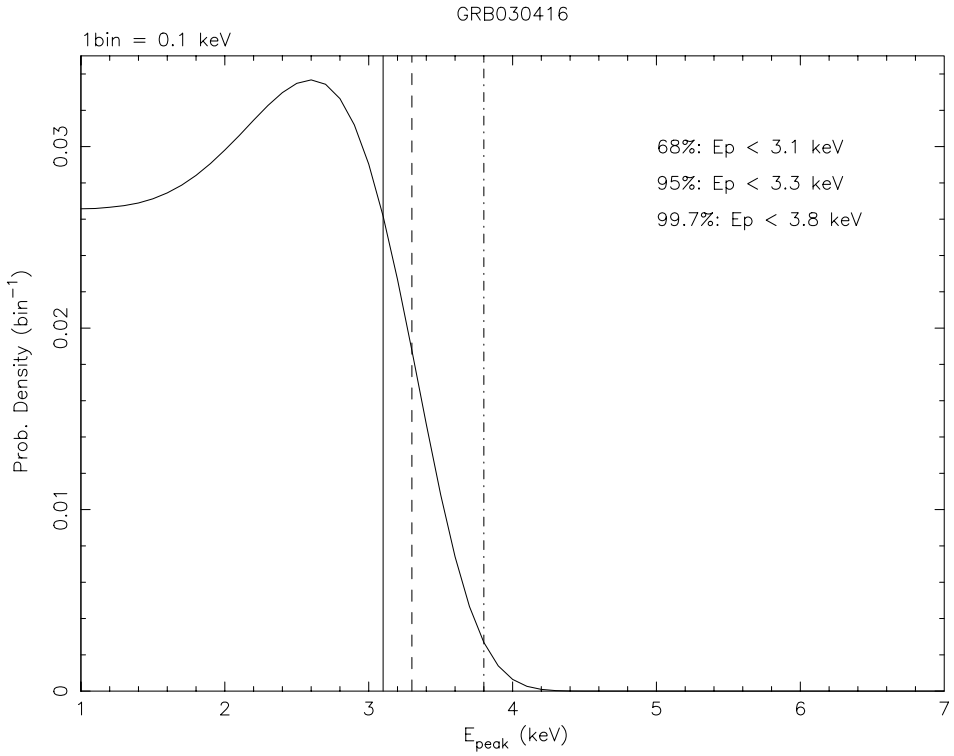

Figure 6.31: The posterior probability density distribution for $E_{\rm peak}$. The solid, the dashed, and the dot-dashed lines show the 68%, 95%, and 99% probability upper limits on $E_{\rm peak}$. $E_{\rm pivot}$ energy is 1.4 keV.

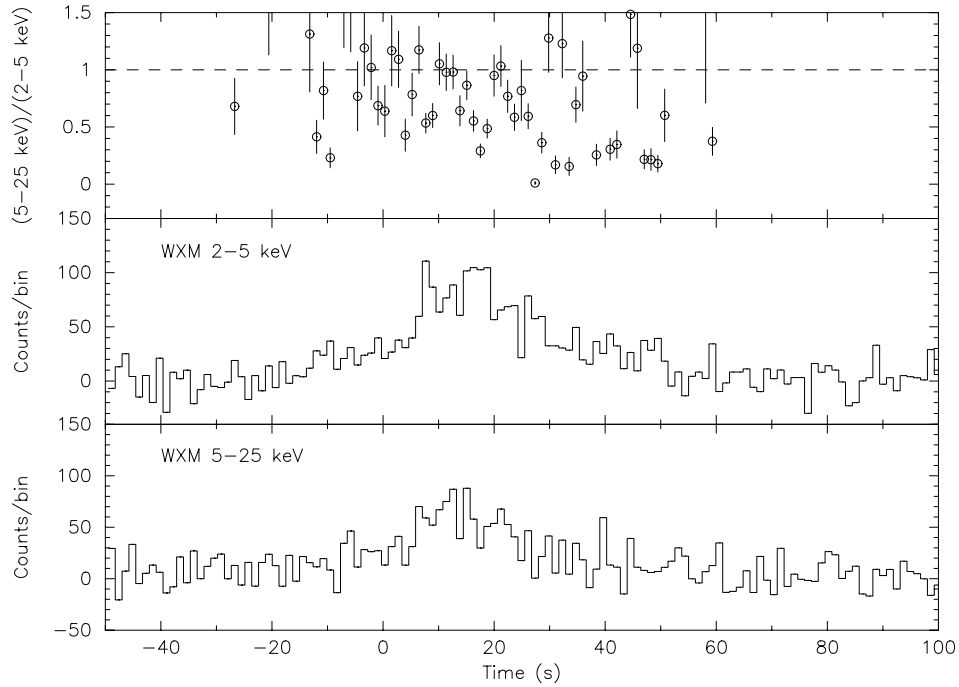

Figure 6.32: The hardness ratio between 5–25 keV and 2–5 keV band. The middle and the bottom panels are the light curves of the WXM 2–5 keV and 5–25 keV band.

Table 6.33: The spectral parameters of GRB030416.

Model	Parameters	
PL	α	$-2.32^{+0.13}_{-0.15}$
	$K_{15}{}^a$	$(9.23\pm1.72)\times10^{-3}$
	χ^2_ν/DOF	0.870/54

[a]Normalization at 15 keV in the unit of photon cm^{-2} s^{-1} keV^{-1}

6.13 GRB030418

FREGATE detected this event in the 32–400 keV band on 18 April 2003 at at 09:59:18.85 UTC [93]. The correct WXM flight localization was reported in a GCN Notice at 215 seconds after the trigger. The WXM localization in the ground analysis can be expressed as a 90% confidence circle that is $9'$ in radius and is centered at: R.A. = $10^{\rm h}54^{\rm m}53^{\rm s}$, Dec. = $-06°59'22''$ (J2000).

The status of the afterglow search is summarized in table 6.34. The candidate of the optical transient (OT) was reported by Price et al. (GCN 2148) at 2.26 hours after the trigger. The decline of the optical flux of this OT candidate was observed by the same authors (GCN 2150). The Magellan 6.5 m telescope also observed this OT and confirmed the decrease in the flux at the power-law decay of $t^{-1.2\pm0.1}$ (Dullighan et al.; GCN 2168 and GCN 2236).

Table 6.34: The afterglow search for GRB030418

Time[a]	Telescope & Instruments	OT	Lim. Mag.[b]	GCN
215 seconds	HETE flight location			
1.73 hours	HETE ground location			
2.26 hours	40-inch Telescope Siding Spring Observatory (Chile)	Y[c]	18.8 mag. (R)	Price et al. (#2148)
4.66 hours	40-inch Telescope (2nd epoch)	Y	19.8 mag. (R)	Price et al. (#2150)
69 minutes	1.05 m Telescope (J) Kiso Observatory	N	13 mag.[d] (J)	Mito et al. (#2151)
238 seconds	ROTSE-IIIa	Y	18.7 - 17.4 mag. (360 s. - 2.3 h)	Smith et al. (#2153)
11-12.5 hours	MASTER system	N	16.5 mag. (R)	Lipunov et al. (#2158)
2.59 days	Magellan 6.5 m (R, I)	Y	23.3±0.1 (R) 23.0±0.1 (I)	Dullighan et al. (#2168)
6.58 days	Magellan 6.5 m (R, I, V) (2nd epoch)	Y	24.9±0.4 (R) >24 (I) 25.1±0.5 (V)	Dullighan et al. (#2236)
9.53 hours	152 cm Telescope (R)	Y	20.50±0.30 (9.53h) 20.65±0.29 (10.18h)	Ferrero et al. (#2284)

[a] Time after the trigger

[b] Limiting magnitude

[c] (R.A., Dec.) = ($10^{\rm h}54^{\rm m}33.69^{\rm s}$, $-7°01'40.8''$)

[d] 3 sigma upper limit

6.13.1 Light curve

The double peak structure was observed in the FREGATE energy bands, whereas, this time profile was closer to the single peak in the WXM 2–10 keV band (figure 6.33). The significant decreasing trend of the background started around t=100 is due to the particle events (this event occurred about 10 minutes before the SAA). The duration is $\sim$ 130 seconds in the FREGATE energy bands and could be much longer in the WXM 2–10 keV band.

6.13.2 Spectrum

Due to the incomplete downlink of the data, we used the SP data for the spectral analysis of FREGATE. The photon data (TAG data) were available for WXM.

The spectral analysis is performed for the three time intervals including the whole burst region (figure 6.33). Since this event occurred 10 minutes before the SAA and the decreasing trend of the background was observed just after the burst, we choose t $\sim$ 100 s as the end of the foreground time region for creating the spectra. The cutoff power-law model is the best representative model for all time regions. The F-test probabilities of the cutoff power-law model over the simple power-law model at the first, the second and the whole burst regions are 1.73×10^{-11}, 2.22×10^{-2}, and 3.78×10^{-4} respectively. The X-ray to γ-ray fluence ratio is 0.99 qualifies this burst as an X-ray rich GRB. The spectrum in the first region has a harder photon index and also a higher $E_{\rm peak}$ energy than that of the second region. The time-average $E_{\rm peak}$ energy is 46 keV.

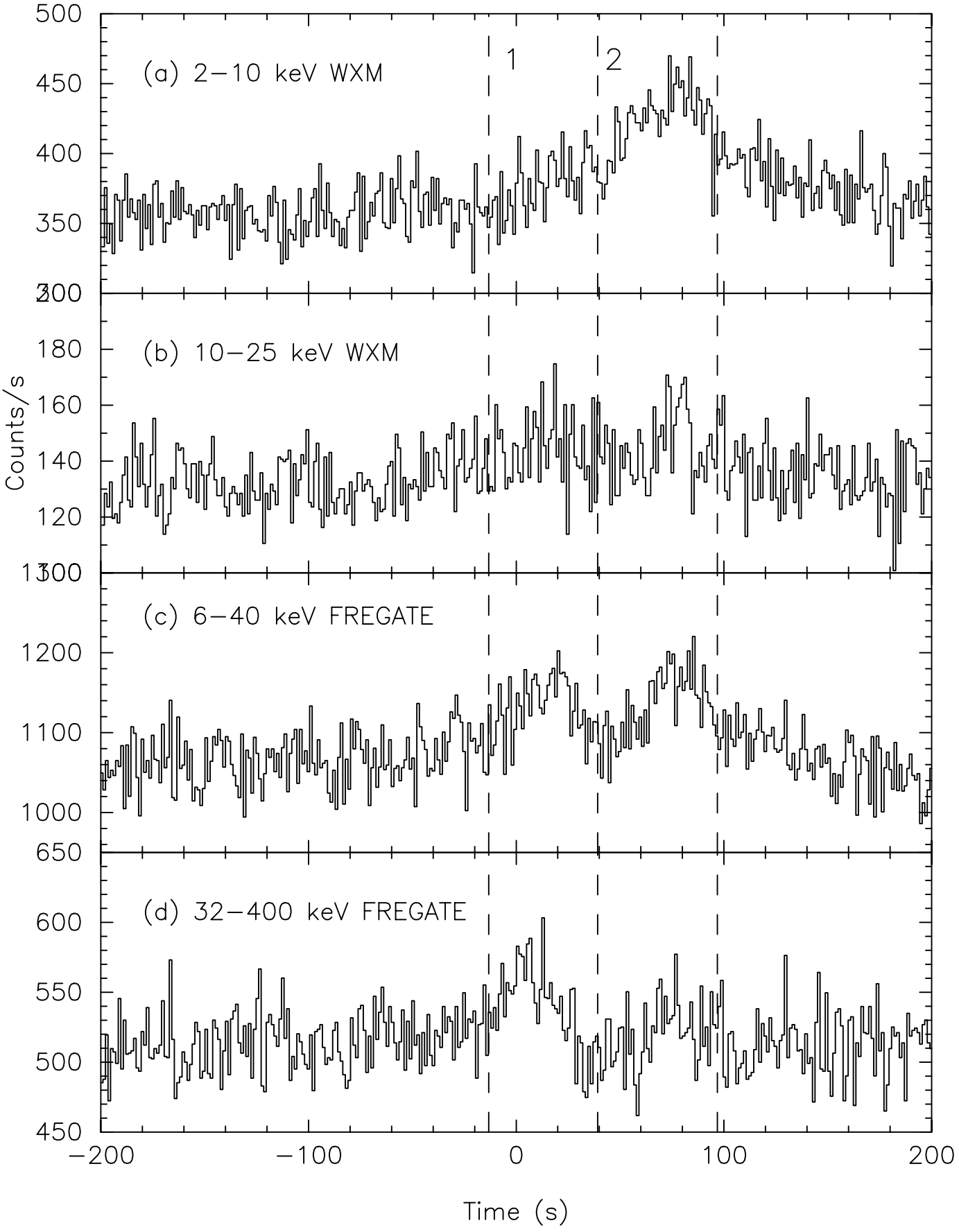

Figure 6.33: The energy resolved light curves of GRB030418 at 1.23 s time bin. The dotted lines correspond to the two foreground intervals used for creating the spectra.

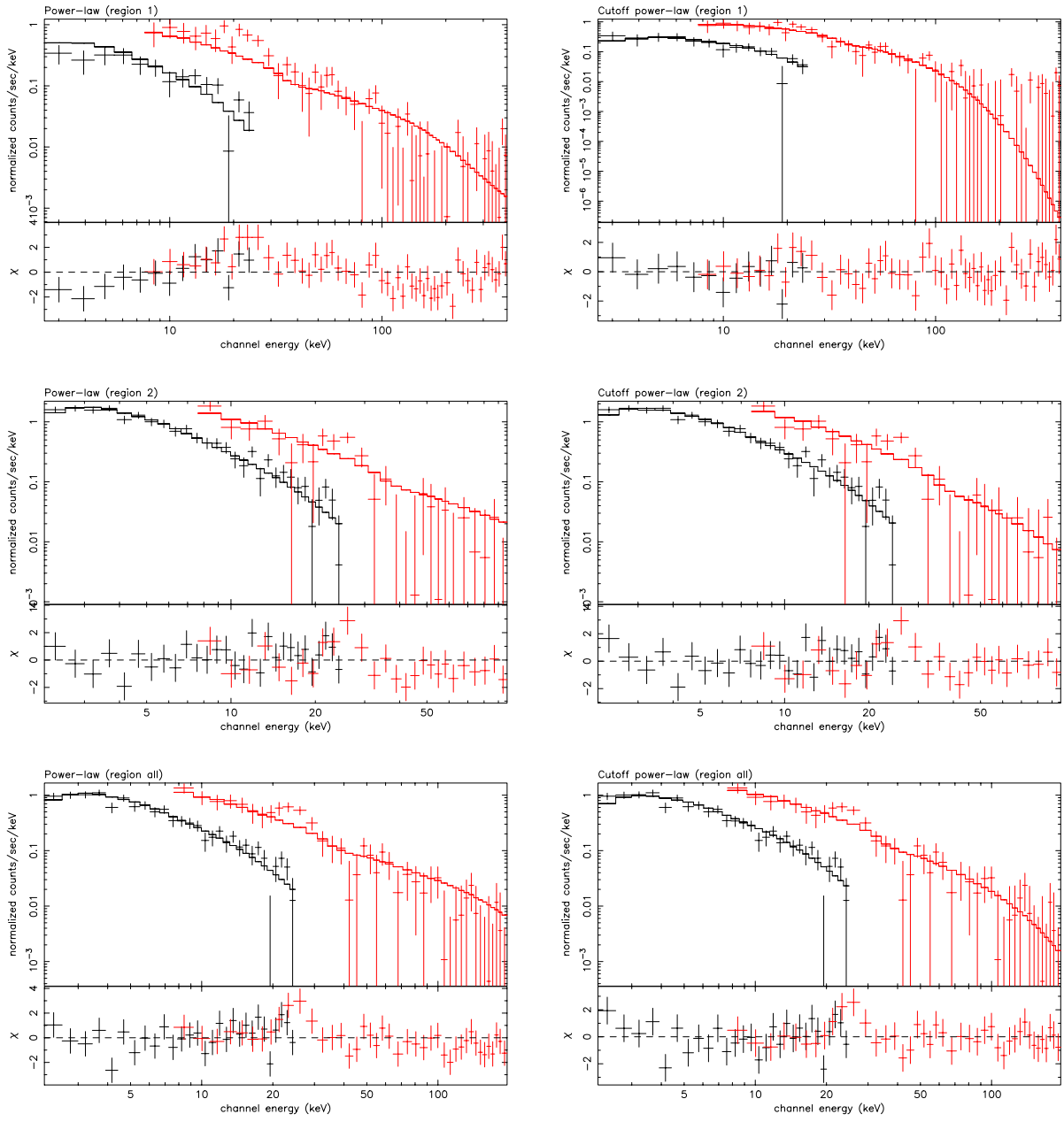

Figure 6.34: The WXM and FREGATE spectra of GRB030418. The spectra of region 1, region 2, and all region are shown from top to bottom. The left and right plots are fitting with the power-law model and cutoff power-law model, respectively.

Table 6.35: The fluences of GRB030418. The spectral model is the cutoff power-law model.

	energy range [keV]	region 1	region 2	all
Duration [sec.]		52.4	57.7	110.1
Photon flux	2–10	3.5±0.8	15.7±1.0	9.9±0.8
[10^{-1} ph cm^{-2} s^{-1}]	2–30	6.9±0.9	18.7±1.0	13.0±0.8
	30–400	2.3±0.4	0.8±0.4	1.5±0.4
	2–400	9.2±1.0	19.5±1.2	14.6±0.9
Energy flux	2–10	$(3.1\pm0.6)\times10^{-1}$	$(10.5\pm0.6)\times10^{-1}$	$(7.1\pm0.5)\times10^{-1}$
[10^{-8} erg cm^{-2} s^{-1}]	2–30	1.3±0.1	1.8±0.1	1.6±0.1
	30–400	2.0±0.5	$0.7^{+0.7}_{-0.3}$	$1.6^{+0.7}_{-0.5}$
	2–400	3.3±0.5	$2.5^{+0.7}_{-0.4}$	$3.1^{+0.7}_{-0.5}$
Photon fluence	2–10	18.6±4.1	90.5±5.8	109.0±8.8
[ph cm^{-2}]	2–30	36.0±4.7	107.8±6.1	143.1±8.8
	30–400	12.0±2.1	4.6±2.2	16.5±3.9
	2–400	60.8±5.2	112.4±6.7	160.7±9.4
Energy fluecne	2–10	1.6±0.3	6.0±0.3	7.8±0.6
[10^{-7} erg cm^{-2}]	2–30	6.7±0.7	10.6±0.7	17.1±1.1
	30–400	10.7±2.6	$3.9^{+3.9}_{-1.8}$	$17.3^{+7.3}_{-5.2}$
	2–400	17.4±2.7	$14.5^{+3.9}_{-2.2}$	$34.5^{+7.2}_{-5.5}$

Table 6.36: The spectral parameters of GRB030418 in the power-law (PL) and the cutoff power-law (Cutoff PL).

Model	Parameters	Region 1	Region 2	All
PL	α	-1.41 ± 0.07	-1.95 ± 0.08	-1.70 ± 0.06
	K_{15}[a]	$(1.36\pm0.14)\times10^{-2}$	$(1.90\pm0.18)\times10^{-2}$	$(1.76\pm0.13)\times10^{-2}$
	χ^2_ν/DOF	1.720/69	1.133/54	1.104/69
Cutoff PL	α	$-0.43^{+0.31}_{-0.27}$	$-1.75^{+0.19}_{-0.16}$	$-1.46^{+0.14}_{-0.13}$
	E_{peak} [keV]	$48.62^{+11.19}_{-8.03}$	$13.74^{+12.37}_{-4.89}$	$46.10^{+31.96}_{-13.70}$
	K_{15}	$(3.35^{+0.99}_{-0.69})\times10^{-2}$	$(2.69^{+0.94}_{-0.63})\times10^{-2}$	$(2.43^{+0.47}_{-0.37})\times10^{-2}$
	χ^2_ν/DOF	0.893/68	1.045/53	0.929/68

[a] Normalization at 15 keV in the unit of photon cm^{-2} s^{-1} keV^{-1}

6.14 GRB030429

At 10:42:22.68 UTC on 29 April 2003, FREGATE, WXM, and SXC observed the γ-ray burst [18]. The burst triggered in the 32–400 keV energy band. The flight position was not sent out to GCN due to the low signal to noise ratio in the WXM data. The WXM ground localization can be expressed as 90% confidence rectangle, whose center is at (R.A., Dec.) = ($12^{\rm h}$ $13^{\rm m}$ $18^{\rm s}$, -20° $51'$ $09''$) (J2000), and whose corners lie at (R.A., Dec.) = ($12^{\rm h}$ $13^{\rm m}$ $32^{\rm s}$, -21° $01'$ $55''$), ($12^{\rm h}$ $12^{\rm m}$ $50^{\rm s}$, -20° $59'$ $56''$), ($12^{\rm h}$ $13^{\rm m}$ $03^{\rm s}$, -20° $40'$ $26''$), ($12^{\rm h}$ $13^{\rm m}$ $46^{\rm s}$, -20° $42'$ $22''$) (J2000). The SXC position is centered at (R.A., Dec.) = ($12^{\rm h}$ $13^{\rm m}$ $06^{\rm s}$, -20° $56'$ $00''$) (J2000) with the 90% confidence circle of $2'$ radius.

The afterglow of GRB030429 was discovered in the optical band at 3.5 hours after the trigger. Several authors reported the confirmations of the optical transient and also the redshift of 2.56 is measured by VLT for this burst (see table 6.37).

6.14.1 Light curve

The duration of the burst is $\sim$ 20 seconds. Although it is hard to see the structure of the light curve in the WXM energy band, the two peaks are clearly visible in the FREGATE light curve.

6.14.2 Spectrum

Since there is a problem in photon data, the survey data are used in the analysis.

The time-averaged flux and fluence are in table 6.38. Since the fluence ratio of 2–30 keV to 30–400 keV is 1.23, this burst is classified as an X-ray flash.

The spectral parameters are summarized in table 6.39. The time-resolved spectral analysis is performed for the first peak, the second peak, and the whole burst region (see figure 6.35). The cutoff power-law model is the best representative model for all spectral regions. Even at the second time region, the F-test probability in the cutoff power-law model against the simple power-law model is 5.41×10^{-3}. Thus, the improvement of the χ^2 is significant. It is possible to see the decrease of the $E_{\rm peak}$ energy from the first to the second peak.

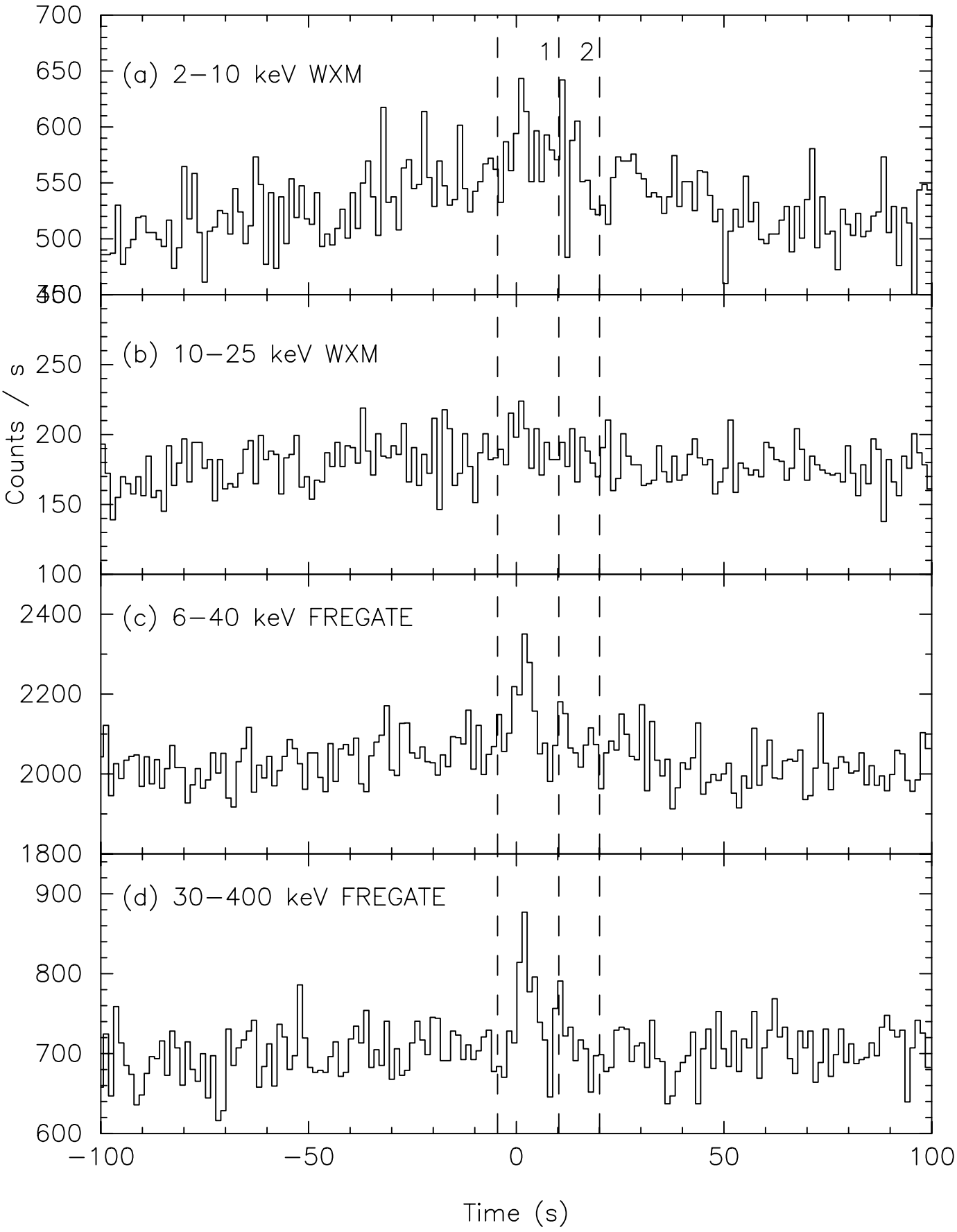

Figure 6.35: The energy resolved light curves of GRB030429 at 1.23 s time bin. The dotted lines correspond to the foreground spectral regions.

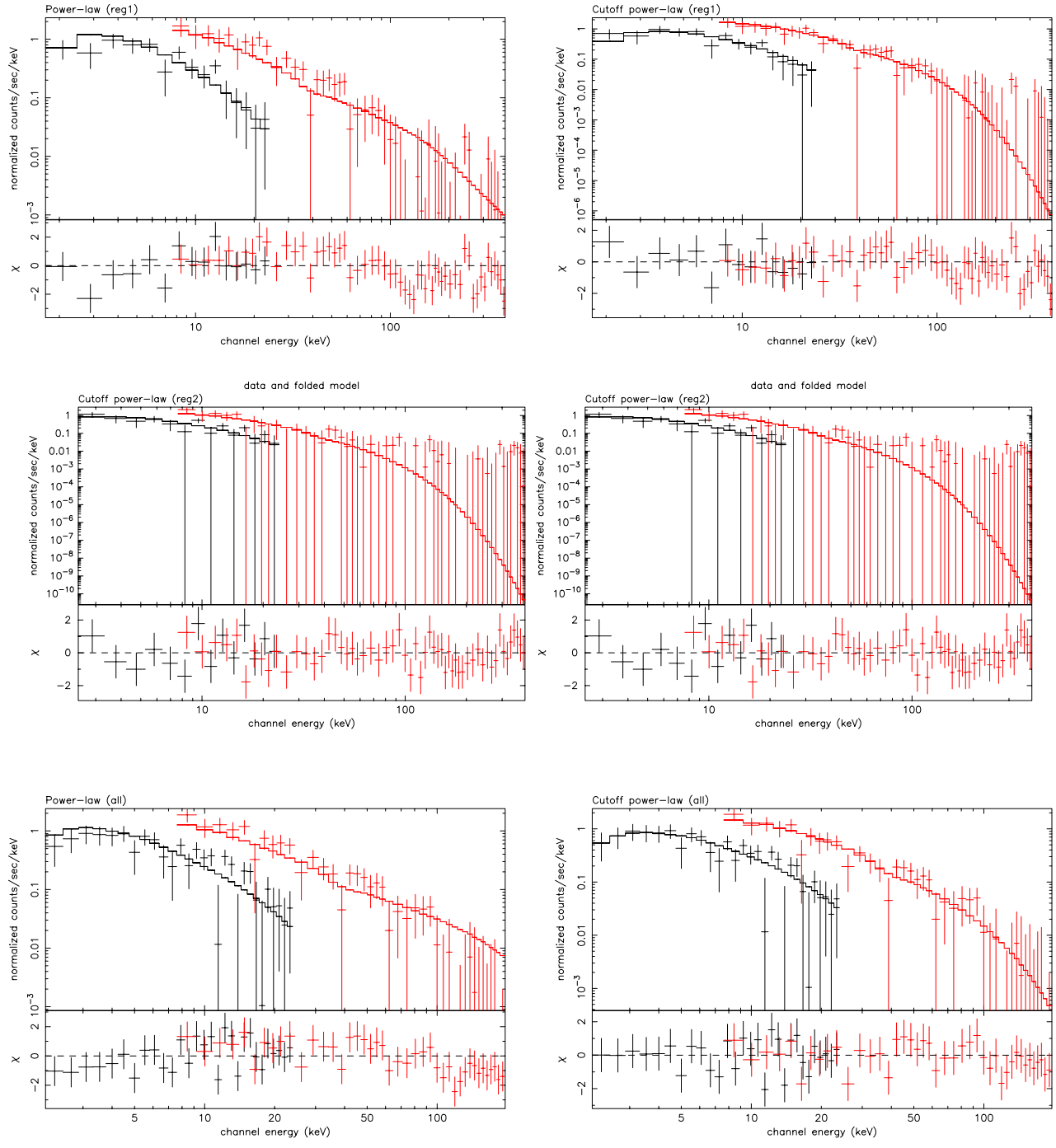

Figure 6.36: The WXM and FREGATE spectrum of GRB030429. The spectrum of the first peak, the second peak and the whole burst region are shown from top to bottom. The model spectrum is the power-law and the cutoff power-law model from left to right.

Table 6.37: The afterglow search for GRB030429

Time[a]	Telescope & Instruments	OT	Lim. Mag.[b]	GCN
1.87 hours	HETE GCN position notice			
1.87 hours	ROTSE-IIIa Siding Spring Ovservatory[c]	N	18∼19 (R)	Smith et al. (#2178)
3.5 hours	0.6 m (unfil.)and 1.55 m (Rc) Tel. Mt. John Obs.[e] and USNOFS	Y[d]		Gilmore et al. (#2184)
8.98 hours	AT-64 Telescope CrAO[f]	Y	20.20±0.15 (R)	Rumyantsev et al. (#2190, #2218)
12.6 hours	VLT (ISAAC and FORS2) Paranal Obervatory[g]	Y	Δm $\sim$ 0.43 (V) in 5.5 h	Fynbo et al. (#2185)
6.74 hours	SIRIUS[h] 1.4 m Telescope (J H Ks)	Y[i]		Nishiyama et al. (#2195)
2.75 days	VLT (FORS1;spectrum) 3800–8000 Å	Y	z=2.65	Weidinger et al. (#2195, #2215)
2.65 days	VLA (8.46 GHz)	N	J(3σ)=0.18 mJy	Berger et al. (#2197)
3.43 days	1.5 m RTT[j]	Y	23.5±0.5(R)	Khamitov et al. (#2208)

[a]Time after the trigger

[b]Limiting magnitude

[c]New South Wales, Australia

[d]OT position: 12:13:07.50 -20:54:49.7 J2000 (err: +/- 0.3arcsec)

UTmid	CRmag	CRerr
Apr 29.591	19.34	0.11
Apr 29.600	19.43	0.13
Apr 29.616	19.71	0.16
Apr 29.660	19.87	0.19

[e]Lake Tekapo, New Zealand

[f]Crimean Astrophysical Observatory, Nauchny, Ukraine

[g]Cerro Paranal, Chile

[h]Simultaneous three-color InfraRed Imager for Unbiased Survey
South Africa Astronomical Obsevatory(SAAO), Sutherland, South Africa

[i]OT info:

UTmid	J	H	Ks
Apr 29.727	18.8	17.8	17.0
Apr 29.873	19.2	18.3	17.5
Apr 30.005	18.9	18.1	17.4
---	---	---	---
Apr 30.768	19.0	18.4	17.8

[j]Russian-Turkish Telescope (Bakyrlytepe, Turkey)

Table 6.38: The time-average fluxes and fluences of GRB030429. The spectral model is the cutoff power-law model.

	energy range [keV]	reg.1	reg.2	all
Duration [sec.]		14.8	9.8	24.6
Photon flux	2–10	1.0±0.2	1.0±0.3	1.0±0.2
[ph cm^{-2} s^{-1}]	2–30	1.5±0.2	1.3±0.3	1.4±0.2
	30–400	(2.4±0.6) $\times10^{-1}$	$5.3^{+6.9}_{-4.8}$ $\times10^{-2}$	(1.8±0.4) $\times10^{-1}$
	2–400	1.8±0.2	1.4±0.3	1.6±0.2
Energy flux	2–10	0.8±0.1	0.7±0.2	0.8±0.1
[10^{-8} erg cm^{-2} s^{-1}]	2–30	2.2±0.3	1.5±0.3	1.9±0.2
	30–400	2.1±0.7	$3.7^{+8.1}_{-3.4}$ $\times10^{-1}$	1.5±0.6
	2–400	4.3±0.7	1.9±0.7	3.5±0.6
Photon fluence	2–10	15.1±3.2	10.0±3.0	24.9±4.4
[ph cm^{-2}]	2–30	22.6±3.3	12.8±3.0	35.2±4.5
	30–400	3.6±0.8	$5.2^{+6.8}_{-4.7}$ $\times10^{-1}$	4.4±1.1
	2–400	26.2±3.4	13.3±3.3	39.6±4.7
Energy fluecne	2–10	1.2±0.2	0.7±0.2	1.9±0.3
[10^{-7} erg cm^{-2}]	2–30	3.3±0.4	1.5±0.3	4.7±0.5
	30–400	3.1±0.1	$3.6^{+7.9}_{-3.4}$ $\times10^{-1}$	3.8±1.3
	2–400	6.4±1.1	1.8±0.7	8.5±1.4

Table 6.39: The spectral parameters of GRB030429.

Model	Parameters	region 1	region 2	all
PL	α	-1.68 ± 0.09	$-1.95^{+0.18}_{-0.23}$	-1.72 ± 0.08
	K_{15}[a]	2.30±0.28	1.41±0.36	2.02±0.22
	χ^2_ν/DOF	1.270/70	0.787/69	1.108/69
Cutoff PL	α	$-0.99^{+0.28}_{-0.24}$	$-1.19^{+1.44}_{-0.61}$	-1.13 ± 0.24
	E_{peak} [keV]	$39.1^{+11.6}_{-8.1}$	$16.5^{+19.8}_{-6.7}$	$35.0^{+11.8}_{-7.9}$
	K_{15}	$4.91^{+1.55}_{-1.08}$	$4.18^{+36.38}_{-2.38}$	$4.05^{+1.32}_{-0.90}$
	χ^2_ν/DOF	0.804/69	0.712/68	0.720/68

[a]Normalization at 15 keV in the unit of 10^{-2} photon cm^{-2} s^{-1} keV^{-1}

6.15 GRB030528

The trigger for this event came from the FREGATE instruments in 32–400 keV energy band, on 28 May 2003 at 13:03:02.83 UT [110]. The WXM flight location was distributed to the GCN at 37 seconds after the trigger. The ground localization by SXC was reported to the GCN at 107 minutes after the trigger. The SXC position was expressed as a 90% confidence circle in a radius of $2'$ with a center of (R.A., Dec.) $= (17^{\rm h}04^{\rm m}02^{\rm s}, -22°38'59'')$ (J2000).

The afterglow was detected in X-ray and infrared, but not in optical band. The status of the afterglow search is summarized in table 6.40. The earliest optical observation was reported in 2.5 minutes after the trigger by Torii at RIKEN (GCN 2252). The Chandra X-ray observation was performed at 5 days after the trigger. Four X-ray afterglow candidates were reported within the SXC error circle (GCN 2269). Greiner et al. (GCN 2271) searched in the near infrared bands of these X-ray sources, and found that only the Chandra source #1 showed the decay in the magnitude. The second epoch of the Chandra X-ray observation confirmed the source #1 was indeed the afterglow of GRB030528 (GCN 2279).

6.15.1 Light curve

As seen in figure 6.37, the light curves show the strong hard-to-soft evolution during the burst. The duration of the burst is $\sim$ 100 seconds in the lower energy bands. On the other hand, in the γ-ray energy band (32-400 keV), the duration is $\sim$ 20 seconds.

The additional peak is seen around 250 seconds after the trigger. Since this peak was not possible to be localized by WXM, we can not confirm whether this peak is originated to this burst or not.

6.15.2 Spectrum

Due to the problem of the primary ground station, the several data were not properly downlinked. There were gaps in various data. For the WXM, the photon data (TAG data) is not possible to use in the analysis. The PHA data is only available every 10 seconds (a half of the data was missing). We use PHA data and multiply the constant factor in the spectral model. Because of this incomplete data downlink problem, it is difficult to perform the time-resolved spectral analysis.

The X-ray to γ-ray fluence ratio of 1.1 qualifies this event as an X-ray flash. However, it is fair to classify this event as the border of an X-ray flash and an X-ray-rich GRB. The

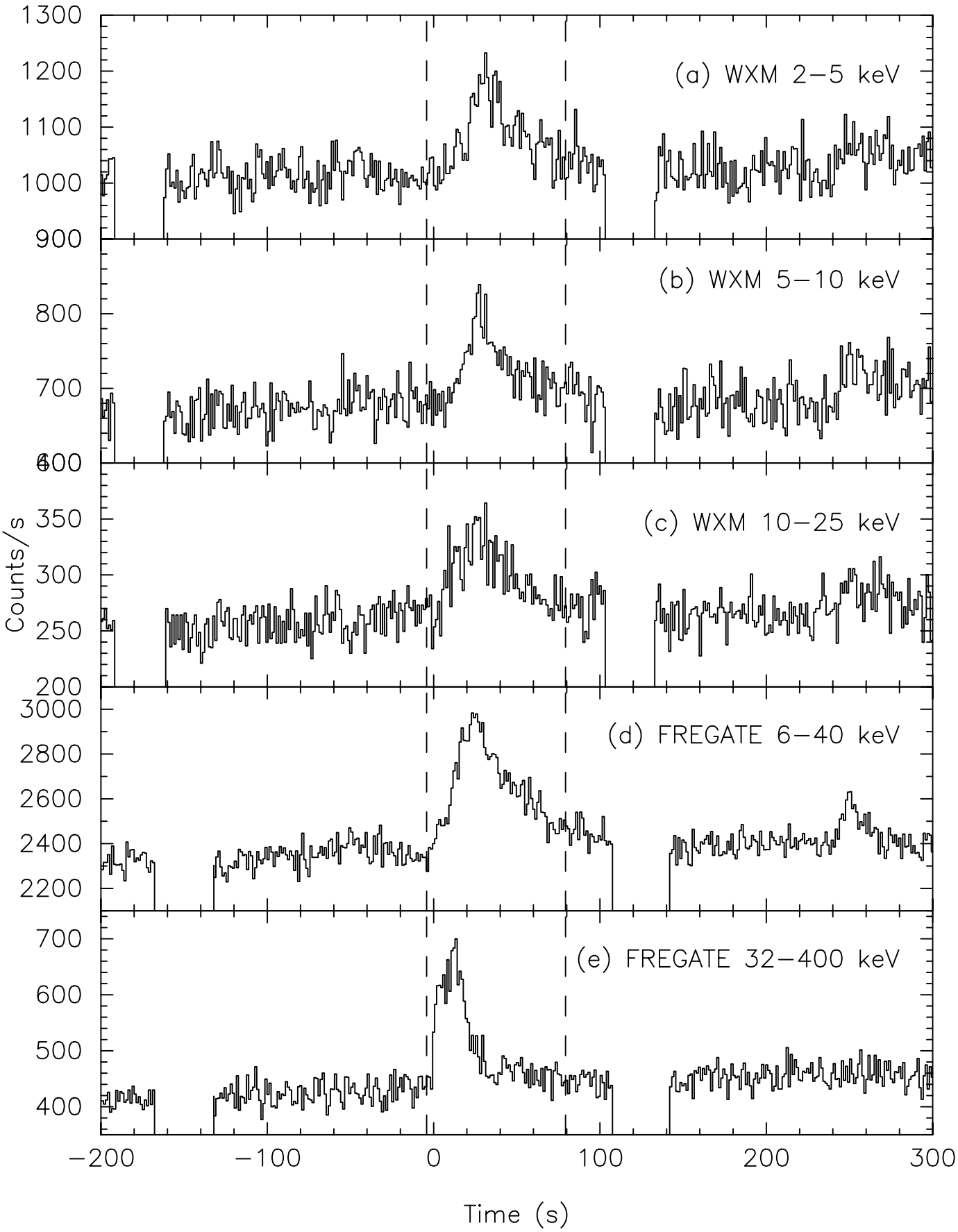

Figure 6.37: The energy resolved light curve of GRB030528 at 1.23 s time bin. The dotted lines correspond to the foreground spectral region. There were data gaps due to the uncomplete downlink in several places.

$E_{\rm peak}$ energy $\sim$ 30 keV is the good evidence that this event is in the border of these two GRB classifications. The time-averaged spectrum is well fitted in the Band function (see table 6.42).

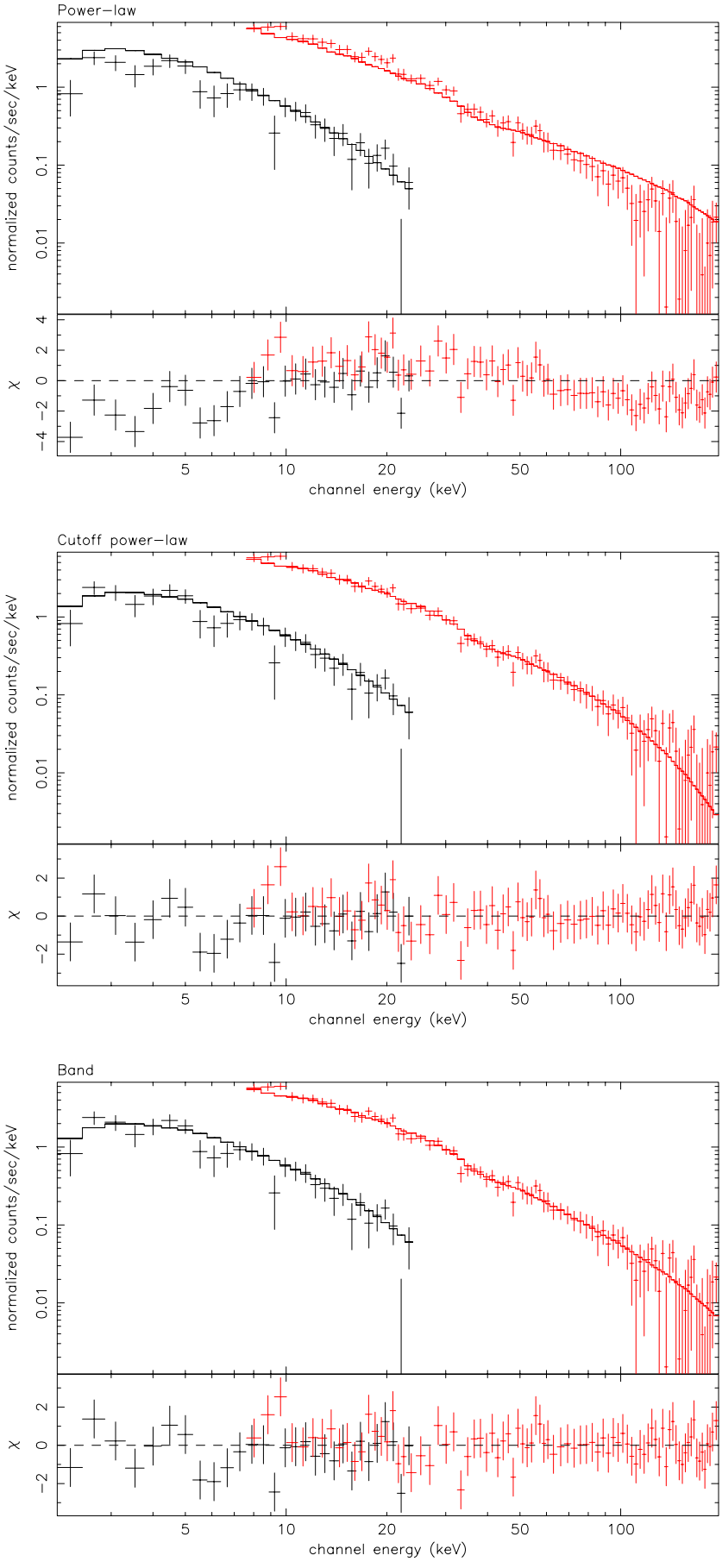

Figure 6.38: The WXM and FREGATE spectra of GRB030528. The model spectrum is the power-law model, the cutoff power-law model and the Band function from top to bottom.

Table 6.40: The afterglow search for GRB030528

Time[a]	Telescope & Instruments	OT	Lim. Mag.[b]	GCN
37 seconds	HETE flight location			
1.78 hours	HETE SXC ground loc.			
105 seconds 148 seconds	0.2 m telescope 0.25 m telescope (RIKEN)	N	 $\sim$ 15.8 mag.	(#2253) Torii
252 seconds	25 cm telescope Kyoto U.	N	$\sim$ 16 mag.	(#2252) Uemura et al.
2.3 hours	1.01 m telescope (R) Bisei Observatory	N	$\sim$ 18.7	(#2257) Ayani et al.
0.5 days	unfil. 0.72 m TNT telescope Astro. Obs. of Collurania[c]	N	$\sim$ 20.5	(#2258) Valentini et al.
4.97 days -5.30 days	Chandra X-ray Obs.	Y[d]		(#2269) Butler et al.
4.78 days	VLA (8.46 GHz)	N	$\sim$350μJy	(#2270) Frail et al.
0.66 days 1.66 days 2.63 days	near-IR NTT[e] SOFI camera La Silla Obs.[f]	Y (Ks)	Chandra src.#1	(#2271) Greiner et al.
6.74 days	MDM[g] 1.3 m telescope (I)	N[h]		(#2273) Mirabal et al.
4.81 days	near-IR (Ks) WIRC camera Palomar 5 m telescope	N[i]		(#2275) Bogosavljevic et al.
10.8 days	Chandra X-ray Obs. (2nd)	Y	Chandra src.#1	(#2279) Butler et al.

[a] Time after the trigger

[b] Limiting magnitude

[c] Teramo, Italy

[d] Chandra src. within the SXC error region:

#	Chandra Name	RA	DEC	dR(s)	dD(")	Cts
1	CXOU J170400.3-223710	17 4 0.31	-22 37 9.99	0.053	0.91	39
4	CXOU J170348.4-223826	17 3 48.39	-22 38 25.93	0.054	0.92	30
9	CXOU J170400.1-223548	17 4 0.11	-22 35 48.10	0.053	0.92	11
10	CXOU J170354.0-223654	17 3 53.95	-22 36 53.67	0.054	0.93	9

[e] The ESO New Technology Telescope, 3.58 m

[f] La Silla, Chile

[g] Tucson, AZ

[h] No Chandra src.#1 in I band image

[i] No Chandra src.#1 in Ks band image

Table 6.41: The fluxes and fluences of GRB030528. The spectral model is the Band function.

	energy range [keV]	all
Duration [sec.]		83.6
Photon flux	2–10	4.6±0.5
[ph cm^{-2} s^{-1}]	2–30	6.1±0.5
	30–400	(6.4±0.4) $\times 10^{-1}$
	2–400	6.8±0.5
Energy flux	2–10	3.3±0.3
[10^{-8} erg cm^{-2} s^{-1}]	2–30	7.5±0.3
	30–400	6.7±0.9
	2–400	14.2±0.9
Photon fluence	2–10	38.4±3.9
[10 ph cm^{-2}]	2–30	51.2±4.0
	30–400	5.4±0.3
	2–400	56.7±4.0
Energy fluecne	2–10	2.8±0.2
[10^{-6} erg cm^{-2}]	2–30	6.3±0.3
	30–400	5.6±0.7
	2–400	11.9±0.8

Table 6.42: The spectral parameters of GRB030528.

Model	Parameters	
PL	α	-1.87 ± 0.03
	K_{15}[a]	$8.62\pm0.30 \times 10^{-2}$
	C (WXM)	0.5 (fixed)
	χ^2_ν/DOF	1.946/111
Cutoff PL	α	-1.39 ± 0.10
	E_{peak} [keV]	$34.95^{+3.68}_{-3.10}$
	K_{15}	$1.30\pm0.10 \times 10^{-1}$
	C (WXM)	0.5 (fixed)
	χ^2_ν/DOF	0.835/110
Band	α	$-1.33^{+0.15}_{-0.12}$
	β	$-2.65^{+0.29}_{-0.98}$
	E_{peak} [keV]	$31.84^{+4.67}_{-4.97}$
	K_{15}	$1.39^{+0.24}_{-0.15} \times 10^{-1}$
	C (WXM)	0.5 (fixed)
	χ^2_ν/DOF	0.809/109

[a]Normalization at 15 keV in the unit of photon cm^{-2} s^{-1} keV^{-1}

[b]Constant parameter of WXM. The constant parameter of FREGATE is fixed to 1.

6.16 GRB030723

FREGATE, WXM and SXC observed the γ-ray burst on 23 July 2003 at 06:28:17.45 UTC [66]. The burst triggered on the WXM 2–25 keV band. The correct flight location was send 42 seconds after the trigger. The 90% confidence circle of the WXM position based on the ground analysis was centered at (R.A., Dec.) $= (21^{\rm h}48^{\rm m}52^{\rm s}, -27^\circ41'16'')$ (J2000) with $9.4'$ radius. The SXC localization was expressed as the center of (R.A., Dec.) $= (21^{\rm h}49^{\rm m}27.4^{\rm s}, -27^\circ42'01'')$ (J2000) with $2'$ radius in the 90% confidence circle.

The optical and infrared afterglow was found in 21.3 and 18.7 magnitude respectively at 1.1 days after the trigger. The temporal behavior of the optical afterglow showed the different decay slope from -1 to -2 around 30–50 hours after the burst (GCN 2336). The spectroscopic observation was performed by VLT. There were no absorption lines and a Lyman-α Forest in the spectrum. This result suggests a redshift of this burst was less than 2.1.

6.16.1 Light curve

The duration of the burst is $\sim$ 20 seconds. The burst signal is not visible in the WXM 17–25 keV band. The duration of the burst could be much longer at the lower energy band (e.g. 2–5 keV). Because of the low signal to noise ratio, it is hard to see the temporal structure of the burst.

6.16.2 Spectrum

The X-ray to γ-ray fluence ratio of 0.9 qualifies this event as an X-ray-rich GRB. However, it is possible to classify this event as the border of an X-ray flash and an X-ray-rich GRB. The power-law is the acceptable model. If we tried the cutoff power-law model, $\Delta\chi^2 = 1.43$ in one additional degree of freedom and this is not a significant improvement in a χ^2. The photon index is ~ -2 and it is difficult to show that the photon index is steeper than -2 in a high significance. Unfortunately, it is not possible to constrain the $E_{\rm peak}$ energy of this burst applying the *constrained* Band function.

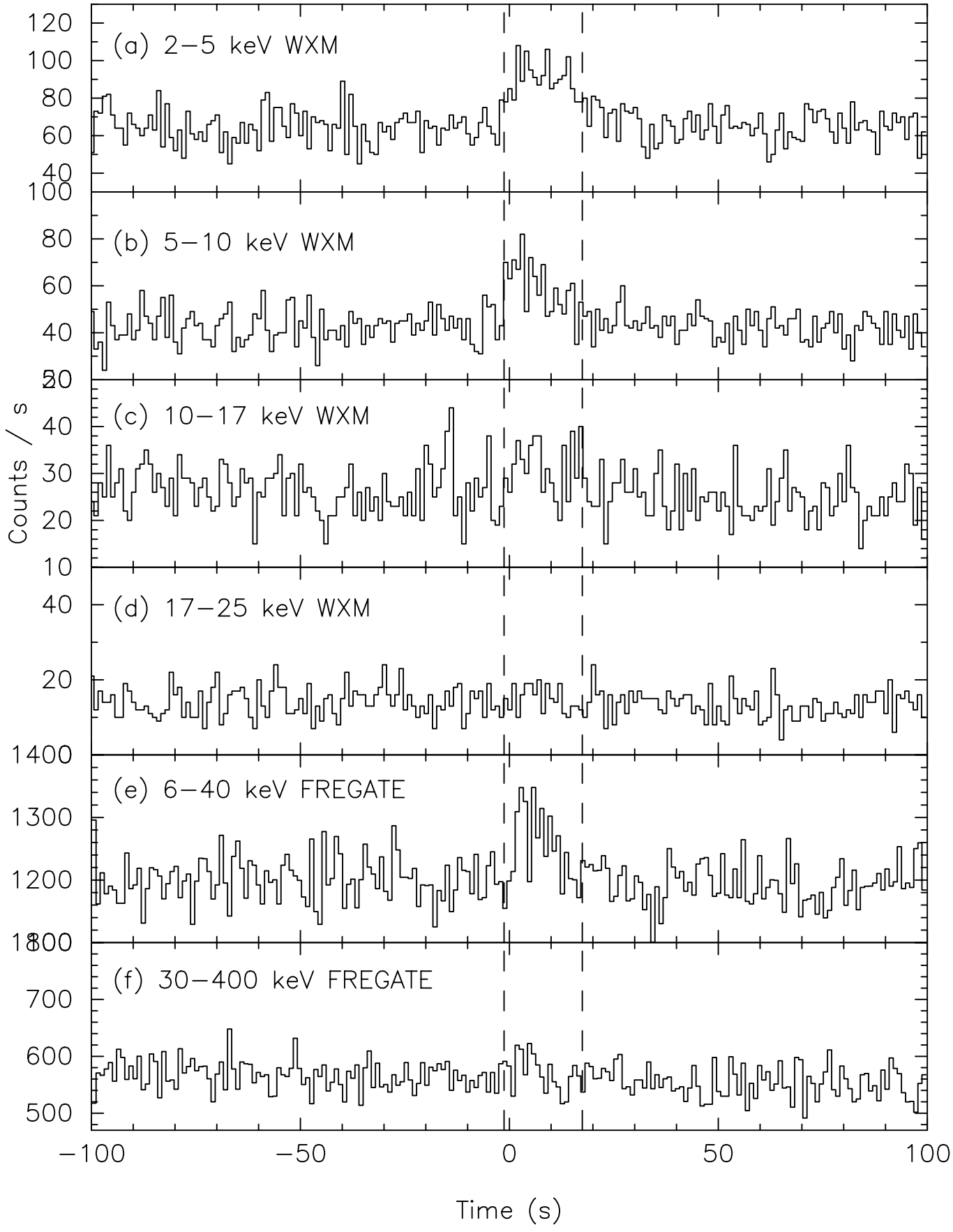

Figure 6.39: The energy resolved light curves of GRB030723 at 1 s time bin. The dotted lines correspond to the foreground spectral region.

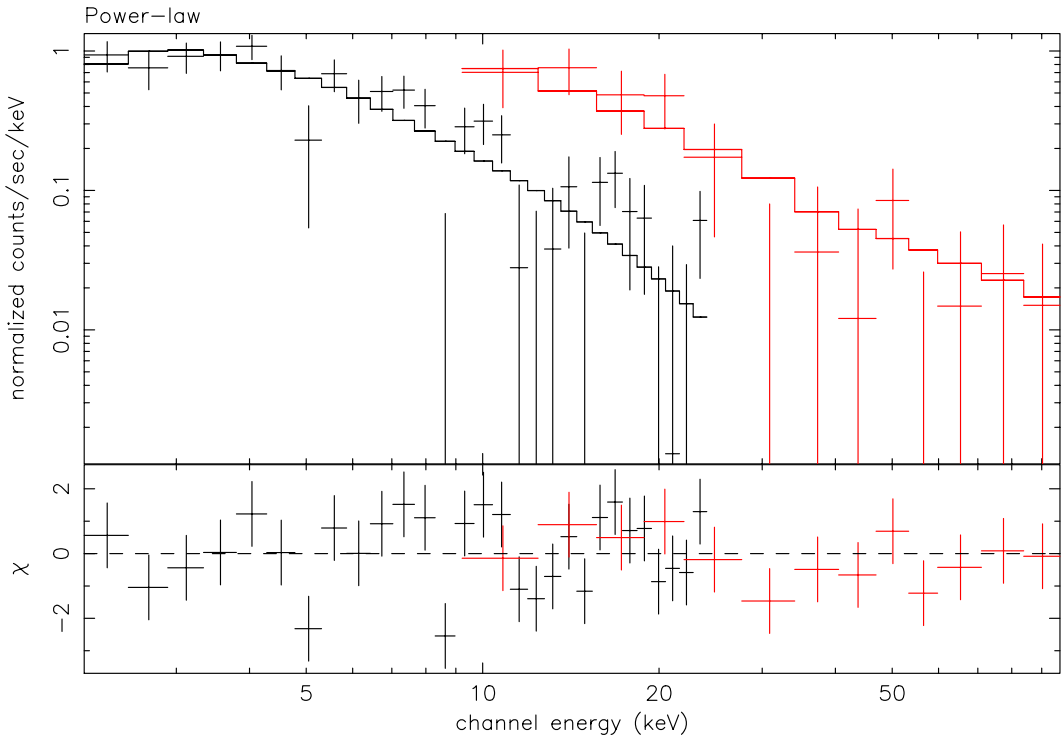

Figure 6.40: The WXM and FREGATE spectrum of GRB030723. The spectral model is the power-law.

Table 6.43: The afterglow search for GRB030723

Time[a]	Telescope & Instruments	OT	Lim. Mag.[b]	GCN
41.6 s	S/C position			
2.90 hours	HETE GCN position notice (WXM)			
7.49 hours	HETE GCN position notice (SXC)			
47 s	ROTSE-IIIb McDonald Ovservatory[c]	N	18∼19 (R)	Smith et al. (#2318, #2338)
1.2 hours 3.3 hours	KAIT[d]	N	19–20 (R)	Chornock et al. (#2315)
7.6 hours	0.6 m Telescope (MOA) Mt. John Obs.[e]	N	DSS lim.	de Ugarte et al. (#2314)
12.9 hours	0.3 m Telescope (unfil.) Bronberg observatory[f]	N	CR=20	Monard et al. (#2312)
19.7/21.8 hours 1.02 days	SMARTS Consortium 1.3 m Tel. (R) Cerro Tololo inter-American Obs.[g]	N	DSS lim.	Bond et al. (#2316)
1.04 days 2.04 days	1.5 m Telescope La Silla Observatory[h]	N	24 (R)	Jensen et al. (#2321)
1.14 days 2.14 days	1.5 m (R)& 5 m (Ks) Telescope Palomar Observatory[i]	Y[j]	21.3/ 22.4 (R) 18.65 / no detection (Ks)	Fox et al. (#2323)
1.03 days 1.05 days	LDSS2 6.5 m Magellan Tel. Las Campanas Obs.[k]	Y	R=21.13±0.05	Dullighan et al. (#2326)
2.99 days	VLT FORS1/UT1, spectrum 3650–7500 Å	Y	z<2.1	Fynbo et al. (#2327)
2.14 days – 2.46 days	Chandra X-ray Obs.	Y[l]		Butler et al. (#2328)
2.15 days	SMARTS 1.3 m Tel. (re-analysis)	Y	R=21.0 (1.91 days) R=20.9 (1.02 days)	Bond et al. (#2329)
3.16 days	VLA (8.46 GHz)	N	180 mJy (3σ)	Soderberg et al. (#2330)
5.13 days	LDSS2 6.5 m Magellan Tel. Las Campanas Obs.	Y	24.2±0.3 (R)	Dullighan et al. (#2336)
10.9 days 14.0 days	VLT	Y	re-brightening 1 mag.	Fynbo et al. (#2345)
12.66 days – 13.67 days	Chandra X-ray Obs.	Y[m]		Butler et al. (#2347)

[a] Time after the trigger [b] Limiting magnitude

[c] Davis Mountains, Austin, TX

[d] Katzman Automatic Imaging Telescope (Lick Observatory, San Jose, CA)

[e] Lake Tekapo, New Zealand f Pretoria, South Africa

[g] La Serena, Chile h La Silla, Chile i San Diego, CA

[j] OT pos: R.A. 21:49:24.40, Dec. -27:42:47.4 (J2000) k Carro Las Campanas, Chile

[l] 3 X-ray sources:

#	Chandra Name	RA	DEC	Cts
1	CXOU J214924.4-274248	21 49 24.421	-27 42 48.00	78
3	CXOU J214926.9-274146	21 49 26.891	-27 41 45.92	19
4	CXOU J214928.7-274211	21 49 28.724	-27 42 11.47	16

[m] 0.5–8.0 keV flux in the power-law model with the index of 1.9 is $(2.2 \pm 0.3) \times 10^{-14}$ erg cm^{-2} s^{-1} and $(3.5 \pm 0.5) \times 10^{-15}$ erg cm^{-2} s^{-1} for the 1st epoch and the 2nd epoch respectively.

Table 6.44: The fluxes and fluences of GRB030723. The spectral model is the power-law model.

energy range [keV]		
Duration [sec.]		18.7
Photon flux	2–10	1.1±0.2
[ph cm^{-2} s^{-1}]	2–30	1.3±0.2
	30–400	(1.1±0.5) $\times 10^{-1}$
	2–400	1.5±0.2
Energy flux	2–10	0.7±0.1
[10^{-8} erg cm^{-2} s^{-1}]	2–30	1.3±0.2
	30–400	1.5±0.8
	2–400	2.8±0.9
Photon fluence	2–10	21.2±2.9
[ph cm^{-2}]	2–30	25.2±3.1
	30–400	2.0±0.8
	2–400	27.2±3.2
Energy fluecne	2–10	1.4±0.2
[10^{-7} erg cm^{-2}]	2–30	2.4±0.3
	30–400	2.8 .6±1.4
	2–400	5.2±1.7

Table 6.45: The spectral parameters of GRB030723.

Model	Parameters	
PL	α	$-1.93^{+0.15}_{-0.17}$
	K_{15}[a]	(1.39±0.28) $\times$ 10^{-2}
	χ^2_ν/DOF	1.117/40

[a]Normalization at 15 keV in the unit of photon cm^{-2} s^{-1} keV^{-1}

6.17 GRB030823

The trigger for this event came from the FREGATE instrument in the 6–80 keV energy band, on 23 August 2003 at 08:52:40.64 UTC [94]. Since the WXM Y-location was extreme edge of the FOV, the flight localization was not send to the ground. The WXM localization could be expressed as a 90% confidence rectangle, whose center was at (R.A., Dec.) = $(21^{\rm h}30^{\rm m}46^{\rm s}, 21°55'43'')$ (J2000), and whose corners lay at (R.A., Dec.) =$(21^{\rm h}31^{\rm m}02.6^{\rm s}, 21°37'55'')$, $(21^{\rm h}30^{\rm m}21.1^{\rm s}, 21°37'23'')$, $(21^{\rm h}30^{\rm m}29.0^{\rm s}, 22°13'30'')$ and $(21^{\rm h}31^{\rm m}10.6^{\rm s}, 22°14'02'')$ (J2000). The SXC Y-camera detected the burst, but the X-camera did not. The joint WXM and SXC location of the burst could be expressed at a 90% confidence rectangle, whose center was at (R.A., Dec.) = $(21^{\rm h}30^{\rm m}47^{\rm s}, 21°59'46'')$ (J2000), and whose corners lay at (R.A., Dec.) = $(21^{\rm h}30^{\rm m}26.9^{\rm s}, 22°01'44'')$, $(21^{\rm h}30^{\rm m}25.9^{\rm s}, 21°57'14'')$, $(21^{\rm h}31^{\rm m}07.4^{\rm s}, 22°02'17'')$, $(21^{\rm h}31^{\rm m}06.5^{\rm s}, 21°57'50'')$ (J2000).

Although there were several deep optical investigations for the transient source, no afterglow has been found for this burst (table 6.46).

6.17.1 Light curve

The signal is clearly visible in the FREGATE 6–40 keV band, but not in the 32–400 keV band. The rising background counts were due to the high energy particles (this event occurred $\sim$ 20 minutes before the SAA). The burst might be started $\sim$ 25 seconds before the trigger time, however, the particle background was also starting to increase around that period, and difficult to say about the starting time of the burst. The burst signal is seen in all WXM energy bands. The low signal to noise ratio in the WXM data was due to the large incident angle of the event ($\sim 35°$). The temporal structure of this burst is characterized in a large single pulse with the duration of $\sim$ 50 seconds.

6.17.2 Spectrum

The X-ray to γ-ray fluence ratio of 1.8 qualifies this burst as an X-ray flash. Since there is a large improvement of χ^2 in the cutoff power-law model against the simple power-law model ($\Delta\chi^2 = 35.23$ with 1 degree of freedom), the cutoff power-law model is the best representative model for the time-average spectrum. The $E_{\rm peak}$ energy is 26.6 keV.

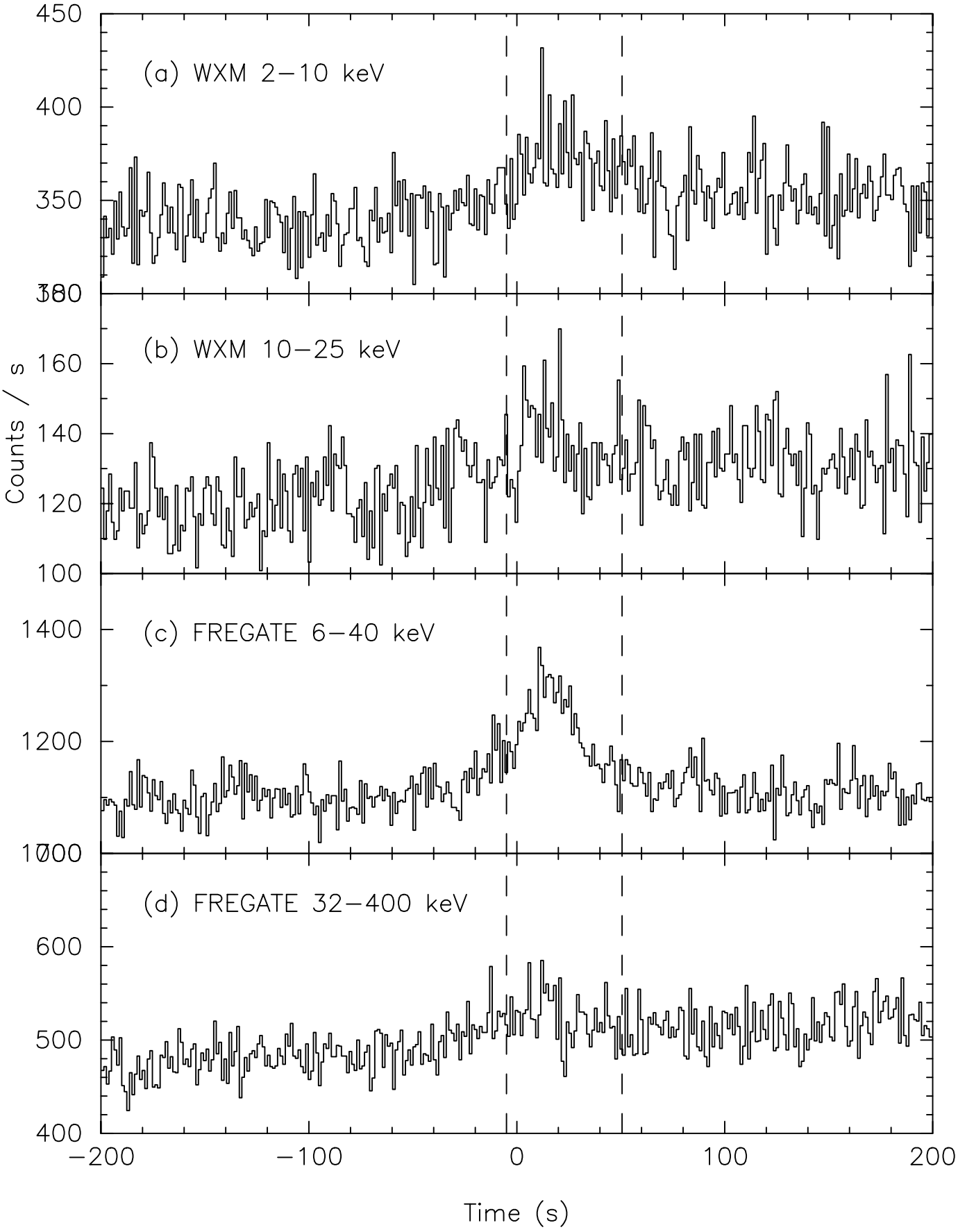

Figure 6.41: The energy resolved light curves of GRB030823 at 1.23 s time bin. The dotted lines represent the foreground region of the spectrum.

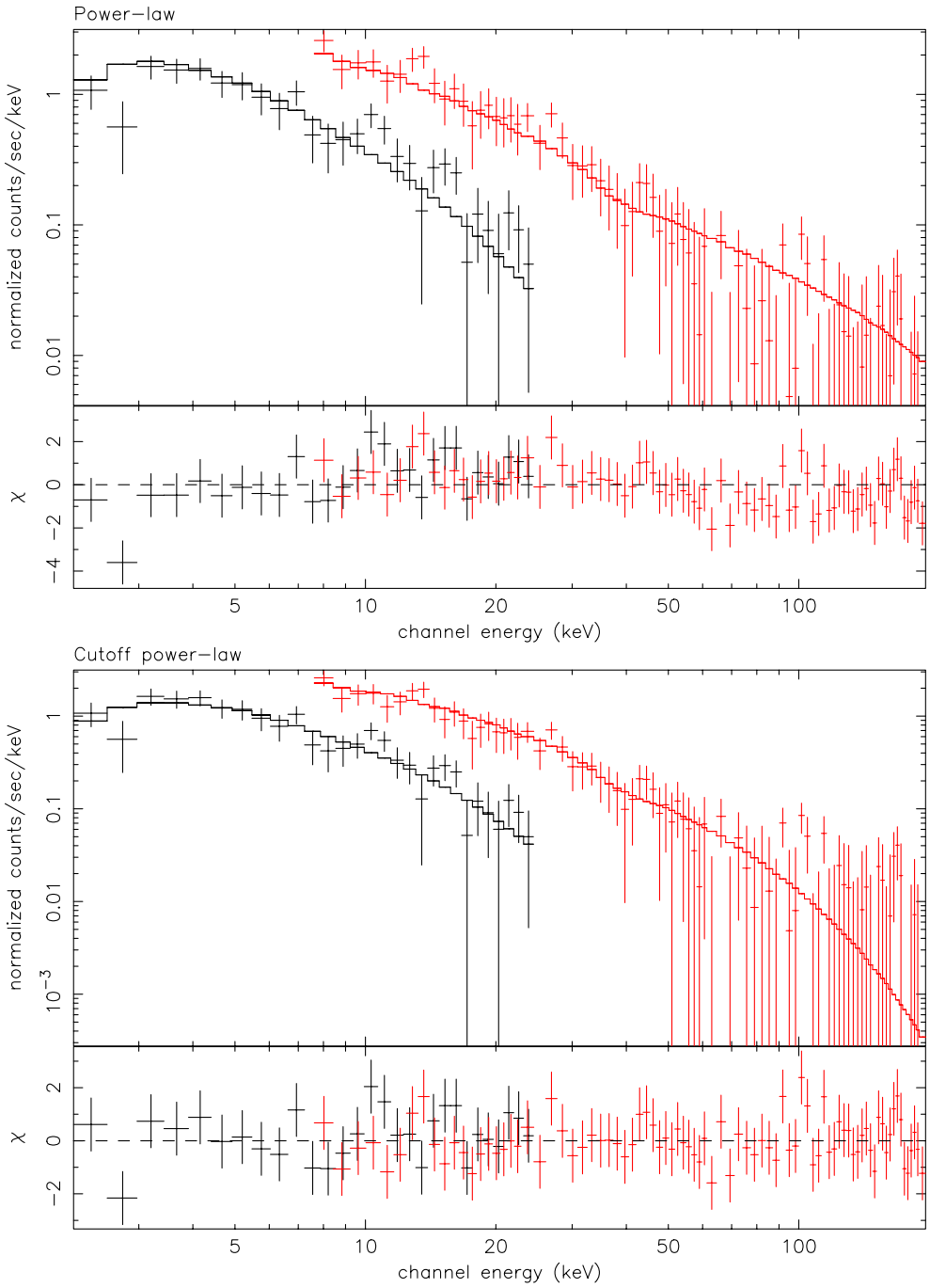

Figure 6.42: The WXM and FREGATE spectrum of GRB030823. The spectral model is the power-law (top) and the cutoff power-law (bottom).

Table 6.46: The afterglow search for GRB030823

Time[a]	Telescope & Instruments	OT	Lim. Mag.[b]	GCN
2.28 hours	WXM ground analysis			
3.19 hours	SXC ground analysis			
1.82 hours	30cm Telescope (un fil.) Titech	N	$\sim$ 16.5	(#2362) Suzuki et al.
2.28 hours	RAPTOR	N	$\sim$ 16.0	(#2361) Wren et al.
3.50 hours	1.0m Telescope (PI1300) Lulin Obs.	N	18.8 (R)	(#2360) Huang et al.
6.86 hours	1.5m Telescope Mavidanak high-altitude Obs.(UBAI) AT-64 and K-380 telescopes Crimean Astrophysical Obs.(CrAO)	N	note[c]	(#2366) Ibrahimov et al.
0.78 days 1.86 days	5m Hale Telescope Mt. Palomar Obs.	N	R>22.5	(#2365) Fox et al.
1.24 days	0.60 m Telescope (Rc) Ouda Obs.	N	20.5 (Rc)	(#2370) Imada et al.

[a]Time after the trigger

[b]Limiting magnitude

[c]Limiting magnitude of various observations are following:

#	Mid. Time (UT)	Telescope	Exposure	Limiting magnitude (R)
1	23.6651	1.5m (UBAI)	300s	19.5
2	23.7805	1.5m (UBAI)	300s	20.5
3	23.7826	AT-64 (CrAO)	7x180s	20.5
4	23.8131	K-380 (CrAO)	6x300s	19.0

Table 6.47: The fluxes and fluences of GRB030823. The spectral model is the cutoff power-law model.

energy range [keV]		
Duration [sec.]		55.6
Photon flux	2–10	2.6±0.3
[ph cm^{-2} s^{-1}]	2–30	3.4±0.3
	30–400	(2.8±0.6) $\times 10^{-1}$
	2–400	3.7±0.3
Energy flux	2–10	1.9±0.2
[10^{-8} erg cm^{-2} s^{-1}]	2–30	4.1±0.3
	30–400	2.3±0.7
	2–400	6.4±0.8
Photon fluence	2–10	14.5±1.8
[10 ph cm^{-2}]	2–30	19.1±1.8
	30–400	1.5±0.3
	2–400	20.7±1.8
Energy fluecne	2–10	1.1±0.1
[10^{-6} erg cm^{-2}]	2–30	2.3±0.2
	30–400	1.3±0.4
	2–400	3.6±0.5

Table 6.48: The spectral parameters of GRB030823.

Model	Parameters	
PL	α	-1.82 ± 0.06
	K_{15}[a]	(4.41±0.31) $\times 10^{-2}$
	χ^2_ν/DOF	1.019/111
Cutoff PL	α	$-1.31^{+0.20}_{-0.18}$
	E_{peak} [keV]	$26.57^{+7.45}_{-5.03}$
	K_{15}	$8.26^{+2.34}_{-1.59} \times 10^{-2}$
	χ^2_ν/DOF	0.708/110

[a]Normalization at 15 keV in the unit of photon cm^{-2} s^{-1} keV^{-1}

6.18 GRB030824

The FREGATE instrument detected the GRB in the 6–40 keV band, on 24 August 2003 at 16:47:35.10 UTC [26]. The WXM flight location was correct, however, it was not distributed to the GCN due to the low signal-to-noise ratio and the burst location at the edge of the FOV. The WXM location based on the ground analysis could be expressed as a 90% confidence circle, whose radius was 11.2′ and whose center was at: (R.A., Dec.) = ($00^{\rm h}05^{\rm m}02^{\rm s}, +19°55'37''$) (J2000).

The afterglow search is summarized at table 6.49. Although there was the optical observation starting 76 minutes after the burst, no afterglow has been found. There was an observation $\sim$ 1 month after the burst in searching for the supernova signal of this burst. Two transients sources were reported in GCN, however, the nature of these sources are still unclear (very red objects, very faint in R band but clearly visible in i′ band, GCN 2418).

6.18.1 Light curve

The burst signal is seen in the soft energy bands of both WXM and FREGATE (figure 6.43). The several spikes are observed in the FREGATE 6–40 keV band, whereas they are hard to see in the WXM 2–10 keV band due to the low signal to noise ratio. This low signal to noise ratio in the WXM data is mainly due to the large incident angle of the burst ($\sim 40°$). Almost no detection of the photons in the WXM 10–25 keV indicate that this burst is very soft. The duration of the burst is $\sim$ 15 seconds.

6.18.2 Spectrum

The time-average spectrum is well reprensented in the simple power-law model with the photon index of -2.1. The X-ray to γ-ray fluence ratio of 1.5 qualifies this event as an X-ray flash.

The the photon index steeper than -2 is rejected in a high significance if we use the FREGATE data only ($> 99.9\%$ confidence level). Thus, this burst is also a good event to apply the *constrained* Band function to calculate the upper limit of $E_{\rm peak}$. The posterior probability density distribution as a function of $E_{\rm peak}$ is shown in figure 6.45. The highest probability is in 6.1 keV and the 99.7% upper limit is 8.1 keV. The $E_{\rm peak}$ energy $\sim$ 10 keV is a typical characteristics of X-ray flashes.

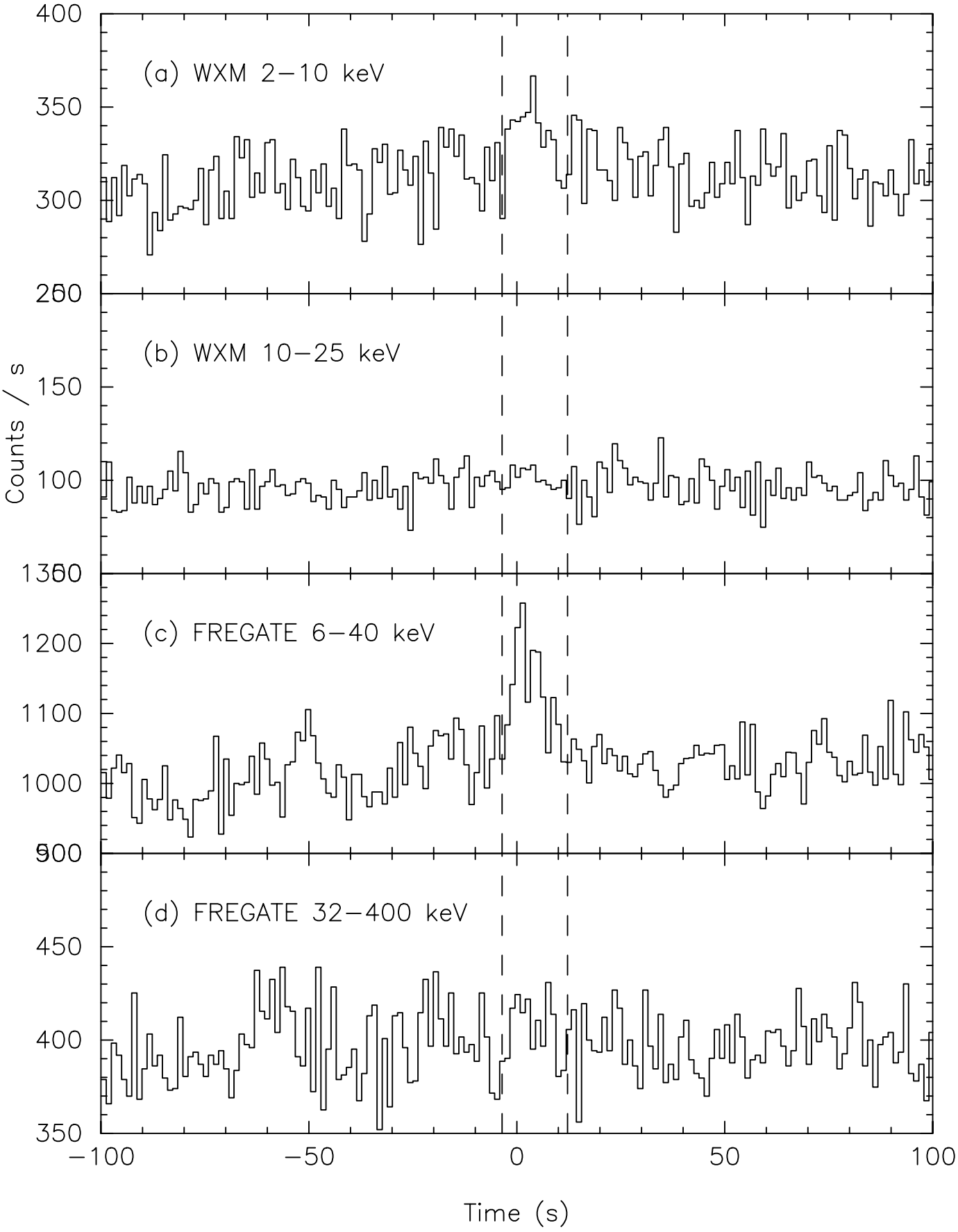

Figure 6.43: The energy resolved light curves of GRB030824 in 1.23 s time bin.

Table 6.49: The afterglow search for GRB030824

Time[a]	Telescope & Instruments	OT	Lim. Mag.[b]	GCN
1.0 hours	WXM ground analysis			
2.43 hours	WXM ground analysis (2nd)			
-	0.6m Telescope Morehead Obs.[d]	Y→N[c]		(#2363) Moran et al.
76-153 min.	1.05m Schumidt Telescope Kiso Obs.	N	$\sim$ 17 (R)	(#2407) Urata et al.
3.87 hours	0.4m Telescope (Rc) Nyrola Obs.[e]	N	17.5-19.0 (Rc)	(#2379) Oksanen et al.
4.52 hours	1.5m Telescope Maidanak Obs.[f]	N	$\sim$ 19.5 (R)	(#2368) Ibrahimov et al.
0.55 days 1.72 days	5m Hale Telescope Palomar Obs.	N	22.5 (R)	(#2364, #2369) Fox et al.
27.63 days	3.6m CFHT Megaprime[g] (i′) Mt. Mauna Kea, Hawaii	2 src.[h]		(#2406, #2418) Klotz et al.

[a] Time after the trigger

[b] Limiting magnitude

[c] The suspicios object was reported in R$\sim$17, however, this transient was an instrumental noise (GCN Circ.#2373).

[d] Chapel Hill, NC

[e] Jyvaskyla, Finlnad

[f] Mt. Maidanak, the Republic of Uzbekistan (altitude, 2000m)

[g] Canada-France-Hawaii Telescope, $1^\circ \times 1^\circ$ FOV with $0.7''$ seeing.

[h] 2 new sources are reported;

```
Object 1: 0h05m12.30s, +20d06'29.4" +-0.2", i'=22.7+-0.2;
(no host galaxy detected)
Object 2: 00h05m06.82s +20d05m00.4s +-0.4", i'=22.6+-0.4;
(offset from apparent host anonymous galaxy 0.56"W and 0.55"N,
host magnitude i' = 21.5+-0.2)
```

Table 6.50: The fluxes and fluences of GRB030824. The spectral model is the power-law model.

energy range [keV]		
Duration [sec.]		15.7
Photon flux	2–10	5.8±0.9
[ph cm^{-2} s^{-1}]	2–30	6.6±1.0
	30–400	(3.0±0.9) $\times 10^{-1}$
	2–400	6.9±1.0
Energy flux	2–10	3.6±0.5
[10^{-8} erg cm^{-2} s^{-1}]	2–30	5.7±0.7
	30–400	3.7±1.4
	2–400	9.4±1.6
Photon fluence	2–10	9.1±1.4
[10 ph cm^{-2}]	2–30	10.3±1.5
	30–400	4.6±1.4
	2–400	10.8±1.5
Energy fluecne	2–10	5.7±0.8
[10^{-7} erg cm^{-2}]	2–30	8.9±1.1
	30–400	5.8±2.1
	2–400	14.7±2.6

Table 6.51: The spectral parameters of GRB030824.

Model	Parameters	
PL	α	$-2.14^{+0.13}_{-0.14}$
	K_{15}[a]	(5.25±0.77) $\times 10^{-2}$
	χ^2_ν/DOF	0.813/53

[a]Normalization at 15 keV in the unit of photon cm^{-2} s^{-1} keV^{-1}

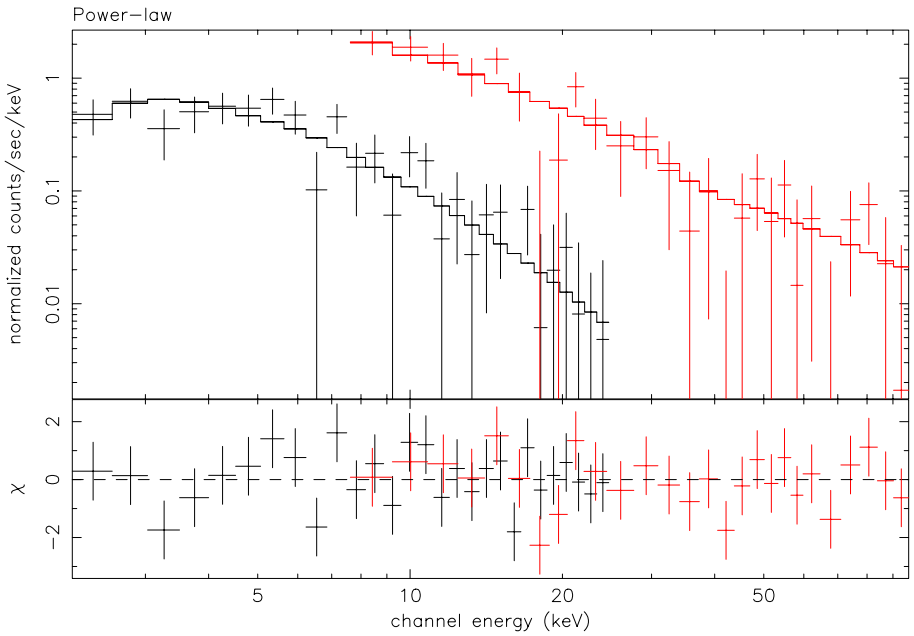

Figure 6.44: The WXM and FREGATE spectrum of GRB030824. The spectrum model is the power-law.

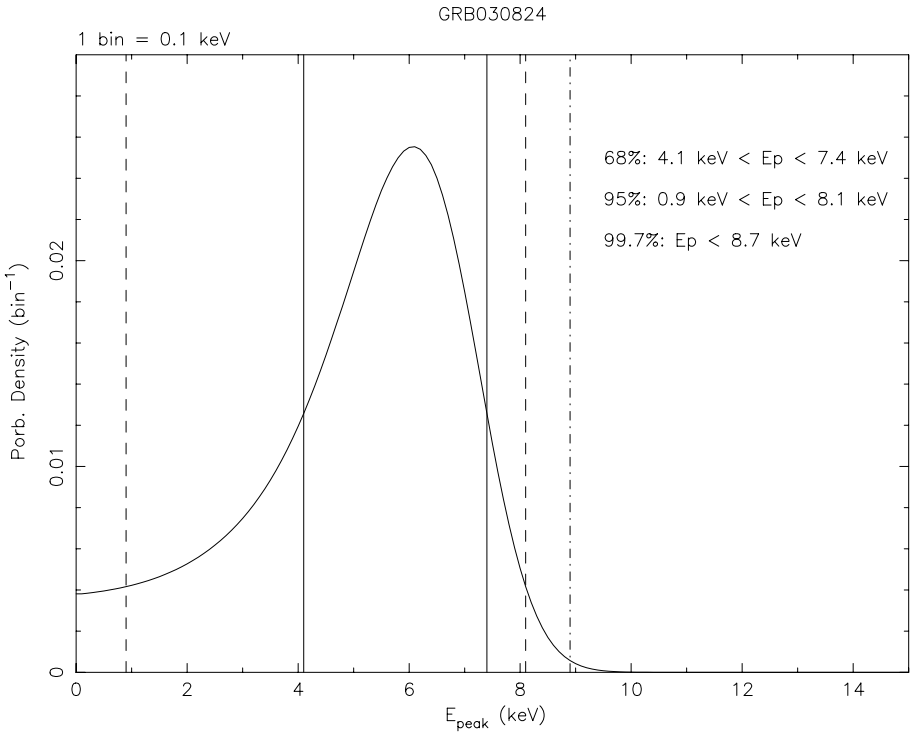

Figure 6.45: The posterior probability density distribution as a function of $E_{\rm peak}$. $E_{\rm pivot}$ is 8.1 keV. The 68% confidence range (solid line) of $E_{\rm peak}$ is 4.1 keV $< E_{\rm peak} <$ 7.4 keV. The 95% confidence range (dashed line) is 0.9 keV $< E_{\rm peak} <$ 8.1 keV. The 99.7% upper limit (dash-dotted line) of $E_{\rm peak}$ is 8.7 keV.

Chapter 7

Global characteristics of X-ray Flashes and X-ray-rich GRBs

We investigated the time-average spectral characteristics of the *HETE* GRB sample. The *HETE* GRB sample is selected to satisfy the following criteria: 1) the burst signal is seen in both WXM and FREGATE, and 2) both WXM and FREGATE data have good enough statistics to carry out the spectral analysis. 45 GRBs satisfy this criteria from January 2001 to September 2003. The summary status of the bursts, the best fit spectral parameters, the photon and energy flux/fluence, and 1-second peak flux in 50–300 keV are summarized in Appendix B. The light curves and the spectra of the bursts which are not shown in chapter 6 are shown in Appendix C.

7.1 The X-ray and γ-ray flux and fluence

The fluence ratio distribution between 2–30 keV ($S_{\rm X}$) and 30-400 keV (S_γ) is shown in figure 7.1. The definitions of X-ray flashes (XRFs), X-ray rich GRBs (XRRs), and hard GRBs are $\log(S_{\rm X}/S_\gamma) > 0$, $-0.5 < \log(S_{\rm X}/S_\gamma) \leq 0$, and $\log(S_{\rm X}/S_\gamma) \leq -0.5$ respectively. The boundaries between hard GRBs and XRRs, and XRRs and XRFs are in the dashed lines. The figure clearly shows that XRFs, XRRs, and hard GRBs form a single broad distribution. The number of bursts are 15, 20, and 10 for XRF, XRR, and hard GRB respectively. The small fraction of hard GRBs could be due to the selection effect that a very hard GRB does not produce signal in the WXM.

The scatter plot of 2–30 keV and 30–400 keV energy fluence is shown in figure 7.2. Each color corresponds to a GRB class (XRF: black, XRR: red, and hard GRB: blue). The different

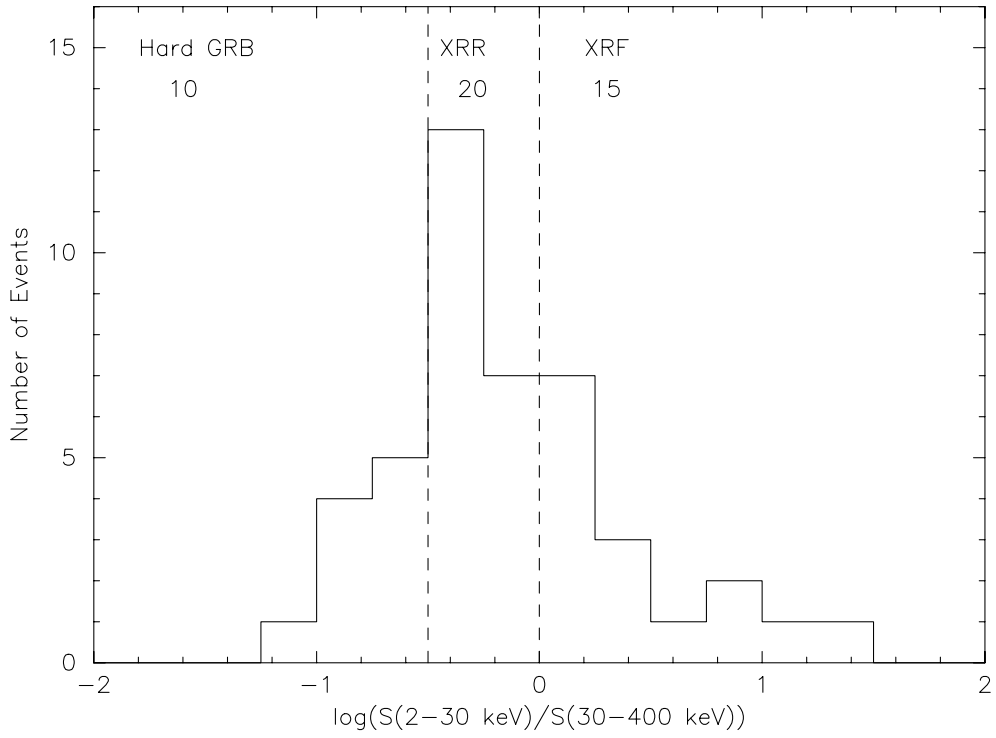

Figure 7.1: Distribution of the fluence ratio of 2–30 keV to 30–400 keV in the logarithmic scale. The dashed lines are the borders of hard GRB vs. XRR, and XRR vs. XRF.

markers represent the best fit spectral models (triangle: power-law model, circle: cutoff power-law model, star: Band function). The dotted line represents the border between hard GRBs and XRRs, and the dashed line is the border between XRRs and XRFs. As we can see in the figure 7.1, these three GRB classes seem to be a single phenomenon. There is a good positive correlation between 2–30 keV and 30–400 keV fluence. This implies that there is no GRB with a high X-ray fluence and a low γ-ray fluence, and vice versa.

The time-average flux of 2–30 keV and 30–400 keV are plotted in figure 7.3. These two values also have a good positive correlation. The 2–30 keV flux (F_{2-30}) and the 30–400 keV flux (F_{30-400}) can be expressed as $F_{30-400} \propto F_{2-30}^{1.1}$.

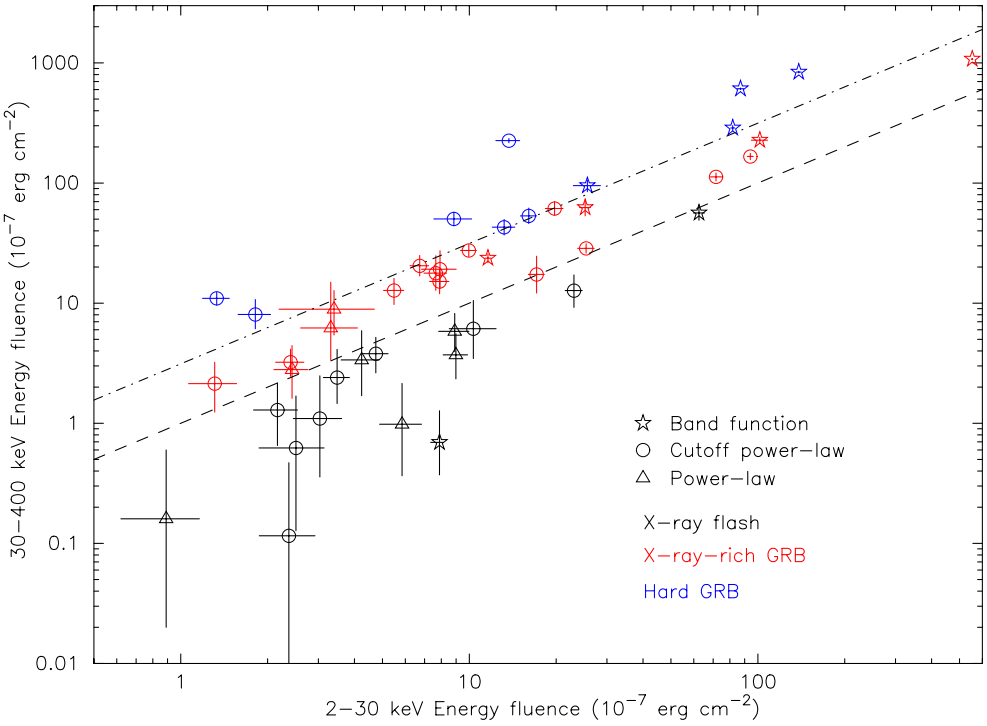

Figure 7.2: The scatter plot of the 2-30 keV and the 30-400 keV energy fluences.

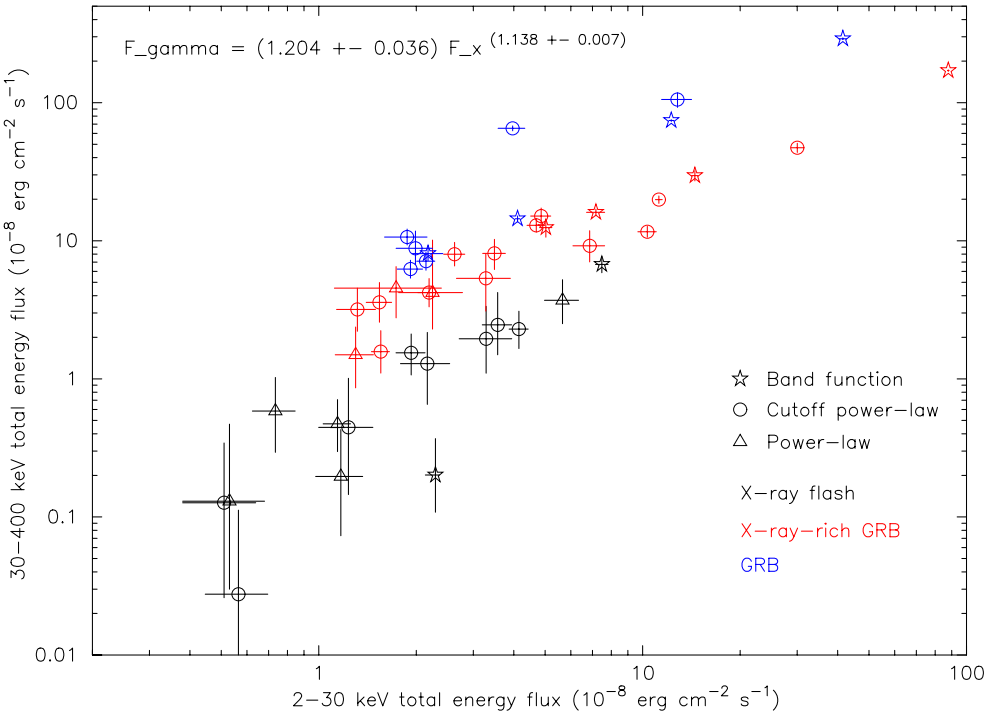

Figure 7.3: The time-average flux in 2-30 keV (F_{2-30}) and 30-400 keV (F_{30-400}). The correlation can be expressed as $F_{30-400} \propto F_{2-30}^{1.14}$.

7.2 The distribution of the Band parameters

Figure 7.4 shows the distribution of the low-energy photon index α. The bursts for which the Band function or the cutoff power-law model are required to represent their energy spectra are in this figure, but not included are the bursts whose spectra can be well represented by simple power-law models. This is due to the fact that the photon index of the simple power-law model could be fitting the high-energy photon index β in the Band function.

The low-energy photon index α is concentrated around -1 and similar to the BATSE α distribution (see figure 2.2). The small number of $\alpha > -0.5$ in the *HETE* sample, as compared with BATSE, could be due to two reasons: the first is the selection effect that our *HETE* sample might be lacking very hard GRBs, and second is that the BATSE α distribution is not the time-average but the time-resolved spectral fit result. Since GRB spectra show time evolution and have a harder spectrum around the peak of the light curve, the harder α distribution of BATSE sample might be due to the contribution of the spectra at the peak.

There is no difference in the α between GRB classes (figure 7.4 bottom). From this α distribution, we conclude that XRFs and XRRs have similar α values as hard GRBs.

Figure 7.5 shows the $E_{\rm peak}$ distribution. The events shown as left arrows are 99.7% upper limits for the $E_{\rm peak}$ derived by using the *constrained* Band function. As seen in this figure, $E_{\rm peak}$ shows a broader distribution than the BATSE sample, especially for the extension to the lower energy range. If we investigate with the GRB classes (figure 7.5 bottom), there is a clear separation between XRFs and XRRs around 30 keV. This is simply because of the fact that we are classifying the GRBs with 30 keV as a boundary. The $E_{\rm peak}$ distributions of the XRRs and the hard GRBs are quite similar.

The distribution of β is shown in figure 7.6. Because of the small number of GRBs with significantly constrained β, only the distribution for all the GRB classes are plotted. The distribution of β is similar to the BATSE GRBs (see figure 2.3).

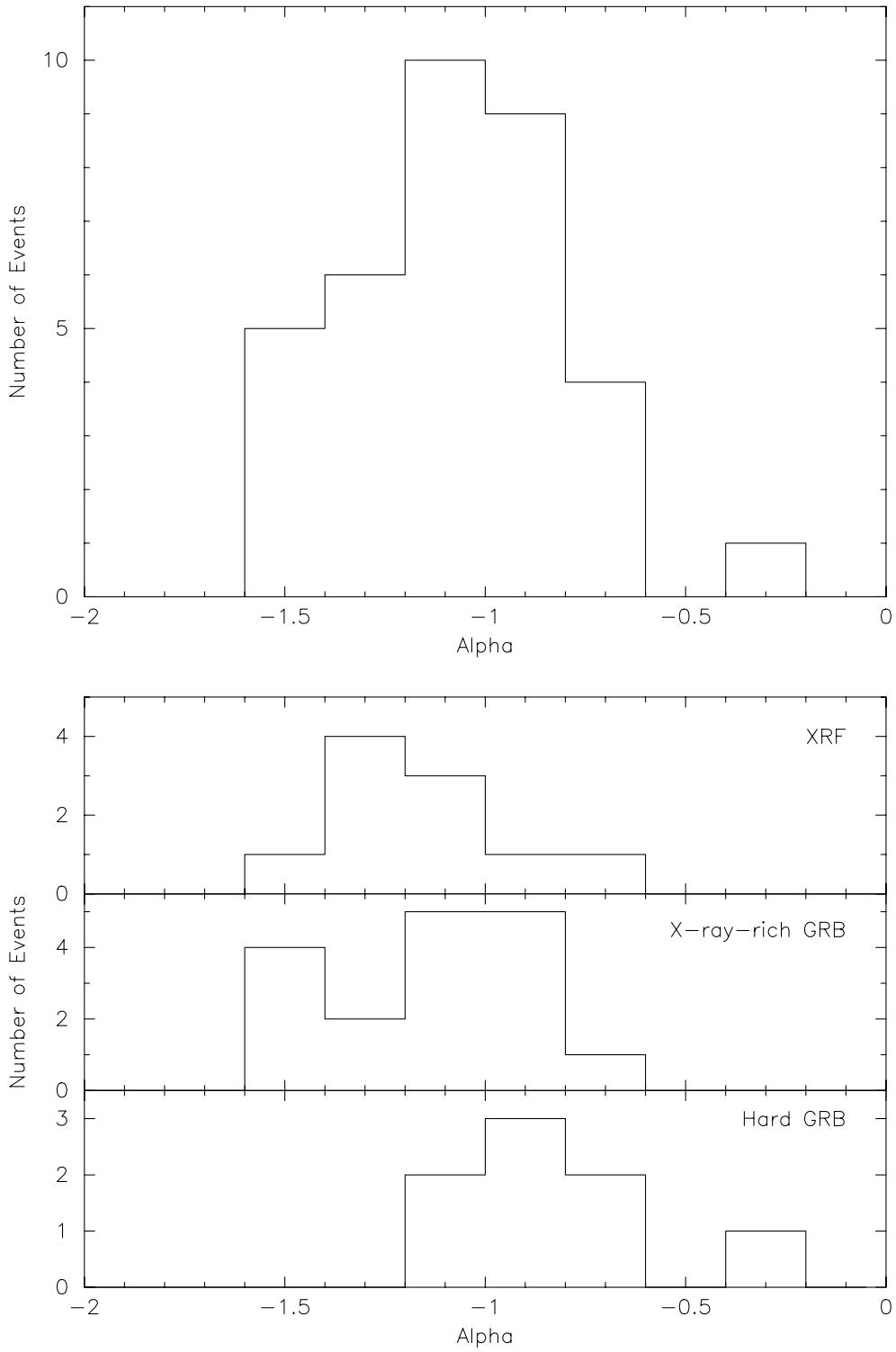

Figure 7.4: Distribution of the low-energy photon index α for all GRB classes (top) and for each of the three different classes (bottom).

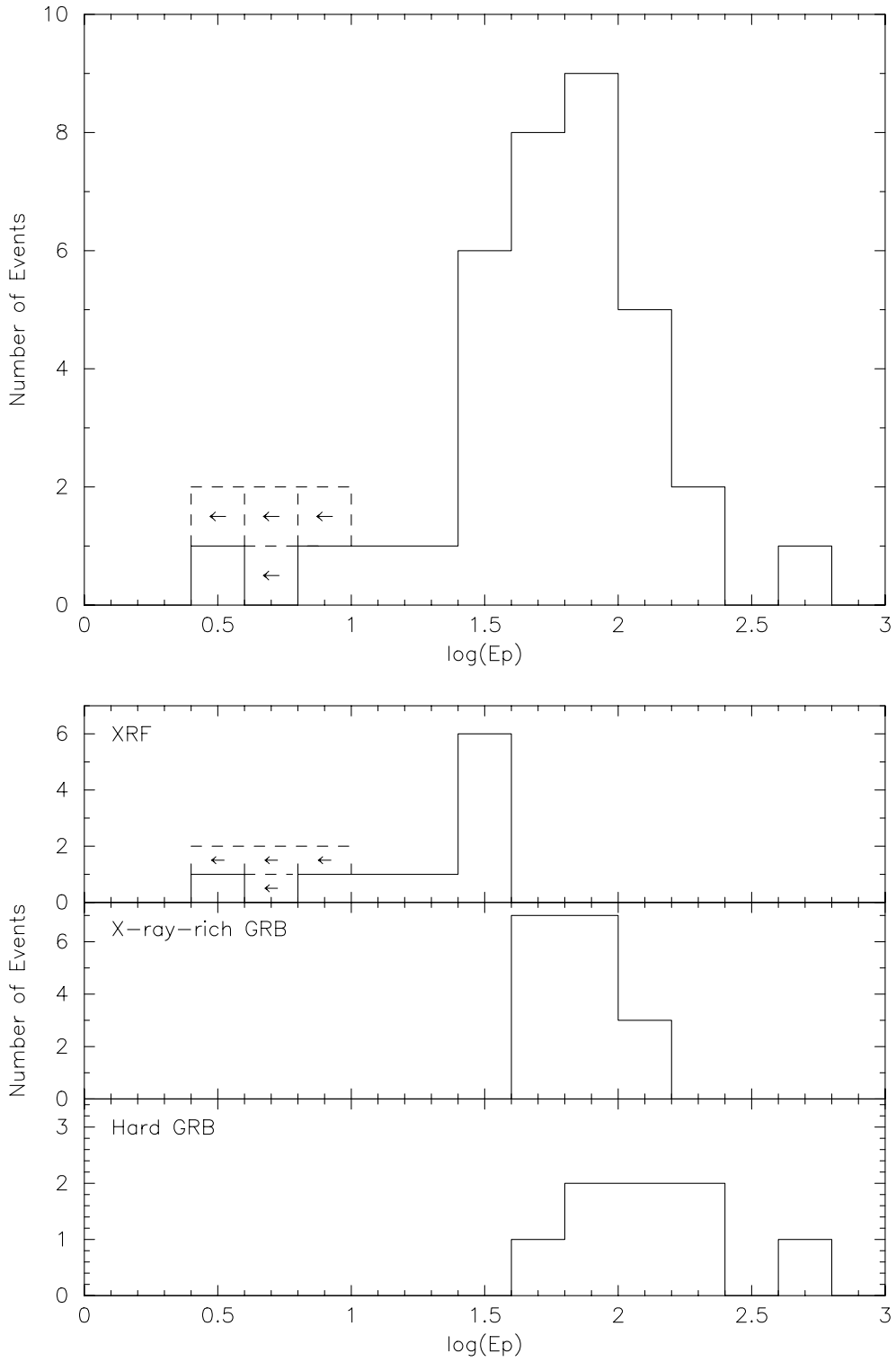

Figure 7.5: Distribution of $E_{\rm peak}$ for all GRB classes (top) and for the three different classes (bottom).

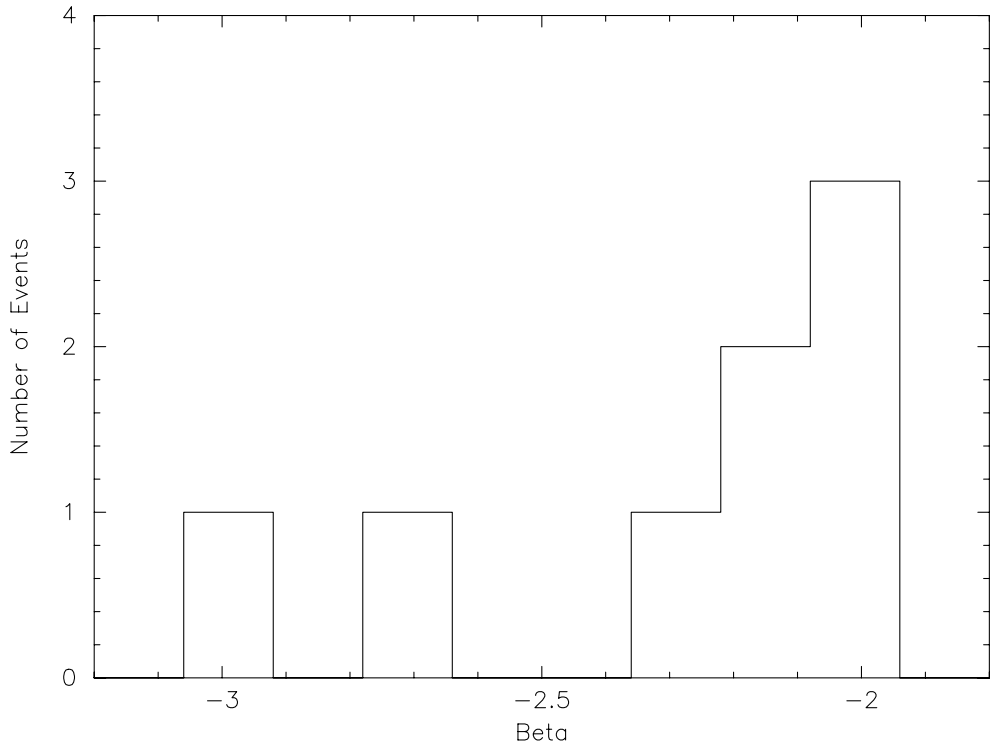

Figure 7.6: Distribution of β for all GRB classes.

7.3 Correlation between $E_{\rm peak}$ and other properties

7.3.1 $E_{\rm peak}$ vs. fluence ratio

The $E_{\rm peak}$ energy and the fluence ratio of 2–30 keV to 30–400 keV are plotted in figure 7.7 (left). Since the fluence ratio is independent of the normalization parameter of the model spectrum, it is possible to calculate the relationship between the fluence ratio and $E_{\rm peak}$. The right of figure 7.7 is the calculated relation assuming the Band function with $\alpha = -1$. The curves correspond to the different values of β ($\beta = -2.5$ (black), -3.0 (red), and -10.0 (blue)). The fluence ratio dependence on β is small in the case of $E_{\rm peak} > 30$ keV. However, this dependence increases when the $E_{\rm peak}$ is less than 30 keV. It implies that the choice of the proper spectral model is needed, especially for XRFs, in our criteria of GRB classes.

7.3.2 α and β vs. $E_{\rm peak}$

The scatter plots of α and β with $E_{\rm peak}$ are shown in figure 7.8. Neither α nor β show a good correlation with $E_{\rm peak}$ or with the GRB classes. Kippen et al. [42] do not find any correlation between α and $E_{\rm peak}$ either in an XRF/GRB sample from WFC/BATSE (see figure 2.7).

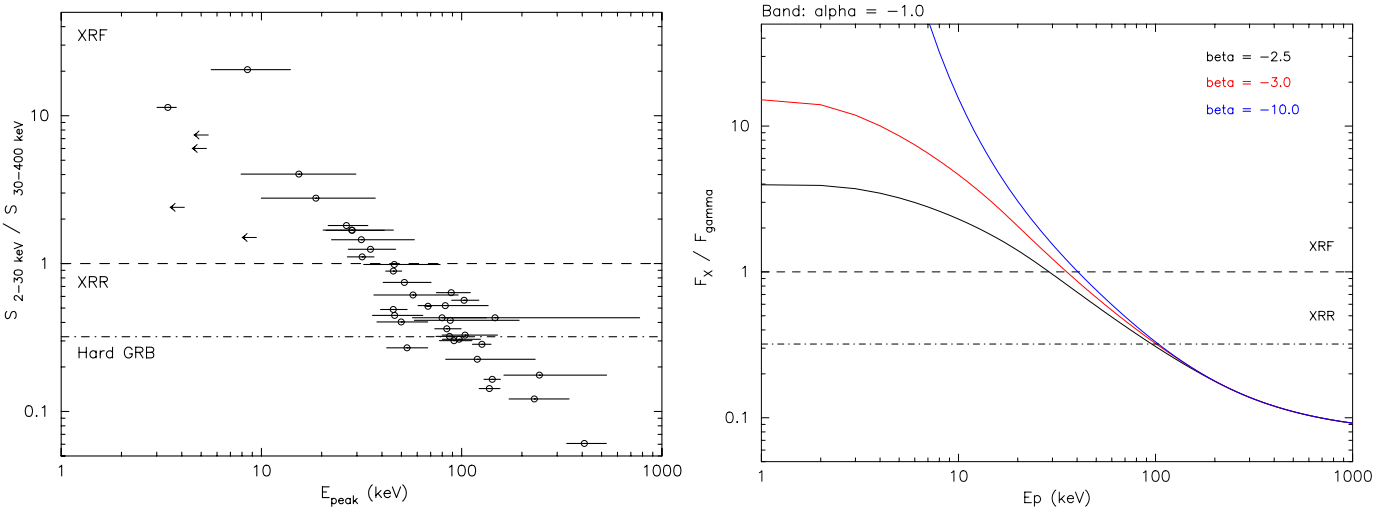

Figure 7.7: Left: The observed $E_{\rm peak}$ vs. X-ray to γ-ray fluence ratio. Right: The calculated $E_{\rm peak}$ vs. X-ray to γ-ray fluence ratio assuming the Band function with $\alpha = -1$.

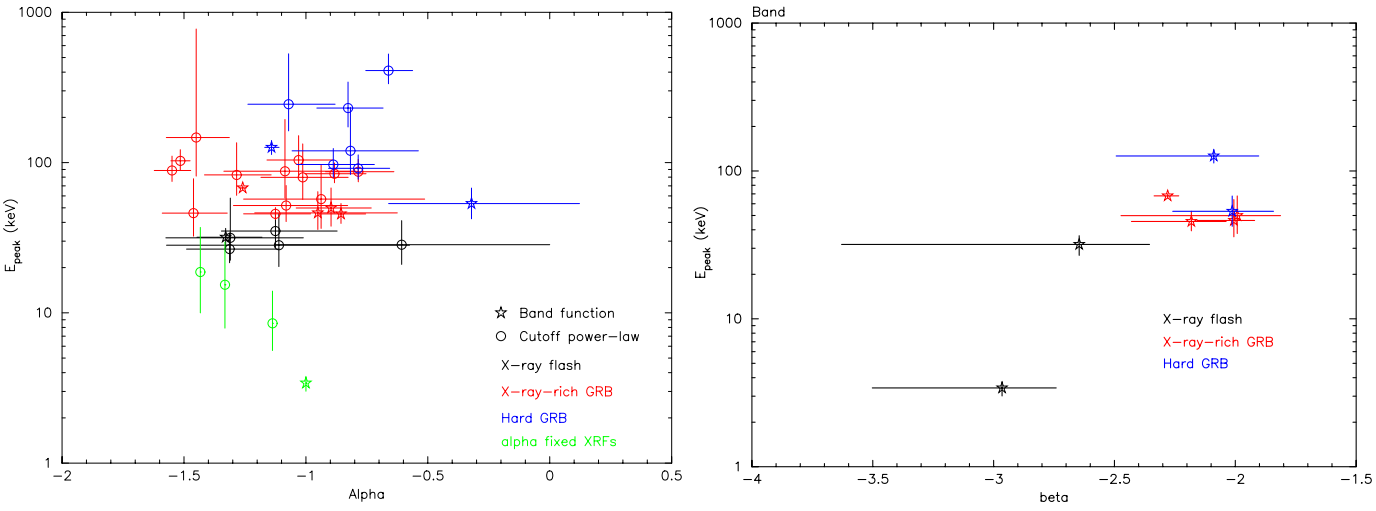

Figure 7.8: α (left) and β (right) vs. $E_{\rm peak}$. Each color corresponds to a GRB class (XRF: black, XRR: red, and hard GRB: blue) and markers correspond to the best fit spectral models (square: cutoff power-law model, star: Band function). Also plotted are the XRFs with fixed values of α (green).

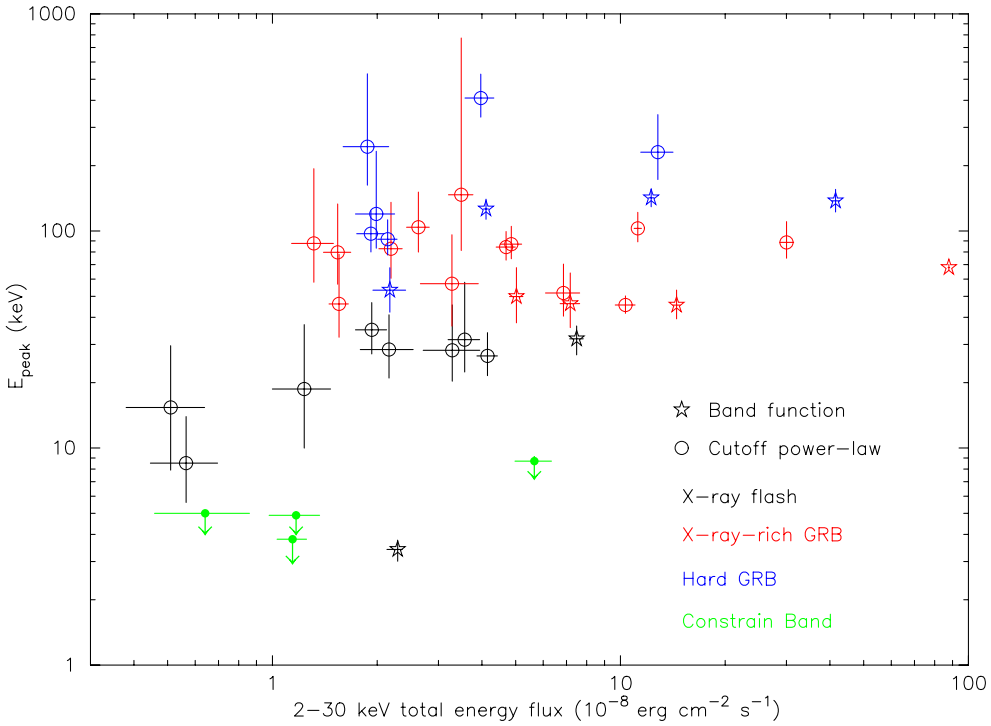

Figure 7.9: The time-average flux in 2-30 keV vs. $E_{\rm peak}$.

7.3.3 The time-average flux vs. $E_{\rm peak}$

The correlation between the time-average flux in 2–30 keV, 2–400 keV, and 30–400 keV and $E_{\rm peak}$ are shown in figure 7.9, 7.10, and 7.11 respectively. Each color corresponds to a GRB class (XRF: black, XRR: red, and hard GRB: blue) and markers correspond to the best fit spectral models (circle: cutoff power-law model, star: Band function). The $E_{\rm peak}$ energies of the four XRFs (green) are calculated using the *constrained* Band function, while their fluxes are computed using the power-law model. The sample correlation coefficients are 0.193, 0.590, and 0.772 between the flux in 2–30 keV, 2–400 keV, and 30–400 keV and $E_{\rm peak}$ respectively. Thus, the time-average fluxes in 2–400 keV and 30–400 keV have a good correlation with $E_{\rm peak}$

.

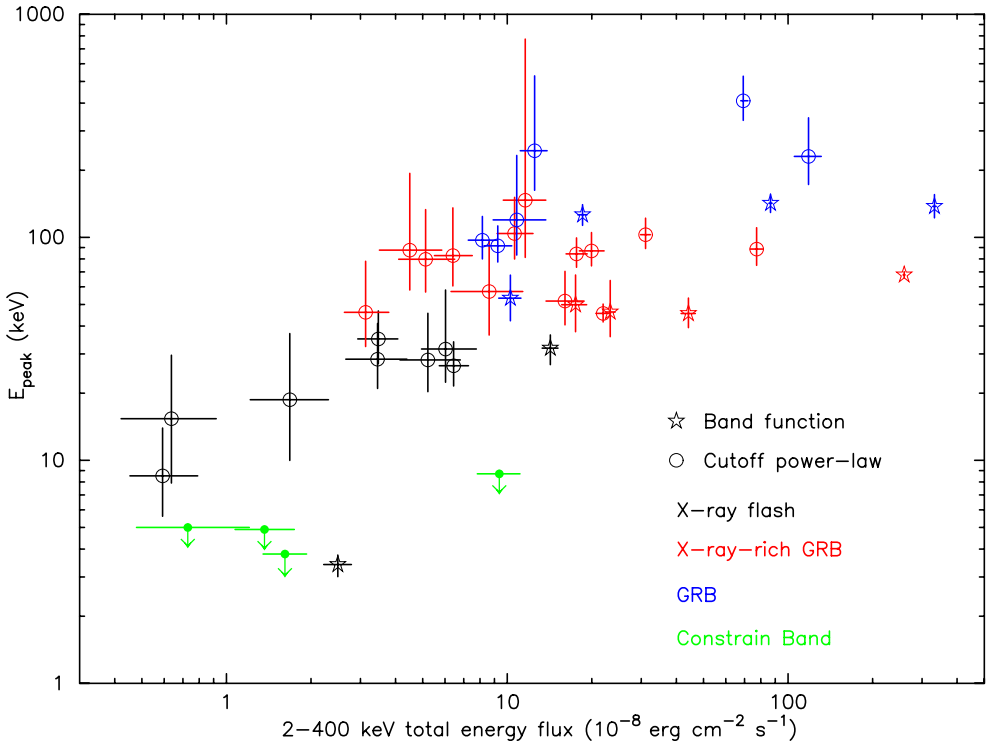

Figure 7.10: The time-average flux in 2-400 keV vs. $E_{\rm peak}$.

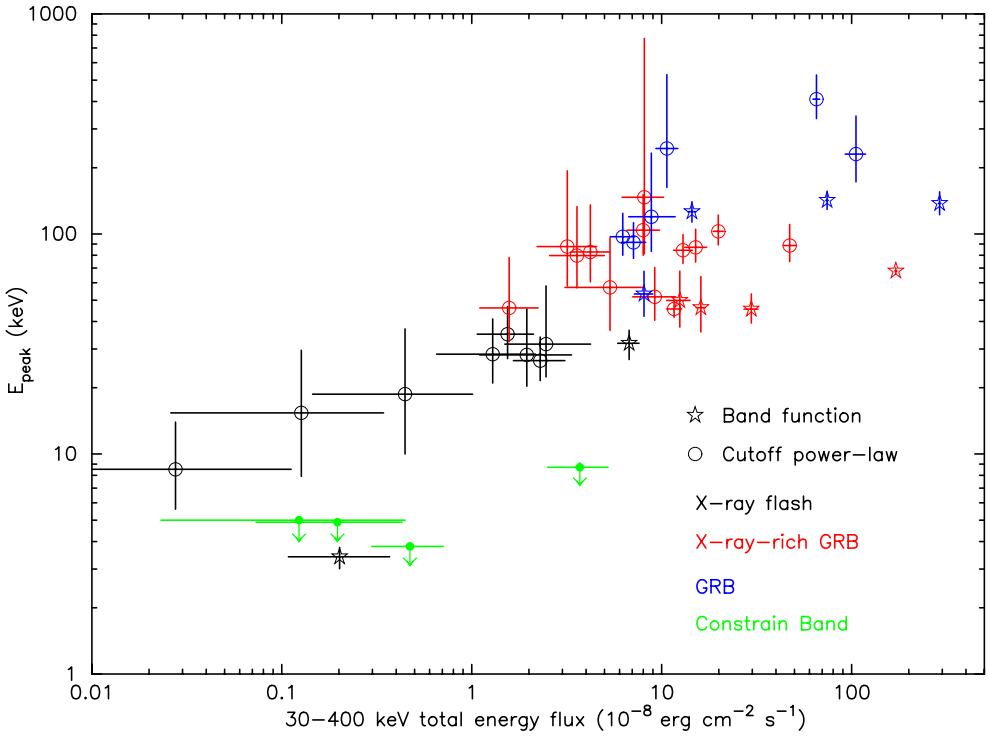

Figure 7.11: The time-average flux in 30-400 keV vs. $E_{\rm peak}$.

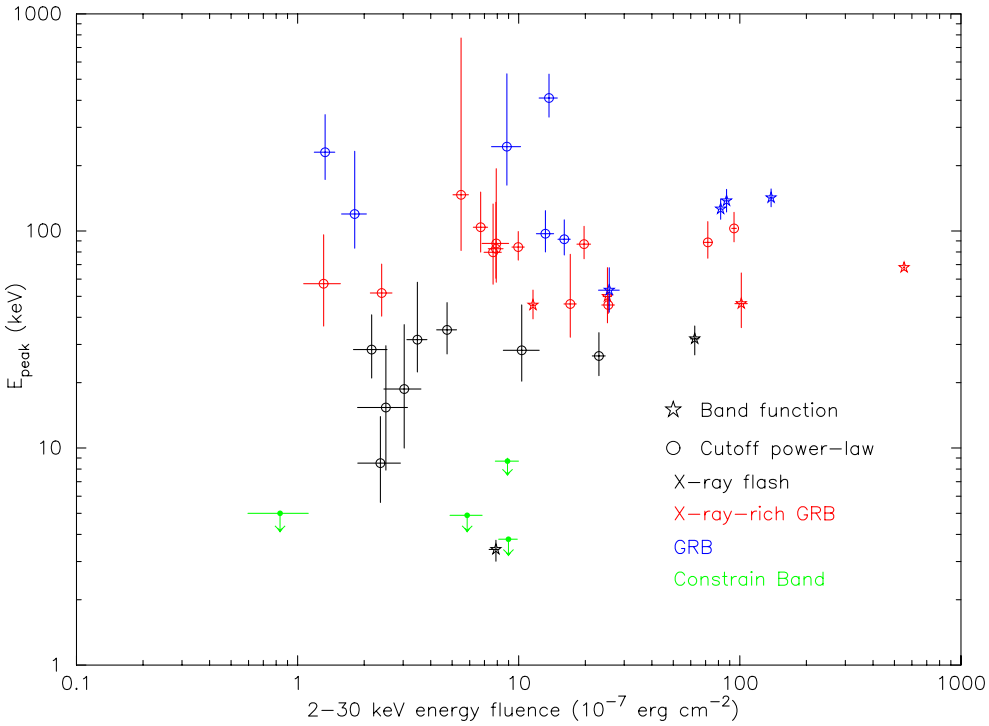

Figure 7.12: The fluence in 2-30 keV vs. $E_{\rm peak}$.

7.3.4 Fluence vs. $E_{\rm peak}$

The correlation between the fluence in 2–30 keV, 2–400 keV, and 30–400 keV and $E_{\rm peak}$ are shown in figure 7.12, 7.13, and 7.14 respectively. The marks and colors correspond to the best fit spectral models and the GRB classes respectively (as same manner as figure 7.9). The tight correlation with $E_{\rm peak}$ is seen at the fluence in 30–400 keV. There is a fairly good correlation between $E_{\rm peak}$ and the fluence in 2–400 keV. These figures also suggest that XRFs, XRRs, and hard GRBs form a continuum.

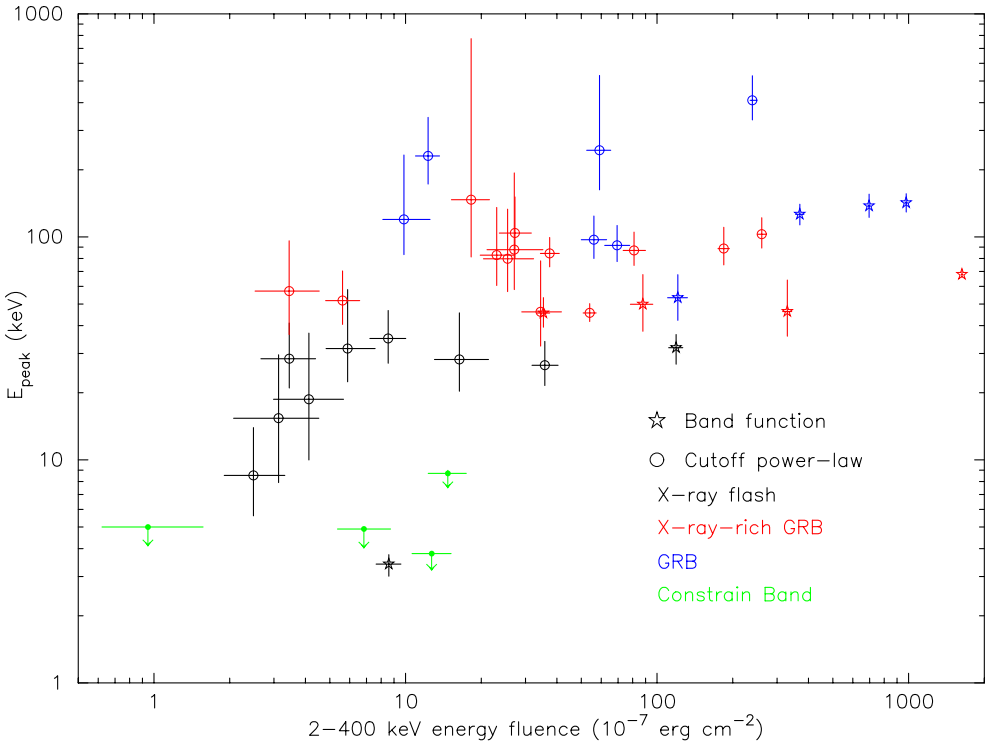

Figure 7.13: The fluence in 2-400 keV vs. $E_{\rm peak}$.

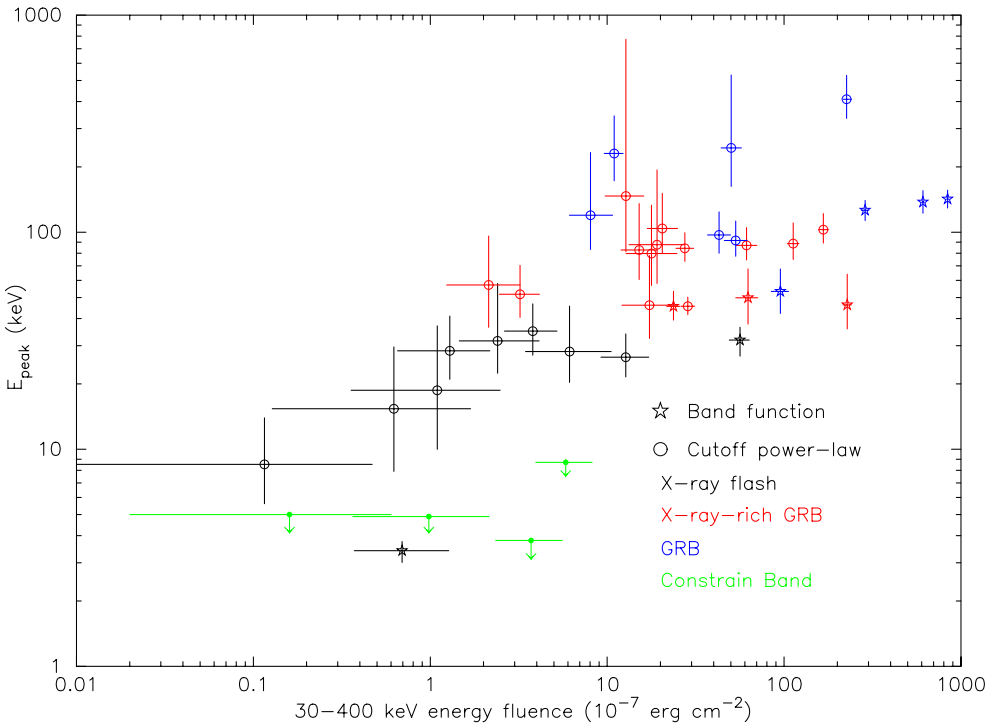

Figure 7.14: The fluence in 30-400 keV vs. $E_{\rm peak}$.

7.3.5 50–300 keV peak flux vs. $E_{\rm peak}$

As was studied for the WFC/BATSE sample by Kippen et al. [42], we investigate the correlation between the 1s peak photon flux and $E_{\rm peak}$. To calculate the peak photon flux in the *HETE* burst sample, we performed the following steps. 1) find the time of the peak counts (T_p) in the light curve, 2) create the 5s WXM and FREGATE spectrum from $T_p - 2.5$ to $T_p + 2.5$, 3) perform the spectral fitting for this 5s spectrum and calculate the flux in the best fit spectral model, 4) calculate the counts from $T_p - 2.5$ to $T_p + 2.5$, and from $T_p - 0.5$ to $T_p + 0.5$ using the background subtracted light curve, 5) calculate the ratio of 1s counts to 5s counts, and 6) multiply this ratio by the flux value calculated in 3) to get the 1s peak photon flux. This procedure is performed for the both the WXM and the FREGATE light curves and we selected the most reliable value for the bursts (in most of the cases, the peak flux of an XRF is the value found using the WXM light curve and the peak flux of an XRR or hard GRB is the value found using the FREGATE light curve).

The result of the 1s peak flux in 50–300 keV (BATSE's trigger band) versus $E_{\rm peak}$ is shown in figure 7.15. Each color corresponds to a GRB class (XRF: black, XRR: red, and hard GRB: blue), and markers correspond to the best fit spectral models (triangle: power-law, circle: cutoff power-law model, star: Band function). The summary table of peak fluxes is in Appendix B. There is a good correlation between these two quantities (sample correlation coefficients, r=0.811). This is a similar trend to that seen for the WFC/BATSE sample, and we will investigate this correlation in detail in the next section.

7.4 Comparison with WFC/BATSE XRF sample

Figure 7.16 shows the 1-second peak flux in 50–300 keV and the $E_{\rm peak}$ of the 523 triggered BATSE bursts, the 29 WFC/BATSE bursts (20 GRBs and 9 XRFs; [42]), and the 41 *HETE* bursts. Figure 7.17 shows the 1s peak flux in 50–300 keV vs $E_{\rm peak}$ for the WFC/BATSE and the *HETE* bursts only. It can be seen that *HETE* is more sensitive to XRFs with much lower peak flux than in the WFC/BATSE sample (figure 7.17). The $E_{\rm peak}$ distributions are compared in figure 7.18. The $E_{\rm peak}$ distributions are generally consistent with a possible deficit of high $E_{\rm peak}$ events and possible excess of low $E_{\rm peak}$ events in the *HETE* sample.

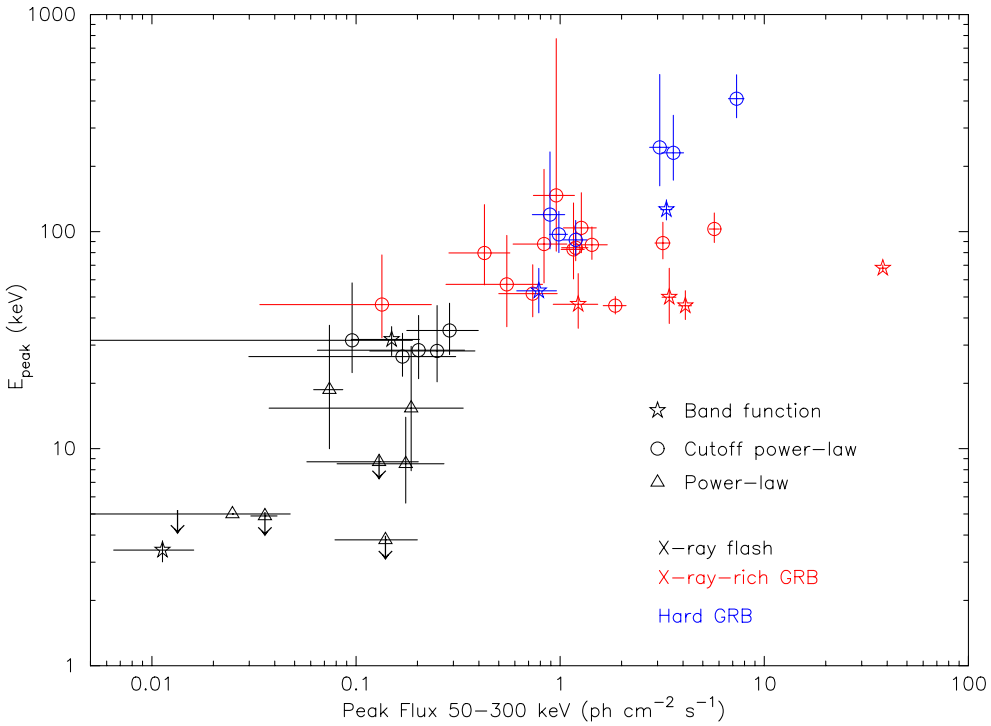

Figure 7.15: 1-second peak photon flux in 50-300 keV vs. $E_{\rm peak}$.

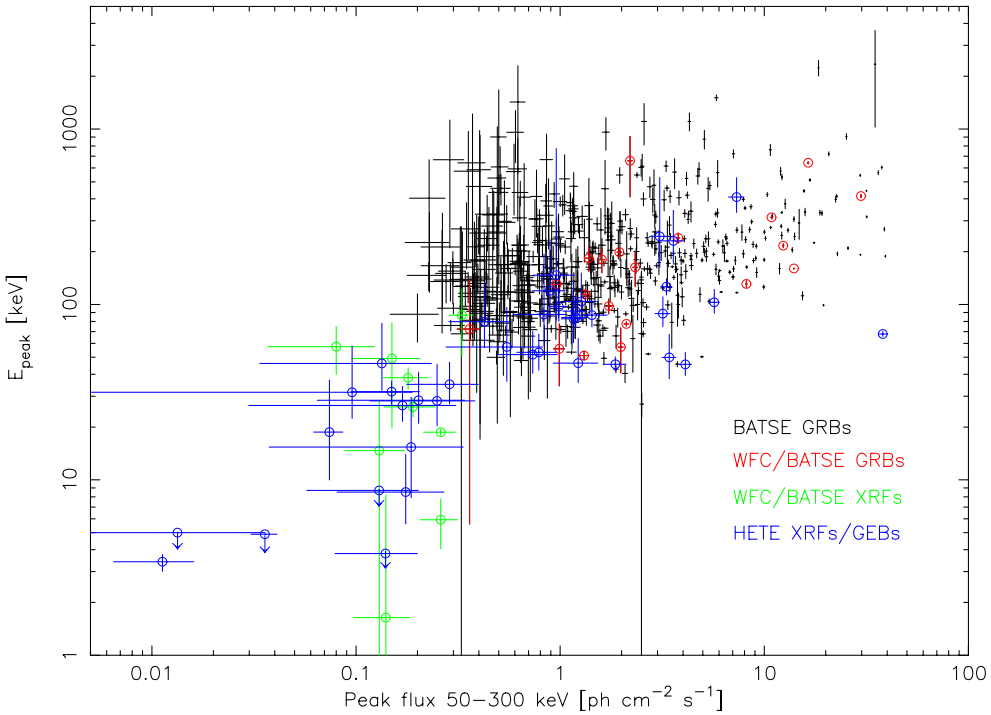

Figure 7.16: 1-second peak flux in 50-300 keV vs. $E_{\rm peak}$. The samples are BATSE bursts (black), WFC/BATSE bursts (red and green), and HETE bursts (blue).

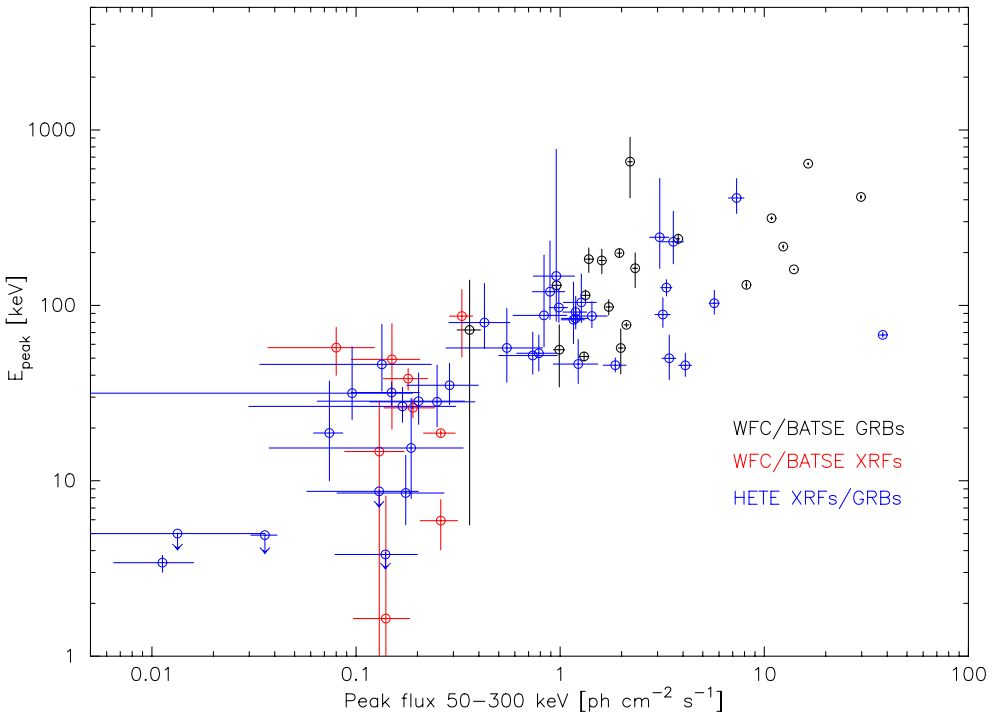

Figure 7.17: 1-second peak flux in 50-300 keV vs. $E_{\rm peak}$. The samples are WFC/BATSE bursts (red and green), and HETE bursts (blue).

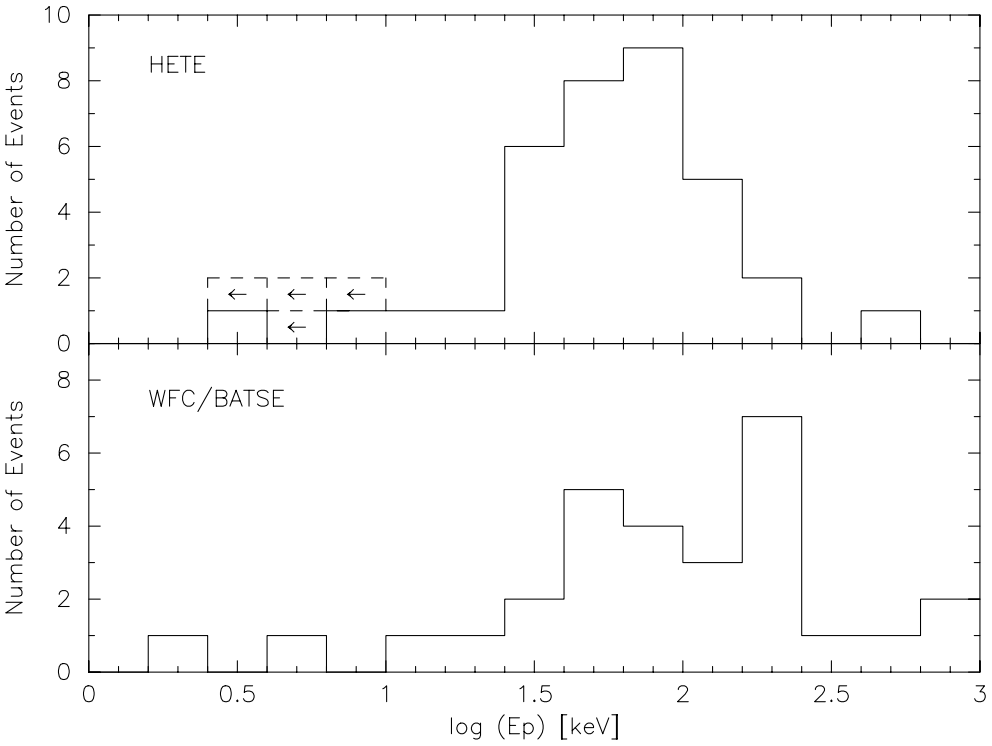

Figure 7.18: The $E_{\rm peak}$ distribution of HETE bursts (top panel) and WFC/BATSE bursts (bottom panel).

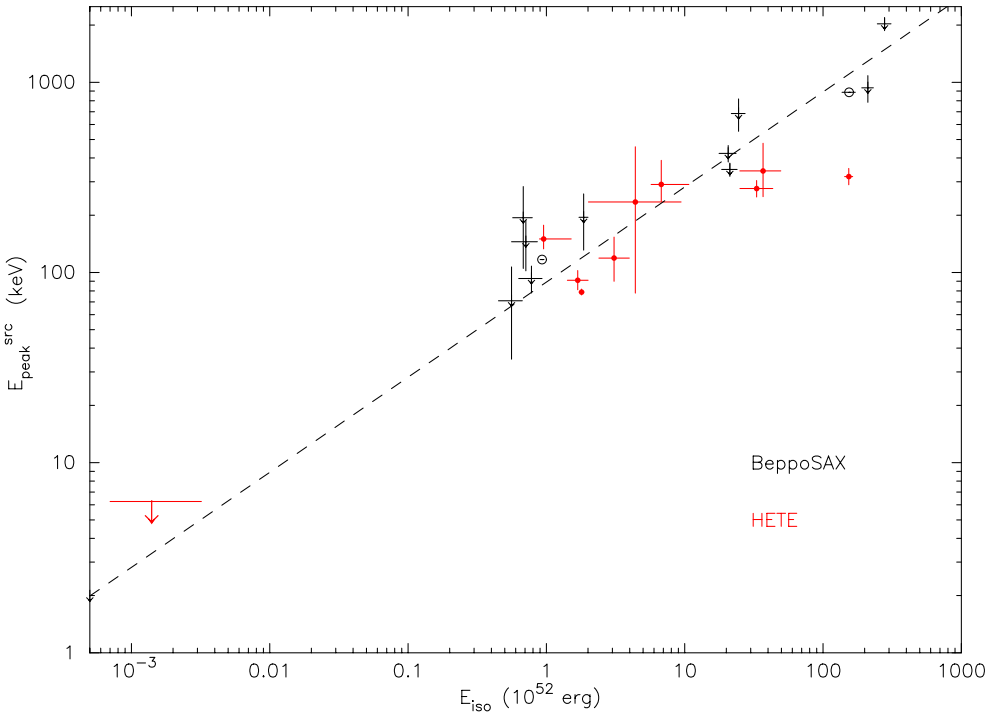

Figure 7.19: The plot of the isotropic-equivalent energy $E_{\rm iso}$ between 1–10000 keV and $E_{\rm peak}$ energy at the GRB source frame. The black points are the *Beppo*SAX sample from Amati et al. [1]. The red points are the *HETE* GRB sample. The dashed line is $E_{\rm peak}^{\rm src} = 89$ ($E_{\rm iso}$ / 10^{52} erg)$^{0.5}$.

7.5 Confirmation and extension of Amati's relation

Redshifts have been measured for 10 HETE GRBs/XRFs with known $E_{\rm peak}$ energies. These events are tested for the relation proposed by [1] (see section 2.1.3). Figure 7.19 is a plot of $E_{\rm peak}$ at the GRB source frame ($E_{\rm peak}^{\rm src}$) and the isotropic-equivalent energy $E_{\rm iso}$ between 1–10000 keV. The *HETE* GRBs (red marks) are overlaid with the *Beppo*SAX sample (black marks) from Amati et al. [1]. As seen in this figure, *HETE* GRBs and XRFs follows this relation remarkably well.

Furthermore. we find that one data point around $E_{\rm iso} \sim 10^{49}$ erg falls on the extension of this relation, despite the fact that its isotropic-equivalent energy is smaller by a factor of 300 than the smallest value in the *Beppo*SAX sample. This data point is the softest XRF, XRF020903. The discovery of the extension of Amati's relation to the XRF region has a great impact on the interpretation of XRF phenomenon as forming a uniform physical picture with GRBs. We will discuss this issue in the next chapter.

Table 7.1: E^{src}_{peak} and E_{iso} of the *HETE* GRBs with known redshift.

GRB	redshift	E^{src}_{peak} [keV]	E_{iso} [10^{52} erg]	Model[b]
GRB010921	0.45	$150.0^{+27.35}_{-16.97}$	$0.954^{+0.556}_{-0.063}$	Band
GRB020124	3.2	$342.2^{+135.86}_{-91.77}$	$36.85^{+12.65}_{-11.84}$	Band
GRB020813	1.25	$319.4^{+33.04}_{-30.07}$	$153.5^{+10.24}_{-10.40}$	Band
GRB020903	0.25	< 6.25	$1.4^{+18.0}_{-0.7} \times 10^{-3}$	Power-law
GRB021004	2.3	$234.7^{+223.21}_{-156.82}$	$4.395^{+5.022}_{-2.383}$	Band
GRB021211	1.01	$91.0^{+11.359}_{-9.936}$	$1.684^{+0.317}_{-0.267}$	Band
GRB030226	1.98	$290.4^{+98.54}_{-53.76}$	$6.766^{+3.951}_{-1.049}$	Band
GRB030323	3.37	–	$19.20^{+63.70}_{-13.0}$	Power-law
GRB030328	1.52	$276.4^{+27.91}_{-27.14}$	$33.10^{+10.24}_{-8.03}$	Band
GRB030329	0.168	$78.91^{+2.85}_{-2.76}$	$1.795^{+0.07}_{-0.071}$	Band
GRB030429	2.65	$119.0^{+34.58}_{-29.19}$	$3.084^{+0.892}_{-0.686}$	Band
GRB030723	~ 0.5	–	$6.07^{+14.0}_{-2.29} \times 10^{-2}$ (z=0.5)	Power-law

a E_{iso} at z = 0.5

b The spectral model used for the calculation of E_{iso}

Chapter 8

Discussion

In chapter 6, we investigated the individual characteristics of the prompt emission of the *HETE* XRFs[1] and XRRs[2]. We found the several similarities between XRFs/XRRs and hard GRBs in their spectral and temporal characteristics. We will discuss the properties of XRFs/XRRs based on these individual characteristics and the global characteristics of XRFs/XRRs which are studied in chapter 7.

8.1 The sky distribution and event rate of X-ray flashes

Figure 8.1 shows the sky distribution of *HETE* XRFs, XRRs, and hard GRBs. The GRBs are populated uniformly in the sky. There is no difference between the GRB classes. This result provides a strong support for XRFs as the same origin of the ordinary GRBs.

As we summarized in chapter 7, HETE saw 15 XRFs, 20 XRRs and 10 GRBs. The total observation time when the WXM high voltage was on from February 2001 to September 2003 was 1.1 years[3]. When we take into account the WXM field of view of $60^\circ \times 60^\circ$, the event rates of each GRBs are estimated to be 160, 220, and 110 events year^{-1} for XRFs, XRRs, and hard GRBs respectively. *Beppo*SAX reports the number of XRFs of ~ 100 year^{-1} [36]. Since both WXM and FREGATE have a good sensitivity for detecting XRFs compared to the *Beppo*SAX instruments, the XRF event rates of ~ 100 year^{-1} could be underestimated. According to the

[1] X-ray flashes

[2] X-ray rich GRBs

[3] There are two main reasons for not operating WXM. The first reason is that the high voltage must be off during orbit day (while *HETE* is pointing the earth). The second reason is due to the automatic high voltage turn-off mechanism which switches the WXM off when the count rates go high (e.g. SAA, Ecuador anomaly [99])

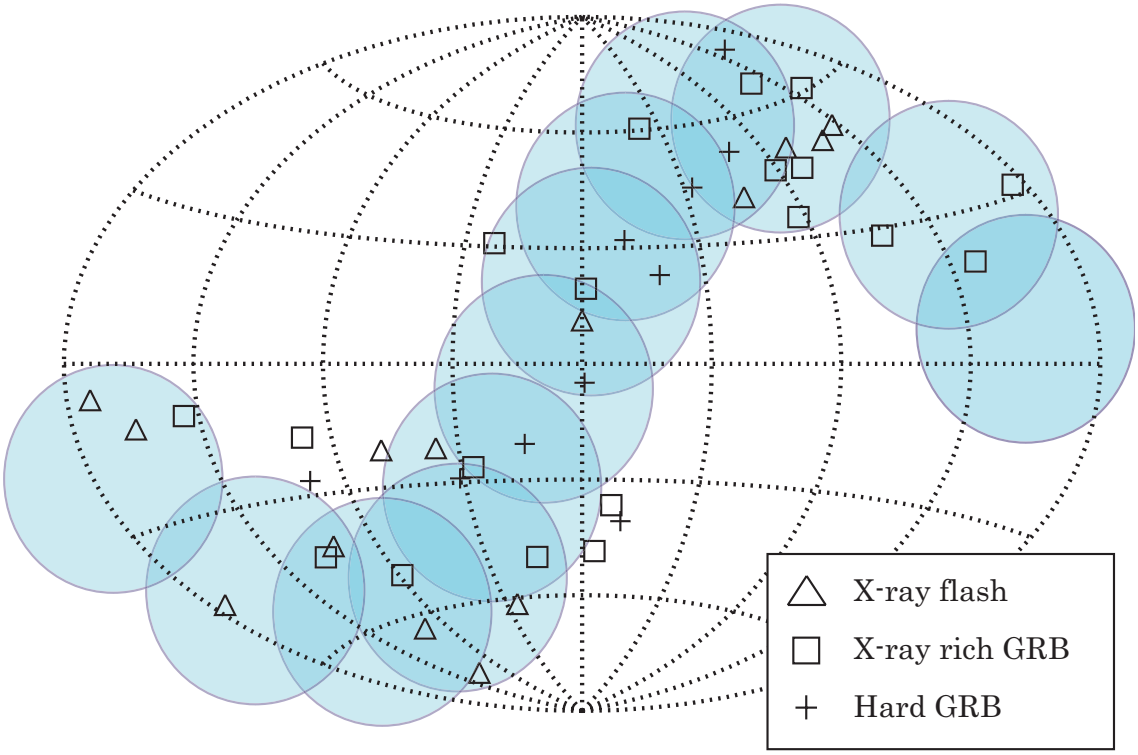

Figure 8.1: The sky distribution of the *HETE* XRFs (triangle), X-ray rich GRBs (square), and hard GRBs (cross) in the galactic coordinate. The light blue circles represent the field of view of WXM (60° × 60°) for each months assuming the anti-solar pointing.

HETE sample, XRFs occupy one third of the whole GRB population. Note that the number of the XRFs is almost the same as that of the hard GRBs.

8.2 The spectrum of X-ray flashes

The low $E_{\rm peak}$ energy is the most noticeable spectral characteristic of XRFs (section 7.2). The correlation between $E_{\rm peak}$ and the energy flux becomes tighter when we measure the flux in the γ-ray range (section 7.3). Almost no correlation has been found between $E_{\rm peak}$ and the 2–30 keV energy flux (figure 7.9). The left panel of figure 8.2 shows the best-fit spectral models in νF_ν spectrum. Although there are variations for each GRB, the flux at the lower energy range is almost consistent with all GRB classes. However, the flux in the γ-ray range is smaller for XRFs. This trend becomes much clearer when we investigate the correlation between the normalization of the spectrum and $E_{\rm peak}$ energy. The figure 8.2 (right) shows the correlation between the normalization at 15 keV and $E_{\rm peak}$ energy. The normalization energy, 15 keV, is close to the $E_{\rm peak}$ energy for XRFs, but below the $E_{\rm peak}$ energies of XRRs and hard GRBs. The

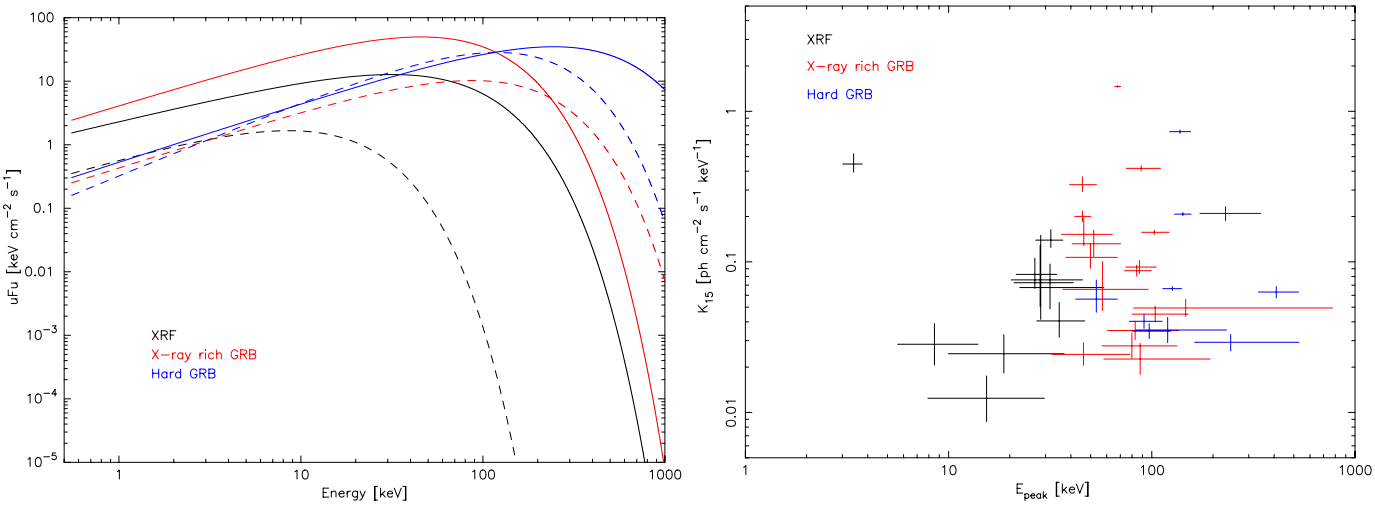

Figure 8.2: Left: the best fit νF_ν spectra of XRFs (black), XRRs (red), and hard GRBs (blue). Right: the scatter plot of $E_{\rm peak}$ and the normalization at 15 keV (XRF: black, XRR: red, hard GRB: blue).

values of the normalization are clustered near an $E_{\rm peak}$ energy of around 30–100 keV.

From these properties, the spectral shape from XRFs to GRBs can be expressed as in figure 8.3. When the $E_{\rm peak}$ energy goes lower, the flux at the $E_{\rm peak}$ energy becomes lower. In this picture, it is possible to explain the good correlation between $E_{\rm peak}$ and the energy flux in γ-ray, and the less correlation between $E_{\rm peak}$ and the energy flux in the X-ray range. XRFs are intrinsically fainter than XRRs/hard GRBs.

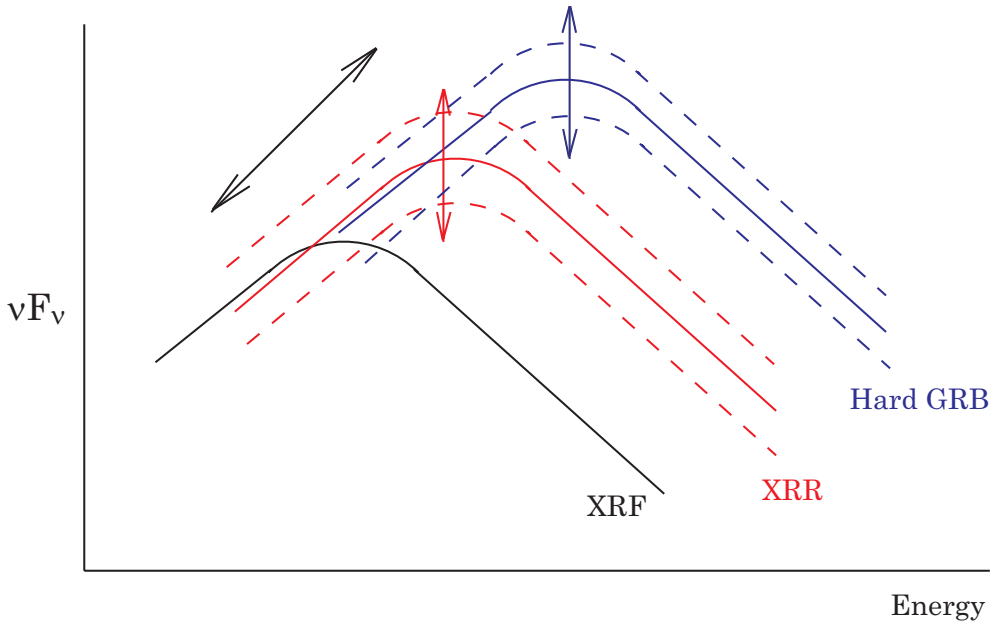

Figure 8.3: The schematic figure of νF_ν spectra of XRFs, XRRs, and hard GRBs.

8.3 The correlation between $E_{\rm peak}$ and γ-ray peak flux

The *HETE* GRB sample confirmed the correlation between $E_{\rm peak}$ and γ-ray peak flux from hard GRBs to XRFs suggested by Kippen et al. [42] (figure 8.4). Even more, *HETE* is observing much weaker XRFs than the WFC/BATSE XRF sample. The relationship between $E_{\rm peak}$ and γ-ray peak flux P is $E_{\rm peak} \propto {\rm P}^{0.379}$.

We will extend the discussion done by Schaefer [89] to XRFs. Two kinematic effects will change the characteristic energy, $E_{\rm rest}$, to the observed energy, $E_{\rm peak}$. They are relativistic beaming effect and the cosmological expansion of the universe. The relativistic beaming effect will blueshift the $E_{\rm rest}$ energy by the factor of the bulk Lorentz factor Γ. The cosmological effect will redshift the energy by a factor of $(1 + {\rm z})^{-1}$. $E_{\rm peak}$ can be expressed as,

$$E_{\rm peak} = E_{\rm rest}\Gamma(1+z)^{-1}. \tag{8.1}$$

The value of $E_{\rm peak}$ can vary from pulse to pulse and burst to burst. In general, $E_{\rm rest}$ might have a power-law dependence on Γ.

$$E_{\rm rest} = E_0\Gamma^M, \tag{8.2}$$

where M is the power-law index.

In the general internal shock model, the burst isotropic luminosity, L, varies as some power of Γ. The index of Γ is model dependent. We can express this with a general formula:

$$L = L_0\Gamma^N, \tag{8.3}$$

where N is the power-law index.

Using (8.1)-(8.3), $E_{\rm peak}$ can be expressed as

$$E_{\rm peak} \;=\; E_0\,(\frac{L}{L_0})^{\frac{M+1}{N}}\,(1+z)^{-1}. \tag{8.4}$$

So, $E_{\rm peak}$ is

$$E_{\rm peak} \propto L^{\frac{M+1}{N}}(1+z)^{-1}. \tag{8.5}$$

If we assume z $\simeq$ 1, the peak luminosity L corresponds to the peak flux P. Equation (8.5) can be expressed as,

$$E_{\rm peak} \propto P^{\frac{M+1}{N}}. \tag{8.6}$$

From the *HETE* and WFC/BATSE samples, (M + 1)/N is 0.379. In the same manner as [89], the variability/luminosity relation (section 2.1.4) is used to constrain the value of N. Since the variability (V) is the "spikiness" of the GRB light curve, V varies as the inverse of the rise times in the light curve. The rise time will be limited by the geometric delays that scale as Γ^{-2} (see [80] problem 4.1), so V $\propto \Gamma^2$. According to the variability/luminosity relation [88], L $\propto$ $V^{1.57\pm0.17}$. Thus, L $\propto \Gamma^{3.14\pm0.34}$ and N = 3.14.

Now it is possible to calculate the value of M using N = 3.14. This gives M = 0.19 $\sim$ 0. This implies that the variation of $E_{\rm peak}$ from a few keV to MeV is only dependent on two effects; the cosmological redshift and the relativistic beaming effect.

Thanks to the redshift measurement of GRB020903, we have the redshift-corrected $E_{\rm peak}$ relation (extended Amati's relation; figure 7.19). This extended Amati's relation indicates that $E_{\rm peak}$ still has a variation from a few keV to MeV even if the redshifts of $E_{\rm peak}$ are corrected. So, we may conclude that the variation of $E_{\rm peak}$ energy is mainly due to the relativistic beaming effect. Finally, $E_{\rm peak}$ can be written as,

$$(1+z)\,E_{\rm peak} = E_0\Gamma. \tag{8.7}$$

$E_{\rm peak}$ can be interpreted as the synchrotron critical frequency $\nu_{\rm m}$ with a minimum Lorentz factor for electrons (section 3.1). $\nu_{\rm m}$ can be expressed as

$$\nu_{\rm m} = \frac{3eB\gamma_{\rm m}^2}{4\pi mc}, \tag{8.8}$$

where $\gamma_{\rm m}$ is the minimum Lorentz factor for electrons, m is the mass of electron, e is the elementary electric charge, c is the speed of light, and B is the magnetic field. If we use the

relation $E_0 = h\nu_{\rm m}$, where h is Plank constant, the magnetic field B can be written as,

$$\begin{aligned} B &= \frac{4\pi mcE_0}{3e\gamma_{\rm m}^2 h} \\ &= 5.76\times10^{10}\gamma_{\rm m}^{-2}E_0. \end{aligned} \tag{8.9}$$

On the other hand, the cooling time of electrons can be written as

$$t_{\rm c} = \frac{\gamma_{\rm m}mc^2}{\frac{4}{3}\gamma_{\rm m}^2\sigma_{\rm T}c\frac{B^2}{8\pi}}, \tag{8.10}$$

where $\sigma_{\rm T}$ is the Thomson cross section. Then $\gamma_{\rm m}$ is

$$\begin{aligned} \gamma_{\rm m} &= \frac{6\pi}{t_{\rm c}}\frac{mc}{\sigma_{\rm T}B^2} \\ &= 7.75\times10^{8}B^{-2}\,t_c^{-1}. \end{aligned} \tag{8.11}$$

In the internal shock model, the cooling time corresponds to the individual spikes in the light curve. The duration of each spike is $<$ ms. If we assume $\rm t_c <$ ms and substitute equation (8.11) into equation (8.9), the magnetic field will be

$$B > 2.18\times10^{4}\left(\frac{E_0}{1\,\rm keV}\right)^{-\frac{1}{3}}\left(\frac{t_c}{1\,\rm ms}\right)^{-\frac{2}{3}} \quad [\rm G]. \tag{8.12}$$

Although we assume $E_0 = 1$ keV from the extended Amati's relation, this minimum energy could be much smaller.

In the unifying picture of XRFs with GRBs, the magnetic field at the shock region is estimated to be $> 10^4$ gauss. It is very important to constrain E_0 energy from the observation of XRFs to estimate the magnetic field at the shock region in much higher precision.

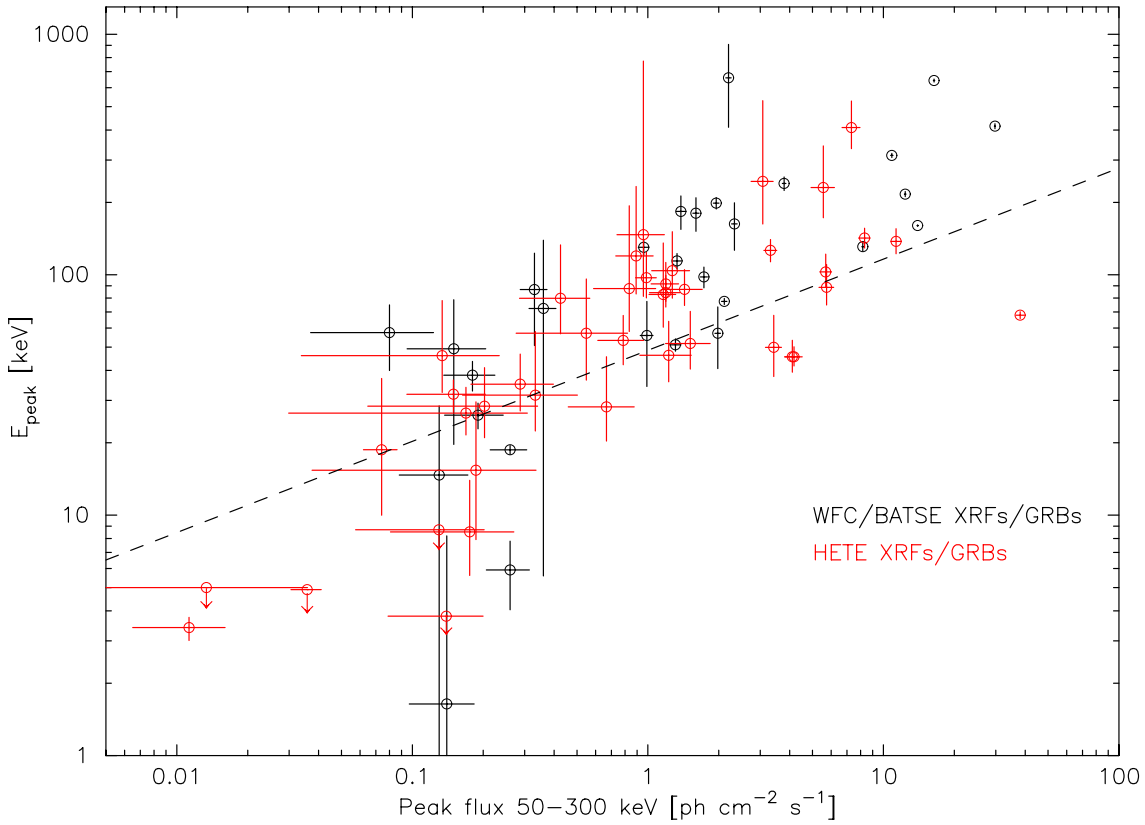

Figure 8.4: The 1-second peak photon flux in 50–300 keV and $E_{\rm peak}$ relation including the *HETE* and *Beppo*SAX/BATSE samples. The dashed line is $\mathrm{E_{peak}} = (48.51 \pm 0.46)\ \mathrm{P}^{0.379\pm0.003}$.

8.4 Distance scale of X-Ray flashes

To discuss the distance scale of XRFs, we investigate the logN-logP for *HETE* GRBs. Figure 8.5 shows the logN-logP plot for each of the GRB classes. The cumulative numbers of each class are normalized to the total numbers of events. Note that this logN-logP plot is not corrected for the trigger efficiency.

From the BATSE/PVO GRBs, we already know that the slope of logN-logP of hard GRBs changes from $-3/2$ to -0.8 ([35], [50]). The slope of $-3/2$ may be derived assuming a homogeneous distribution of sources in Euclidean space. Based on this result, we tried to compare the logN-logP distribution of XRFs and hard GRBs. We select the *HETE* GRBs with $E_{\rm peak}$ greater than 50 keV as a hard GRB sample (total 22 bursts). Figure 8.6 shows the overlaid logN-logP distribution of XRF (black) and hard GRBs (red). The peak flux is calculated in 2–30 keV. The logN-logP distribution of hard GRBs (red line) is normalized to adjust for that of XRFs around the peak flux of 3 photons cm^{-2} s^{-1}. The vertical dot-dot-dashed lines are the sensitivity limits as a function of $E_{\rm peak}$ (10 keV, 30 keV, and 100 keV from right to left)

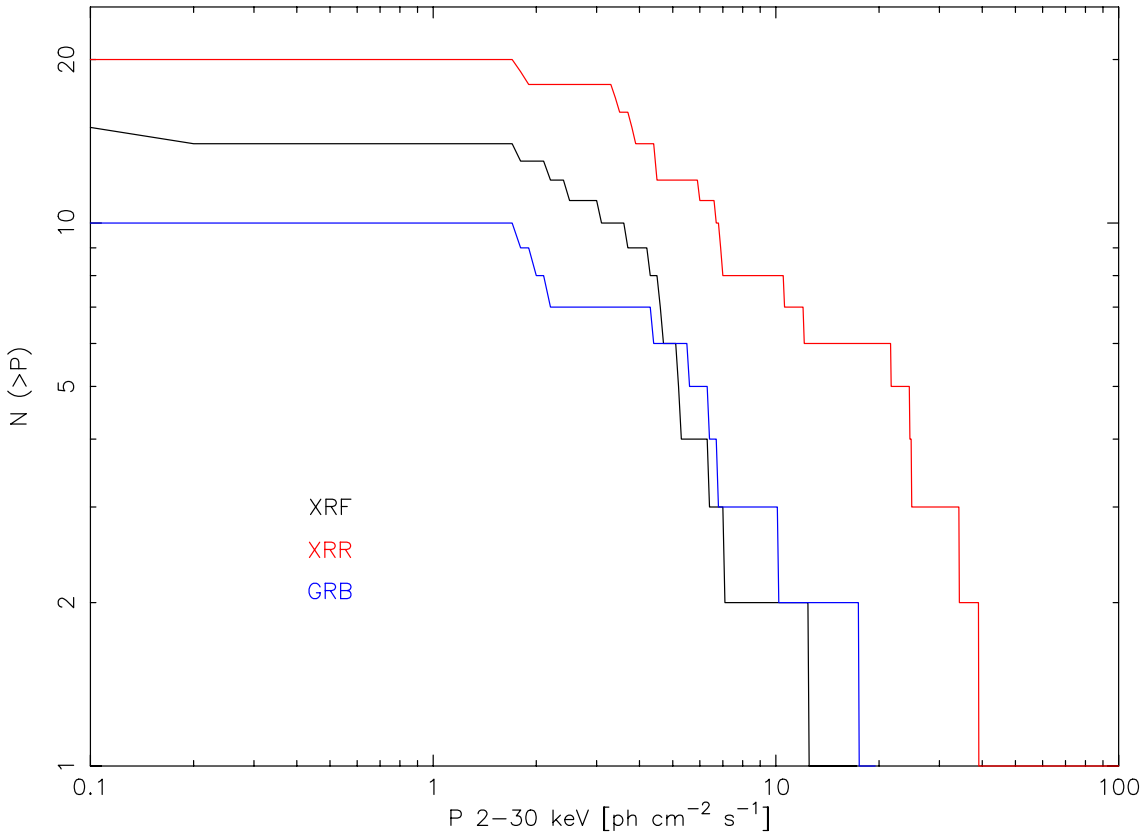

Figure 8.5: logN-logP for XRFs (black), XRRs(red), and hard GRBs(blue). The vertical axis is the cumulative number of the bursts. The horizontal exis is 1s peak flux in 2–30 keV. See text for the details.

calculated by Band [7] assuming the Band function of $\alpha = -1$, $\beta = -3$. Since at a peak flux of less than 3 photons cm^{-2} s^{-1} we might suffer from a threshold effect, we will discuss the region larger than this peak flux. The dashed lines are the slope of $-3/2$.

The logN-logP distribution of hard GRBs shows a clear offset from the $-3/2$ slope around peak flux of 10 photons cm^{-2} s^{-1}. However, it is important to note that the logN-logP distribution of XRFs follows on the slope of $-3/2$. This might indicate that the distace scale of XRFs are different from that of hard GRBs. The distance of XRFs are consistent with Euclidean geometory, which means z $\leq$ 0.2.

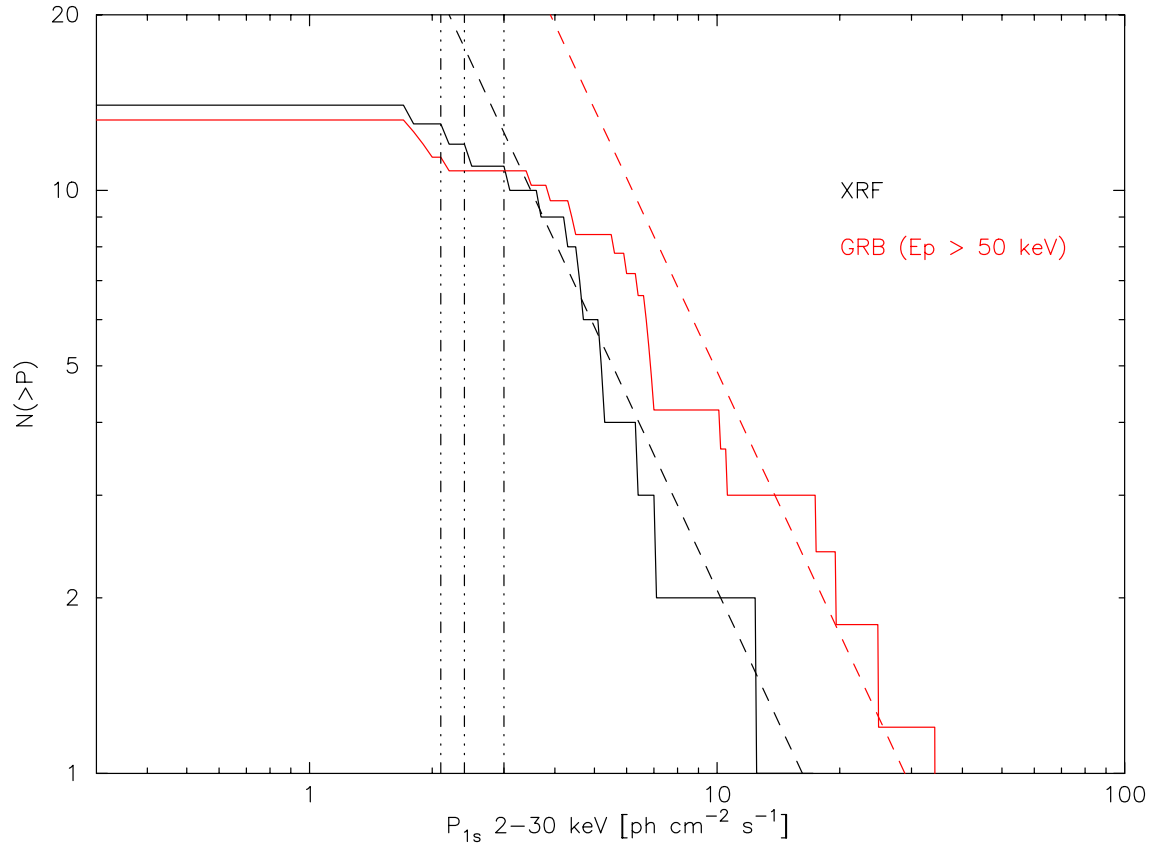

Figure 8.6: logN-logP for XRFs (black) and GRBs with $E_{\rm peak} > 50$ keV. See text for the details about the plot.

8.5 Theoretical models for X-ray flashes

We will discuss in details for three promising theoretical models of XRFs: the off-axis jet model ([112]; [113]; see also section 3.2.1), the structure jet model ([79]; see also section 3.2.4), the unified jet model ([47]) and the jet beaming model which is based on the result on this paper.

8.5.1 Off-axis jet model

In this model, XRF is a collimated GRB jet with a large viewing angle (see figure 3.4). Their original model [112] can explain the low $E_{\rm peak}$ energy, the peak flux and flunece of XRF based on *Beppo*SAX observation. This model also predicted that the distance scale of XRF is z $<$ 0.2, which matches with the observed event rate of XRFs.

The redshift-corrected $E_{\rm peak}$ energy of GRB020903 is $\sim$ 5 keV (see section 6.9). If we estimate the viewing angle, $\theta_{\rm v}$, with and $E_{\rm peak}$ energy of 5 keV and assuming that the $E_{\rm peak}$ energy in the on-axis jet is 300 keV and also that the bulk Lorentz factor of 100, then $\theta_{\rm v}$ is 8 degrees with the jet half opening angle, $\Delta\theta$, of 1 degree. Yamazaki et al. [112] discuss the event rate of XRF in a formula of $R_{\rm XRF} = r_{\rm GRB} n_g (4\pi D_{\rm XRF}^3/3)(f_{\rm XRF}/f_{\rm GRB})$, where $r_{\rm GRB}$ and n_g are the event rate of the GRBs and the number density of galaxies, resectively. The $D_{\rm XRF}(D_{\rm GRB})$ is the distance of XRF (GRB). The $f_{\rm XRF}(f_{\rm GRB})$ is the fraction of the solid angle observed as XRF (GRB). Since $\theta_{\rm v} \sim 8\Delta\theta$ in the case of GRB020903, $f_{\rm XRF}/f_{\rm GRB} \sim (8^2 - 1^2)/1^2 = 63$.

From *HETE* observations, the event rate of XRFs and hard GRBs are about the same. If the event rates of XRFs and GRBs are the same, as observed by *HETE*, the distance of XRF will be calculated as

$$\begin{aligned} \left(\frac{D_{\rm XRF}}{D_{GRB}}\right)^3 &= \left(\frac{f_{\rm XRF}}{f_{\rm GRB}}\right)^{-1} = \frac{1}{63} \\ D_{\rm XRF} &\sim 0.25\, D_{\rm GRB}. \end{aligned} \tag{8.13}$$

Thus, if GRBs are z $\sim$ 1, then the XRF population lies around 1.8 Gpc. This is consistent with our discussion of the distance scale of XRFs based on the logN-logP distribution.

On the other hand, the authors also proposed the cosmological off-axis jet model for XRFs [113]. It is possible to produce XRFs in a viewing angle of 2.9 degrees with the jet half opening angle of 1.7 degrees at the redshift of 1.5. In this case, $E_{\rm peak}$ will be around 30 keV. Because the viewing angle is much closer to the jet opening angle, the distance scale of XRFs will then be similar to that of GRBs.

The most plausible way of explaining the all observations of XRFs, XRRs, and hard GRBs in the off-axis model will be to consider a combination of the above two models. $E_{\rm peak}$ above

$\sim$ 30 keV will be a cosmological off-axis GRB jet and a few keV events will be a off-axis jet with z $<$ 0.2. This off-axis jet model has a unique prediction to $E^{\rm src}_{\rm peak}$ - $E_{\rm iso}$ relation (extended Amati's relation). When the viewing angle is larger than the jet opening angle, $E_{\rm iso} \propto \delta^3$ and $E^{\rm src}_{\rm peak} \propto \delta$, where δ is the Doppler factor $\delta^{-1} \equiv \Gamma[1 - \beta\cos(\theta_{\rm v} - \Delta\theta)]$. Thus, $E^{\rm src}_{\rm peak} \propto E^{1/3}_{\rm iso}$. The $E_{\rm iso}$ dependence of δ will be $E_{\rm iso} \propto \delta^2$ when the viewing angle is within the jet opening angle ([115], [49]). In this case, $E^{\rm src}_{\rm peak} \propto E^{1/2}_{\rm iso}$.

Another interesting prediction of the off-axis jet model is the different behavior of the afterglow light curve. According to [103], when the viewing angle of the collimated jet is larger than several tens of degrees, the afterglow light curve shows a sharp rise at t $>$ $\rm t_j$ [4], and continues to rise till t = $\rm t_p$ when $\Gamma = \theta_{\rm v}$ ($\theta_{\rm v}$ is the viewing angle) is achieved. At t $>$ $\rm t_p$, the afterglow light curve becomes similar to that of the on-axis jet, hence starts to fall. Since the viewing angle of the jet will be few tens of degrees in XRFs with $E_{\rm peak}$ of a few keV at the off-axis jet model, this rise-and-fall afterglow light curve should be observed.

8.5.2 Structure jet model

In the structure jet model, the bulk Lorentz factor and also the energy per unit solid angle changes with the viewing angle of the jet. An XRF can be interpreted as a GRB structured jet with a large viewing angle.

The bulk Lorentz factor dependence of the viewing angle ($\theta_{\rm v}$) can be described as $\Gamma = \theta_{\rm v}^{-k}$ ([79], [114]). We consider the case of k = 2 in the same manner as Rossi et al. [79]. In the structure jet model, the jet opening angle which is interpreted in the Frail relation ([22], see also section 2.2.3) corresponds to the viewing angle $\theta_{\rm v}$. According to Zhang and Mészáros [114], k has to be 2 in order to not violate the Frail relation. Thus, $E_{\rm iso} \propto \theta_{\rm v}^{-2}$. Since the $E_{\rm peak}$ energy at the source frame is proportional to Γ, $E_{\rm iso}$-$E_{\rm peak}$ relation should be $E^{\rm src}_{\rm peak} \propto E_{\rm iso}$. This relation is inconsistent with the extended Amati's relation found by *HETE* (figure 7.19).

Another difficulty is the event rate of XRFs. Since the $E_{\rm iso}$ has a variation of five orders of magnitude, the viewing angle $\theta_{\rm v}$ has a variation through a factor of 100 ($E_{\rm iso} \propto \theta_{\rm v}^{-2}$). So, the event rate of the large viewing angle (e.g. XRF) must exceed the on-axis event (e.g. hard GRBs) by the factor of $\sim$ 50 if we assume the $\theta_{\rm v} \sim 2$ degrees for the on-axis event. This is also inconsistent with the observation of *HETE*.

[4] $\rm t_j$ is the "jet-break time," the time when $\Gamma = \theta_{\rm jet}^{-1}$ and the observer "sees" the entire jet surface and a break in the light curve.

8.5.3 Unified jet model

Lamb et al. [47] proposed a GRB jet model which could explain the observational characteristics from XRFs through hard GRBs in the unified picture. Their model is based on two important observational results: 1) jet opening angle corrected radiation energy is concentrated in 1.3×10^{51} ergs [22], and 2) the $E_{\rm iso} - E^{\rm src}_{\rm peak}$ relation [1] seems to be valid from XRFs through hard GRBs [82]. Assuming these two results, it is possible to construct a uniform jet model having the various jet opening angles from XRFs to hard GRBs.

When we defined the isotropic-equivalent energy $E_{\rm iso}$, the jet opening angle corrected energy $E_\gamma = 1.3 \times 10^{51}$ ergs, and the jet opening angle $\theta_{\rm jet}$, the relation discovered by Frail et al. [22] is

$$E_\gamma \propto E_{\rm iso}\, \theta^2_{\rm jet}. \tag{8.14}$$

If we substitute eq. (8.14) into $E^{\rm src}_{\rm peak} \sim E^{0.5}_{\rm iso}$,

$$E^{\rm src}_{\rm peak} \propto E^{0.5}_{\rm iso} \propto E^{0.5}_\gamma\, \theta^{-1}_{\rm jet} \propto \theta^{-1}_{\rm jet}. \tag{8.15}$$

XRFs (low $E_{\rm peak}$ energy) are then interpreted as those jets which have a large opening angle, whereas hard GRBs are those with a fine collimated jet. Because of $E_{\rm iso} \propto \theta^{-2}_{\rm jet}$, if the number of the bursts has a dependence of $\propto \theta^{-2}_{\rm jet}$, this model predicts the same number of XRFs as hard GRBs.

There is a potential difficulty with this model. If the "standard energy" in γ-ray, $E_\gamma \sim 10^{51}$ ergs, is valid, $E_{\rm iso}$ should not go below this standard energy. However, $E_{\rm iso}$ of GRB020903 is $\sim 10^{49}$ ergs. Although Lamb et al. [47] claimed that E_γ inferred by Frail et al. [22] might be too large by the factor of 100, the observed results of E_γ by Bloom et al. [9] seem to be quite solid.

8.5.4 Jet beaming model

Since the unified jet model has some difficulty in explaning the low isotropic-equivalent energy in the case of the extremely large jet opening angle, we propose the jet model in which the GRB jet itself is collimated; however, the relativistic beaming angles of γ-rays are different due to the difference of the bulk Lorentz factors. We interpret the relativistic beaming angle $\theta_{\rm beam}$ instead of the jet opening angle $\theta_{\rm jet}$ in the unified jet model. So,

$$E^{\rm src}_{\rm peak} \propto \theta^{-1}_{\rm beam}. \tag{8.16}$$

From our study in section 8.3 (see equation 8.7), $E^{\rm src}_{\rm peak}$ is proportional to the bulk Lorentz factor Γ. And we have

$$\theta_{\rm beam} \propto \Gamma^{-1}. \tag{8.17}$$

This relation is exactly same as the relativistic beaming effect. The produced γ-rays are highly (less) collimated at the shock region in the case of high (low) Lorentz factor due to the relativistic beaming effect. We assume the similarly collimated jet in the case of both high and low Lorentz factor.

In the fully adiabatic fireball, the equation of motion for the relativistic ejecta can be written as

$$(\gamma - 1)M_0c^2 + (\gamma^2 - 1)mc^2 = E_{\rm K0}, \tag{8.18}$$

where γ is the Lorentz factor of the materials which are swept up by the shell and has a relation with the bulk Lorentz factor Γ in $\gamma = \Gamma\sqrt{2}$, M_0 is the rest mass of baryons, m is the rest mass of the swept-up materials, and $E_{\rm K0}$ is the total kinetic energy of the explosion and is a constant [106]. In the ultrarelativistic limit ($m \gg M_0/\gamma$ and $\gamma \gg$1), $\gamma^2 m = const.$ Substituting this relation to the equation (8.17), we have the relation between the beaming angle and the mass of the swept-up materials in the form of

$$\theta_{\rm beam} \propto \sqrt{m}. \tag{8.19}$$

So, the low Γ GRBs (e.g. XRF) have a less of a beaming effect because of a larger mass of swept-up materials (figure 8.7).

8.5.5 Summary of XRF theoretical models

Figure 8.8 summarized the predicted $E^{\rm src}_{\rm peak}$-$E_{\rm iso}$ relations for three XRF models. The power-law dependence in the off-axis jet model will change when the viewing angle becomes larger than the jet opening angle. The structure jet model has a relation of $E^{\rm src}_{\rm peak} \propto E_{\rm iso}$ in the case of index k = 2, and it is inconsistent with the data. The unified jet model is assuming the extended Amati's relation. As seen in this figure, the key observations will be the $E^{\rm src}_{\rm peak}$ energies from a few keV to a few tens of keV.

From the overall characteristics of XRFs, the off-axis jet model might be the most promising model for explaining the observed properties of XRFs. This model has several observational predictions, and could be investigated by further observations.

When we try to interpret from the variation of bursts from XRFs to hard GRBs in the unified physical picture, it is possible to study: 1) the kinematics of the relativistic shells (variation of the bulk Lorentz factor), 2) the jet structure of GRBs (whether the jet is the structure jet, the uniform jet, or the off-axis jet), and 3) the magnetic field of the shock region when we have observed the minimum $E_{\rm peak}$ energy in the source frame. To accomplish these studies, we

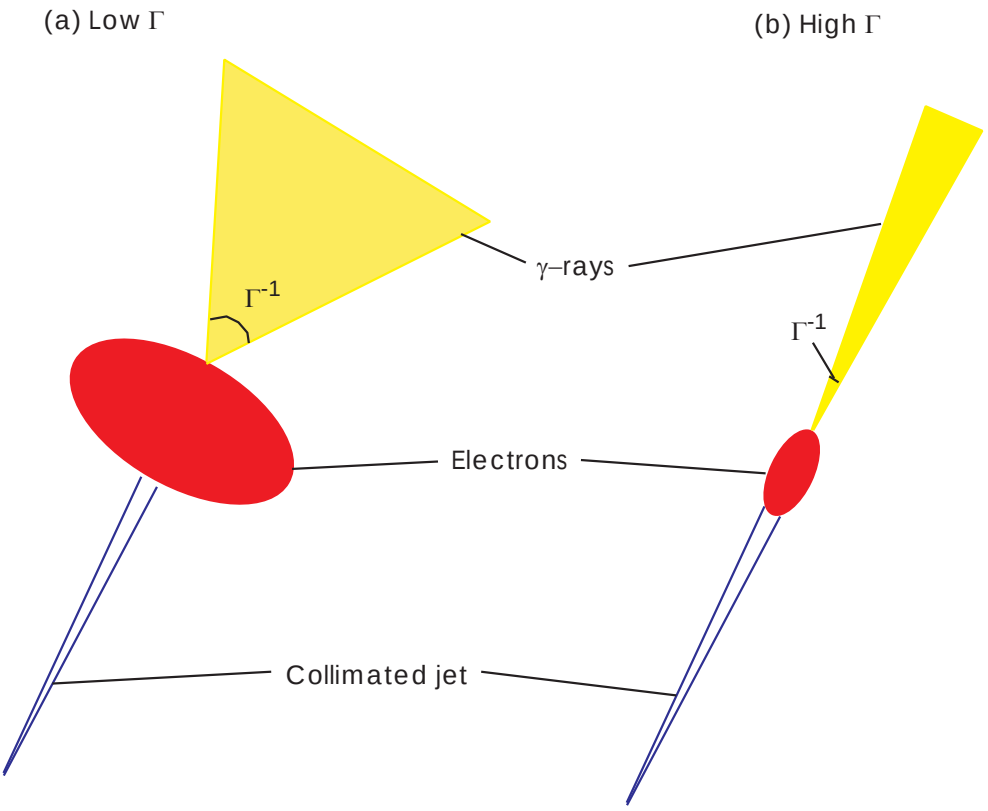

Figure 8.7: The schematic figure of the jet beaming model. The left (right) panel is in the case of the low (high) bulk Lorentz factor Γ.

definitely need a larger sample of XRFs with an $E_{\rm peak}$ energy of a few keV and also with the redshift measurements from the afterglow. The afterglow behavior of XRFs is also important to investigate. The simultaneous operation of *HETE* and *Swift* will progress the observation of XRFs which directly reflect the understanding of the prompt emission of GRBs.

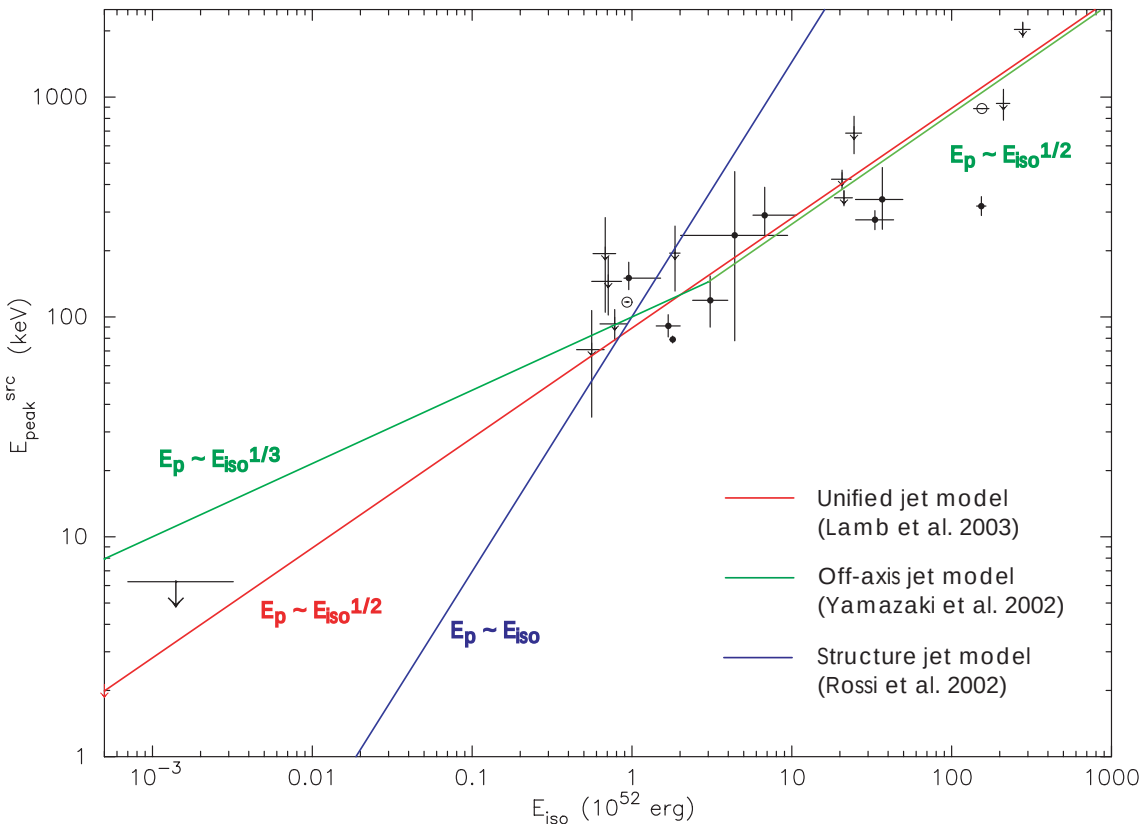

Figure 8.8: The predicted $E_{\rm peak}^{\rm src}$-$E_{\rm iso}$ relations for the unified jet model (red), the off-axis jet model (green), and the structure jet model (blue). Note that the structure jet model is in the case of the same dependence in the viewing angle for the energy per solid angle and the bulk Lorentz factor.

Chapter 9

Conclusion

Based on the detailed study of 17 *HETE*-observed X-ray flashes (XRFs) and X-ray rich GRBs (XRRs) [1], we found the following characteristics:

- Typical durations of XRFs/XRRs are similar to those of hard GRBs (a few tens of seconds).
- Most XRFs/XRRs exhibit complex time-structures similar to those of hard GRBs.
- Most XRFs/XRRs exhibit spectral softening during the burst.
- The $E_{\rm peak}$ energies of XRFs/XRRs are generally lower than those of hard GRBs.
- Six events from our sample of XRFs/XRRs had the $E_{\rm peak}$ energies as low as a few keV.
- Afterglows were found for only three XRFs — GRB020903, GRB030528, and GRB030723. This may imply that the afterglows of XRFs are generally very faint.

In the systematic study of 45 *HETE*-localized GRBs including 17 XRFs and XRRs, we found,

- The distribution of the X-ray to γ-ray fluence ratio has a single profile.
- The numbers of XRFs, XRR, and hard GRBs are roughly comparable: 15, 20, and 10 respectively in our sample.

[1] Our definitions of X-ray flashes (XRFs), X-ray rich GRBs (XRRs), and hard GRBs are the X-ray (2–30 keV; $S_{\rm X}$) to the γ-ray (30–400 keV; S_γ) fluence ratio $S_{\rm X}/S_\gamma$ of $\log(S_{\rm X}/S_\gamma) > 0$, $-0.5 < \log(S_{\rm X}/S_\gamma) \leq 0$, and $\log(S_{\rm X}/S_\gamma) \leq -0.5$ respectively.

- *HETE* XRFs/XRRs/hard GRBs are uniformly distributed in the sky.
- In spectral fits of XRFs/XRRs, low-energy photon indices are similar to those of hard GRBs, whereas, $E_{\rm peak}$ energies are systematically lower than those of hard GRBs. In particular, the $E_{\rm peak}$ energy distribution of our XRF/XRR sample is shifted to lower energy with respect to the BATSE $E_{\rm peak}$ distribution.
- The correlation between $E_{\rm peak}$ energy and time-averaged flux becomes tighter when the flux in higher energy range (i.e. γ-ray) is used. This may imply that the XRFs are intrinsically fainter than ordinary GRBs.
- The logN-logP distribution of XRFs is consistent with that expected from a uniform distribution in a Euclidean spatial geometry. This may imply that the characteristic distance scale to XRFs is shorter than that to weak hard GRBs.

There is a strong correlation between $E_{\rm peak}$ and the γ-ray peak photon flux. Using this correlation and the extended Amati relation, we found evidence that the variation of the $E_{\rm peak}$ energy from a few keV to a few MeV is only due to the relativistic beaming effect. We also estimated the magnetic field at the shock region to be $> 10^4$ gauss, by interpreting the $E_{\rm peak}$ energy as the synchrotron critical frequency of the minimum energy of electrons.

For 10 *HETE* GRBs with known-redshifts, including one XRF (GRB020903), we confirm and extend the correlation between $E_{\rm peak}$ energy in the source frame and the isotropic-equivalent energy (the extended Amati relation) to the XRF region. The Amati relation is now known to extend over five orders of magnitude in $E_{\rm iso}$. This relation gives a crucial constraint on theoretical models. For example, 1) The relativistic jets that produce GRBs must be capable of exhibiting bulk Lorentz factors ranging over three orders of magnitude, in order to produce variations in source-frame $E_{\rm peak}$ from a few keV to a few MeV , 2) the Amati relation's power-law index of 0.5 ($E_{\rm peak} \propto E_{\rm iso}^{0.5}$) must be valid from XRFs to hard GRBs, and 3) GRB models must be capable of producing isotropic-equivalent energies ranging over five orders of magnitude.

Finally, the observation of XRFs suggests that XRFs, XRRs, and hard GRBs form a continuum and are different aspects of a single phenomenon. Theoretical models must explain all these phenomena in a uniform physical picture. Further progress in observational aspects of XRFs will be achieved with a larger sample of XRFs with afterglows and redshifts. *HETE* and *Swift* should produce the required observations of XRFs, and should make possible further progress in understanding the prompt emission of GRBs.

Appendix A

WXM energy response matrix

A.1 The WXM Detector Response Matrix (DRM) Calculation

A.1.1 The WXM instrumental effects

Our DRM is calculated for each GRB event using the formula based on the calibration data taken before launch. The main formulae which we need for creating the WXM DRM are following:

1. The signal pulse height as a function of the three-dimensional location inside the detector where an X-ray photon is absorbed.
2. The empirical formula of the energy resolution for the mono-chromatic X-rays
3. The empirical formula for the energy and pulse height conversion
4. The X-ray absorption coefficients of PSPC gas (Xe, 1.36 atm, 293 K, 25.5 mm thickness), PSPC window (Be, 100 μm thickness), and thermal shield (Kapton, 7.62 μm thickness)
5. The mask shadow pattern on the detector surface (specific incident angles θ_x and θ_y)

Our code is using the various functions created for the ground localization code [92]. We summarized the major internal characteristics of the WXM PSPC.

The gain variation at both end of the anode wires ("∼" curve)

Due to the internal mechanical structure of the WXM PSPC, there is a gain variation at both end of the anode wires. As seen in figure A.1, the gas gain rises steeply at the left side, whereas

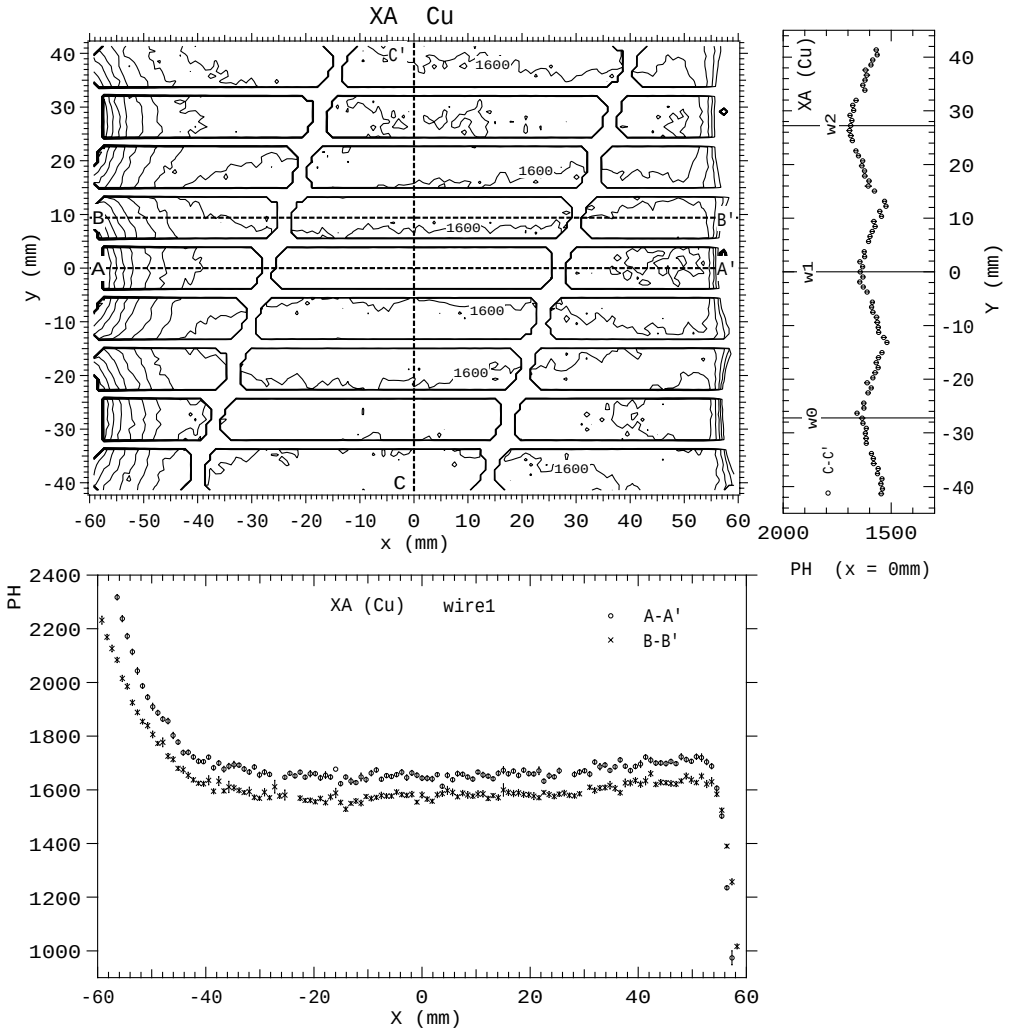

Figure A.1: The gain measurement of the XA detector at Cu K energy ($\sim$ 8 keV). Left top: a contour plot of the gas gain, bottom: the gain distribution along the A–A′ and B–B′, and right: the gain distribution along the C–C′ [92].

it drops sharply at the right side. Since the shape of the curve looks like the character "$\sim$", we called "$\sim$" (tilda) curve.

The high gain region surrounding the anode wires (M curve)

Although the physical reason is still unclear, there is the region having the maximum gas gain around 3 mm away from the anode wires. The gain also has a dip near the on-wires position. The pulse height distribution for the depth direction resembles to the character "M", so we call this effect as "M" curve. According to Sakurai et al. [83], the M curve gain structure traces the electrical field very well. Thus, the electrical fields may be playing a crucial role for this

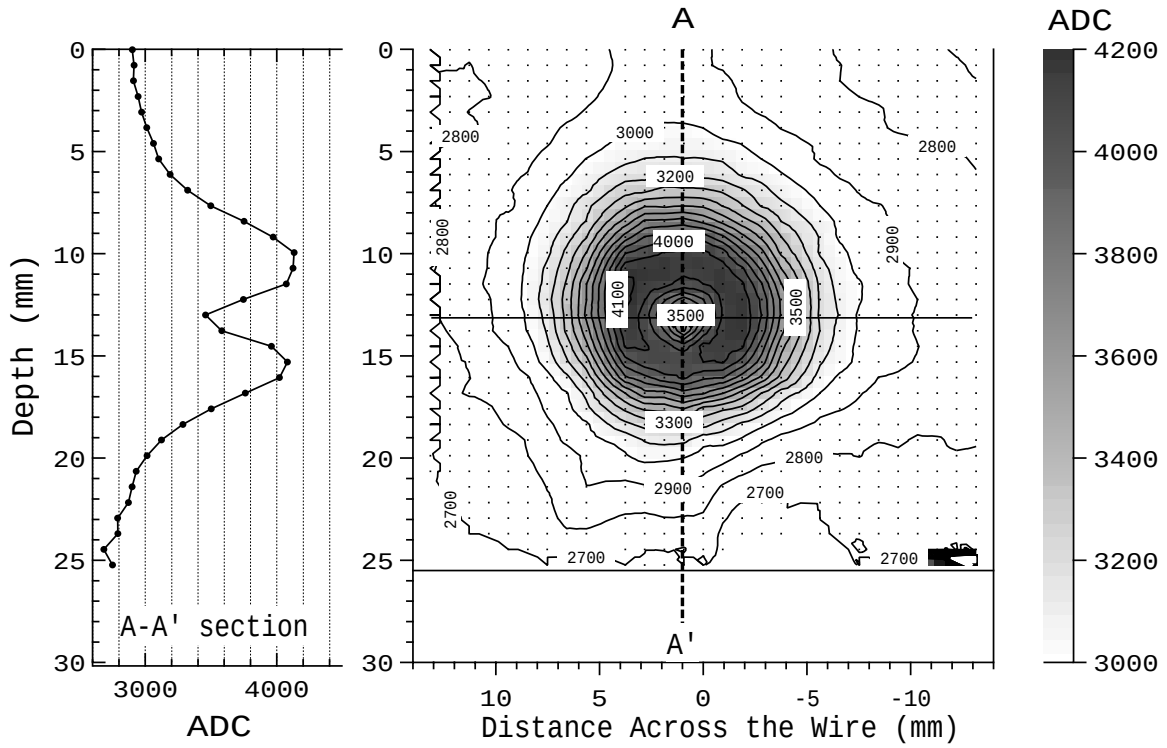

Figure A.2: The gas gain profile inside PSPC at bias voltage of 1700 V. The right contour plot shows the pulse height distribution around the wire. The left plot is the pulse height distribution as a function of the depth of PSPC [91].

anomalous gas gain.

The energy resolution

The energy resolutions as a function of incident energies at the various bias voltages are plotted in figure A.3. At the low bias voltage 1400 V, the energy resolution follows the $\sim E^{-0.5}$ law, however, it no longer follows the same law at higher voltages due to the space charge effect (see details [44]). Shirasaki et al. [91] found the empirical relation which can express the energy resolution at various operational bias voltages. This empirical relation is used in the WXM DRM calculations.

The energy and pulse height relation

The relation between the pulse height and the X-ray incident energy at various bias voltages (1300 $\sim$ 1700 V) is shown in figure A.4. As seen in this figure, the linearity between the the

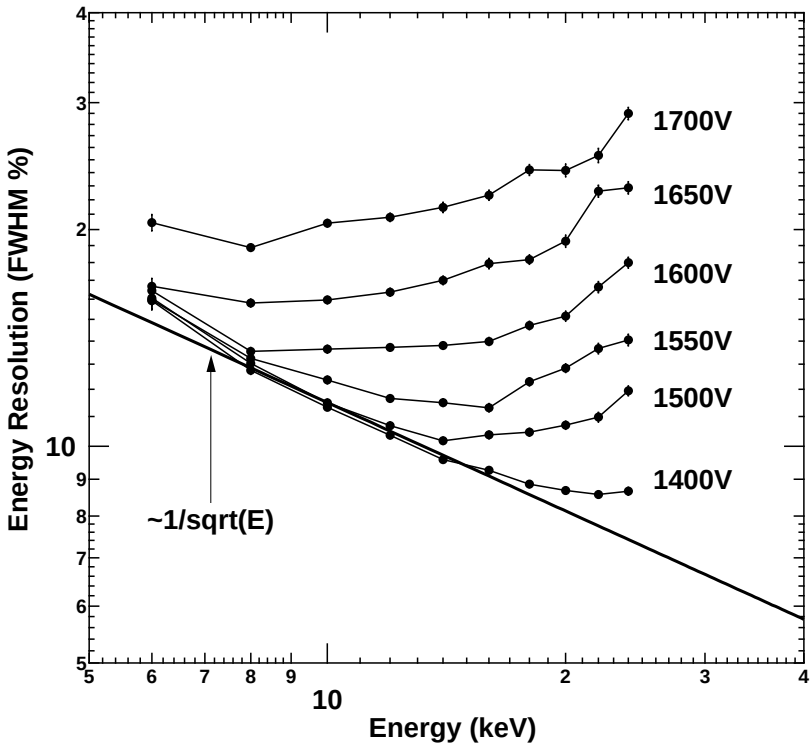

Figure A.3: The energy resolution at energies from 6 to 24 keV for bias voltage form 1400 to 1700 V. The WXM bias voltage of the normal operation is 1650 V [92].

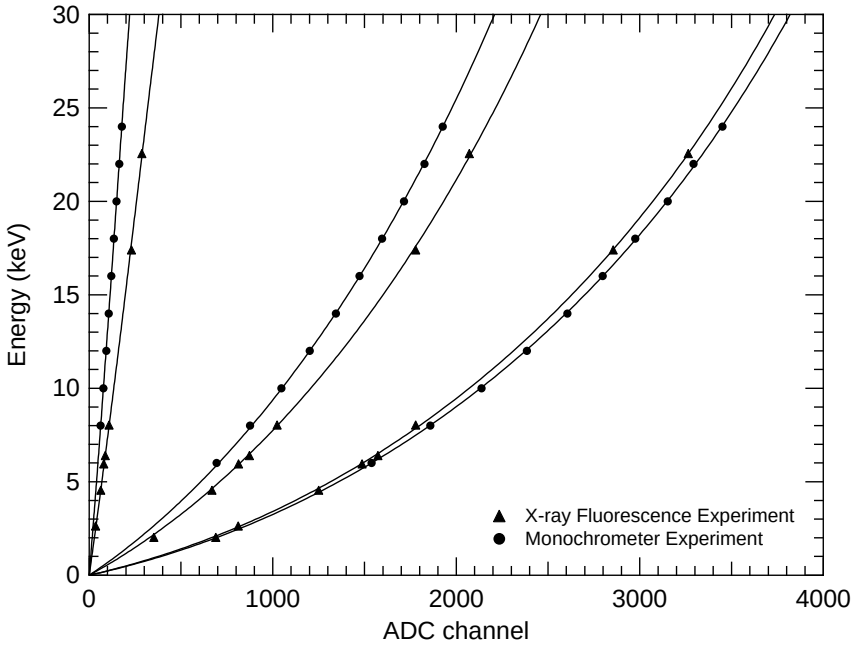

Figure A.4: Energy and pulse height relation for several bias voltages. The bias voltages are 1299, 1361, 1599, 1618, 1649, 1699 from left to right respectively [91].

pulse height and the photon energy is lost above 1600 V. Since WXM is operated with high voltage $\sim$ 1650 V, we need a non-linear formula to convert the pulse height to the photon energy. The experimental result is well represented by the following formula:

$$E = a \cdot (PH/c) + b \cdot \sinh(PH/c) + d \cdot (PH/c)^2 \tag{A.1}$$

where PH is the pulse height, a, b, c, and d are the coefficients which are a function of "effective" bias voltage[1].

A.1.2 The flow chart of the DRM code

The coordinate system used in the code is shown in figure A.5. We assume that the spectrum of the monochromatic X-ray can be expressed as a gaussian. The code calculates a gaussian for each point at (x, y, z) and sums the individual gaussian for all detector points. This summed gaussian is the spectrum including the instrumental effects such as an energy resolution, M curve, and "$\sim$" curve.

The flow chart of the main part of the code is following (see figure A.6):

[1] "effective" means that it is not the actual operating bias voltage. This "effective" bias voltage is a function of position inside the detector and also reproduces the internal gain variation of WXM (because the gain variation of WXM can be expressed as the difference of the electrical fields ("effective" bias voltage))

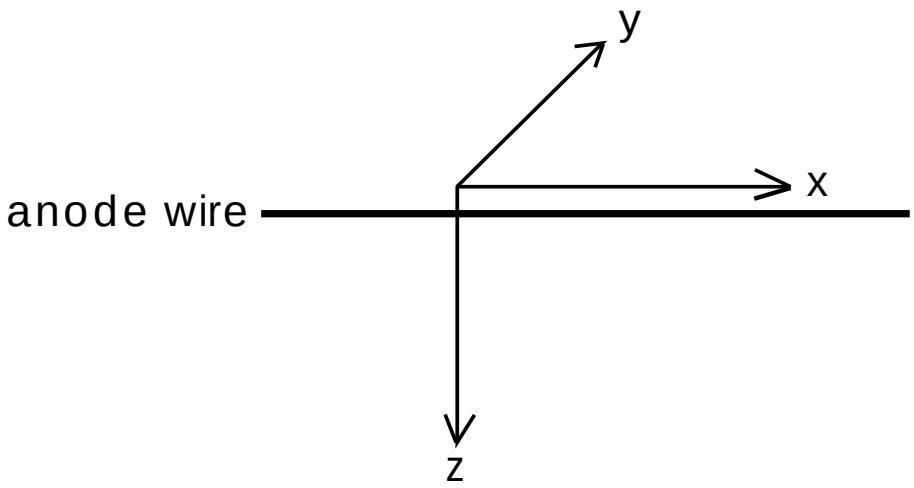

Figure A.5: The coordinate system using in the DRM code.

1. Input $\theta_{\rm x}$, $\theta_{\rm y}$, energy, and wire ID. Since the DRM code calculates the input energy from 1.5 keV to 30.0 keV in 0.1 keV step, this routine is executed 286 times.

2. Set the gain parameter ("gc" parameter). This parameter corrects for the gain difference according to the specific observing period. The gain variation of each wires at the specific observing period is corrected referring the results of ^{55}Fe gain monitoring which are automatically processed every week.

3. Calculate the absorption probability of the thermal shield (aluminum coated kapton foil, 7.6 μm), Be window (100 μm), and Xe gas (Xe 97 %/CO_2 3 %, 25.5 mm) taking into account the incidence angle of the source.

4. Start the loop for the x-direction in 1 mm step. The minimum and maximum range of the x-direction can be adjusted by the user.

5. Call the function for calculating the mask pattern at the specific θ_x and θ_y. And judge whether the x position is in the shadow of the mask or not. If the position is not illuminated by the source, the position is skipped and calculation is moved the the next x position.

6. Calculate the "effective" bias voltage, v parameter with function cal_v(). cal_v() is a function of wire ID and x position.

7. Start the loop for the y-direction in 1 mm step. The y range depends on the wires (top, middle, or bottom wire).

8. Start the loop for the z-direction in 1 mm step. The z range is from 0 to 25 mm.

9. Call the function for checking the shadow due to the support structure. If this position is in the shadow of this structure, the calculation of this position is skipped and is moved to the next position.

10. Calculate the pulse height and the energy resolution at that position. Two function, ene2adc_3d() and adc_flc() are used for this purpose. The ene2adc_3d() and adc_flc() return the pulse heigh and the 1 sigma energy resolution in ADC channels. The ene2adc_3d() is the function of wire ID, energy, and 3-dimensional position. adc_flc() is the function of the v parameter and the pulse height.

11. Start the loop for the ADC channels. The dynamic range of ADC channels depends on the data type.

12. Calculate the pulse height distribution in the gaussian with the centroid and sigma as the value of step 10. Then multiply the normalization by the Xe gas absorption probability. The pulse height distributions of all the positions are summed.

13. When all the x, y, z loop calculations are finished, multiply the normalization by the absorption probability of the thermal shield and Be window and scales by the calculation steps.

14. The effective area per energy bin will be the multiplication of the geometrical area at one wire cell and the open fraction of the mask to the result of step 13.

After this DRM calculations, the FITS conversion function is called and generates the FITS response files.

Figure A.7 shows the 2-dimensional image of the WXM DRMs. The extra tail in the high ADC channels is seen in the most of the spectra. This is due to the M-curve effect. The width of the spectrum is almost constant from 2 to 10 keV. The spectrum becomes very broad above 20 keV.

Two major effects, "M" and "∼" curves are also successfully reproduced in our DRMs (figure A.8).

A.1.3 Comparison with GRMC-flight

GRMC-flight is the Monte Carlo simulation code developed by Edward E. Fenimore (LANL). This code is used for creating the templates of the mask pattern for the on-board localization.

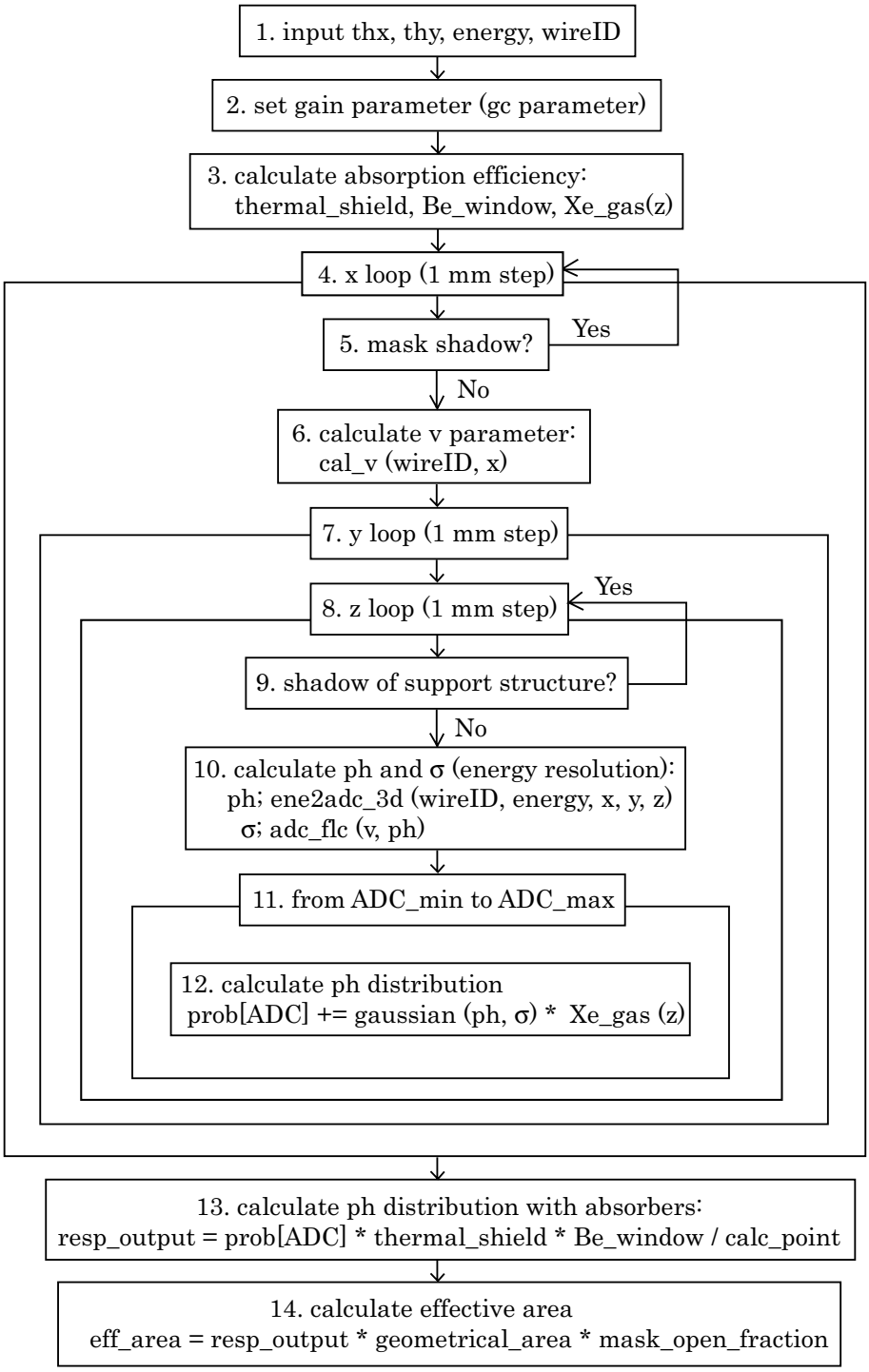

Figure A.6: The flow chart of the main part of the DRM calculation code.

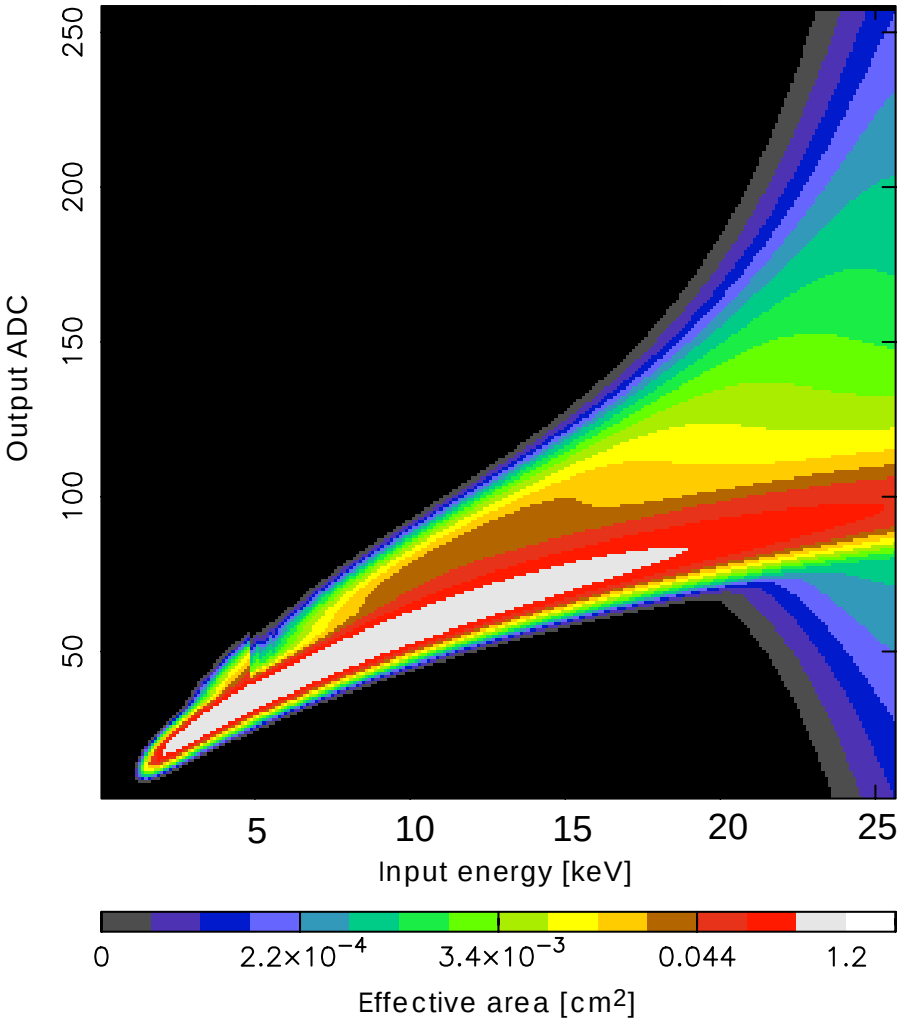

Figure A.7: The WXM DRM of XA0 wire. The horizontal axis is the input energy and the vertical axis is the output ADC channels.

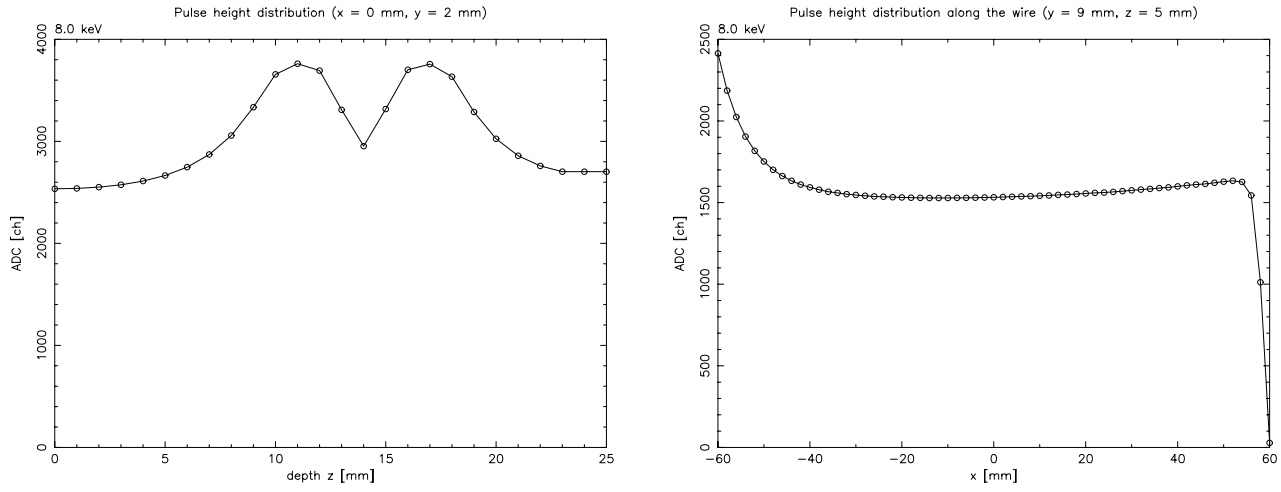

Figure A.8: Modeling two major characteristics of the WXM detector; "M" curve (left) and "∼" curve (right).

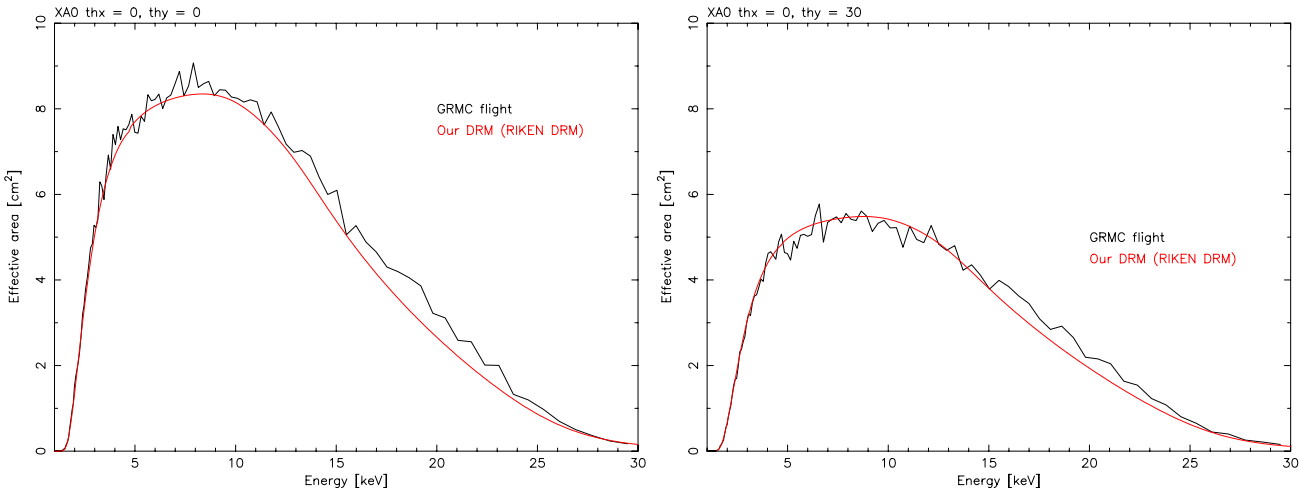

Figure A.9: The effective areas with the calculation by GRMC flight and our method are overlaied. Left: the conditions are $\theta_x = 0°$, $\theta_y = 0°$, and XA0 wire. Right: the conditions are $\theta_x = 0°$, $\theta_y = 30°$, and XA0 wire.

GRMC-flight also has been used for the DRM of *Ginga* GRBM and various simulations for the *Swift* BAT instrument.

We compare the effective area curves of our DRM and GRMC flight DRMs calculation. In figure A.9, the effective area curves by these two different calculations at the same conditions are plotted. The overall shape and normalization agree quite well. The GRMC flight calculation seems to have a larger effective area above 15 keV, however, the difference between these two calculation is less than 5%.

A.2 Crab calibration

The RAW data of the Crab nebula were collected for the purpose of calibration from December 2001 to January 2002. Since we need to check the DRMs with various incident angles, the Crab data with the different incident angles were recorded.

The Crab spectral parameters in the current DRMs (version 6.1) are shown in figure A.11. The overall spectral parameters of the Crab are mostly consistent with the known values. However, there are several problems. The N_H values show relatively small value at the large incident angle. The normalization among the wires are not completely consistent; there are 10–20% uncertainties in the normalization for individual anode wires in the current DRM.

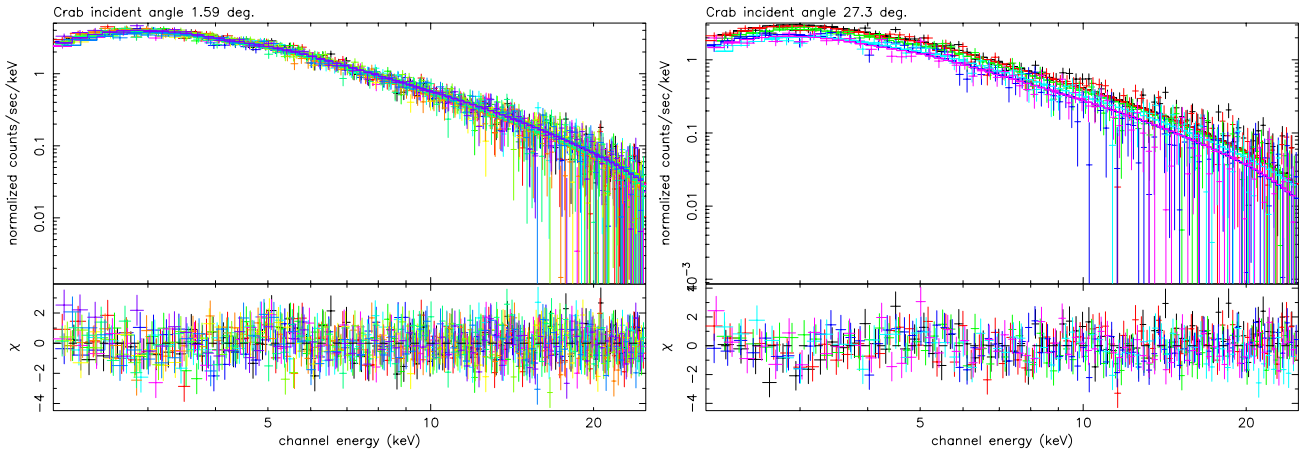

Figure A.10: The WXM Crab spectrum at the incident angle of 1.6° (Left) and 27.3° (Right).

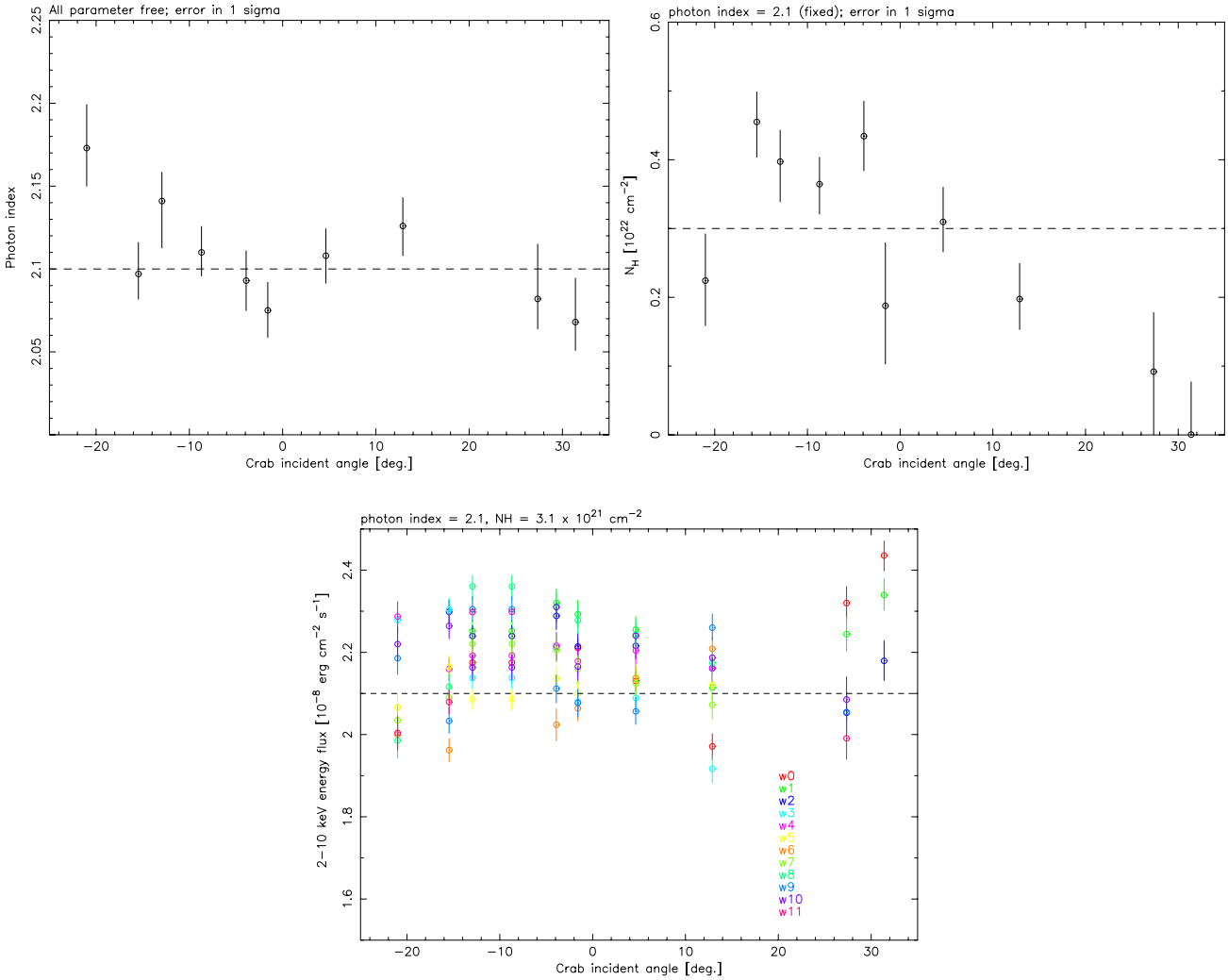

Figure A.11: The Crab spectral parameters in the various incident angles. Top left: photon index vs. incident angles, Top right: N_H vs. incident angles, Bottom: 2–10 keV energy flux vs. incident angles, Each colors represent the individual wires.

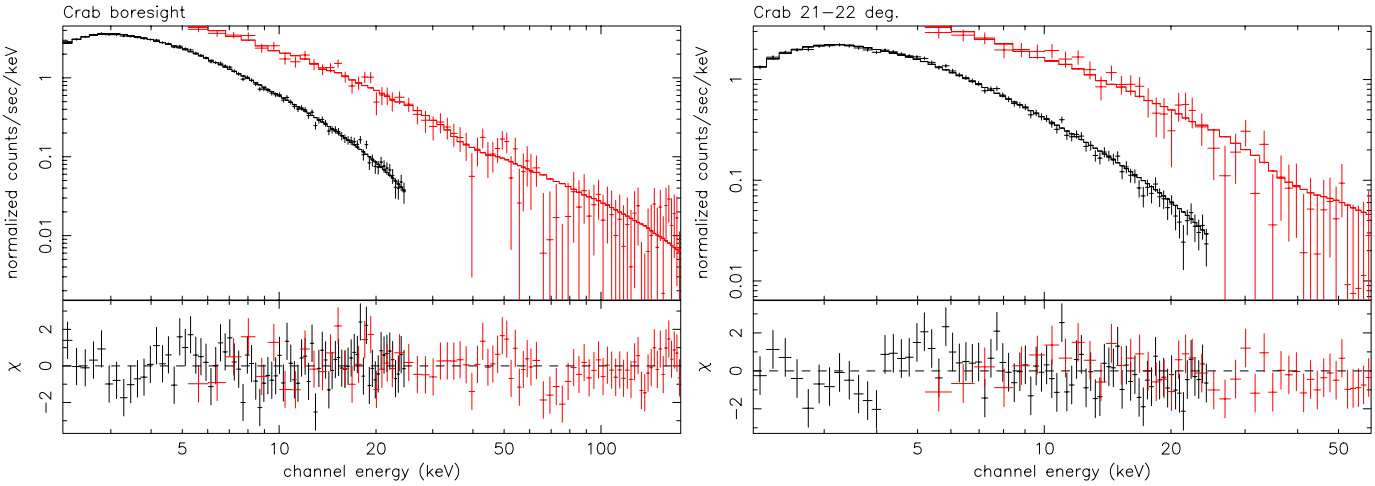

Figure A.12: The Crab spectrum of WXM (black) and FREGATE (red). Left: boresight angle, right: incident angle of 21-22°.

A.3 Cross calibration of WXM and FREGATE DRMs

The cross calibration of WXM and FREGATE DRM is performed using the Crab nebula. The WXM and FREGATE data of the Crab nebula were corrected on December 2001, and December 2002 respectively. The data with the Crab at incident angles of the boresight and 20–21° are available. The occultations of the Crab are used to accumulate the FREGATE data. We linked the value of N_H and photon index for both the WXM and FREGATE data. The normalizations of each data are kept as free parameters.

The joint fit spectral parameters of the Crab nebula are summarized in table A.1. The WXM and FREGATE DRMs can successfully represent the known spectral parameters of the Crab nebula. There is no systematic difference in the normalization between two instruments.

Table A.1: The joint fit results of the WXM and FREGATE Crab data. The quoted error is 90% confidence region.

Spectral parameters	Incident angle	
	∼0°	21–22°
N_H [10^{21} cm^{-2}]	$2.3^{+1.9}_{-1.8}$	3.0 (fixed)
Photon index	2.09 ± 0.03	2.17 ± 0.02
K^a_{15} (WXM)	(3.44 ± 0.09) × 10^{-2}	(3.10 ± 0.10) × 10^{-2}
K_{15} (FREGATE)	(3.40 ± 0.14) × 10^{-2}	(2.91 ± 0.19) × 10^{-2}
χ^2 (D.O.F.)	136.07 (156)	108.36 (117)

a normalization at 15 keV in the unit of photons cm^{-2} s^{-1} keV^{-1}

Appendix B

HETE GRB summary

Table B.1: The HETE GRBs summary table

GRB	BID	θ_X	θ_Y	TT[a]	TS[b]	EB[c]	R.A.	Dec.	error[d]	OT[e]
GRB010213	10805	-2.41	13.60	—	—	—	10h31m36s	+05d30m39s	30.2′	N
GRB010225	1491	-23.10	0.97	G	1.3s	5-120	—	—	—	N
GRB010326B	1496	7.97	-15.02	G	160ms	5-120	11h24m24s	-11d09m57s	36′	N
GRB010612	1546	13.81	1.17	G	160ms	30-400	18h03m18s	-32d08m01s	36′	N
GRB010613	1547	-30.50	25.17	G	1.3s	30-400	17h00m40s	+14d16m05s	36′	N
GRB010629B	1573	-26.60	8.29	G	1.3s	5-120	16h32m38s	-18d43m	15′	N
GRB010921	1761	-23.95	39.45	G	1.3s	5-120	22h55m35s	+40d56m	20d*15′	Y
GRB010928	1770	-2.99	35.00	G	1.3s	30-400	23h25m52s	+32d47m46s	16.4′x11°	N
GRB011019	10823	-18.29	-17.63	—	—	—	00h42m50s	-12d27m	35′	N
GRB011103	1829	-0.32	-10.94	XG	5.12s	—	03h20m37s	17d40m01s		
GRB011130	1864	-13.03	22.83	XG	5.12s	—	03h05m36s	+03d48m36s	10′	N
GRB011212	10827	-1.60	9.71	—	—	—	05h00m05s	+32d07m39s	11′	N
GRB020124	1896	14.65	-31.57	G	1.3s	30-400	09h32m49s	-11d27m35s	12′	Y
GRB020127	1902	-7.51	20.76	G	5.12s	30-400	08h15m06s	+36d44m31s	8′	Y
GRB020317	1959	-17.14	15.15	G	1.3s	5-120	10h23m21s	+12d44m38s	18′	N
GRB020331	1963	6.91	-14.33	G	160ms	30-400	13h16m34s	-17d52m29s	10′	Y
GRB020531	2042	22.94	11.33	G	20ms	30-400	15h14m45s	-19d21m35s	38′	N
GRB020625	2081	5.64	10.12	G	5.2s	30-400	20h44m14s	+07d10m12s	13.8′	N
GRB020801	2177	4.73	35.44	G	1.3s	30-400	21h02m14s	-53d46m13s	13.9′	N
GRB020812	2257	-15.30	-12.13	G	1.3s	30-400	20h38m48s	-05d23m34s	13.8′	N
GRB020813	2262	0.04	-3.81	G	1.3s	30-400	19h46m38s	-19d35m16s	1′(S)	Y
GRB020819	2275	17.70	-22.45	G	160ms	30-400	23h27m07s	+06d21m50s	7′	Y
GRB020903	2314	4.20	12.64	XG	5.12s	—	22h49m25s	-20d53m59s	16.7′	Y?
GRB021004	2380	3.92	-12.39	G	5.2s	30-400	00h26m57s	+18d55m44s	2′(S)	Y
GRB021021	10623	15.24	11.92	—	—	—	00h17m23s	-01d37m00s	20′	N
GRB021104	2434	22.56	22.38	G	1.3s	5-120	03h53m48s	+37d57m12s	26′	N
GRB021112	2448	12.24	27.06	G	1.3s	5-120	02h36m52s	+48d50m56s	20′	N
GRB021211	2493	-12.55	-0.01	G	160ms	30-400	08h09m00s	+06d44m20s	2′(S)	Y
GRB030115	2533	13.01	-3.11	G	1.3s	30-400	11h18m30s	+15d02m17s	2′(S)	Y
GRB030226	10893	-13.00	-16.27	—	—	—	11h33m01s	+25d53m56s	2′(S)	Y
GRB030323	2640	4.05	35.06	XG	320ms	—	11h06m54s	-21d51m00s	18′	Y
GRB030324	2641	-26.35	0.57	G	1.3s	30-400	13h37m11s	-00d19m22s	7′	Y
GRB030328	2650	5.05	7.14	G	1.3s	5-120	12h10m51s	-09d21m05s	1′(S)	Y
GRB030329	2652	26.68	-29.00	G	1.3s	5-120	10h44m49s	+21d28m44s	2′(S)	Y
GRB030416	10897	-1.98	-11.32	—	—	—	11h06m51s	-02d52m58s	7′	N
GRB030418	2686	7.45	-9.66	XG	13.280s	—	10h54m53s	-06d59m22s	9′	Y
GRB030429	2695	8.88	11.83	XG	6.72s	—	12h13m06s	-20d56m00s	1′(S)	Y
GRB030519	2716	-41.00	16.18	G	160ms	30-400	14h58m18s	-32d56m57s	30′	N
GRB030528	2724	20.66	6.14	G	1.3s	30-400	17h04m02s	-22d38m59s	2′(S)	Y
GRB030723	2777	1.55	10.93	XG	6.72s	WXM	21h49m30s	-27d42m06s	2′(S)	Y
GRB030725	2779	18.41	33.10	G	160ms	5-120	20h33m47s	-50d45m49s	14.4′	Y
GRB030821	2814	12.13	32.47	G	1.3s	30-400	21h42m33s	-45d12m12s	120′x10′	N
GRB030823	2818	11.67	-32.65	G	5.2s	5-120	21h30m47s	+21d59m46s	5.4′	N
GRB030824	2821	-29.79	-31.43	G	1.3s	5-120	00h05m02s	+19d55m37s	11.2′	N
GRB030913	2849	-2.05	4.62	G	1.3s	30-400	20h58m02s	-02d12m32s	30′	N

a Triggered type; G: FREGATE triggered, XG: FREGATE triggered by XDSP

b Triggered time-scale

c Triggered energy band in keV

d Location error radius in (90% confidence)

e Whether optical transient was discovered (Y) or not (N)

Table B.2: The HETE GRBs spectral parameters

GRB	Class[a]	Model[b]	α	β	$E_{\rm peak}$ [keV]	K_{15}^{c}	χ^2_ν	D.O.F.
GRB010213	XRF	Band	-1.00(fixed)	$-2.96^{+0.22}_{-0.54}$	$3.41^{+0.35}_{-0.40}$	$44.63^{+7.63}_{-5.19}$	0.940	44
GRB010225	XRF	CPL	$-1.31^{+0.30}_{-0.26}$	—	$31.57^{+26.50}_{-9.17}$	$6.75^{+2.93}_{-1.87}$	0.925	39
GRB010326B†	XRR	CPL	$-1.08^{+0.25}_{-0.22}$	—	$51.77^{+18.61}_{-11.25}$	$13.19^{+3.07}_{-2.31}$	0.856	111
GRB010612	GRB	CPL	$-1.07^{+0.19}_{-0.17}$	—	$244.50^{+285.07}_{-81.97}$	$2.93^{+0.37}_{-0.36}$	0.884	65
GRB010613	XRR	Band	$-0.95^{+0.33}_{-0.26}$	$-2.01^{+0.09}_{-0.15}$	$46.25^{+17.78}_{-10.38}$	$15.24^{+4.37}_{-2.43}$	0.785	134
GRB010629B	XRR	CPL	$-1.12^{+0.14}_{-0.13}$	—	$45.57^{+4.61}_{-3.84}$	$20.05^{+1.77}_{-1.56}$	0.817	110
GRB010921†	XRR	CPL	$-1.55^{+0.08}_{-0.07}$	—	$88.63^{+21.76}_{-13.79}$	$41.79^{+1.75}_{-1.63}$	0.939	140
GRB010928†	GRB	CPL	$-0.66^{+0.10}_{-0.09}$	—	$409.50^{+118.46}_{-74.98}$	$6.30^{+0.55}_{-0.55}$	0.825	125
GRB011019	XRF	CPL	-1.43 (fixed)	—	$18.71^{+18.33}_{-8.72}$	$2.46^{+0.82}_{-0.63}$	0.854	68
GRB011103	XRR	PL	$-1.73^{+0.24}_{-0.29}$	—	—	$2.72^{+0.88}_{-0.88}$	1.266	38
GRB011130	XRF	PL	$-2.65^{+0.26}_{-0.33}$	—	< 4.9[d]	$0.69^{+0.29}_{-0.26}$	1.016	40
GRB011212	XRF	PL	$-2.07^{+0.19}_{-0.22}$	—	—	$0.72^{+0.17}_{-0.18}$	0.795	54
GRB020124	XRR	CPL	$-0.79^{+0.15}_{-0.14}$	—	$86.93^{+18.11}_{-12.45}$	$9.24^{+0.98}_{-0.88}$	0.710	95
GRB020127	XRR	CPL	$-1.03^{+0.14}_{-0.13}$	—	$104.00^{+47.00}_{-24.10}$	$4.50^{+0.58}_{-0.51}$	0.746	110
GRB020317	XRF	CPL	$-0.61^{+0.61}_{-0.52}$	—	$28.41^{+12.68}_{-7.41}$	$7.27^{+7.73}_{-3.12}$	0.923	53
GRB020331	GRB	CPL	$-0.79^{+0.13}_{-0.12}$	—	$91.57^{+20.99}_{-14.09}$	$4.03^{+0.46}_{-0.41}$	0.732	111
GRB020531	GRB	CPL	$-0.83^{+0.14}_{-0.13}$	—	$230.60^{+113.10}_{-58.11}$	$20.99^{+2.31}_{-2.21}$	0.831	141
GRB020625	XRF	CPL	-1.14 (fixed)	—	$8.52^{+5.44}_{-2.91}$	$2.84^{+1.05}_{-0.78}$	0.781	55
GRB020801†	GRB	Band	$-0.32^{+0.44}_{-0.34}$	$-2.01^{+0.17}_{-0.25}$	$53.35^{+14.37}_{-11.12}$	$5.66^{+1.92}_{-1.02}$	0.638	140
GRB020812	XRR	CPL	$-1.09^{+0.29}_{-0.25}$	—	$87.62^{+106.03}_{-29.57}$	$2.27^{+0.61}_{-0.47}$	0.664	68
GRB020813†	GRB	Band	$-0.94^{+0.03}_{-0.03}$	$-1.57^{+0.03}_{-0.04}$	$142.10^{+14.05}_{-12.91}$	$20.74^{+0.51}_{-0.47}$	1.160	140
GRB020819	XRR	Band	$-0.90^{+0.17}_{-0.14}$	$-1.99^{+0.18}_{-0.48}$	$49.90^{+17.88}_{-12.19}$	$10.71^{+2.47}_{-1.65}$	0.945	108
GRB020903	XRF	PL	$-2.62^{+0.42}_{-0.55}$	—	< 5.0[d]	$0.41^{+0.34}_{-0.25}$	0.845	26
GRB021004	XRR	CPL	$-1.01^{+0.19}_{-0.17}$	—	$79.79^{+53.35}_{-22.97}$	$2.77^{+0.60}_{-0.48}$	0.949	68
GRB021021	XRF	CPL	-1.33 (fixed)	—	$15.38^{+14.24}_{-7.47}$	$1.24^{+0.50}_{-0.37}$	0.879	41
GRB021104†	XRF	CPL	$-1.11^{+0.54}_{-0.46}$	—	$28.21^{+17.41}_{-7.88}$	$7.59^{+5.31}_{-2.55}$	0.744	38
GRB021112	XRR	CPL	$-0.94^{+0.42}_{-0.32}$	—	$57.15^{+38.90}_{-20.70}$	$6.57^{+3.47}_{-1.83}$	1.126	61
GRB021211	XRR	Band	$-0.86^{+0.10}_{-0.09}$	$-2.18^{+0.14}_{-0.25}$	$45.56^{+7.84}_{-6.23}$	$32.58^{+4.16}_{-3.32}$	1.149	140
GRB030115	XRR	CPL	$-1.28^{+0.14}_{-0.13}$	—	$82.79^{+52.82}_{-22.26}$	$3.50^{+0.53}_{-0.46}$	0.812	67
GRB030226	GRB	CPL	$-0.89^{+0.17}_{-0.15}$	—	$97.12^{+26.98}_{-17.06}$	$3.47^{+0.42}_{-0.38}$	0.894	139
GRB030323	XRR	PL	$-1.62^{+0.24}_{-0.25}$	—	—	$2.19^{+0.64}_{-0.67}$	0.835	33
GRB030324	XRR	CPL	$-1.45^{+0.14}_{-0.12}$	—	$146.80^{+627.57}_{-65.49}$	$4.94^{+0.72}_{-0.60}$	0.882	76
GRB030328	GRB	Band	$-1.14^{+0.03}_{-0.03}$	$-2.09^{+0.19}_{-0.40}$	$126.30^{+13.89}_{-13.10}$	$6.64^{+0.20}_{-0.18}$	0.982	140
GRB030329	XRR	Band	$-1.26^{+0.01}_{-0.02}$	$-2.28^{+0.05}_{-0.06}$	$67.86^{+2.31}_{-2.15}$	$146.20^{+1.70}_{-1.70}$	1.537	139
GRB030416	XRF	PL	$-2.31^{+0.13}_{-0.15}$	—	< 3.8[d]	$0.92^{+0.17}_{-0.17}$	0.870	54
GRB030418	XRR	CPL	$-1.46^{+0.14}_{-0.13}$	—	$46.10^{+31.96}_{-13.70}$	$2.43^{+0.48}_{-0.37}$	0.929	68
GRB030429	XRF	CPL	$-1.12^{+0.25}_{-0.22}$	—	$35.04^{+11.75}_{-7.90}$	$4.05^{+1.32}_{-0.90}$	0.720	68
GRB030519†	GRB	Band	$-0.75^{+0.07}_{-0.06}$	$-1.72^{+0.05}_{-0.07}$	$137.60^{+17.80}_{-15.36}$	$73.21^{+2.06}_{-1.90}$	0.742	124
GRB030528†	XRF	Band	$-1.33^{+0.15}_{-0.12}$	$-2.65^{+0.29}_{-0.98}$	$31.84^{+4.67}_{-4.97}$	$13.94^{+2.44}_{-1.48}$	0.809	109
GRB030723	XRR	PL	$-1.93^{+0.15}_{-0.17}$	—	—	$1.39^{+0.28}_{-0.28}$	1.117	40
GRB030725	XRR	CPL	$-1.51^{+0.04}_{-0.04}$	—	$102.80^{+19.05}_{-13.73}$	$15.71^{+0.54}_{-0.50}$	1.069	141
GRB030821	XRR	CPL	$-0.88^{+0.13}_{-0.12}$	—	$84.26^{+15.12}_{-10.88}$	$8.74^{+0.77}_{-0.70}$	0.971	98
GRB030823	XRF	CPL	$-1.31^{+0.20}_{-0.18}$	—	$26.57^{+7.45}_{-5.02}$	$8.26^{+2.34}_{-1.59}$	0.708	110
GRB030824	XRF	PL	$-2.14^{+0.13}_{-0.14}$	—	< 8.7[d]	$5.25^{+0.76}_{-0.78}$	0.813	53
GRB030913	GRB	CPL	$-0.82^{+0.28}_{-0.24}$	—	$119.70^{+113.25}_{-36.47}$	$3.53^{+0.75}_{-0.62}$	0.740	53

a GRB classification; XRF: X-ray-flash, XRR: X-ray-rich GRB, GRB: Hard GRB

b Spectral model; PL: Power-law, CPL: Cutoff power-law, Band: Band function

c Normalization at 15 keV in the unit of 10^{-2} photon cm^{-2} s^{-1} keV^{-1}

d 99.7% upper limit derived by the *constrain* Band function

† The constant factor is multiplied to the spectral model.

Table B.3: The HETE GRBs time-average photon flux and fluence

GRB	Duration	Photon flux[a]			Photon fluence[b]		
	[sec.]	2–30 keV	30–400 keV	2–400 keV	2–30 keV	30–400 keV	2–400 keV
GRB010213	34.41	$3.23^{+0.15}_{-0.14}$	$0.02^{+0.02}_{-0.01}$	$3.25^{+0.16}_{-0.14}$	$11.11^{+0.52}_{-0.48}$	$0.07^{+0.07}_{-0.03}$	$11.18^{+0.55}_{-0.48}$
GRB010225	9.76	$2.90^{+0.38}_{-0.39}$	$0.28^{+0.10}_{-0.09}$	$3.18^{+0.40}_{-0.40}$	$2.83^{+0.37}_{-0.38}$	$0.27^{+0.10}_{-0.09}$	$3.10^{+0.39}_{-0.39}$
GRB010326B	3.50	$4.79^{+0.81}_{-0.79}$	$0.93^{+0.15}_{-0.16}$	$5.71^{+0.83}_{-0.79}$	$1.68^{+0.28}_{-0.28}$	$0.33^{+0.05}_{-0.06}$	$2.00^{+0.29}_{-0.28}$
GRB010612	47.19	$1.20^{+0.28}_{-0.25}$	$0.62^{+0.05}_{-0.04}$	$1.82^{+0.29}_{-0.26}$	$5.66^{+1.32}_{-1.18}$	$2.93^{+0.24}_{-0.19}$	$8.59^{+1.37}_{-1.23}$
GRB010613	141.56	$4.75^{+0.79}_{-0.64}$	$1.19^{+0.04}_{-0.04}$	$5.94^{+0.79}_{-0.65}$	$67.24^{+11.18}_{-9.06}$	$16.85^{+0.56}_{-0.57}$	$84.09^{+11.18}_{-9.20}$
GRB010629B	24.58	$7.44^{+0.87}_{-0.82}$	$1.22^{+0.07}_{-0.07}$	$8.66^{+0.87}_{-0.82}$	$18.29^{+2.14}_{-2.02}$	$3.00^{+0.17}_{-0.17}$	$21.29^{+2.13}_{-2.02}$
GRB010921	23.85	$25.58^{+2.05}_{-1.92}$	$3.71^{+0.15}_{-0.15}$	$29.30^{+2.02}_{-1.91}$	$61.01^{+4.89}_{-4.58}$	$8.85^{+0.36}_{-0.36}$	$69.88^{+4.82}_{-4.55}$
GRB010928	34.55	$2.04^{+0.28}_{-0.26}$	$3.03^{+0.09}_{-0.09}$	$5.06^{+0.29}_{-0.27}$	$7.05^{+0.97}_{-0.90}$	$10.47^{+0.31}_{-0.31}$	$17.48^{+1.00}_{-0.93}$
GRB011019	24.57	$1.12^{+0.23}_{-0.23}$	$0.06^{+0.05}_{-0.04}$	$1.18^{+0.23}_{-0.23}$	$2.75^{+0.57}_{-0.56}$	$0.15^{+0.12}_{-0.10}$	$2.90^{+0.57}_{-0.56}$
GRB011103	14.75	$2.09^{+0.34}_{-0.34}$	$0.28^{+0.27}_{-0.15}$	$2.37^{+0.46}_{-0.43}$	$3.08^{+0.50}_{-0.50}$	$0.41^{+0.40}_{-0.22}$	$3.50^{+0.68}_{-0.64}$
GRB011130	50.00	$1.72^{+0.26}_{-0.26}$	$0.02^{+0.02}_{-0.01}$	$1.74^{+0.25}_{-0.26}$	$8.60^{+1.30}_{-1.30}$	$0.10^{+0.10}_{-0.05}$	$8.70^{+1.25}_{-1.30}$
GRB011212	57.68	$0.82^{+0.12}_{-0.12}$	$0.04^{+0.03}_{-0.01}$	$0.86^{+0.13}_{-0.12}$	$4.73^{+0.69}_{-0.69}$	$0.23^{+0.17}_{-0.06}$	$4.96^{+0.75}_{-0.69}$
GRB020124	40.63	$2.83^{+0.29}_{-0.29}$	$1.26^{+0.09}_{-0.10}$	$4.08^{+0.32}_{-0.30}$	$11.50^{+1.18}_{-1.18}$	$5.12^{+0.37}_{-0.41}$	$16.58^{+1.30}_{-1.22}$
GRB020127	25.63	$1.70^{+0.16}_{-0.16}$	$0.61^{+0.07}_{-0.06}$	$2.31^{+0.18}_{-0.18}$	$4.36^{+0.41}_{-0.41}$	$1.56^{+0.18}_{-0.15}$	$5.92^{+0.46}_{-0.46}$
GRB020317	10.00	$1.38^{+0.35}_{-0.33}$	$0.17^{+0.08}_{-0.07}$	$1.55^{+0.37}_{-0.34}$	$1.38^{+0.35}_{-0.33}$	$0.17^{+0.08}_{-0.07}$	$1.55^{+0.37}_{-0.34}$
GRB020331	75.00	$1.24^{+0.10}_{-0.09}$	$0.58^{+0.05}_{-0.05}$	$1.82^{+0.11}_{-0.11}$	$9.30^{+0.75}_{-0.68}$	$4.35^{+0.38}_{-0.38}$	$13.65^{+0.83}_{-0.83}$
GRB020531	1.04	$7.25^{+1.08}_{-1.05}$	$5.94^{+0.46}_{-0.46}$	$13.19^{+1.18}_{-1.16}$	$0.75^{+0.11}_{-0.11}$	$0.62^{+0.05}_{-0.05}$	$1.37^{+0.12}_{-0.12}$
GRB020625	41.94	$0.59^{+0.10}_{-0.09}$	$0.00^{+0.01}_{-0.00}$	$0.60^{+0.09}_{-0.09}$	$2.47^{+0.42}_{-0.38}$	$0.02^{+0.05}_{-0.02}$	$2.52^{+0.38}_{-0.38}$
GRB020801	117.97	$1.11^{+0.23}_{-0.20}$	$0.59^{+0.04}_{-0.04}$	$1.70^{+0.23}_{-0.20}$	$13.09^{+2.72}_{-2.35}$	$6.96^{+0.47}_{-0.47}$	$20.05^{+2.72}_{-2.35}$
GRB020812	60.16	$0.88^{+0.17}_{-0.16}$	$0.26^{+0.06}_{-0.05}$	$1.14^{+0.18}_{-0.16}$	$5.29^{+1.02}_{-0.96}$	$1.56^{+0.36}_{-0.30}$	$6.86^{+1.08}_{-0.96}$
GRB020813	113.00	$7.48^{+0.20}_{-0.19}$	$4.25^{+0.04}_{-0.04}$	$11.73^{+0.21}_{-0.20}$	$84.52^{+2.26}_{-2.14}$	$48.02^{+0.46}_{-0.45}$	$132.50^{+2.40}_{-2.20}$
GRB020819	50.16	$3.25^{+0.17}_{-0.18}$	$0.91^{+0.07}_{-0.06}$	$4.16^{+0.19}_{-0.19}$	$16.30^{+0.85}_{-0.90}$	$4.57^{+0.35}_{-0.30}$	$20.87^{+0.95}_{-0.96}$
GRB020903	13.00	$0.99^{+0.20}_{-0.20}$	$0.01^{+0.03}_{-0.01}$	$0.98^{+0.21}_{-0.21}$	$1.26^{+0.27}_{-0.26}$	$0.02^{+0.03}_{-0.01}$	$1.27^{+0.27}_{-0.27}$
GRB021004	49.70	$1.00^{+0.10}_{-0.09}$	$0.31^{+0.05}_{-0.06}$	$1.31^{+0.11}_{-0.11}$	$4.97^{+0.50}_{-0.45}$	$1.54^{+0.25}_{-0.30}$	$6.51^{+0.55}_{-0.55}$
GRB021021	49.15	$0.47^{+0.11}_{-0.11}$	$0.02^{+0.02}_{-0.01}$	$0.49^{+0.11}_{-0.12}$	$2.31^{+0.54}_{-0.54}$	$0.09^{+0.11}_{-0.07}$	$2.41^{+0.54}_{-0.59}$
GRB021104	31.41	$2.51^{+0.95}_{-0.67}$	$0.24^{+0.10}_{-0.08}$	$2.75^{+0.96}_{-0.68}$	$7.88^{+2.99}_{-2.11}$	$0.75^{+0.31}_{-0.25}$	$8.64^{+3.01}_{-2.14}$
GRB021112	4.00	$2.12^{+0.52}_{-0.50}$	$0.53^{+0.16}_{-0.16}$	$2.65^{+0.55}_{-0.53}$	$0.85^{+0.21}_{-0.20}$	$0.21^{+0.06}_{-0.06}$	$1.06^{+0.22}_{-0.21}$
GRB021211	8.00	$9.32^{+0.30}_{-0.30}$	$2.36^{+0.11}_{-0.11}$	$11.68^{+0.33}_{-0.32}$	$7.46^{+0.24}_{-0.24}$	$1.89^{+0.09}_{-0.09}$	$9.34^{+0.26}_{-0.26}$
GRB030115	36.00	$1.63^{+0.15}_{-0.15}$	$0.35^{+0.04}_{-0.05}$	$1.98^{+0.16}_{-0.16}$	$5.87^{+0.54}_{-0.54}$	$1.26^{+0.14}_{-0.18}$	$7.13^{+0.58}_{-0.58}$
GRB030226	68.81	$1.16^{+0.15}_{-0.15}$	$0.49^{+0.05}_{-0.04}$	$1.66^{+0.15}_{-0.16}$	$7.98^{+1.03}_{-1.03}$	$3.37^{+0.34}_{-0.28}$	$11.42^{+1.03}_{-1.10}$
GRB030323	19.61	$1.49^{+0.82}_{-0.64}$	$0.28^{+0.08}_{-0.09}$	$1.77^{+0.79}_{-0.64}$	$2.92^{+1.61}_{-1.25}$	$0.55^{+0.16}_{-0.18}$	$3.47^{+1.55}_{-1.26}$
GRB030324	15.73	$2.78^{+0.29}_{-0.27}$	$0.57^{+0.08}_{-0.08}$	$3.35^{+0.30}_{-0.29}$	$4.37^{+0.46}_{-0.43}$	$0.90^{+0.13}_{-0.13}$	$5.27^{+0.47}_{-0.46}$
GRB030328	199.23	$2.79^{+0.06}_{-0.05}$	$0.97^{+0.03}_{-0.02}$	$3.77^{+0.06}_{-0.06}$	$55.59^{+1.19}_{-1.00}$	$19.33^{+0.59}_{-0.40}$	$75.11^{+1.20}_{-1.20}$
GRB030329	62.94	$65.47^{+0.66}_{-0.66}$	$13.40^{+0.09}_{-0.09}$	$78.86^{+0.67}_{-0.65}$	$412.10^{+4.10}_{-4.20}$	$84.34^{+0.57}_{-0.57}$	$496.30^{+4.30}_{-4.00}$
GRB030416	78.64	$1.45^{+0.12}_{-0.13}$	$0.04^{+0.02}_{-0.01}$	$1.49^{+0.13}_{-0.13}$	$11.40^{+0.95}_{-1.02}$	$0.31^{+0.16}_{-0.08}$	$11.72^{+1.02}_{-1.02}$
GRB030418	110.10	$1.30^{+0.08}_{-0.08}$	$0.15^{+0.04}_{-0.03}$	$1.46^{+0.08}_{-0.09}$	$14.31^{+0.88}_{-0.88}$	$1.65^{+0.44}_{-0.33}$	$16.07^{+0.89}_{-0.99}$
GRB030429	24.58	$1.43^{+0.19}_{-0.18}$	$0.18^{+0.04}_{-0.05}$	$1.61^{+0.19}_{-0.19}$	$3.52^{+0.47}_{-0.44}$	$0.44^{+0.10}_{-0.12}$	$3.96^{+0.47}_{-0.47}$
GRB030519	20.97	$23.16^{+1.17}_{-1.14}$	$17.05^{+0.11}_{-0.21}$	$40.21^{+1.16}_{-1.12}$	$48.57^{+2.45}_{-2.39}$	$35.75^{+0.23}_{-0.44}$	$84.32^{+2.43}_{-2.35}$
GRB030528	83.56	$6.13^{+0.48}_{-0.47}$	$0.64^{+0.04}_{-0.04}$	$6.77^{+0.49}_{-0.46}$	$51.22^{+4.01}_{-3.93}$	$5.35^{+0.33}_{-0.33}$	$56.57^{+4.09}_{-3.84}$
GRB030723	18.70	$1.34^{+0.17}_{-0.16}$	$0.11^{+0.05}_{-0.04}$	$1.45^{+0.17}_{-0.17}$	$2.51^{+0.32}_{-0.30}$	$0.21^{+0.09}_{-0.07}$	$2.71^{+0.32}_{-0.32}$
GRB030725	83.88	$9.36^{+0.33}_{-0.33}$	$1.51^{+0.05}_{-0.05}$	$10.87^{+0.34}_{-0.33}$	$78.51^{+2.77}_{-2.77}$	$12.67^{+0.42}_{-0.42}$	$91.18^{+2.85}_{-2.77}$
GRB030821	21.21	$2.86^{+0.29}_{-0.27}$	$1.09^{+0.07}_{-0.07}$	$3.95^{+0.30}_{-0.28}$	$6.07^{+0.62}_{-0.57}$	$2.31^{+0.15}_{-0.15}$	$8.38^{+0.64}_{-0.59}$
GRB030823	55.56	$3.44^{+0.33}_{-0.31}$	$0.28^{+0.06}_{-0.06}$	$3.72^{+0.33}_{-0.33}$	$19.11^{+1.84}_{-1.72}$	$1.56^{+0.33}_{-0.33}$	$20.67^{+1.83}_{-1.84}$
GRB030824	15.73	$6.57^{+0.97}_{-0.96}$	$0.30^{+0.09}_{-0.09}$	$6.86^{+0.96}_{-0.94}$	$10.33^{+1.53}_{-1.50}$	$0.47^{+0.14}_{-0.14}$	$10.79^{+1.51}_{-1.48}$
GRB030913	9.12	$1.15^{+0.20}_{-0.20}$	$0.64^{+0.09}_{-0.09}$	$1.79^{+0.22}_{-0.23}$	$1.05^{+0.18}_{-0.18}$	$0.58^{+0.08}_{-0.08}$	$1.63^{+0.20}_{-0.21}$

a The time-average photon flux in the unit of photon cm^{-2} s^{-1}

b The photon fluence in the unit of 10 photons cm^{-2}

Table B.4: The HETE GRBs time-average energy flux and fluence

GRB	Energy flux[a]			Energy fluence[b]			X/γ ratio
	2–30 keV	30–400 keV	2–400 keV	2–30 keV	30–400 keV	2–400 keV	
GRB010213	$2.29^{+0.07}_{-0.16}$	$0.20^{+0.17}_{-0.09}$	$2.49^{+0.29}_{-0.27}$	$7.88^{+0.25}_{-0.54}$	$0.69^{+0.58}_{-0.32}$	$8.58^{+1.01}_{-0.94}$	11.38
GRB010225	$3.57^{+0.37}_{-0.37}$	$2.46^{+1.76}_{-0.97}$	$6.03^{+1.73}_{-1.08}$	$3.48^{+0.36}_{-0.36}$	$2.40^{+1.72}_{-0.94}$	$5.89^{+1.69}_{-1.06}$	1.45
GRB010326B	$6.86^{+0.77}_{-0.77}$	$9.20^{+2.64}_{-2.17}$	$16.06^{+2.72}_{-2.31}$	$2.40^{+0.27}_{-0.27}$	$3.22^{+0.92}_{-0.76}$	$5.62^{+0.95}_{-0.81}$	0.75
GRB010612	$1.87^{+0.29}_{-0.28}$	$10.64^{+1.51}_{-1.31}$	$12.51^{+1.35}_{-1.38}$	$8.84^{+1.35}_{-1.31}$	$50.23^{+7.12}_{-6.21}$	$59.05^{+6.37}_{-6.53}$	0.18
GRB010613	$7.17^{+0.46}_{-0.47}$	$16.08^{+0.89}_{-0.89}$	$23.27^{+0.97}_{-0.98}$	$101.50^{+6.60}_{-6.54}$	$227.60^{+12.60}_{-12.50}$	$329.40^{+13.70}_{-13.80}$	0.45
GRB010629B	$10.34^{+0.68}_{-0.68}$	$11.62^{+1.10}_{-1.01}$	$21.96^{+1.35}_{-1.28}$	$25.41^{+1.67}_{-1.66}$	$28.56^{+2.69}_{-2.47}$	$53.97^{+3.32}_{-3.13}$	0.89
GRB010921	$30.02^{+1.44}_{-1.34}$	$47.20^{+3.62}_{-3.52}$	$77.25^{+4.06}_{-3.99}$	$71.60^{+3.42}_{-3.20}$	$112.60^{+8.60}_{-8.40}$	$184.20^{+9.70}_{-9.50}$	0.64
GRB010928	$3.97^{+0.36}_{-0.39}$	$65.31^{+2.65}_{-2.72}$	$69.26^{+2.66}_{-1.39}$	$13.71^{+1.24}_{-1.35}$	$225.70^{+9.10}_{-9.50}$	$239.30^{+9.20}_{-4.80}$	0.06
GRB011019	$1.24^{+0.24}_{-0.24}$	$0.45^{+0.56}_{-0.30}$	$1.68^{+0.63}_{-0.46}$	$3.03^{+0.58}_{-0.58}$	$1.10^{+1.39}_{-0.74}$	$4.13^{+1.54}_{-1.14}$	2.77
GRB011103	$2.24^{+0.53}_{-0.48}$	$4.22^{+5.91}_{-1.92}$	$6.46^{+5.92}_{-2.92}$	$3.31^{+0.79}_{-0.71}$	$6.22^{+8.72}_{-2.84}$	$9.53^{+8.73}_{-4.30}$	0.53
GRB011130	$1.17^{+0.20}_{-0.19}$	$0.20^{+0.23}_{-0.12}$	$1.37^{+0.38}_{-0.29}$	$5.85^{+0.98}_{-0.96}$	$0.98^{+1.17}_{-0.62}$	$6.83^{+1.90}_{-1.46}$	5.96
GRB011212	$0.73^{+0.11}_{-0.11}$	$0.58^{+0.44}_{-0.29}$	$1.32^{+0.50}_{-0.37}$	$4.24^{+0.64}_{-0.64}$	$3.37^{+2.53}_{-1.68}$	$7.61^{+2.90}_{-2.16}$	1.26
GRB020124	$4.86^{+0.34}_{-0.35}$	$15.09^{+2.17}_{-1.87}$	$19.95^{+2.18}_{-1.90}$	$19.74^{+1.40}_{-1.41}$	$61.33^{+8.79}_{-7.63}$	$81.04^{+8.86}_{-7.70}$	0.32
GRB020127	$2.63^{+0.20}_{-0.20}$	$7.99^{+1.75}_{-1.42}$	$10.62^{+1.73}_{-1.42}$	$6.73^{+0.51}_{-0.50}$	$20.49^{+4.48}_{-3.65}$	$27.22^{+4.43}_{-3.63}$	0.33
GRB020317	$2.16^{+0.37}_{-0.38}$	$1.29^{+0.88}_{-0.64}$	$3.45^{+0.94}_{-0.79}$	$2.16^{+0.37}_{-0.38}$	$1.29^{+0.88}_{-0.64}$	$3.45^{+0.94}_{-0.79}$	1.68
GRB020331	$2.14^{+0.14}_{-0.14}$	$7.11^{+1.14}_{-0.99}$	$9.25^{+1.13}_{-0.99}$	$16.07^{+1.04}_{-1.03}$	$53.32^{+8.52}_{-7.39}$	$69.40^{+8.45}_{-7.45}$	0.30
GRB020531	$12.81^{+1.35}_{-1.37}$	$105.40^{+13.00}_{-12.90}$	$118.20^{+13.00}_{-13.00}$	$1.33^{+0.14}_{-0.14}$	$10.96^{+1.35}_{-1.34}$	$12.30^{+1.35}_{-1.35}$	0.12
GRB020625	$0.56^{+0.13}_{-0.12}$	$0.03^{+0.08}_{-0.03}$	$0.59^{+0.20}_{-0.14}$	$2.37^{+0.55}_{-0.50}$	$0.12^{+0.35}_{-0.11}$	$2.49^{+0.83}_{-0.58}$	20.49
GRB020801	$2.18^{+0.24}_{-0.23}$	$8.07^{+0.90}_{-0.89}$	$10.26^{+0.93}_{-0.93}$	$25.66^{+2.83}_{-2.72}$	$95.23^{+10.67}_{-10.54}$	$121.00^{+11.00}_{-10.90}$	0.27
GRB020812	$1.32^{+0.18}_{-0.18}$	$3.18^{+1.36}_{-0.97}$	$4.50^{+1.35}_{-0.99}$	$7.91^{+1.09}_{-1.09}$	$19.15^{+8.18}_{-5.86}$	$27.06^{+8.11}_{-5.98}$	0.41
GRB020813	$12.26^{+0.24}_{-0.21}$	$74.30^{+1.09}_{-1.10}$	$86.61^{+1.13}_{-1.13}$	$138.50^{+2.70}_{-2.30}$	$839.60^{+12.30}_{-12.50}$	$978.70^{+12.70}_{-12.80}$	0.16
GRB020819	$5.02^{+0.22}_{-0.22}$	$12.47^{+1.66}_{-1.85}$	$17.50^{+1.68}_{-1.88}$	$25.20^{+1.10}_{-1.11}$	$62.53^{+8.33}_{-9.27}$	$87.80^{+8.39}_{-9.47}$	0.40
GRB020903	$0.68^{+0.20}_{-0.20}$	$0.13^{+0.34}_{-0.10}$	$0.73^{+0.48}_{-0.25}$	$0.83^{+0.28}_{-0.24}$	$0.16^{+0.44}_{-0.14}$	$0.95^{+0.62}_{-0.33}$	7.31
GRB021004	$1.54^{+0.14}_{-0.14}$	$3.58^{+1.41}_{-1.01}$	$5.12^{+1.38}_{-1.01}$	$7.65^{+0.69}_{-0.69}$	$17.79^{+7.01}_{-5.00}$	$25.45^{+6.85}_{-5.04}$	0.43
GRB021021	$0.51^{+0.13}_{-0.13}$	$0.13^{+0.22}_{-0.10}$	$0.64^{+0.28}_{-0.22}$	$2.51^{+0.63}_{-0.64}$	$0.62^{+1.07}_{-0.49}$	$3.13^{+1.39}_{-1.06}$	4.03
GRB021104	$3.29^{+0.66}_{-0.58}$	$1.95^{+1.40}_{-0.85}$	$5.21^{+1.59}_{-1.06}$	$10.32^{+2.06}_{-1.80}$	$6.13^{+4.40}_{-2.67}$	$16.38^{+5.00}_{-3.34}$	1.69
GRB021112	$3.28^{+0.62}_{-0.62}$	$5.34^{+2.71}_{-2.25}$	$8.62^{+2.73}_{-2.31}$	$1.31^{+0.25}_{-0.25}$	$2.14^{+1.08}_{-0.90}$	$3.45^{+1.09}_{-0.93}$	0.61
GRB021211	$14.50^{+0.36}_{-0.36}$	$29.64^{+2.54}_{-2.51}$	$44.18^{+2.58}_{-2.58}$	$11.60^{+0.29}_{-0.29}$	$23.71^{+2.03}_{-2.01}$	$35.34^{+2.07}_{-2.06}$	0.49
GRB030115	$2.19^{+0.17}_{-0.17}$	$4.21^{+1.12}_{-0.89}$	$6.40^{+1.10}_{-0.90}$	$7.89^{+0.61}_{-0.61}$	$15.17^{+4.02}_{-3.20}$	$23.05^{+3.98}_{-3.23}$	0.52
GRB030226	$1.92^{+0.17}_{-0.17}$	$6.24^{+1.00}_{-0.88}$	$8.16^{+1.01}_{-0.89}$	$13.20^{+1.18}_{-1.18}$	$42.92^{+6.85}_{-6.02}$	$56.12^{+6.93}_{-6.14}$	0.31
GRB030323	$1.73^{+0.66}_{-0.61}$	$4.54^{+1.96}_{-1.78}$	$6.27^{+1.87}_{-1.75}$	$3.40^{+1.29}_{-1.21}$	$8.91^{+3.84}_{-3.48}$	$12.30^{+3.68}_{-3.43}$	0.38
GRB030324	$3.49^{+0.28}_{-0.28}$	$8.11^{+2.13}_{-1.92}$	$11.59^{+2.12}_{-1.91}$	$5.49^{+0.44}_{-0.44}$	$12.75^{+3.35}_{-3.01}$	$18.23^{+3.34}_{-3.01}$	0.43
GRB030328	$4.11^{+0.07}_{-0.07}$	$14.43^{+0.69}_{-0.71}$	$18.55^{+0.70}_{-0.71}$	$81.86^{+1.31}_{-1.29}$	$287.40^{+13.90}_{-14.10}$	$369.50^{+14.00}_{-14.20}$	0.28
GRB030329	$87.88^{+0.48}_{-0.51}$	$171.00^{+2.10}_{-2.20}$	$259.00^{+2.20}_{-2.20}$	$553.10^{+3.10}_{-3.20}$	$1076.00^{+13.00}_{-14.00}$	$1630.00^{+14.00}_{-13.00}$	0.51
GRB030416	$1.14^{+0.11}_{-0.11}$	$0.47^{+0.24}_{-0.17}$	$1.61^{+0.31}_{-0.27}$	$8.98^{+0.87}_{-0.87}$	$3.72^{+1.85}_{-1.38}$	$12.70^{+2.47}_{-2.09}$	2.42
GRB030418	$1.55^{+0.10}_{-0.10}$	$1.58^{+0.66}_{-0.47}$	$3.13^{+0.66}_{-0.50}$	$17.11^{+1.09}_{-1.10}$	$17.34^{+7.27}_{-5.22}$	$34.45^{+7.23}_{-5.48}$	0.99
GRB030429	$1.93^{+0.20}_{-0.20}$	$1.54^{+0.57}_{-0.48}$	$3.47^{+0.60}_{-0.54}$	$4.74^{+0.49}_{-0.49}$	$3.80^{+1.40}_{-1.17}$	$8.54^{+1.48}_{-1.32}$	1.25
GRB030519	$41.51^{+1.16}_{-1.13}$	$290.60^{+4.60}_{-4.70}$	$332.20^{+4.80}_{-4.70}$	$87.05^{+2.43}_{-2.38}$	$609.30^{+9.70}_{-9.70}$	$696.70^{+9.90}_{-9.90}$	0.14
GRB030528	$7.48^{+0.34}_{-0.33}$	$6.74^{+0.85}_{-0.88}$	$14.24^{+0.92}_{-0.93}$	$62.54^{+2.80}_{-2.79}$	$56.34^{+7.13}_{-7.32}$	$119.00^{+7.60}_{-7.80}$	1.11
GRB030723	$1.30^{+0.18}_{-0.18}$	$1.49^{+0.88}_{-0.63}$	$2.79^{+0.99}_{-0.77}$	$2.43^{+0.33}_{-0.33}$	$2.79^{+1.64}_{-1.18}$	$5.22^{+1.86}_{-1.44}$	0.87
GRB030725	$11.22^{+0.27}_{-0.27}$	$19.87^{+1.23}_{-1.20}$	$31.09^{+1.26}_{-1.23}$	$94.12^{+2.27}_{-2.25}$	$166.70^{+10.30}_{-10.10}$	$260.80^{+10.60}_{-10.40}$	0.56
GRB030821	$4.69^{+0.30}_{-0.30}$	$12.95^{+1.58}_{-1.41}$	$17.64^{+1.61}_{-1.44}$	$9.96^{+0.63}_{-0.64}$	$27.47^{+3.35}_{-2.99}$	$37.43^{+3.41}_{-3.07}$	0.36
GRB030823	$4.15^{+0.28}_{-0.28}$	$2.29^{+0.80}_{-0.64}$	$6.44^{+0.83}_{-0.72}$	$23.05^{+1.56}_{-1.55}$	$12.74^{+4.43}_{-3.53}$	$35.80^{+4.63}_{-3.97}$	1.81
GRB030824	$5.66^{+0.68}_{-0.68}$	$3.71^{+1.52}_{-1.20}$	$9.37^{+1.74}_{-1.54}$	$8.90^{+1.07}_{-1.07}$	$5.83^{+2.38}_{-1.89}$	$14.73^{+2.72}_{-2.42}$	1.53
GRB030913	$1.99^{+0.26}_{-0.26}$	$8.82^{+2.95}_{-2.11}$	$10.81^{+2.91}_{-1.90}$	$1.81^{+0.23}_{-0.23}$	$8.04^{+2.69}_{-1.93}$	$9.86^{+2.66}_{-1.73}$	0.23

a The time-average energy flux in the unit of 10^{-8} erg cm^{-2} s^{-1}

b The energy fluence in the unit of 10^{-7} erg cm^{-2}

Table B.5: The HETE GRB 1s peak flux

GRB	Class[a]	Model[b]	5s Photon flux[c]	Count ratio[d]	1s Peak flux[e]
GRB010213	XRF	Band (W)	$(8.50 \pm 3.54) \times 10^{-3}$	1.325 ± 0.097	$(1.13 \pm 0.48) \times 10^{-2}$
GRB010225	XRF	CPL (F)	$(6.58 \pm 6.34) \times 10^{-2}$	1.454 ± 0.149	$(9.57 \pm 9.33) \times 10^{-1}$
GRB010326B	XRR	CPL (F)	$(2.85 \pm 0.89) \times 10^{-1}$	2.576 ± 0.188	$(7.33 \pm 2.33) \times 10^{-1}$
GRB010612	GRB	CPL (F)	(1.33 ± 0.10)	2.314 ± 0.171	(3.07 ± 0.33)
GRB010613	XRR	Band (W)	$(3.77 \pm 0.62) \times 10^{-1}$	3.249 ± 0.597	(1.23 ± 0.30)
GRB010629B	XRR	CPL (F)	(1.04 ± 0.13)	1.792 ± 0.084	(1.87 ± 0.24)
GRB010921	XRR	CPL (F)	(2.78 ± 0.20)	1.147 ± 0.056	(3.19 ± 0.27)
GRB010928	GRB	CPL (F)	(3.84 ± 0.20)	1.905 ± 0.132	(7.31 ± 0.64)
GRB011019	XRF	PL (W)	$(3.73 \pm 3.65) \times 10^{-2}$	1.984 ± 0.196	$(7.40 \pm 7.35) \times 10^{-2}$
GRB011103	XRR	PL (F)	$(4.71 \pm 2.95) \times 10^{-2}$	1.392 ± 0.229	$(6.56 \pm 4.24) \times 10^{-2}$
GRB011130	XRF	PL (W)	$(2.52 \pm 2.23) \times 10^{-2}$	1.419 ± 0.208	$(3.58 \pm 0.52) \times 10^{-2}$
GRB011212	XRF	PL (W)	$< 2.79 \times 10^{-2}$	1.754 ± 0.281	$< 4.89 \times 10^{-2}$
GRB020124	XRR	CPL (F)	$(9.16 \pm 1.55) \times 10^{-1}$	1.562 ± 0.129	$(1.43 \pm 0.27) \times 10^{-1}$
GRB020127	XRR	CPL (W)	$(7.36 \pm 0.98) \times 10^{-1}$	1.726 ± 0.215	(1.27 ± 0.23)
GRB020317	XRF	CPL (F)	$(9.67 \pm 6.52) \times 10^{-2}$	2.093 ± 0.198	$(2.02 \pm 1.38) \times 10^{-1}$
GRB020331	GRB	CPL (F)	$(9.64 \pm 1.06) \times 10^{-1}$	1.236 ± 0.092	(1.19 ± 0.16)
GRB020531	GRB	CPL (F)	$(9.90 \pm 0.10) \times 10^{-1}$	3.620 ± 0.229	(3.58 ± 0.44)
GRB020625	XRF	PL (W)	$(8.70 \pm 4.42) \times 10^{-2}$	2.015 ± 0.363	$(1.75 \pm 0.94) \times 10^{-1}$
GRB020801	GRB	Band (F)	$(5.69 \pm 1.12) \times 10^{-1}$	1.381 ± 0.139	$(7.86 \pm 1.73) \times 10^{-1}$
GRB020812	XRR	CPL (F)	$(3.45 \pm 0.94) \times 10^{-1}$	2.415 ± 0.264	$(8.34 \pm 2.46) \times 10^{-1}$
GRB020813	GRB	Band (W)	(7.74 ± 0.19)	1.074 ± 0.054	(8.31 ± 0.47)
GRB020819	XRR	Band (F)	(2.38 ± 0.14)	1.436 ± 0.071	(3.42 ± 0.27)
GRB020903	XRF	PL (W)	$(1.36 \pm 1.23) \times 10^{-2}$	1.822 ± 0.299	$(2.48 \pm 2.28) \times 10^{-2}$
GRB021004	XRR	CPL (F)	$(2.92 \pm 0.92) \times 10^{-1}$	1.458 ± 0.150	$(4.26 \pm 1.41) \times 10^{-1}$
GRB021021	XRF	PL (W)	$(7.86 \pm 6.07) \times 10^{-2}$	2.368 ± 0.490	$(1.86 \pm 1.49) \times 10^{-1}$
GRB021104	XRF	CPL (F)	$(1.70 \pm 0.89) \times 10^{-1}$	1.469 ± 0.163	$(2.49 \pm 1.33) \times 10^{-1}$
GRB021112	XRR	CPL (F)	$(2.47 \pm 1.19) \times 10^{-1}$	2.220 ± 0.252	$(5.48 \pm 2.72) \times 10^{-1}$
GRB021211	XRR	Band (F)	(2.03 ± 0.13)	2.021 ± 0.069	(4.10 ± 0.30)
GRB030115	XRR	CPL (F)	$(9.82 \pm 1.01) \times 10^{-1}$	1.183 ± 0.094	(1.16 ± 0.15)
GRB030226	GRB	CPL (F)	$(4.81 \pm 0.95) \times 10^{-1}$	1.305 ± 0.132	$(6.28 \pm 1.40) \times 10^{-1}$
GRB030323	XRR	PL (F)	$(1.89 \pm 0.91) \times 10^{-1}$	1.538 ± 0.226	$(2.91 \pm 1.47) \times 10^{-1}$
GRB030324	XRR	CPL (F)	$(5.98 \pm 1.29) \times 10^{-1}$	1.600 ± 0.120	$(9.57 \pm 2.18) \times 10^{-2}$
GRB030328	GRB	Band (F)	(2.90 ± 0.10)	1.145 ± 0.059	(3.32 ± 0.20)
GRB030329	XRR	Band (W)	(28.90 ± 0.42)	1.317 ± 0.051	(38.06 ± 1.58)
GRB030416	XRF	PL (W)	$(1.12 \pm 0.46) \times 10^{-1}$	1.247 ± 0.167	$(1.39 \pm 0.60) \times 10^{-1}$
GRB030418	XRR	CPL (W)	$(9.04 \pm 6.62) \times 10^{-2}$	1.481 ± 0.216	$(1.34 \pm 1.00) \times 10^{-1}$
GRB030429	XRF	CPL (F)	$(1.83 \pm 0.68) \times 10^{-1}$	1.570 ± 0.157	$(2.87 \pm 1.10) \times 10^{-1}$
GRB030519	GRB	Band (F)	$(5.38 \pm 0.25) \times 10^{-1}$	2.101 ± 0.040	(11.31 ± 0.57)
GRB030528	XRF	Band (F)	$(1.38 \pm 0.50) \times 10^{-1}$	1.082 ± 0.073	$(1.49 \pm 0.55) \times 10^{-1}$
GRB030723	XRR	PL (W)	$(1.34 \pm 0.65) \times 10^{-1}$	1.224 ± 0.208	$(1.65 \pm 0.84) \times 10^{-1}$
GRB030725	XRR	CPL (F)	(5.46 ± 0.22)	1.043 ± 0.043	(5.69 ± 0.33)
GRB030821	XRR	CPL (F)	$(9.75 \pm 1.17) \times 10^{-1}$	1.222 ± 0.106	(1.19 ± 0.18)
GRB030823	XRF	CPL (F)	$(1.13 \pm 0.93) \times 10^{-1}$	1.490 ± 0.150	$(1.69 \pm 1.39) \times 10^{-1}$
GRB030824	XRF	PL (W)	$(8.90 \pm 4.66) \times 10^{-2}$	1.457 ± 0.276	$(1.30 \pm 0.72) \times 10^{-1}$
GRB030913	GRB	CPL (F)	$(6.01 \pm 0.92) \times 10^{-1}$	1.485 ± 0.144	$(8.92 \pm 1.61) \times 10^{-1}$

a GRB classification; XRF: X-ray-flash, XRR: X-ray-rich GRB, GRB: Hard GRB

b Spectral model; PL: Power-law, CPL: Cutoff power-law, Band: Band function,
W: peak counts using WXM data, F: peak counts using FREGATE data

c The photon flux in 50–300 keV using 5s WXM/FREGATE spectrum

d Count ratio between 1s and 5s time interval including the highest peak

e The 1s peak flux in 50–300 keV

Table B.6: The HETE GRB 1s peak flux (continue)

GRB	2–30 keV	30–400 keV	2–400 keV
GRB010213	(6.33 ± 0.71)	$(2.28 \pm 7.73) \times 10^{-3}$	(6.34 ± 0.75)
GRB010225	(5.12 ± 2.31)	$(3.33 \pm 1.69) \times 10^{-1}$	(5.45 ± 2.34)
GRB010326B	(10.52 ± 3.18)	(1.51 ± 0.33)	(12.04 ± 3.19)
GRB010612	(4.32 ± 1.15)	(4.35 ± 0.44)	(8.67 ± 1.33)
GRB010613	(24.58 ± 10.35)	(2.67 ± 0.67)	(27.25 ± 9.59)
GRB010629B	(39.08 ± 7.01)	(4.17 ± 0.35)	(43.26 ± 7.04)
GRB010921	(34.20 ± 3.84)	(5.74 ± 0.41)	(39.94 ± 3.93)
GRB010928	(5.58 ± 0.39)	(10.06 ± 0.70)	(15.63 ± 1.08)
GRB011019	(3.61 ± 1.27)	$(1.47 \pm 1.27) \times 10^{-1}$	(3.76 ± 1.29)
GRB011103	(4.44 ± 1.04)	$(1.36 \pm 0.77) \times 10^{-1}$	(4.57 ± 1.05)
GRB011130	(5.28 ± 1.22)	$(8.22 \pm 6.27) \times 10^{-2}$	(5.36 ± 1.22)
GRB011212	(1.13 ± 0.99)	$(1.13 \pm 4.40) \times 10^{-2}$	(1.14 ± 0.99)
GRB020124	(6.90 ± 1.57)	(2.49 ± 0.36)	(9.38 ± 1.67)
GRB020127	(5.95 ± 0.98)	(2.17 ± 0.35)	(8.13 ± 1.21)
GRB020317	(4.63 ± 0.93)	$(6.35 \pm 2.38) \times 10^{-1}$	(5.27 ± 1.00)
GRB020331	(1.93 ± 0.35)	(1.72 ± 0.21)	(3.65 ± 0.46)
GRB020531	(17.42 ± 4.29)	(5.56 ± 0.63)	(22.98 ± 4.41)
GRB020625	(2.86 ± 0.73)	$(3.05 \pm 1.50) \times 10^{-1}$	(3.16 ± 0.80)
GRB020801	(6.37 ± 1.02)	(1.38 ± 0.22)	(7.74 ± 2.04)
GRB020812	(4.46 ± 1.18)	(1.50 ± 0.35)	(5.96 ± 1.28)
GRB020813	(19.54 ± 1.09)	(12.89 ± 0.70)	(32.33 ± 1.72)
GRB020819	(12.09 ± 0.95)	(5.60 ± 0.38)	(17.69 ± 1.17)
GRB020903	(2.43 ± 0.71)	$(3.16 \pm 4.39) \times 10^{-2}$	(2.46 ± 0.72)
GRB021004	(1.80 ± 0.35)	$(8.86 \pm 1.92) \times 10^{-1}$	(2.69 ± 0.45)
GRB021021	(2.14 ± 0.92)	$(3.13 \pm 2.27) \times 10^{-1}$	(2.46 ± 1.00)
GRB021104	(4.23 ± 1.76)	$(6.67 \pm 2.08) \times 10^{-1}$	(4.89 ± 1.78)
GRB021112	(3.45 ± 1.06)	(1.03 ± 0.35)	(4.48 ± 1.16)
GRB021211	(21.61 ± 1.04)	(8.36 ± 0.46)	(29.97 ± 1.32)
GRB030115	(6.97 ± 1.25)	(1.16 ± 0.15)	(8.14 ± 1.29)
GRB030226	(1.71 ± 0.17)	$(9.86 \pm 1.00) \times 10^{-1}$	(2.69 ± 0.27)
GRB030323	(3.39 ± 2.08)	$(4.88 \pm 2.19) \times 10^{-1}$	(3.87 ± 2.08)
GRB030324	(6.64 ± 0.89)	(1.64 ± 0.27)	(8.28 ± 1.01)
GRB030328	(6.72 ± 0.45)	(4.92 ± 0.27)	(11.65 ± 0.74)
GRB030329	(378.64 ± 16.82)	(72.21 ± 2.86)	(450.94 ± 19.31)
GRB030416	(4.50 ± 0.83)	$(2.62 \pm 1.01) \times 10^{-1}$	(4.76 ± 0.85)
GRB030418	(3.71 ± 0.73)	$(2.98 \pm 1.47) \times 10^{-1}$	(4.01 ± 0.78)
GRB030429	(3.08 ± 0.68)	$(7.08 \pm 1.78) \times 10^{-1}$	(3.79 ± 0.73)
GRB030519	(10.17 ± 2.02)	(16.09 ± 0.71)	(26.26 ± 2.15)
GRB030528	(17.29 ± 1.26)	$(6.15 \pm 1.21) \times 10^{-1}$	(17.91 ± 1.31)
GRB030723	(1.73 ± 0.47)	$(2.73 \pm 1.28) \times 10^{-1}$	(2.00 ± 0.52)
GRB030725	(24.83 ± 1.64)	(9.12 ± 0.48)	(33.96 ± 1.91)
GRB030821	(3.84 ± 0.68)	(1.92 ± 0.24)	(5.77 ± 0.80)
GRB030823	(7.03 ± 1.48)	$(5.67 \pm 2.52) \times 10^{-1}$	(7.59 ± 1.55)
GRB030824	(12.42 ± 3.43)	$(2.80 \pm 1.37) \times 10^{-1}$	(12.70 ± 3.47)
GRB030913	(2.20 ± 0.44)	(1.36 ± 0.22)	(3.56 ± 0.55)

Appendix C

Light curve and Spectrum

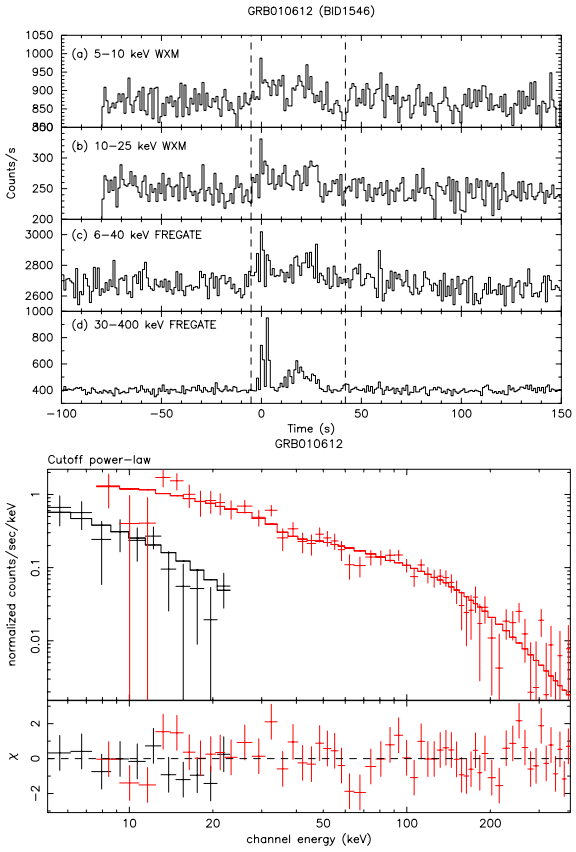

Figure C.1: GRB010612

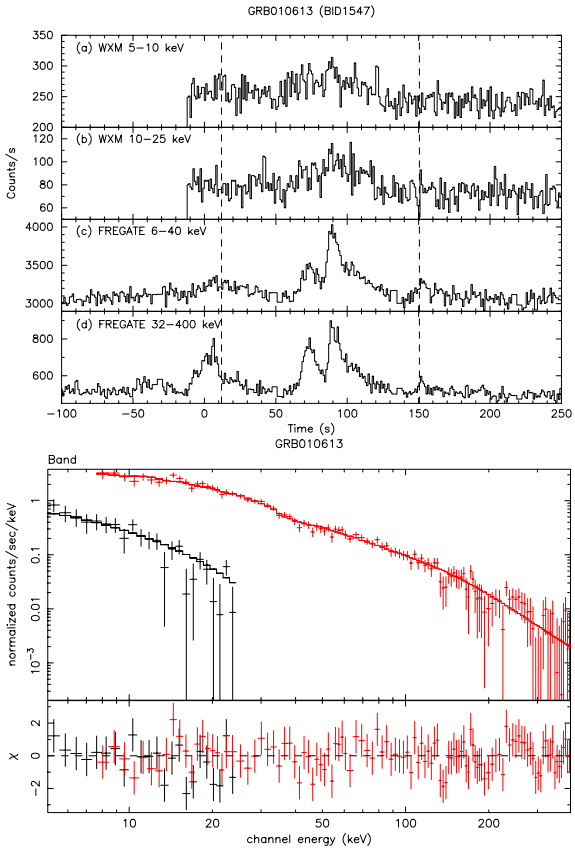

Figure C.2: GRB010613

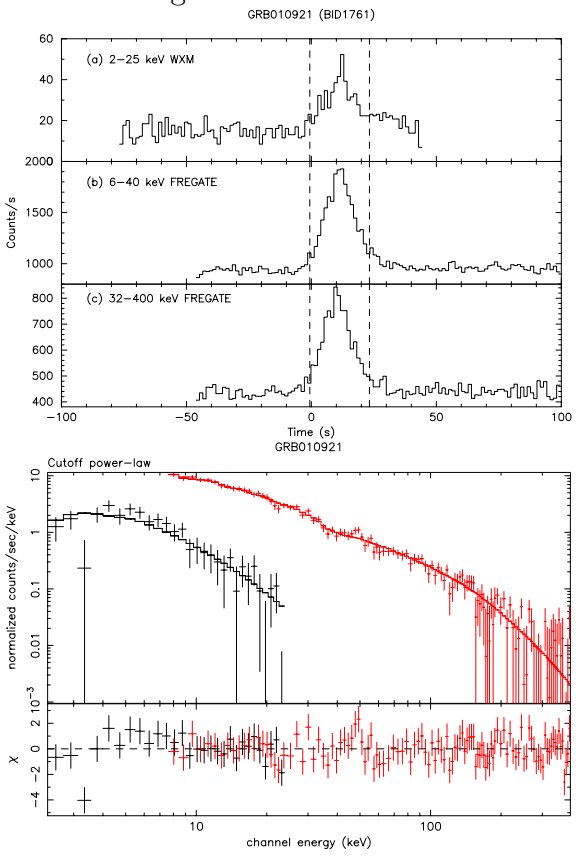

Figure C.3: GRB010921

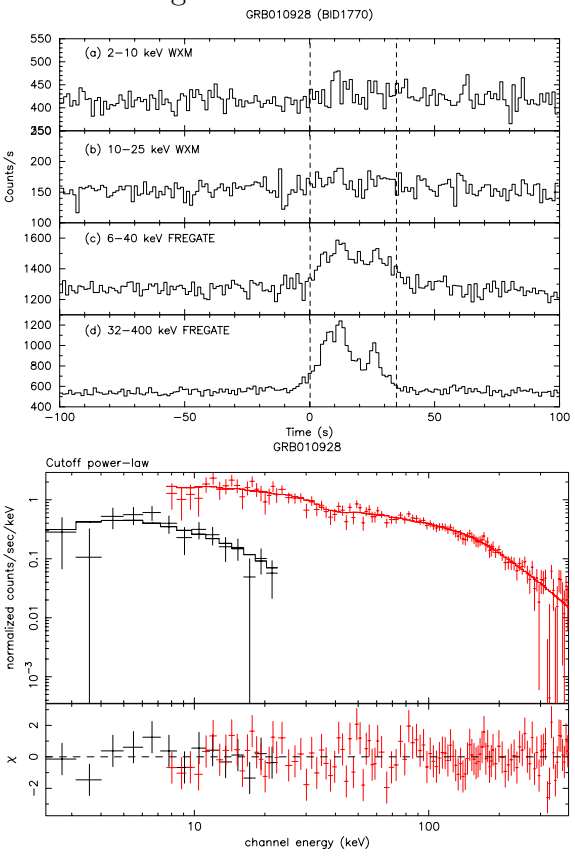

Figure C.4: GRB010928

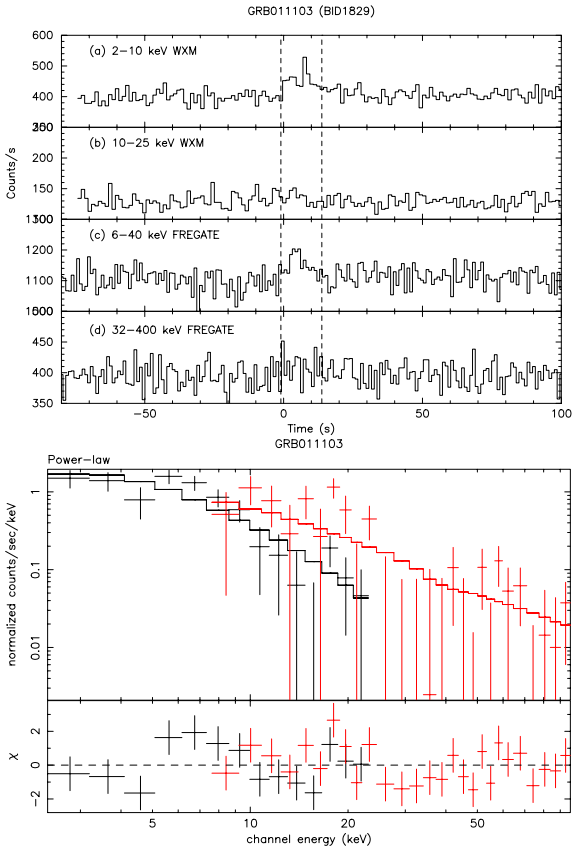

Figure C.5: GRB011103

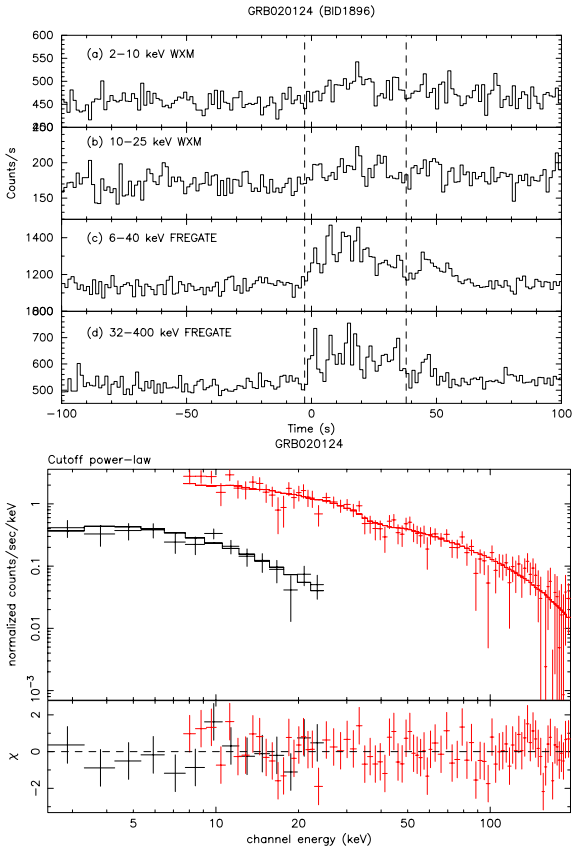

Figure C.6: GRB020124

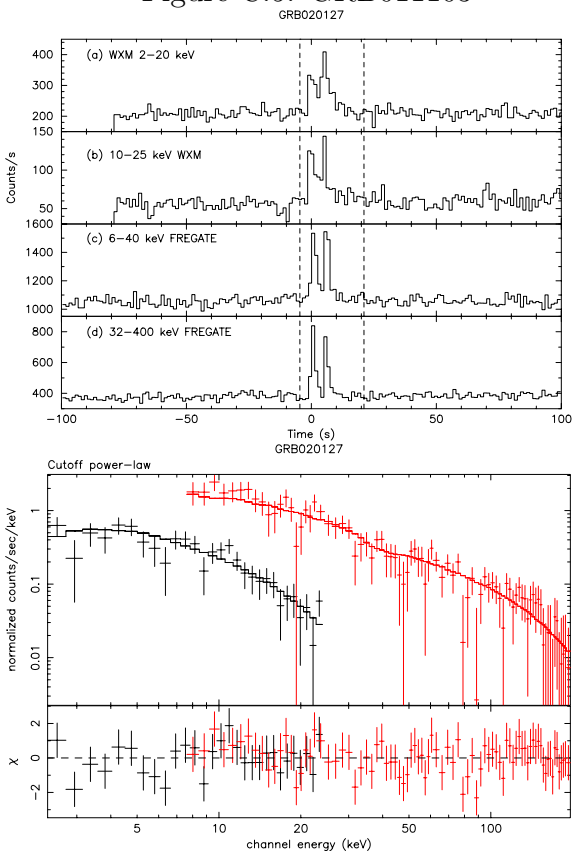

Figure C.7: GRB020127

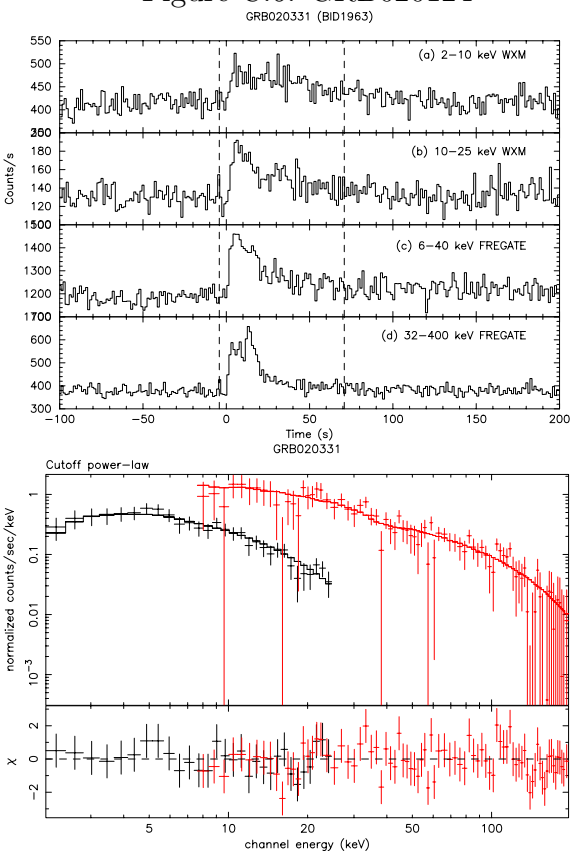

Figure C.8: GRB020331

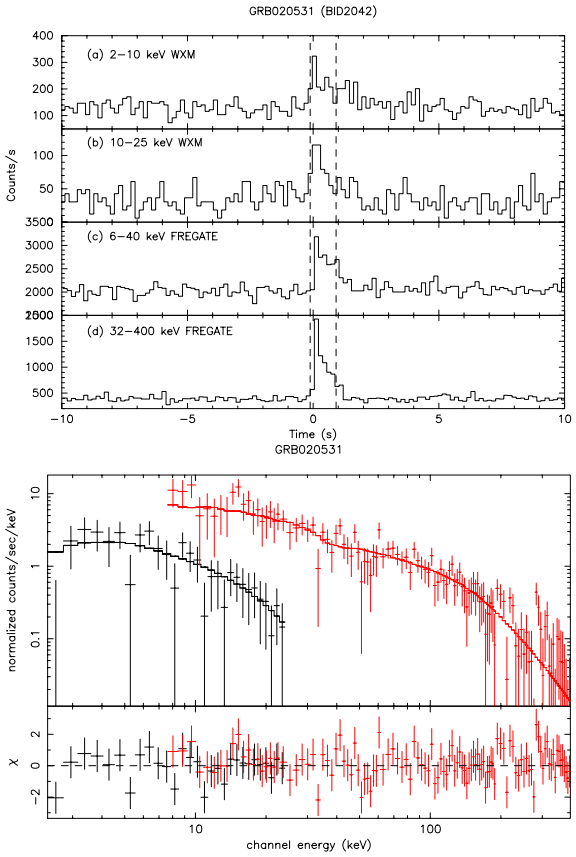

Figure C.9: GRB020531

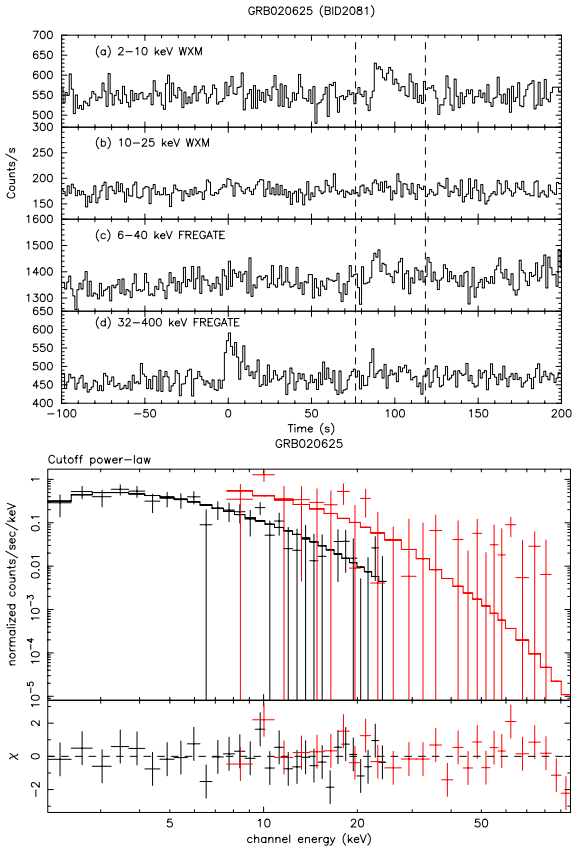

Figure C.10: GRB020625

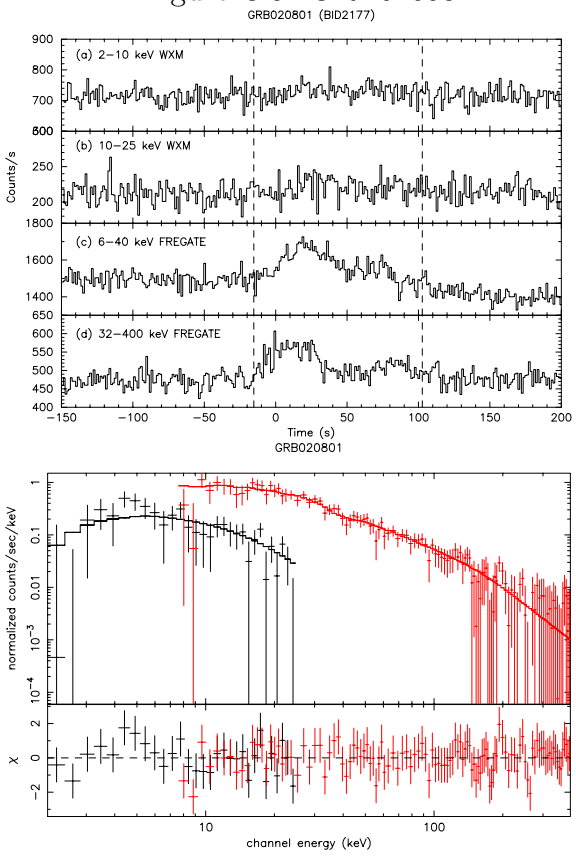

Figure C.11: GRB020801

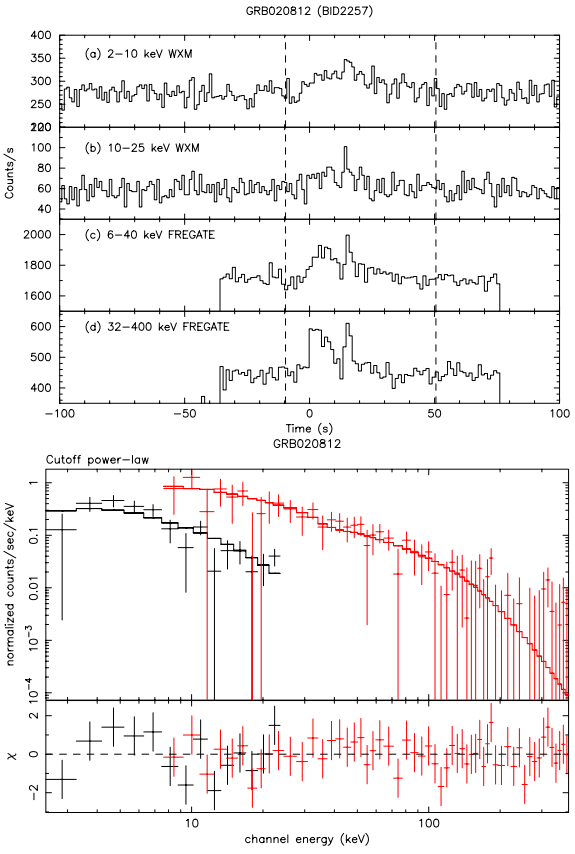

Figure C.12: GRB020812

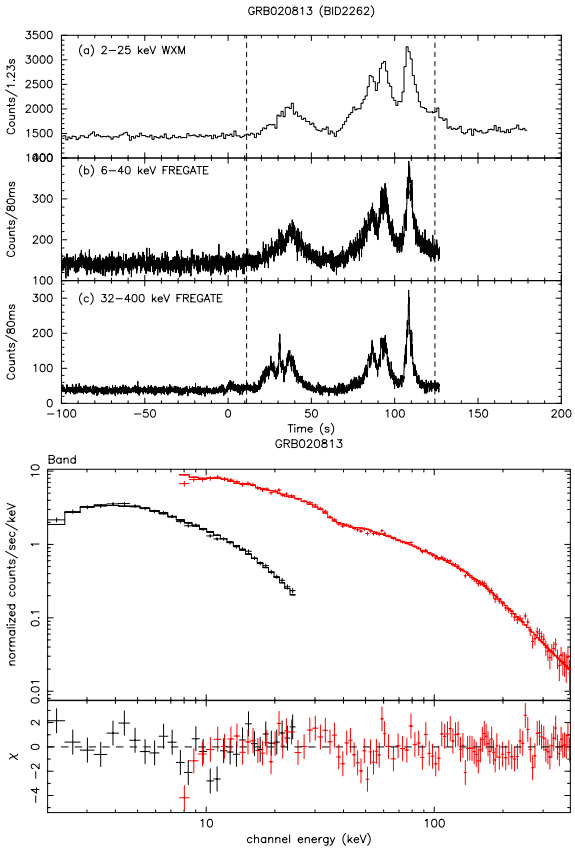

Figure C.13: GRB020813

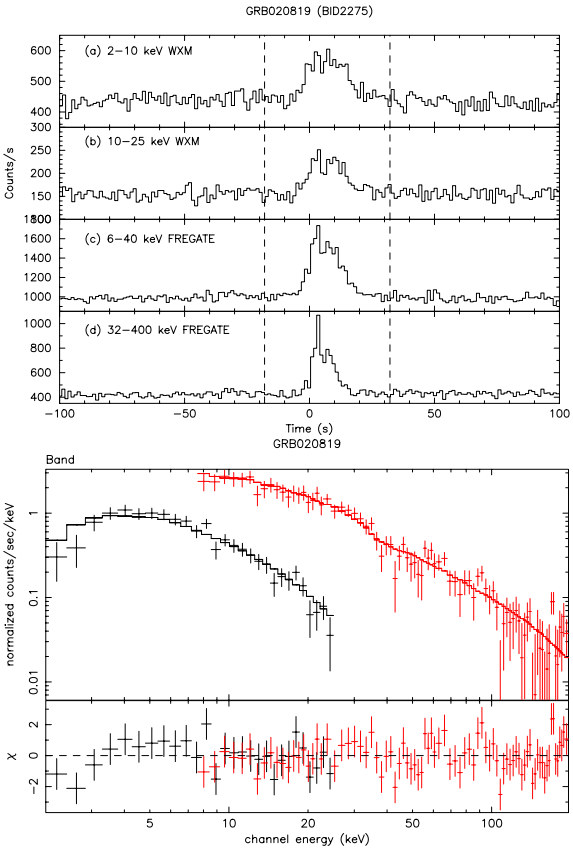

Figure C.14: GRB020819

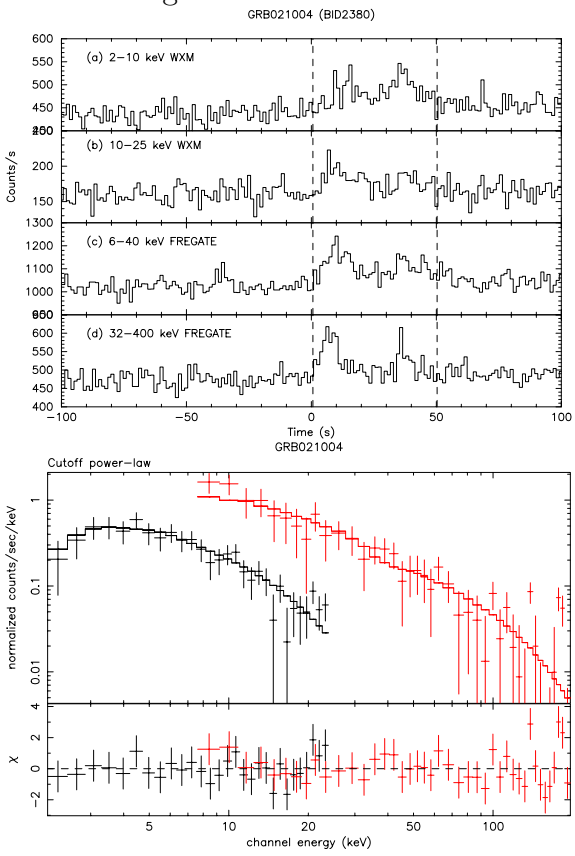

Figure C.15: GRB021004

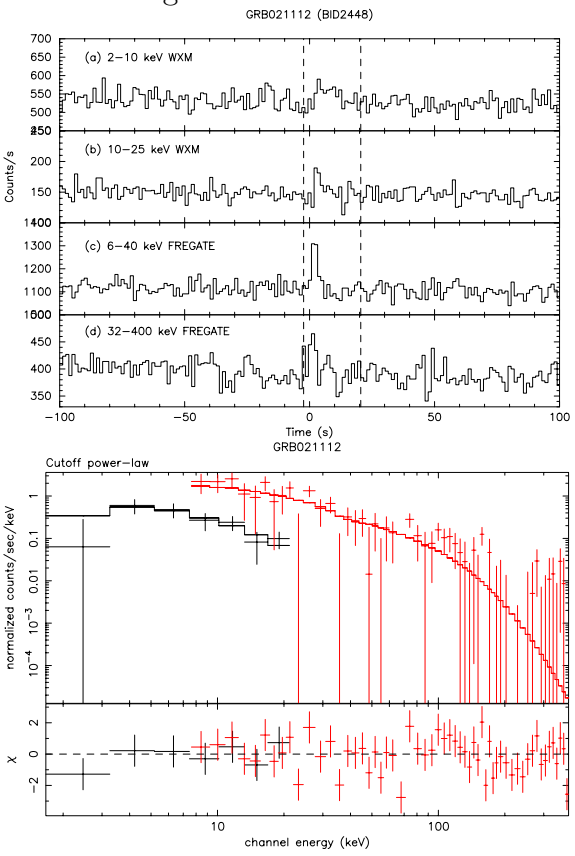

Figure C.16: GRB021112

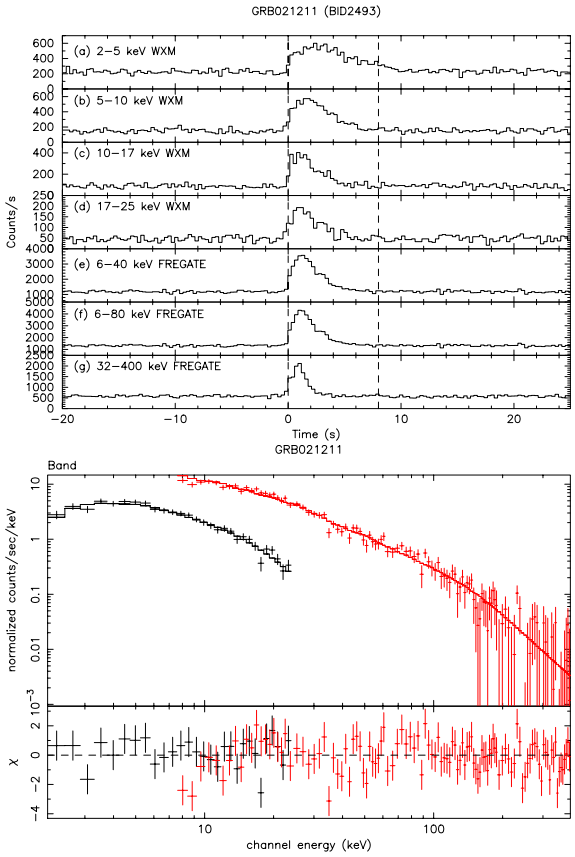

Figure C.17: GRB021211

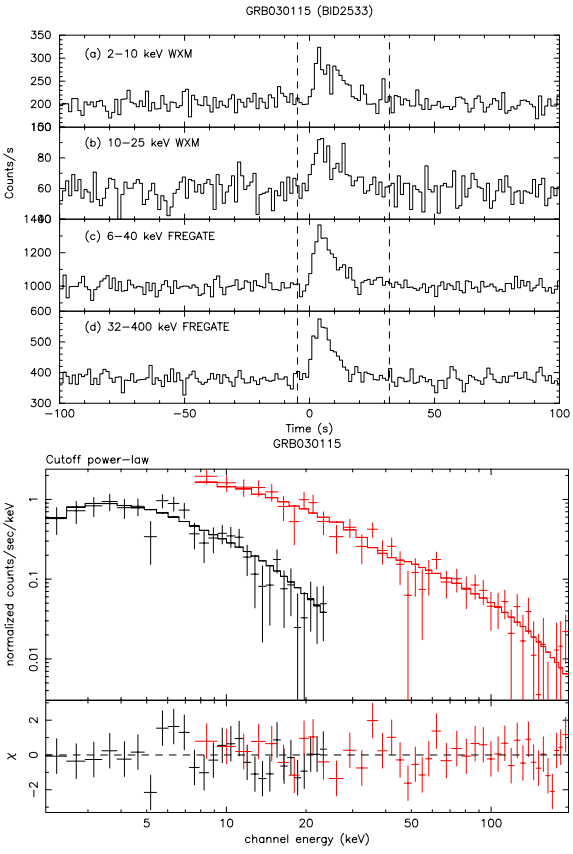

Figure C.18: GRB030115

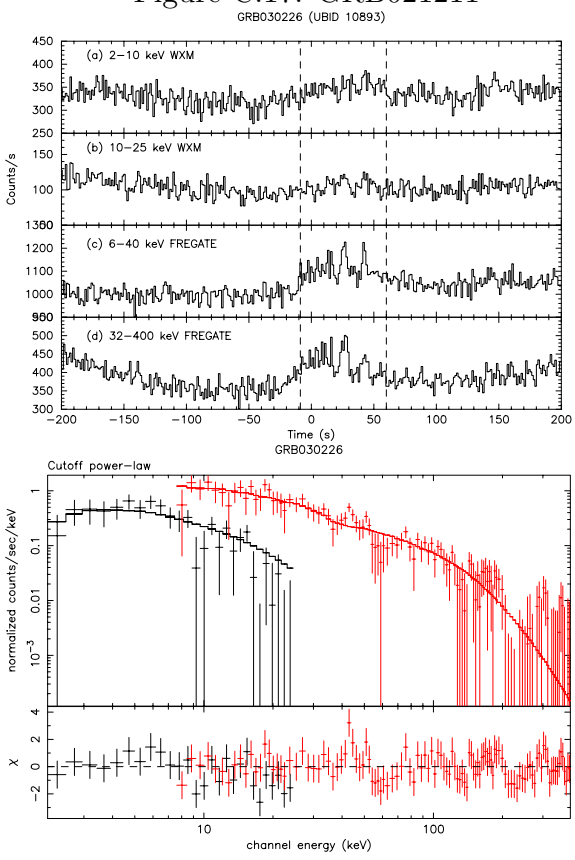

Figure C.19: GRB030226

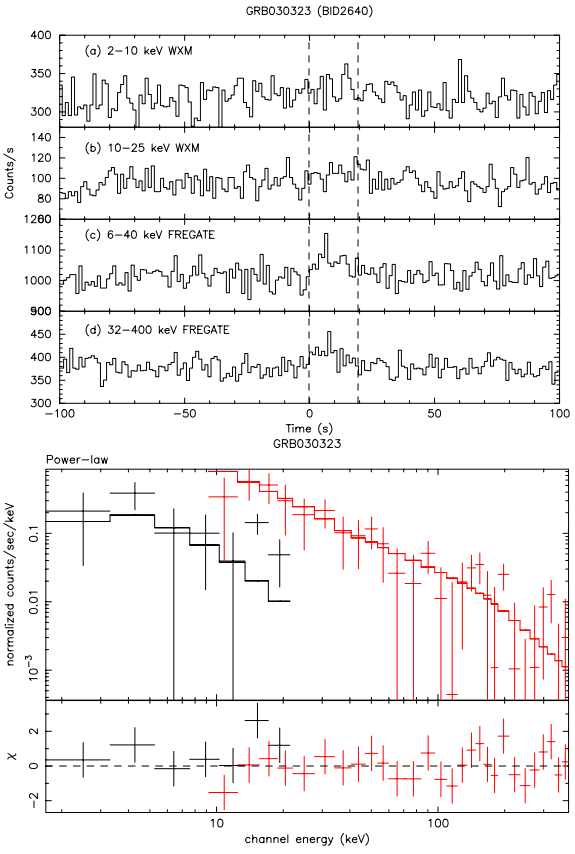

Figure C.20: GRB030323

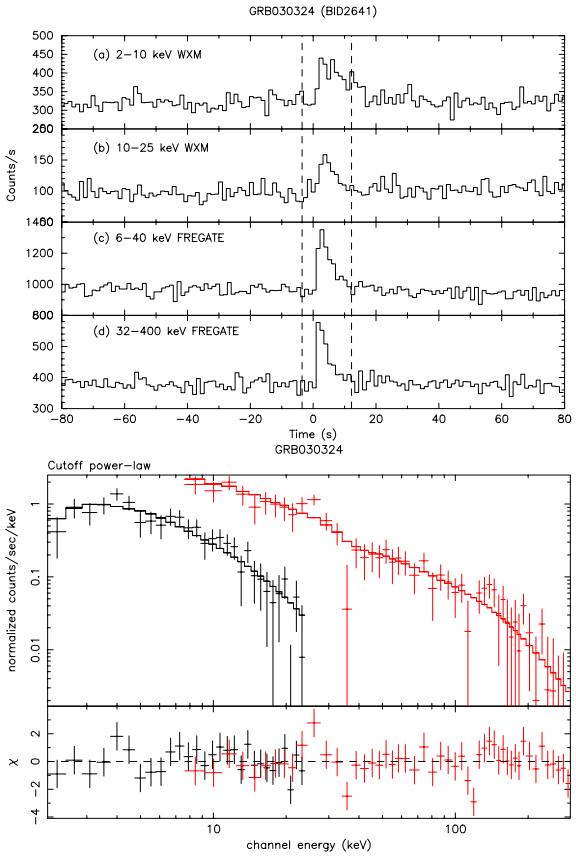

Figure C.21: GRB030324

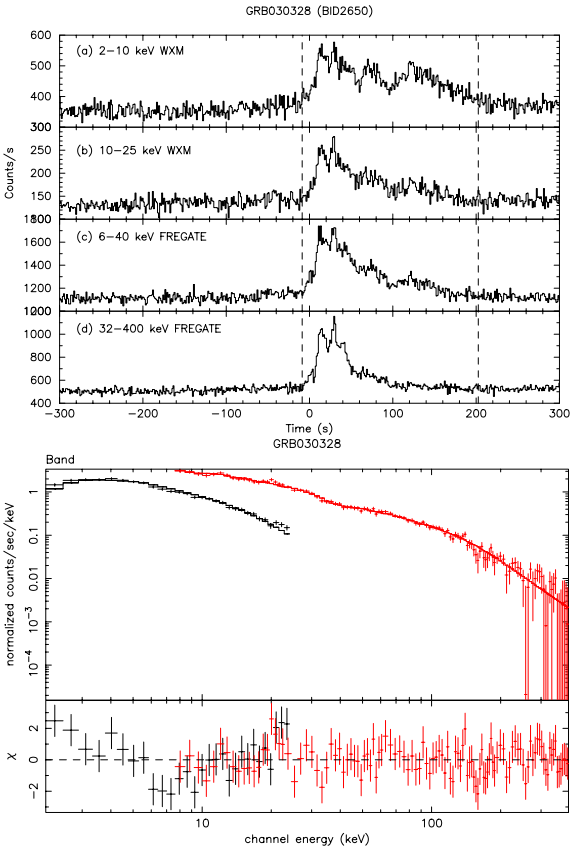

Figure C.22: GRB030328

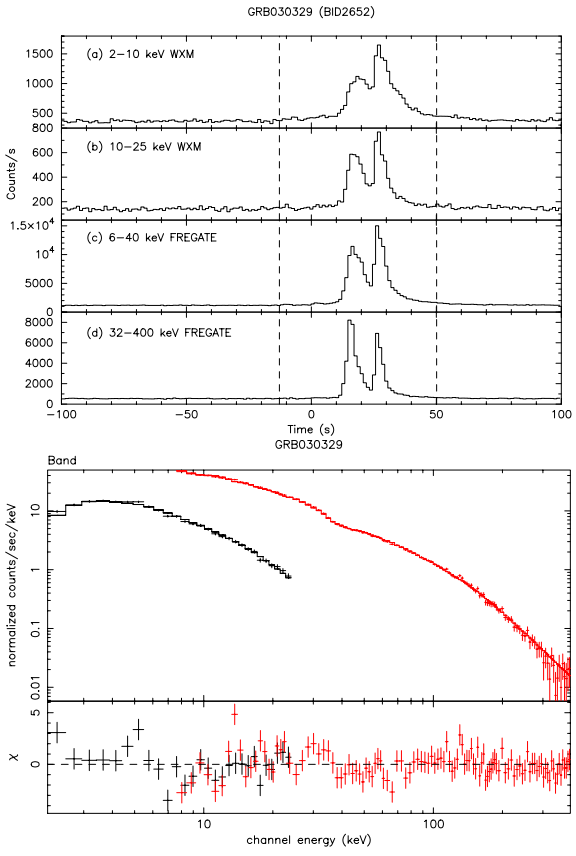

Figure C.23: GRB030329

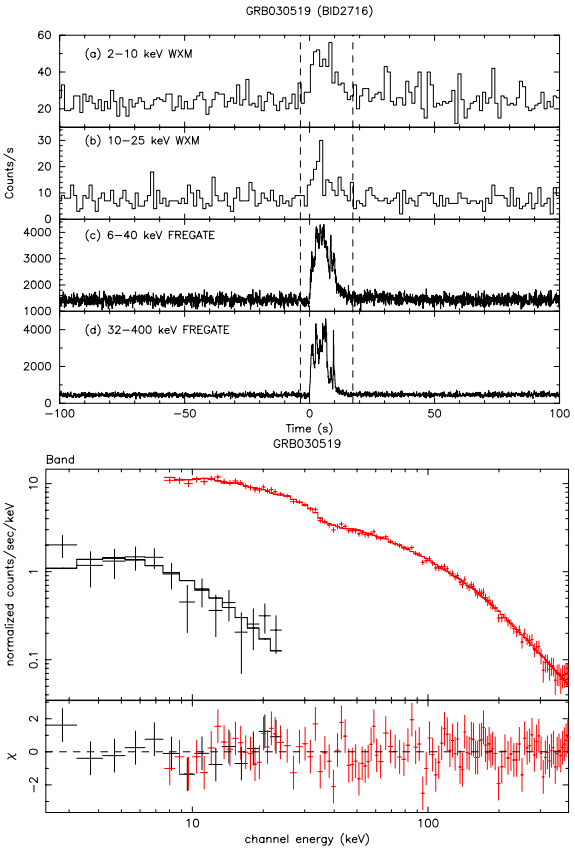

Figure C.24: GRB030519 (WXM:1.23s, FREGATE 82ms)

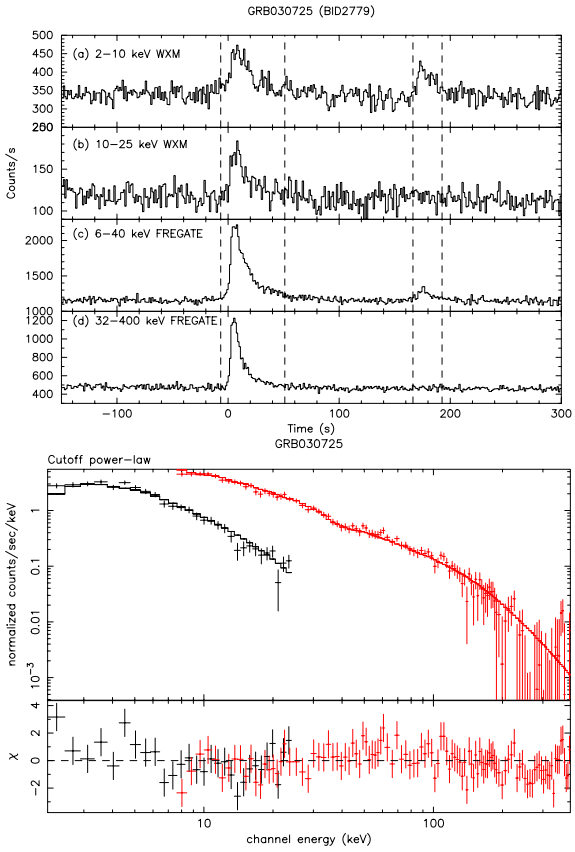

Figure C.25: GRB030725

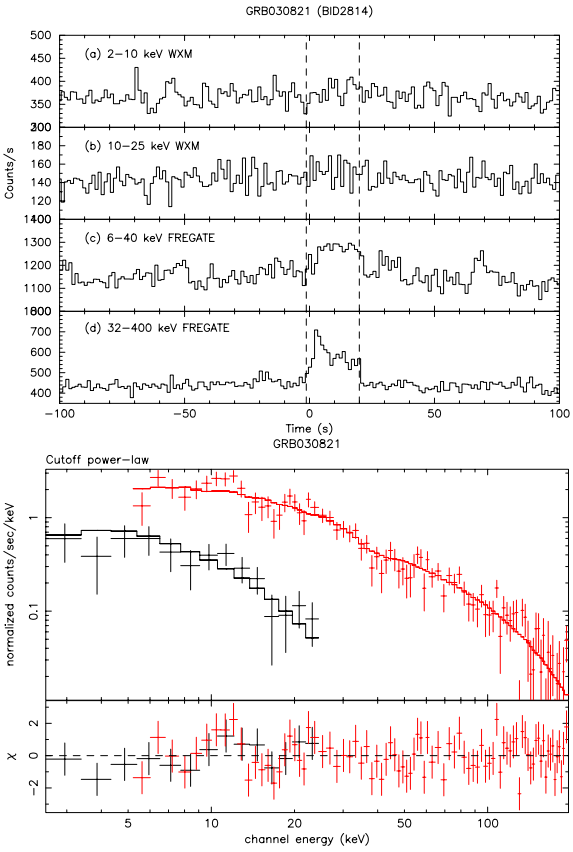

Figure C.26: GRB030821

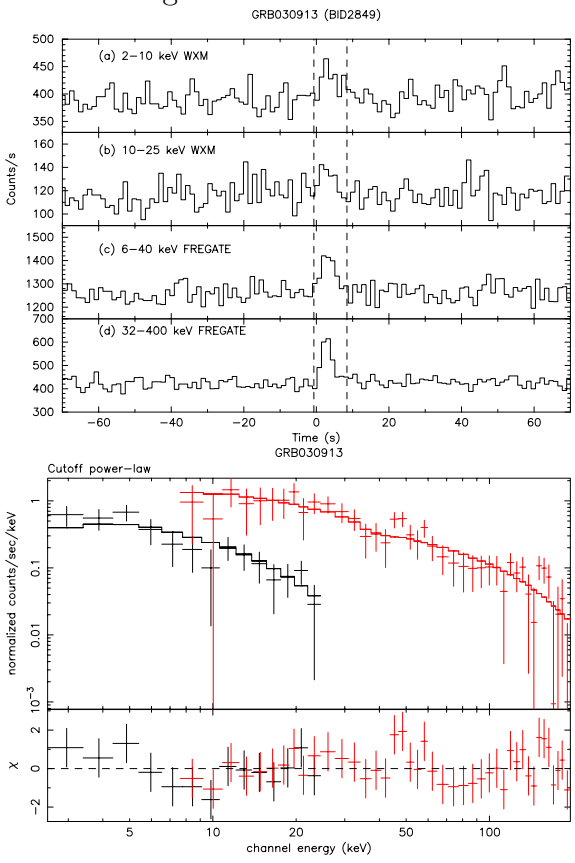

Figure C.27: GRB030913

Appendix D

The "constrained" Band function

In the spectral analysis of GRBs, one occasionally encounters events (such as XRF 020903) that are so soft that they present themselves as pure power-laws with power-law index $\beta < -2$ in the energy range of the detector. The natural interpretation of such spectra is that the break energy $E_{\rm break}$ separating the two functional parts of the Band function is near or below the lower boundary of the detector energy range.

This situation creates a problem for fits of the Band function, in that the Band function has two distinct ways of conforming to a power-law in the detector energy range:

1. $E_{\rm break} \to 0$, so that only the high-energy, pure power-law part of the Band function is visible in the energy range of the detector.

2. $E_{\rm break} \to \infty$, $E_0 \to \infty$, where E_0 is the "cutoff energy" of the cutoff power-law that constitutes the low-energy part of the Band function. In this limit, the limiting power-law is actually the cutoff power-law, but the cutoff energy is so large that the curvature of the model is imperceptible in the detector energy range.

Therefore, despite the fact that the numerical value of the power-law index is such that we are certain that we should be dealing with the high-energy part of the Band function (i.e., the index is < -2, the low-energy part of the function can "horn in" on the fit, altering the physical inferences drawn from the spectrum.

This situation is particularly a problem for the estimation of $E_{\rm peak}$. Since we know that we are in case 1, we also know that we ought to have at least a firm upper limit on $E_{\rm peak}$, since $E_{\rm peak}$ is always necessarily less than $E_{\rm break}$, which is at the low end of the detector energy range. On the other hand, the case 2 limit implies $E_{\rm peak} \to \infty$. Unfortunately, the data doesn't care

which side of the Band function makes the power-law, so no discrimination is possible between the two cases. Consequently, we can't constrain $E_{\rm peak}$ at all using a normal Band function fit.

The approach we have chosen to deal with this situation in the case of XRF 020903 is to fit a *constrained* Band function to the data. That is, we consider a three-dimensional subspace of the full four-dimensional Band function parameter space, choosing the subspace with a view to satisfying the following criteria:

1. It is perfectly possible to make both pure power-laws and cutoff power-laws of the any desired curvature in the detector energy range.

2. Only the high-energy part of the Band function is allowed to produce a pure power-law.

We define the three-dimensional subspace in the following way: consider a Band function parametrized by low- and high-energy indices α and β, and by a cutoff energy E_0. The well-known relation between E_0 and $E_{\rm break}$ is $E_{\rm break} = (\alpha-\beta)E_0$. We impose the constraint condition on our family of fitting functions

$$E_{\rm break} = E_{\rm pivot} \times (E_0/E_{\rm pivot})^{-1}, \tag{D.1}$$

where $E_{\rm pivot}$ is some suitably chosen energy, in the general neighborhood where the GRB has appreciable emission. $E_{\rm break}$ and E_0 are then inversely related, and are equal to each other when both are equal to $E_{\rm pivot}$.

When $E_0 < E_{\rm pivot}$, then $E_{\rm break} > E_{\rm pivot}$, and the function is essentially a cutoff power-law in the energy range of interest.

On the other hand, when $E_0 > E_{\rm pivot}$, then $E_{\rm break} < E_{\rm pivot}$, and as $E_0 \to \infty$, $E_{\rm break} \to 0$. In other words, when the low-energy part of the Band function is trying to imitate a power law, the break energy becomes small enough to force the low-energy part of the function below the energy range of interest, where it cannot be seen and therefore can do no harm. Any pure power-law work must thus be done by the high-energy part of the Band function.

The resulting spectral function has three parameters (including the scale), rather than four. The two input shape parameters can be chosen arbitrarily from the set $\{\alpha, \beta, E_0, E_{\rm break}, E_{\rm peak}\}$. The remaining parameters may then be determined by algebraic relationships.

We have found it most convenient to adopt $E_{\rm peak}$ and β as our parameters. The choice of $E_{\rm peak}$ is dictated by the necessity of estimating its value, or at least an upper bound on its value. The choice of β is convenient because one may then impose the parameter bound $\beta < -2$, which guarantees that the formal expression for $E_{\rm peak}$ may be meaningfully interpreted

as the energy of the peak of the νF_ν distribution. This bound on β is an important part of the specification of the fitting family of models. Were it not imposed, it would be possible for the formal expression for $E_{\rm peak}$ to exceed $E_{\rm break}$, so that at large values of $E_{\rm peak}$ the fit could always produce a $\beta \gtrsim -2$ power-law in the detector energy range. The result would be an extended tail of constant χ^2 for arbitrarily large values of $E_{\rm peak}$.

Figure D.1 shows the constrained Band function, with $\beta = -2.5$ and $E_{\rm pivot} = 4$ keV, for different values of $E_{\rm peak}$. This figure shows that $E_{\rm peak}$ increases, $E_{\rm break}$ also necessarily increases, so that E_0 is forced to smaller and smaller values by the constraint, which increases the curvature (and the value of α).

Figure D.2 shows the constrained Band function, with $E_{\rm peak} = 4$ keV and $E_{\rm pivot} = 4$ keV, for different values of β. The progression from some curvature at low energy ($\beta = -2.0$) to almost none ($\beta = -4.0$) is evident, as is the fact that as the curvature disappears, the resulting power-law is produced by the high-energy part of the Band function.

Figures D.1 and D.2 show that the constrained Band function is perfectly able to make both pure power-laws, and cutoff power-laws with any desired curvature in the detector energy range. Figure D.2 demonstrates that, in the constrained Band function, a power-law spectrum is always produced by the high-energy part of the Band function.

The choice of $E_{\rm pivot}$ is dictated by the following considerations:

1. $E_{\rm pivot}$ must be low enough to prevent the low-energy part of the Band function from making a power-law in the energy range of interest. If $E_{\rm pivot}$ were 1 GeV (say), then the Band function would have no difficulty making E_0 large and $\alpha \lesssim -2$, which is what we are trying to prevent by introducing the constraint. So $E_{\rm pivot}$ should be "as low as possible."

2. $E_{\rm pivot}$ must not be so low that we cannot adequately fit any curvature that may exist in the spectrum. If $E_{\rm pivot}$ were 1 eV (say), then whenever $E_{\rm break}$ was in or above the energy range where the spectrum is appreciable, E_0 would be so tiny that the curvature of the model would be huge, much too large to fit the data well.

One way of choosing $E_{\rm pivot}$ is to calculate it's value using the best-fit parameters from a fit of a *free* Band function, using $E_{\rm pivot} = (E_0 E_{\rm break})^{1/2}$. This choice, which effectively chooses the unique constrained subspace of the full parameter space that contains the best-fit free Band function, allows the constrained family of functions to optimally fit whatever curvature the data may seem to hint is required.

We must require that the inferences that we draw from the spectral fit should be robust, in the sense that they should not depend strongly on the specific choice of $E_{\rm pivot}$. So the proper use of this constrained Band model involves not only choosing a representative value of $E_{\rm pivot}$, but also varying $E_{\rm pivot}$ in some reasonable range, to make sure that the conclusions about parameter estimates and bounds are unaffected by the choice of $E_{\rm pivot}$.

Figure D.3 shows the constrained Band function, with $E_{\rm peak} = 4$ keV and $\beta = 2.0$, for different values of $E_{\rm pivot}$. Once again, as the low-energy curvature disappears, the resulting power-law is produced by the high-energy part of the Band function. Figure D.3 also shows that the shape of the spectrum in the detector energy range is insensitive to the specific choice of $E_{\rm pivot}$, within a reasonable range. Thus the conclusions about parameter estimates and bounds are unaffected by the choice of $E_{\rm pivot}$.

Figure D.4 shows the constrained Band functions with parameters that best fit the 13 s spectrum of XRF 020903, for different fixed values of $E_{\rm pivot}$. This figure illustrates the fact that the shape of the best-fit model is essentially unchanged in the energy range of the WXM for choices of $E_{\rm pivot}$ within a reasonable range.'

Finally, we give the algebraic relationships necessary to recover the remaining Band function parameters assuming that $E_{\rm peak}$ and β are given. Let $x \equiv E_{\rm peak}/E_{\rm pivot}$. Then,

$$\alpha = -2 + \frac{1}{2}x^2 + \sqrt{\frac{1}{4}x^4 - x^2(\beta+2)}, \tag{D.2}$$

$$E_0 = (2+\alpha)E_{\rm peak}. \tag{D.3}$$

In Equation (D.2), we have resolved the ambiguity in the choice of root of a quadratic equation by requiring that when $\beta + 2 < 0$, then $\alpha + 2 > 0$, so that $E_{\rm peak}$ is in fact the peak energy of the νF_ν distribution.

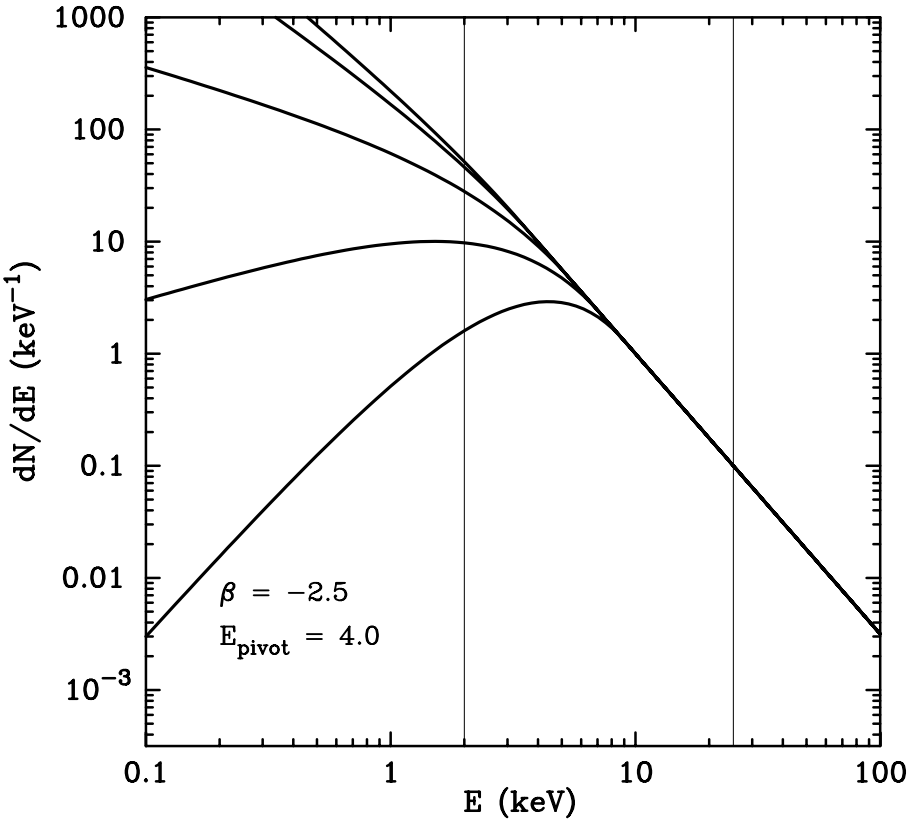

Figure D.1: Constrained Band functions, with $\beta = -2.5$ and $E_{\rm pivot} = 4$ keV, for different values of $E_{\rm peak}$. All functions have been normalized to 1 keV^{-1} at 10 keV. The two vertical lines at 2 keV and at 25 keV show the WXM bandpass. The spectra shown are (decreasing monotonically from the top at low energy), $E_{\rm peak}$ =1 keV, 2 keV, 4 keV, 6 keV, and 8 keV, respectively. As $E_{\rm peak}$ increases, $E_{\rm break}$ also necessarily increases, so that E_0 is forced to smaller and smaller values by the constraint, increasing the curvature and the value of α.

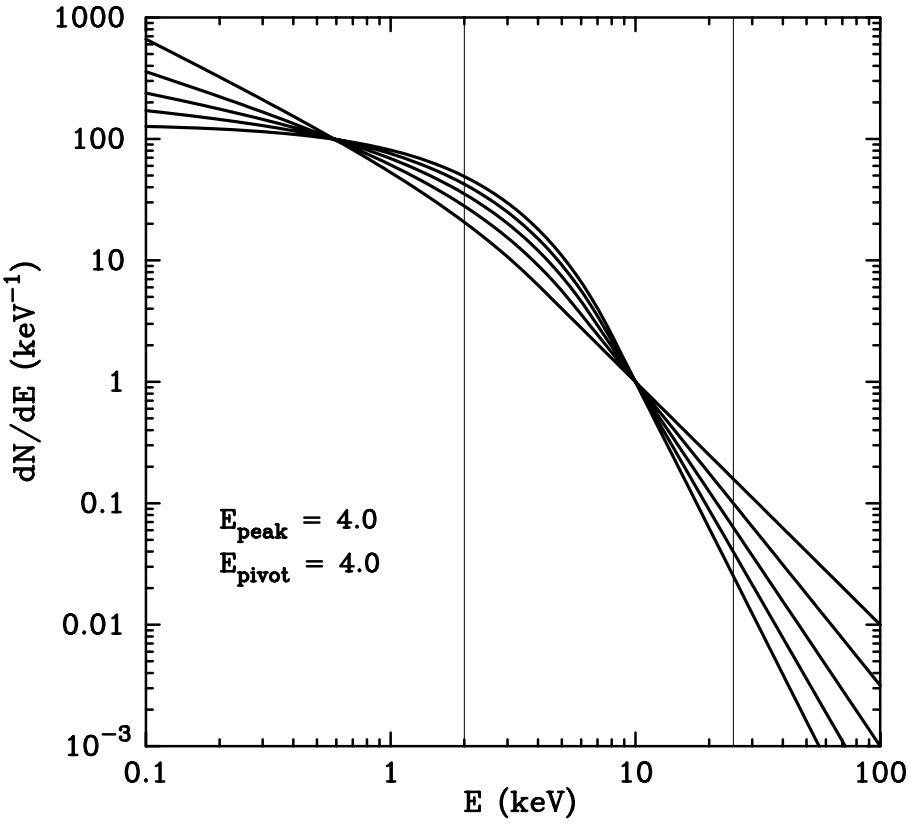

Figure D.2: Constrained Band functions, with $E_{\rm peak} = 4$ keV and $E_{\rm pivot} = 4$ keV, for different values of β. All functions have been normalized to 1 keV^{-1} at 10 keV. The two vertical lines at 2 keV and at 25 keV show the WXM bandpass. The spectra shown are for β = -2.0, -2.5, -3.0, -3.5, and -4.0, which can be distinguished by the increasing steepness of their slopes at high energy. The progression from some curvature at low energy ($\beta = -2.0$) to almost none ($\beta = -4.0$) is evident, as is the fact that as the curvature disappears, the resulting power-law is produced by the high-energy part of the Band function.

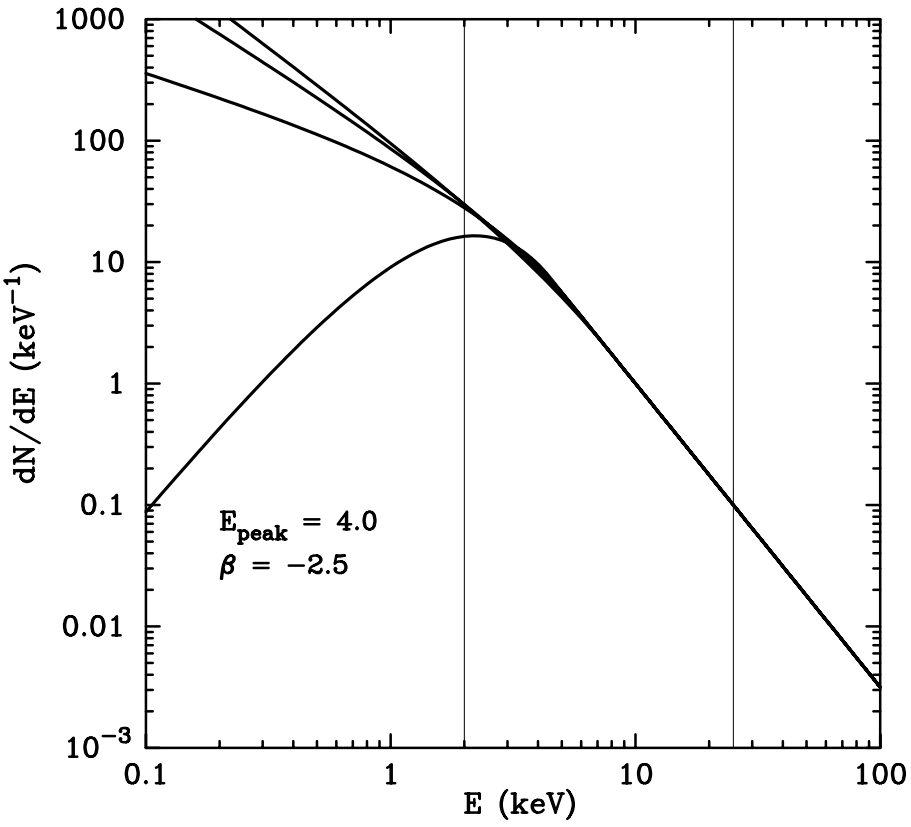

Figure D.3: Constrained Band functions, with $E_{\rm peak} = 4$ keV and $\beta = 2.0$, for different values of $E_{\rm pivot}$. All functions have been normalized to 1 keV^{-1} at 10 keV. The two vertical lines at 2 keV and at 25 keV show the WXM bandpass. The spectra shown are (increasing monotonically at low energy) for $E_{\rm pivot} = 2$ keV, 4 keV, 6 keV, and 8 keV, respectively. Once again, as the low-energy curvature disappears, the resulting power-law is produced by the high-energy part of the Band function. Note also that the shape of the constrained Band function is insensitive to the specific choice of $E_{\rm pivot}$ within a reasonable range.

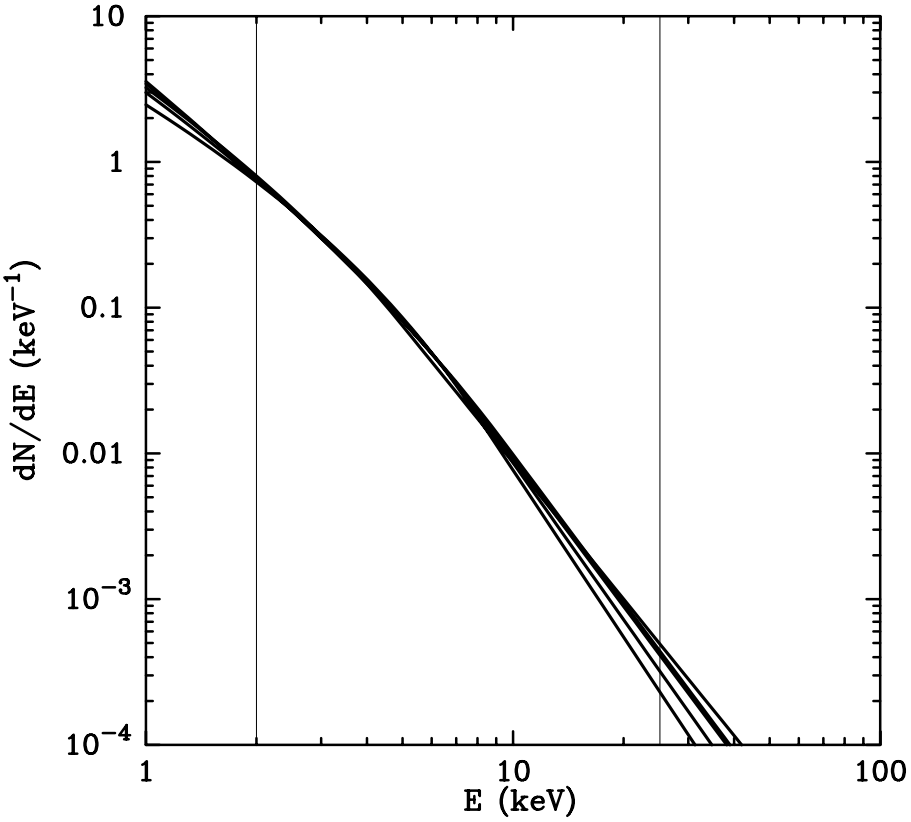

Figure D.4: Constrained Band functions with parameters that best fit the 13 s spectrum of XRF020903, for different fixed values of $E_{\rm pivot}$. The two vertical lines at 2 keV and at 25 keV show the WXM bandpass. All functions have been normalized so that the integral from 2 keV to 25 keV is one photon. The five spectra shown in the plot corresponding to $E_{\rm pivot} = 4$ keV, 5 keV, 6 keV, 7 keV, and 8 keV (the 7 keV and 8 keV largely overlap each other). This figure illustrates a robust aspect of the constraint procedure: the best-fit model is essentially unchanged in the WXM spectral band despite a factor-of-two change in the value of $E_{\rm pivot}$.

Appendix E

The selection effect of 45 GRB sample

We investigated the possible selection effect in our 45 GRB sample which is studied in chapter 7. Figure E.1 shows 2–400 keV fluence divided by the square root of the duration as a function of the incident angle. This vertical axis corresponds to the signal to noise ratio of each GRB. As seen in this plot, the selection effect becomes apparent at the incident angle of larger than 20 degrees, but not at less than 20 degrees. The scatter plots of 2–400 keV fluence and the incident angle, and 2–400 keV peak flux and the incident angle are shown in figure E.2 and E.3 respectively. These figures also show the selection effect of our sample at the incident angle of larger than 20 degrees. As seen in the plots, the minimum fluence and peak flux of our GRB sample are $\sim 1 \times 10^{-7}$ ergs cm^{-2} and ~ 2 photons cm^{-2} s^{-1} at the boresight angle respectively.

There are three main instrumental effects on WXM which might cause the selection effect in our sample. First is the shadow due to the frames on top of the proportional counters. Since the frame is made of titanium with the thickness of 3.52 mm, this effect causes the shadow in the case of the event at large incident angle. However, this effect must be apparent when the incident angle starts to increase. The second effect is the decrease of the source flux at the large incident angle. This effect should occur as a function of the incident angle, and it is also difficult to explain the trend of figure E.1. The last effect is the shadow due to the support structure. There are "walls" (support structure) around the coded mask and the counters, and between X and Y counters (figure 4.8). Since the area of the coded mask is twice as large as the detectors and they are separated in 187.37 mm, the shadow of the support structure appears at the incident angle of larger than 20 degrees. Thus, this effect is the most possible selection effect in our GRB sample.

In summary, the threshold level of our 45 GRB sample is $\sim 1 \times 10^{-7}$ erg cm^{-2} in 2-400 keV fluence and ~ 2 photons cm^{-2} s^{-1} in 2-400 keV peak flux at the boresight. The most plausible

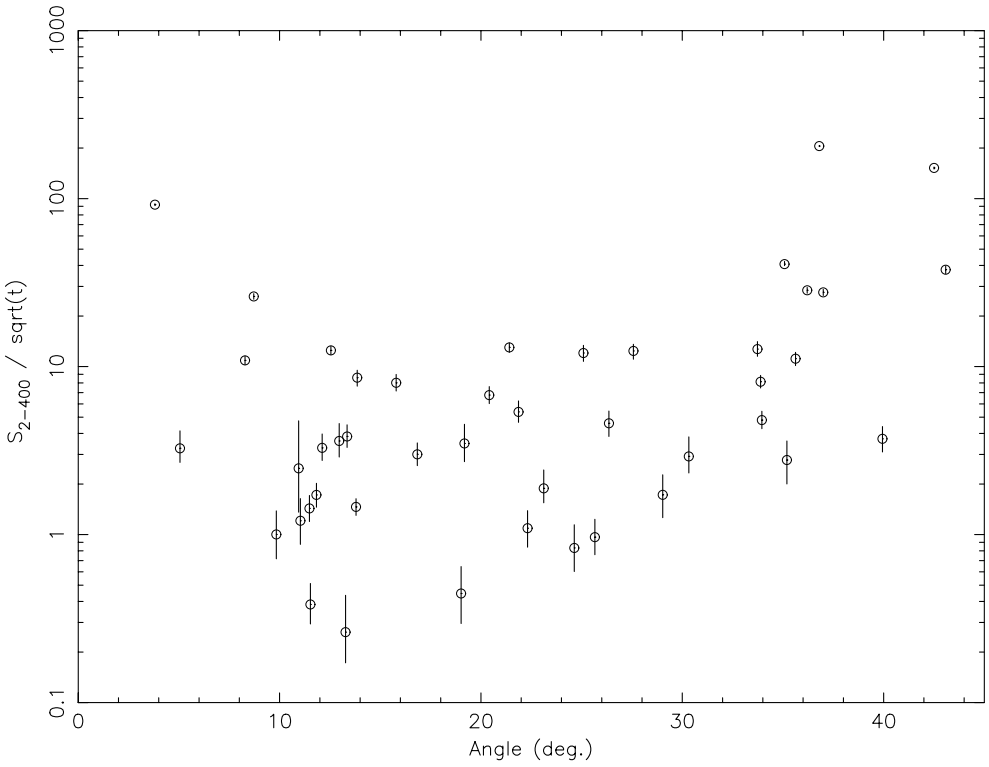

Figure E.1: 2-400 keV fluence divided by square root of duration as a function of the incident angle.

selection effect in our sample is the shadow due to the support structure of WXM.

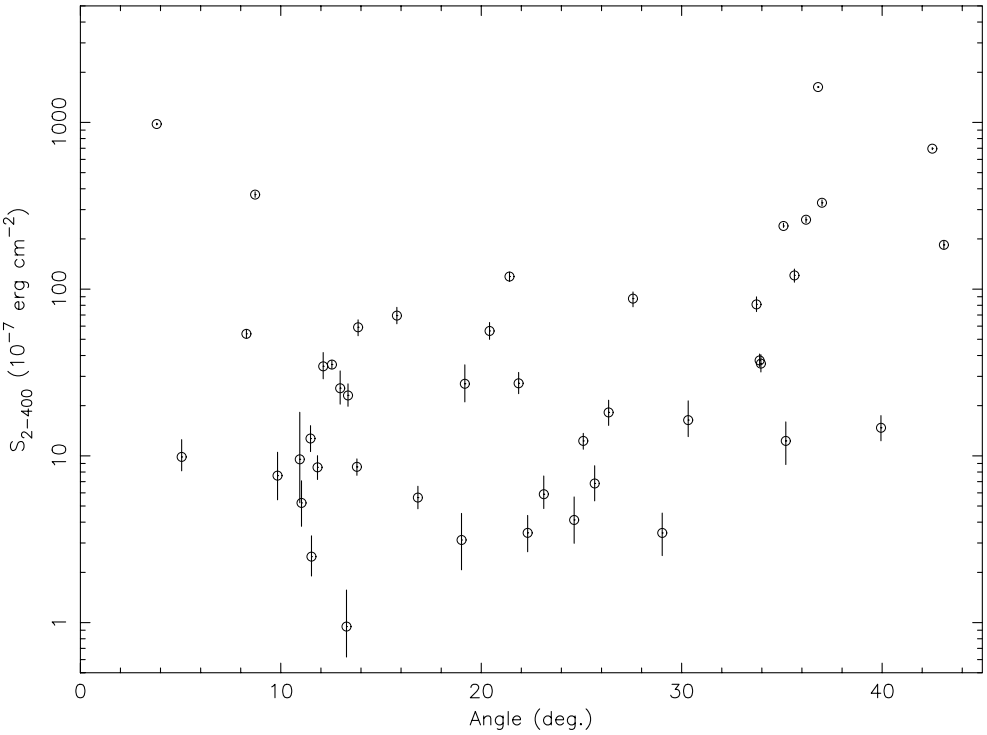

Figure E.2: 2–400 keV fluence as a function of the incident angle.

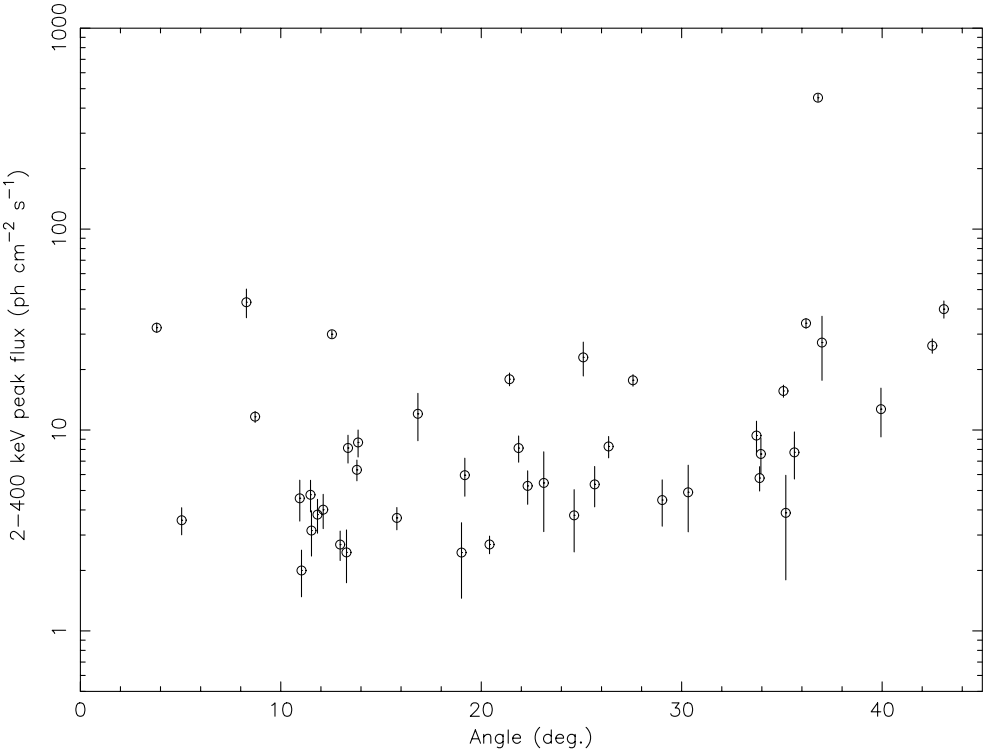

Figure E.3: 2–400 keV peak flux as a function of the incident angle.

Bibliography

[1] Amati, L., Frontera, F., Tavani, M., in't Zand, J.J.M., Antonelli, A., Costa, E., Feroci, M., Guidorzi, C., Heise, J., Masetti, N., Montanari, E., Nicastro, L., Palazzi, E., Pian, E., Piro, L., and Soffitta, P., 2002, "Intrinsic Spectra and Energetics of BeppoSAX Gamma-Ray Bursts with Known Redshifts," A&A, 390, 81

[2] Ambruster, C., Wood, K. S., Meekins, J. F., Yentis, D. J., Smathers, H. W., Byram, E. T., Chubb, T. A., and Friedman, H. 1983, "H0547–14: X-Ray Flux From a Weak Gamma-Ray Burst?," ApJ, 269, 779

[3] Ambruster, C. W., and Wood, K. S., 1986, "The *HEAO* A-1 All-Sky Survey of Fast X-ray Transients," ApJ, 311, 258

[4] Atteia, J-L., Boer, M., Cotin, F., Couteret, J., Dezalay, J-P., Ehanno, M., Evrad, J., Lagrange, D., Niel, M., Olive, J-F., Rouaix, G., Souleille, P., Vedrenne, G., Hurley, K., Ricker, G., Vanderspek, R., Crew, G., Doty, J. and Butler, N. 2003, "In-Flight Performance and First Results of FREGATE," in AIP Conf. Proc. 662, Gamma-Ray Burst and Afterglow Astronomy 2001, ed. G. R. Ricker & R. K. Vanderspek (New York: AIP), 17 (astro-ph/0202515)

[5] Atteia, J-L., 2003, "A Simple Empirical Redshift Indicator for Gamma-Ray Bursts," A&A, 407, L1

[6] Band, D., Matteson, J., Ford, L., Shaefer, B., Palmer, D., Teegarden, B., Cline, T., Briggs, M., Paciesas, W., Pendleton, G., Fishman, G., Kouveliotou, C., Meegan, C., and Wilson, R. 1993, "BATSE Observation of Gamma-Ray Burst Spectra. I. Spectral Diversity," ApJ, 413, 281

[7] Band, D., 2003, "Comparison of the Gamma-Ray Burst Sensitivity of Different Detectors," ApJ, 588, 945

[8] Bloom, J.S., Kulkarni, S.R., Djorgovski, S.G., Elchelberger, A.C., C*ôté*, P., Blakeslee, J.P., Odewahn, S.C., Harrison, F.A., Frail, D.A., Fllippenko, A.V., Leonard, D.C., Riess, A.G., Spinrad, H., Stern, D., Bunker, A., Dey, A., Grossan, B., Perlmutter, S., Knop, R.A., Hook, I.M., Feroci, M. 1999, "The Unusual Afterglow of the γ-Ray Burst of the 26 March 1998 as Evidence for a Supernova Connection," Nature, 401, 453

[9] Bloom, J.S., Frail, D.A., and Kulkarni, S.R. 2003, "GRB Energetics and the GRB Hubble Diagram: Promises and Limitations," accepted to ApJ (astro-ph/0302210)

[10] Bloom, J.S, Fox, D., van Dokkum, P.G., Kulkarni, S.R., Berger, E., Djorgovski, S.G., and Frail, D.A. 2003, "The First Two Host Galaxies of X-ray Flashes: XRF011030 and XRF020427," in preperation (astro-ph/0303514)

[11] Connaughton, V. 2002, "BATSE Observation of Gamma-Ray Burst Tails," ApJ, 567, 1028

[12] Costa, E., Frontera, F., Heise, J., Feroci, M., in 't Zand, J., Fiore, F., Cinti, M. N., dal Fiume, D., Nicastro, L., Orlandini, M., Palazzi, E., Rapisarda, M., Zavattini, G., Jager, R., Parmar, A., Owens, A., Molendi, S., Cusumano, G., Maccarone, M. C., Giarrusso, S., Coletta, A., Antonelli, L. A., Giommi, P., Muller, J. M., Piro, L., Butler, R. C. 1997, "Discovery of an X-ray Afterglow Associated with the Gamma-Ray Burst of 28 February 1997," Nature, 387, 783

[13] Crew, G.B., Vanderspek, R., Doty, J., Villasenor, J., Monnelly, G., Butler, N., Prighozin, G., Ricker, G. 2003, "HETE Mission Operations," in AIP Conf. Proc. 662, Gamma-Ray Burst and Afterglow Astronomy 2001, ed. G. R. Ricker & R. K. Vanderspek (New York: AIP), 70

[14] Crew, G.B., Villasenor, J., Monnelly, G., Doty, J., Vanderspek, R., Ricker, G. 2003, "Real-Time Message from the HETE Spececraft via the HETE Burst Alert Network," in AIP Conf. Proc. 662, Gamma-Ray Burst and Afterglow Astronomy 2001, ed. G. R. Ricker & R. K. Vanderspek (New York: AIP), 66

[15] Crew, G.B., Lamb, D.Q., Ricker, G.R., Atteia, J.-L., Kawai, N., Vanderspek, R., Villasenor, J., Doty, J., Prigozhin, G., Jernigan, J.G., Graziani, C., Shirasaki, Y., Sakamoto, T., Suzuki, M., Butler, N., Hurley, K., Tamagawa, T., Yoshida, A., Matsuoka, M., Fenimore, E.E., Galassi, M., Barraud, C., Boer, M., Dezalay, J.-P., Olive, J.-F., Levine, A., Monnelly, G., Martel, F., Morgan, E., Donaghy, T.Q., Torii, K., Woosley, S.E., Cline, T.,

Braga, J., Manchanda, R., Pizzichini, G., Takagishi, K., and Yamauchi, M. 2003, "HETE-2 Localization and Observation of the Bright, X-Ray-Rich Gamma-Ray Burst GRB021211," ApJ, 599, 387

[16] Dermer, C.D., Chiang, J., and Mötttcher, M. 1999, "Fireball Loading and the Blast-wave Model of Gamma-Ray Bursts," ApJ, 513, 656

[17] De Pasquale, M., Piro, L., Perna, R., Costa, E., Feroci, M., Gandolfi, G., in't Zand, J., Nicastro, L., Frontera, F., Antonelli, L.A., Fiore, F., and Stratta, G. 2003, "A Comparative Study of the X-Ray Afterglow Properties of Optically Bright and Dark Gamma-Ray Bursts," ApJ, 592, 1018

[18] Doty, J. et al. 2003, GCN Circ. 2211

[19] Fenimore, E. E., in't Zand, J. J. M., Norris, J. P., Bonnell, J. T., Nemiroff, R. J. 1995, "Gamma-Ray Burst Peak Duration as a Function of Energy," ApJL, 448, 101

[20] Fenimore, E.E, Ramirez-Ruiz, R. 2000, "Redshifts for 220 BATSE Gamma-Ray Bursts Determined by Variability and the Cosmological Consequences," submitted to ApJ (astro-ph/0004176)

[21] Fox, D.W., Price, P.A., Soderberg, A.M., Berger, E., Kulkarni, S.R., Sari, R., Frail, D.A., Harrison, F.A., Yost, S.A., Matthews, K., Peterson, B.A., Tanaka, I., Chiristiansen, J., and Moriarty-Chieven, G.H. 2003, "Discovery of Early Optical Emission from GRB021211," ApJL, 586, 5

[22] Frail, D.A., Kulkarni, S.R., Sari, R., Djorgovski, S. G., Bloom, J.S., Galama, T.J., Reichart, D.E., Berger, E., Harrison, F.A., Price, P.A., Yost, S.A., Diercks, A., Goodrich, R.W., and Chaffee, F. 2001, "Beaming in Gamma-Ray Bursts: Evidence for a Standard Energy Reservoir," ApJL, 562, 55

[23] Fynbo, J. U., Jensen, B. L., Gorosabel, J., Hjorth, J., Pedersen, H., Mϕller, P., Abbott, T., Castro-Tirado, A. J., Delgado, D., Greiner, J., Henden, A., Magazz$\grave{u}$, A., Masetti, N., Merlino, S., Masegosa, J., Østensen, R., Palazzi, E., Pian, E., Schwarz, H. E., Cline, T., Guidorzi, C., Goldsten, J., Hurley, K., Mazets, E., McClanahan, T., Montanari, E., Starr, R., and Trombka, J. 2001, "Detection of the Optical Afterglow of GRB 000630: Implication for dark bursts," A&A, 369, 373

[24] Galama, T.J., Vreeswlijk, P.M., Van Paradijs, J., Kouvellotou, C., Augusteijn, T., Böhnhardt, H., Brewer, J.P., Doublier, V., Gonzalez, J.-F., Leibundgut, B., Lidman, C., Hainaut, O.R., Patat, F., Heise, J., in't Zand, J., Hurley, K., Groot, P.J., Strom, R.G., Mazzali, P.A., Iwamoto, K., Nomoto, K., Umeda, H., Nakamura, T., Young, T.R., Suzuki, T., Shigeyama, T., Koshut, T., Kippen, M., Robinson, C., de Wildt, P., Wijers, R.A.M.J., Tanvir, N., Greiner, J., Pian, E., Palazzi, E., Frontera, F., Masatti, N., Nicastro, L, Feroci, M., Costa, E., Piro, L, Peterson, B.A., Tinney, C., Boyle, B., Cannon, R., Stathalis, R., Sadler, E., Begam, M.C., and Ianna, P. 1998, "An Usual Supernova in the Error Box of the $-gamma$-Ray Burst of 25 April 1998," Nature, 395, 670

[25] Galama, T.J., Nanvir, N., Vreeswijk, P.M., Wijers, A.M.J., Groot, P.J., Rol, E., Van Paradijs, J., Kouveliotou, C., Fruchter, A.S., Masetti, N., Pedersen, H., Margon, B., Deutsch, E.W., Metzger, M., Armus, L., Klose, S., and Stecklum, B. 2000, "Evidence for A Supernova in Reanalyzed Optical and Near-infrared Images of GRB970228," ApJ, 536, 185

[26] Galassi, M., et al., GCN Circ. 2402

[27] Giblin, T.W., Van Paradijs, J., Kouveliotou, C., Connaughton, V., Wijers, R.A.M.J., Briggs, M.S., Preece, R.D., and Fishman, G.J. 1999, "Evidence for an Early High-Energy Afterglow Observed with BATSE from GRB 980923," ApJL, 524, 47

[28] González, M.M., Dingus, B.L., Kaneko, Y., Preece, R.D., Dermer, C.D., and Briggs, M.S., 2003 "A γ-Ray Burst with a High-Energy Spectral Component Inconsistent with the Synchrotron Shock Model," Nature, 424, 749

[29] Granot J., Piran, T., and Sari, R. 2000, "The Synchrotoron Spectrum of Fast Cooling Electrons Revisited," ApJL, 534, 163

[30] Greiner, J., et al. 2003, GCN Circular 2020

[31] Groot P. J, Galma, T. J., van Paradijs, Melnick, G., vander Steene, G., et al. 1997, IAU Circ. 6584

[32] Groot P. J, Galma, T. J., van Paradijs, Melnick, G., vander Steene, G., et al. 1997, IAU Circ. 6588

[33] Gotthelf, E. V., Hamilton, T. T., and Helfand, D. J. 1996, "The *Einstein* Observatory Detection of Faint X-ray Flashes," ApJ, 466, 779

[34] Greiner, J., Hartmann, D. H., Voges, W., Boller, T., Schwar, R., and Zharikov, S. V. 2000, "Search for GRB X-ray Afterglow in the ROSAT All-Sky Survey," A&A, 353, 998

[35] Hakkila, J., Meegan, C.A., Horack, J.M., Pendleton, G.N., Briggs, M.S., Mallozzi, R.S., Koshut, T.M., Preece, R.D., and Paciesas, W.S. 1996, "Luminosity Distributions of Cosmological Gamma-Ray Bursts," ApJ, 462, 125

[36] Heise, J., in't Zand, J. J. M., Kippen, R. M., and Woods, P. M. 2001, "X-ray Flashes and X-ray Rich Gamma Ray Bursts," in conference proceedings, Gamma-Ray Bursts in the Afterglow Era, ed. Costa, E., Frontera, F., and Hjorth, J. (Berlin Heidelberg: Springer, 2001), 16, Astro-ph/0111246

[37] Hjorth, J., Sollerman, J., Mϕller, P., Fynbo, J.P.U., Woosley, S.E., Kouvellotou, C., Tanvir, N.R., Greiner, J., Anderson, M.I., Castro-Tirado, A.J., Cerón, J.M.C., Fruchter, A.S., Gorosabel, J., Jakobsson, P., Kaper, L, Klose, S., Masatti, N., Pedersen, H., Pedersen, K., Pian, E., Palazzi, E., Rhoads, J.E., Rol, E., van den Heuvel, E.P.J., Vreeswijk, P.M., Watson, D., and Wijers, R.A.M.J. 2003, "A Very Energetic Supernova Associated with the γ-Ray Burst of 29 March 2003," Nature, 423, 847

[38] Hurley, K. et al. 2001, GCN Circ. 1076

[39] Iwamoto, K., Mazzali, P.A., Nomoto, K., Umeda, H., Nakamura, T., Patat, F., Danziger, I.J., Young, T.R., Suzuki, T., Shigeyama, T., Augusteijn, T., Doublier, V., Gonzalez, J.-F., Boehnhardt, H., Brewer, J., Hainaut, O.R., Lidman, C., Leibundgut, B., Cappellaro, E., Turatto, M., Galama, T.J., Vreeswijk, P.M., Kouvellotou, C., Van Paradijs, J., Pian, E., Palazzi, E., and Frontera, F. 1998, "A Hypernova Model for the Supernova Associated with the γ-Ray Burst of 25 April 1998," Nature, 395, 672

[40] Jernigan et al. 2003, GCN Circ. 2209

[41] Kawai, N., Yoshida, A., Matsuoka, M., Shirasaki, Y., Tamagawa, T., Torii, K., Sakamoto, T., Takahashi, D., Fenimore, E., Galasi, M., Tavenner, T., Lamb, D.Q., Graziani, C., Donaghy, T., Vanderspek, R., Yamauchi, M., Takagishi, K., Hatsukade, I. and HETE-2 Science Team 2003, "In-Orbit Performance of WXM (Wide-Field X-Ray Monitor)," in AIP Conf. Proc. 662, Gamma-Ray Burst and Afterglow Astronomy 2001, ed. G. R. Ricker & R. K. Vanderspek (New York: AIP), 25

[42] Kippen, R. M., Woods, P. M., Heise, J., in't Zand, J. J. M., Briggs, M. S., and Preece, R. D. 2002, "Spectral Characteristics of X-ray Flashes compared to Gamma-Ray Bursts," in AIP Conf. Proc. 662, Gamma-Ray Burst and Afterglow Astronomy 2001, ed. G. R. Ricker & R. K. Vanderspek (New York: AIP), 244 (astro-ph/0203114)

[43] Klebesadel, R. W., Strong, I. B., and Olson, R. A. "Observation of Gamma-Ray Bursts of Cosmic Origin," ApJL, 182, 85

[44] Knoll, G.F. 1997, "Radiation Detection and Measurement (2nd Edition)," (section 6.3.3)

[45] Lamb, D.Q. 1995, "The Distance Scale to Gamma-Ray Bursts," PASP, 107, 1152

[46] Lamb, D.Q., Reichart, D.E. 2000, "Gamma-Ray Bursts as a Probe of the Very High Redshift Universe," ApJ, 536, 1

[47] Lamb, D.Q., Donaghy, T.Q., and Graziani, C. 2003, "A Unified Jet Model of X-Ray Falshes and Gamma-Ray Bursts," in proc. 2nd VERITAS Symposium on TeV Astrophysics, Chicago, Illinois (astro-ph/0309456)

[48] Lamb, D.Q., et al. in preparation

[49] Lloyd, N. M., Petrosian, V., and Mallozzi, R. S. 2000, "Cosmological versus Intrinsic: The Correlation between Intensity and the Peak of the νF_ν Spectrum of Gamma-Ray Bursts," ApJ, 534, 227

[50] Mao, S. and Paczyński, B. 1992, "On the Cosmological Origin of Gamma-Ray Bursts," ApJL, 388, 45

[51] Mészáros, P., Ramirez-Ruiz, E., Rees, M.J., and Zhang, B. 2002, "X-ray Rich GRB, Photosperees and Variability," ApJ, 578, 812

[52] Metzger, A. R., Parker, R. H., Gilman, D., Peterson. L. E., and Trombka, J. I. 1974, "Observation of a Cosmic Gamma-Ray Burst on *Apollo 16*. I Temporal Variability and Energy Spectrum," ApJL, 194, 19

[53] Metzger, M. R., Kulkarni, S. R., Djorgovski, S. G., Gal, R., Steidel, C. C., Frail, D. A. 1997, IAU Circ. 6588

[54] Mochkovitch, R., Daigne, F., Barraud, C., and Atteia, J.L. 2003, "On the Nature of X-Ray Flashes," in "Gamma-ray bursts in the afterglow era", 3rd workshop, Rome (astro-ph/0303289)

[55] Monnelly, G., Villasenor, J.N, Jernigan, J.G., Prighozin, G., Vanderspek, R., Crew, G.B., Doty, J., Levine, A. and Ricker G. 2003, "HETE Soft X-ray Camera Imaging: Calibration, Performance, and Sensitivity," in AIP Conf. Proc. 662, Gamma-Ray Burst and Afterglow Astronomy 2001, ed. G. R. Ricker & R. K. Vanderspek (New York: AIP), 88 (astro-ph/0203079)

[56] Norris, J.P., Marani, G.F., and Bonnell, J.T. 2000, "Connection Between Energy-Dependent Lags and Peak Luminosity in Gamma-Ray Burst," ApJ, 534, 248

[57] Olive, J-F., Dezalay, J-P., Atteia, J-L., Barraud, C., Butler, N., Crew, G.B., Doty, J., Ricker, G. and Vanderspek, R. 2003, "In-Flight Verification of the FREGATE Spectral Response," in AIP Conf. Proc. 662, Gamma-Ray Burst and Afterglow Astronomy 2001, ed. G. R. Ricker & R. K. Vanderspek (New York: AIP), 88 (astro-ph/0203079)

[58] Paciesas, W. S., Meegan, C. A., Pendleton, G. N., Briggs, M. S., Kouveliotou, C., Koshut, T. M., Lestrade, J. P., McCollough, M. L., Brainerd, J. J., Hakkila, J., Henze, W., Preece, R. D., Connaughton, V., Kippen, R. M., Mallozzi, R. S., Fishman, G. J., Richardson, G. A., Sahi, M. 1999, "The Fourth BATSE Gamma-Ray Burst Catalog (Revised)," ApJS, 122, 465

[59] Paczyński, B. 1995, "How Far Away Are Gamma-Ray Bursts?" PASP, 107, 1167

[60] Pendleton, G.N, Mallozzi, R.S., Paciesas, W.S., Briggs, M.S., Preece, R.D., Koshut, T.M., Horack, J.M., Meedan, C.A., Fishman, G.J., Kakkila, J., and Kouveliotou, C., 1996, "The Intensity Distribution for Gamma-Ray Bursts Observed with BATSE," ApJ, 464, 606

[61] Piran, T. 1999, "The Gamma-Ray Bursts and the Fireball Model," Physics Reports, 314, 575

[62] Preece, R.D., Briggs, M.S., Mallozzi, R.S., Pendleton, G.N., Paciesas, W.S., and Band, D.L. 1998, "The Synchrotron Shock Model Confronts A "Line of Death" in the BATSE Gamma-Ray Burst Data," ApJL, 506, 23

[63] Preece, R. D., Briggs, M. S., Mallozzi, R. S., Pendleton, G. N., and Paciesas, W. S. 2000, "The BATSE Gamma-Ray Burst Spectral Catalog. I. High Time Resolution Spectroscopy of Bright Bursts using High Energy Resolution Data," ApJS, 126, 19

[64] Preece, R.D., Briggs, M.S., Giblin, T.W., Mallozzi, R.S., Pendletion, G.N., and Paciesas, W.S. 2002, "On The Consistency of Gamma-Ray Burst Spectral Indices with The Synchrotron Shock Model," ApJ, 581, 1248

[65] Price, P. A., Axelrod, T. S., Schmidt, B.P. (RSAA, ANU), and Reichart D. E. 2001, GCN Circ. 1020

[66] Prigozhin, G. et al. 2003, GCN Circ. 2313

[67] Pye, J. P., and McHardy, I. M. 1983, "The *Ariel V* sky survey of fast-transient X-ray sources," MNRAS, 205, 875

[68] Reichart, D.E., Lamb, D.Q, Fenimore, E.E, Ramirez-Ruiz, E., Cline, T.L, and Hurley, K., 2001, "A Possible Cepheid-like Luminosity Estimator for the Long Gamma-Ray Burst," ApJ, 552, 57

[69] Ricker, G. et al. 2001, GCN Circ. 934

[70] Ricker, G. et al. 2001, GCN Circ. 1018

[71] Ricker, G. et al. 2001, GCN Circ. 1075

[72] Ricker, G. et al. 2001, GCN Circ. 1109

[73] Ricker, G. et al. 2001, GCN Circ. 1165

[74] Ricker, G. et al. 2001, GCN Circ. 1169

[75] Ricker, G. et al. 2001, GCN Circ. 1194

[76] Ricker, G. et al. 2001, GCN Circ. 1280

[77] Ricker, G. et al. 2001, GCN Circ. 1530

[78] Ricker, G.R., Atteia, J-L., Crew, G.B., Doty, J.P., Fenimore, E.E., Galassi, M., Graziani, C., Hurley, K., Jernigan, J.G., Kawai, N., Lamb, D.Q., Matsuoka, M., Pizzichini, G., Shirasaki, Y., Tamagawa, T., Vanderspek, R., Vedrenne, G., Villasenor, J., Woosley, S.E and Yoshida, A. 2003, "The High Energy Transient Explorer (HETE): Mission and Science Overview," in AIP Conf. Proc. 662, Gamma-Ray Burst and Afterglow Astronomy 2001, ed. G. R. Ricker & R. K. Vanderspek (New York: AIP), 3

[79] Rossi, E., Lazzati, D., Rees, M.J. 2002, "Afterglow Light Curves, Viewing Angle and the Jet Structure of Gamma-Ray Bursts," MNRAS, 332, 945

[80] Rybicki, G. R., and Lightman, A. P., 1979, Radiative Processes in Astrophysics, Wiley-Interscience

[81] Sakamoto, T. et al. 2002, GCN Circ. 1649

[82] Sakamoto, T., Lamb, D.Q., Graziani, C., Donaghy, T.Q., Suzuki, M., Ricker, G., Atteia, J.-L., Kawai, N., Yoshida, A., Shirasaki, Y., Tamagawa, T., Torii, K., Matsuoka, M., Fenimore, E.E., Galassi, M., Tavenner, T., Doty, J., Vanderspek, R., Crew, G.B., Villasenor, J., Butler, N., Prigozhin, G., Jernigan, J.G., Barraud, C., Boer, M., Dezalay, J.-P., Olive, J.-F., Hurley, K., Levine, A., Monnelly, G., Martel, F., Morgan, E., Woosley, S.E., Cline, T., Braga, J., Manchanda, R., Pizzichini, G., Takagishi, K., and Yamauchi, M. 2003, "HETE-2 Observation of the Extremely Soft X-Ray Flash XRF020903," ApJ in press (astro-ph/0309455)

[83] Sakurai, I., Mihara, T., Kawai, N., Yoshida, A., Shirasaki, Y., Matuoka, M., Sugizaki, M., and Kamae, T. 2000, "Dependence of gas gain on x-ray-absorbed position in the proportional counter," Proc. SPIE Vol. 4140, p. 511-519, X-Ray and Gamma-Ray Instrumentation for Astronomy XI

[84] Sari, R., Narayan, R., and Piran, T. 1996, "Cooling Timescales and Temporal Structure of Gamma-Ray Bursts," ApJ, 473, 204

[85] Sari, R., Piran, T., and Narayan, R. 1998, "Spectra and Light Curves of Gamma-Ray Burst Afterglow," ApJL, 497, 17

[86] Sato, R., Kawai, N., Suzuki, M., Yatsu, Y., Kataoka, J., Takagi, R., Yanagisawa, K., and Yamaoka, H. 2003, "Earliest Detection of the Optical Afterglow of GRB030329 and Its Variability," ApJL, 599, 9

[87] Schaefer, B.E., Deng, M., and Band, D.L, 2001, "Redshifts and Luminosity for 112 Gamma-Ray Bursts," ApJL, 563, 123

[88] Schaefer, B. E., 2003, "Gamma-Ray Burst Hubble Diagram to z = 4.5," ApJL, 583, 67

[89] Schaefer, B. E., 2003, "Explaining the Gamma-Ray Burst E_{peak} Distribution," ApJL, 583, 71

[90] Schmidt, M., Higdon, J.C., and Hueter, G., 1988, "Application of the V/V_{max} Test to Gamma-Ray Burst," ApJL, 329, 85

[91] Shirasaki, Y., Kawai, N., Yoshida, A., Matsuoka, M., Namiki, M., Sakurai, I., Yamauchi, M., Takagishi, K., Hatsukade, I., Fenimore, E.E., and Galassi, M. 2000, "Performance of the wide-field x-ray monitor on board the high-energy transient explorer 2," Proc. SPIE Vol. 4012, p. 166-177, X-Ray Optics, Instruments, and Missions III

[92] Shirasaki, Y., Kawai, N., Yoshida, A., Matsuoka, M., Tamagaawa, T., Torii, K., Sakamoto, T., Suzuki, M., Urata, Y, Sato, R., Nakagawa, Y., Takahashi, D., Fenimore, E.E., Galassi, M., Lamb, D.Q., Graziani, C., Donaghy, T.Q., Vanderspek, R., Yamauchi, M., Takagishi, K. and Hatsukade, I. 2003, "Design and preformance of the Wide-Field X-Ray Monitor on Board the High-Energy Transient Explorer 2," Publ. Astorn. Soc. Japan, 55, 1033

[93] Shirasaki, Y. et al. 2003, GCN Circ. 2210

[94] Shirasaki, Y. et al. 2003, GCN Circ. 2401

[95] Soderberg, A.M., Kulkarni, S.R., Berger, E., Fox, D.B., Price, P.A., Yost, S., Hunt, M., Frail, D.A., Walker, C., Hamuy, M., Shectman, S., Halpern, J., and Mirabal N. 2003, "A Redshift Determination for XRF 020903: First Spectroscopic Observations of an X-Ray Flash," submitted to ApJ (astro-ph/0311050)

[96] Stanek, K. Z., Matheson, T., Garnavichi, P. M., Martini, P., Berlind, P., Caldwell, N., Challis, P., Brown, W. R., Schild, R., Krisciunas, K., Calkins, M. L., Lee, J. C., Hathi, N., Jansen, R. A., Windhorst, R., Echevarria, L., Eisenstein, D. J., Pindor, B., Olszewski, E. W., Harding, P., Holland, S. T., and Bersier, D., 2003, "Spectroscopic Discovery of the Supernova 2003dh Associated with GRB 030329," ApJL, 591, 17

[97] Strohmayer, T. E., Fenimore E. E., Murakami, T., and Yoshida, A. 1998, "X-Ray Spectral Characteristics of GINGA Gamma-Ray Bursts," ApJ, 500, 873

[98] Tamagawa, T. et al. 2001, GCN Circ. 1675

[99] Tamagawa, T., Nakagawa, Y.E., Nagai, T., Kawai, N., Yoshida, A., Miyasaka, H., Shirasaki, Y., Torii, K., Sakamoto, T., Ricker, G.R., Vanderspek, R., Crew, G.B., Doty, J.P., Lamb, D.Q., and Graziani, C. 2004, "Discovery of a new particle precipitation region: The Ecuador Anomaly," submitted to Science

[100] Tavani, M. 1996, "A Shock Emission Model for Gamma-Ray Bursts. II. Spectral Properties," ApJ, 466, 768

[101] Totani, T. 1997, "Cosmological Gamma-Ray Bursts and Evolution of Galaxies," ApJL, 486, 71

[102] Totani, T. 2000, "Probing the Cosmic Star Formation History by the Brightness Distribution of Gamma-Ray Bursts," ApJ, 511, 41

[103] Totani, T., and Panaitescu, A. 2002, "Orphan Afterglows of Collimated Gamma-Ray Bursts: Rate Predictions and Prospects for Detection," ApJ, 576, 120

[104] Trombka, J. I., Eller, E. L., Schmadebeck, R. L., Adler, I., Metzger, A. E., Gilman, D., Gorenstein, P., and Bjorkholm, P. 1974, "Observation of a Cosmic Gamma-Ray Burst on *Apollo 16*. II X-ray Time Profile and Source Location," ApJL, 194, 27

[105] van Paradijs, J., Groot, P. J., Galama, T., Kouveliotou, C., Strom, R. G., Telting, J., Rutten, R. G. M., Fishman, G. J., Meegan, C. A., Pettini, M., Tanvir, N., Bloom, J., Pedersen, H., Nordgaard-Nielsen, H. U., Linden-Vornle, M., Melnick, J., van der Steene, G., Bremer, M., Naber, R., Heise, J., in 't Zand, J., Costa, E., Feroci, M., Piro, L., Frontera, F., Zavattini, G., Nicastro, L., Palazzi, E., Bennet, K., Hanlon, L., Parmar, A. 1997, "Transient Optical Emission from the Error Box of the Gamma-Ray Burst of 28 February 1997," Nature, 386, 686

[106] van Paradijs, J., Kouveliotou, C., and Wijers, R.A.M.J. 2000 "Gamma-Ray Burst Afterglows," Anuual Review of Astronomy & Astrophysics, 38, 379

[107] Vanderspek, R., Sakamoto, T., Barraud, C., Tamagawa, T., Graziani, C., Suzuki, M., Shirasaki, Y., Prigozhin, G., Villasenor, J., Jernigan, J.G., Crew, G.B., Atteia, J.-L., Hurley, K., Kawai, N., Lamb, D.Q., Ricker, G.R., Woosley, S.E., Butler, N., Doty, J., Dullighan, A., Donaghy, T.Q., Fenimore, E.E., Galassi, M., Matsuoka, M., Takagishi, K., Torii, K., Yoshida, A., Boer, M., Dezalay, J.-P., Olive, J.-F., Braga, J., Manchanda, R., and Pizzichini, G. 2003, "HETE-2 Observation and Localization of the Bright Gamma-Ray Burst GRB030329," in preparation

[108] Villasenor, J., Crew, G., Monnelly, G., Doty, J., Foster, R., Ricker, G., Vanderspek, R., Kawai, N., Yoshida, A., Boer, M., Hurley, K., Manchanda, R., Pizzichini, G., Braga, J. and Azzibrouck, G. 2003, "First Year Operations of the HETE Burst Alert Network," in

AIP Conf. Proc. 662, Gamma-Ray Burst and Afterglow Astronomy 2001, ed. G. R. Ricker & R. K. Vanderspek (New York: AIP), 107

[109] Villasenor, J.N., Dill, R., Doty, J.P., Monnelly, G., Vanderspek, R., Kissel, S., Prigozhin, G., Crew, G.B. and Ricker G.R. 2003, "An Overview of the HETE Soft X-ray Camera," in AIP Conf. Proc. 662, Gamma-Ray Burst and Afterglow Astronomy 2001, ed. G. R. Ricker & R. K. Vanderspek (New York: AIP), 33

[110] Villasenor, J. et al. 2003, GCN Circ. 2261

[111] Wheaton, W. A., Ulmer, M. P., Baity, W. A., Datlowe, D. W., Elcan, M. J., Peterson, L. E., Klebesadel, R. W., Strong, I. B., Cline, T. L., and Desai, U. D. 1973, "The Direction and Spectral Variability of a Cosmic Gamma-Ray Burst," ApJL, 185, 57

[112] Yamazaki, R., Ioka, K., and Nakamura, T. 2002, "X-ray Flashes from Off-axis Gamma-Ray Bursts," ApJL, 571, 31

[113] Yamazaki, R., Ioka, K., and Nakamura, T. 2003, "Cosmological X-ray Flashes in the Off-axis Jet Model," ApJ, 593, 941

[114] , Zhang, B., and Mészáros, P. 2002, "Gamma-Ray Burst Beaming: a Universal Configuration with a Standard Energy Reservoir?," ApJ, 571, 876

[115] , Zhang, B., and Mészáros, P. 2002, "An Analysis of Gamma-Ray Burst Spectral Break Models," ApJ, 581, 1236

[116] Zhang, W., Woodley, S.E., and MacFadyen, A.I. 2003, "Relativistic Jets In Collapsars," ApJ, 586, 336

Acknowledgments

First of all, I am most grateful to Prof. N. Kawai for his support and concern for my entire Ph.D. program. I also would like to thank Dr. E. E. Fenimore for giving me a opportunity to working at Los Alamos National Laboratory for a year. For the scientific guidance and advice for GRBs, I appreciate the great support from Prof. D. Q. Lamb and Dr. C. Graziani. I would like to express my deepest gratitude for the first three "senior" members of the WXM operation, Dr. Y. Shirasaki, Dr. T. Tamagawa, and Dr. K. Torii. Without their supports, I would not possible to express the great results of *HETE*.

I express my thank to Dr. J.-L. Atteia and Ms. C. Barraud for teaching and providing us their spectral analysis software of the FREGATE data. I also would like to thank Dr. M. Kippen for discussing about the spectral analysis of XRFs/GRBs and providing me the WFC/BATSE spectral parameters.

HETE is operated by the international collaborations of seven different countries. I am greatful to the all *HETE* members for developing and operating the *HETE* satellite and also give me the opportunity for joint the team and analyzing the data.

I want to thank Prof. K. Makishima, who is the chief scientist of the cosmic radiation laboratory at the Institute of Physical and Chemical Research (RIKEN), for supporting my graduate work. Last but not least, I wish to thank all the staffs, the post doctorates, and the graduate students of RIKEN, Tokyo Institute of Technology, and Los Alamos National Laboratory.